## *The seismic characterisation of layer 2 in oceanic crust around ODP borehole 504B*

GREGORY, EMMA,PHILIPPA,MAYO

# The seismic characterisation of layer 2 in oceanic crust around ODP borehole 504B

**Emma P. M. Gregory**

Department of Earth Sciences
University of Durham
UK


A thesis submitted for the degree of
*Doctor of Philosophy*
August, 2018

Software used:
This thesis was written using LaTeX. The references and citations were produced using BibTeX. All figures were plotted using *Generic Mapping Tools (GMT)*, written by Wessel and Smith (1998). *Inkscape* was used for image conversion and manipulation post-plotting. *Seismic Unix (Stockwell, 1999)* was used in conjunction with *GLOBE Claritas*$^{TM}$ to process and manipulate seismic data prior to plotting.

# Abstract

The seismic velocity structure of the oceanic crust is commonly used to ascertain its lithological structure and, as such, understand the dynamic processes of its formation at spreading ridges, its evolution as it ages off-axis, and its composition when it enters subduction zones. However, the interpretation of velocity models is complicated and hindered by a number of factors, namely the differences between various seismic modelling approaches; discrepancies between how the different velocity layers within the crust are defined; and a scarcity of velocity models with direct groundtruth. The complex nature of the controls on the measured velocity, such as the effects of hydrothermal alteration and the general increase in velocity as the crust ages, has lead to disparities in terminology used to describe the structure (i.e. seismic layers 2A, 2B, 2C and 3) and debates about whether the seismic layers represent different crustal lithologies, or other changes such as alteration fronts.

In this study, 3D seismic velocity models are produced of a 40 x 40 $km^2$ area of ~7 Ma oceanic crust at the location of DSDP/ODP borehole 504B - the deepest borehole currently drilled into in-situ oceanic crust - which are then interpreted alongside results from other seismic modelling approaches to produce a consistent definition of the seismic structure. At borehole 504B, the P-wave velocity structure comprises a 0.8 km-thick layer 2A, consisting of an upper, 0.5 km-thick low gradient region at ~4.5 km $s^{-1}$ overlying a 0.3 km-thick high gradient region where velocity increases from 4.7 to 5.5 km $s^{-1}$, termed the layer 2A/2B transition zone. Layer 2B increases in velocity gradually to reach 6.5 km $s^{-1}$ at 1.7 km bb, which is interpreted as the layer 2/3 boundary.

Using the velocity-depth gradient profile to define the seismic structure, rather than absolute velocity alone, results in greater consistency between different modelling approaches and different ages of crust. At borehole 504B, the layer 2A/2B transition zone is characterised by Vp gradients of >2 $s^{-1}$ in smooth tomographic inversion models, consistent with results from analysis of the 2A caustic arrival from long-offset MCS gathers. Groundtruthing to the borehole shows that this high velocity gradient region corresponds to a significant decrease in porosity, primarily caused by the change in lithology from extrusive lavas to sheeted dykes but also likely exacerbated by an alteration front to greenschist facies mineralisation. Similar correlations observed at another deep crustal borehole, ODP Hole 1256D, suggest that the gradient proxy could help to locate the extrusive-intrusive transition from seismic studies of magmatically-accreted crust which do not have a groundtruth.

The velocity structure at borehole 504B is typical of the surrounding oceanic crust, with little lateral variation within the study area. The relatively high layer 2A velocity shows that hydrothermal alteration has resulted in the decrease in open porosity in the crust since formation. Anisotropy and Poisson's ratio analyses, however, indicate that open, wider fractures remain in the crust, with a strong ridge-axis alignment below ~0.5 km into the basement.

# Declaration

This thesis describes my original work except where acknowledgement is made in the text. It does not exceed the word limit and is not substantially the same as any work that has been, or is being, submitted to any other university for any degree, diploma, or any other qualification.

Emma P. M. Gregory
August 2018

# Acknowledgements

First and foremost, my thanks must go to Richard and Christine for your effort, support and guidance throughout this project. Specifically, Richard, for your encouragement to pursue a PhD in the first place, and the example set by your interest in a huge variety of scientific problems and commitment to understanding uncertainties, and Christine, for your training in robust scientific methodology and attention to detail (and grammar!). Thanks also to Dean, for your encouragement and help along the way, and the many others involved in the OSCAR project for always keeping the picture big and interesting.

During this project my PhD fees and stipend were funded by the Charles Waites Scholarship. I am hugely indebted to the generosity of Charles and Millie Waites, who made an endowment for the scholarship in memory of their son, Charles, who studied for a Geology degree in the Department. My research costs were funded by the OSCAR project through grant NE/I0270010/1 from the UK's Natural Environment Research Council.

I would like to thank all involved in the planning and acquisition of data during research cruises JC114 and SO238, including the officers, engineers and crew of the RRS James Cook and R/V Sonne, the scientific parties, and all seagoing technicians. The NERC Ocean-Bottom Instrumentation Facility (Minshull et al., 2005) provided the OBSs used in this study, together with their technical support at sea. Special thanks must go to those that kept me (relatively) sane during the long months at sea, especially Anna on JC112/113 and Ben on JC114. The good company, and not just the excitement of shiny new data, is what made those experiences so enjoyable.

The postgraduate community in the Department has always been a source of entertainment, support, and cake, and I am particularly indebted to the past and present members of Geophysics Bay (although there will now be only one geophysicist - hold the fort, Olly!), especially Matt, Adam, Olly, Chris and Kit. Thank you for the coffee, crosswords, code sharing, and for putting up with my messiness. The leaders, volunteers and guests at FoodCycle Durham and Chester-le-Street have also given me many fond memories of my time in Durham, and helped provide a much-needed escape from the PhD bubble. My housemates over the past few years - Erin, Ben and, recently, Chris - have provided much laughter, good food, and ridiculousness, and I would like to particularly thank Erin for helping keep my spirits high over the past few months. Thanks also to Nico for putting me up for the last few hectic weeks.

I must also thank my family for their support and encouragement over the years, without which I wouldn't be where I am today. Finally, I would like to thank Edward, for supporting me as best he could from across the Channel and, more importantly, for always reminding me that there is much more to life than a PhD.

# Contents

# List of Figures

# List of Tables

## List of abbreviations and acronyms

**1D** - One-dimensional

**2D** - Two-dimensional

**3D** - Three-dimensional

**CDT** - Conductivity-Temperature-Depth

**CMP** - Common mid-point

**CRR** - Costa Rica Rift

**DSDP** - Deep Sea Drilling Project

**FAST** - First Arrival Seismic Tomography

**GEBCO** - General bathymetric chart of the oceans

**IODP** - International Ocean Discovery Program

**MCS** - Multichannel seismic

**NMO** - Normal moveout

**OBS** - Ocean bottom seismograph

**ODP** - Ocean Drilling Program

**RMS** - Root mean squared

**SAP** - Synthetic aperture profile

**SG** - South Grid

**SNR** - Signal-to-noise ratio

**TWTT** - Two-way travel time

**Vp** - P-wave velocity

**Vs** - S-wave velocity

**VSP** - Vertical seismic profile

**WA** - Wide-angle

$\sigma$ - Poisson's ratio

# Chapter 1

# Introduction and geological setting

## 1.1 Mid-ocean ridges and oceanic crust

The oceanic crust, created at mid-ocean ridges and recycled back into the mantle at subduction zones, forms over 60% of the Earth's surface (Figure 1.1). Mantle upwelling at mid-ocean ridges (MORs), driven by rifting and extension primarily caused by the pull of subducting slabs, results in a hot, crystalline mush zone and magma lenses at spreading centres (Langmuir et al., 1992) from which magma both erupts onto the surface and cools intrusively to form new, magmatic oceanic crust (Cann, 1970). Asthenospheric material cools and accretes to the base of the crust, forming the lower part of the oceanic lithosphere (Stein and Stein, 1992). However, the variety of plate separation, or spreading rates, from super-fast (>130-150 mm $yr^{-1}$ full spreading rate, Sinton et al., 1991) to ultra-slow (<20 mm $yr^{-1}$, Grindlay et al., 1998), alongside mantle temperature and compositional heterogeneities (Klein and Langmuir, 1987; Langmuir et al., 1992; Niu and O'Hara, 2008), introduces variability into the formation mechanism of the crust, with a lack of melt supply at some spreading centres resulting in large-scale faulting, necking and even mantle exhumation in order to accommodate the extension (Cann et al., 1997; Escartín et al., 1999; Dick et al., 2003; Cannat et al., 2006; Behn and Ito, 2008; Grevemeyer et al., 2018a). This variability in crustal composition and structure is exacerbated by the alteration of the crust by hydrothermal circulation as it moves off-axis, cools, subsides and is increasingly covered by sediment as it ages (Christensen, 1970; Stein and Stein, 1992; Ridley, 1994; Alt et al., 1996; Carlson, 2011; Hasterok, 2013; Harris et al., 2015; Patten et al., 2016). The structure and composition of the oceanic crust when it is subducted into the upper mantle is a primary control on slab dehydration mechanisms (Schmidt and Poli, 1998), with implications for earthquake nucleation (Kerrick and Connolly, 2001; Hacker et al., 2003) and the dynamics of arc volcanism (Elliott et al., 1997) at convergent plate boundaries. Therefore, the current lack of understanding of the variable nature of the oceanic crust is a crucial problem that requires further research.

The primary method of mapping the structure of oceanic crust is through velocity models derived from seismic surveys (Raitt, 1963; Houtz, 1976; White et al., 1992; Chris-

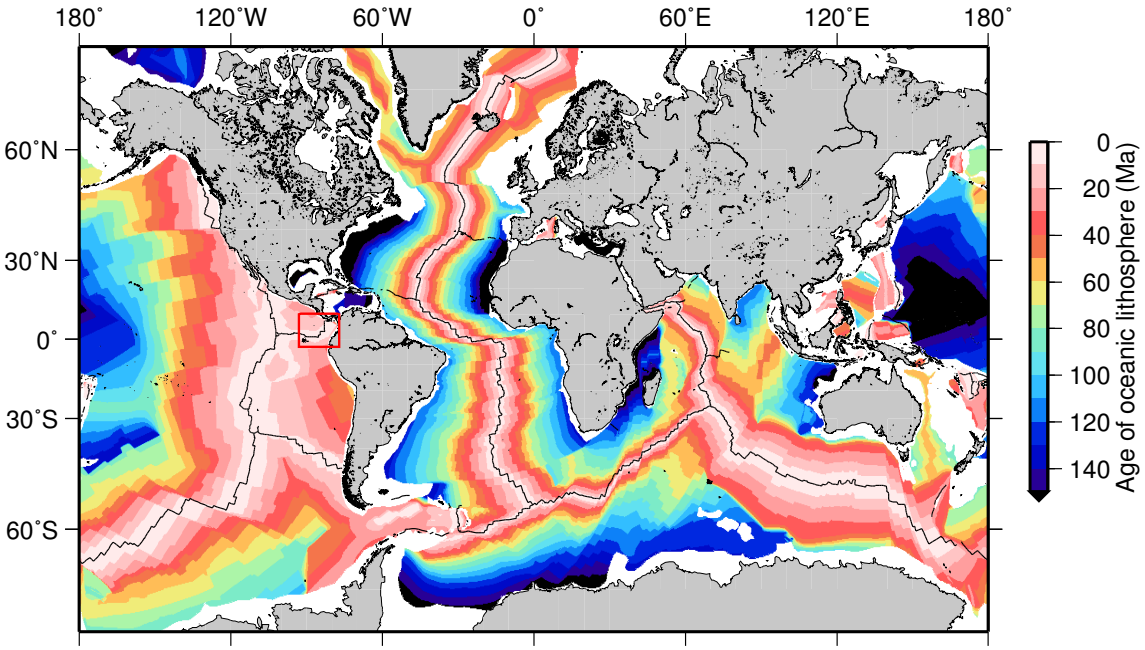


Figure 1.1: Global map of the age of oceanic lithosphere (Müller et al., 2008), showing the mid-ocean ridge system and other oceanic spreading centres (black lines). The study area, the Panama Basin, is outlined by the red box and area shown in focus in Figure 1.4.

teson et al., 1992; Harding et al., 1993; Hooft et al., 2000; Dunn et al., 2005; Van Avendonk et al., 2017; Grevemeyer et al., 2018b). However, accurate interpretation of lithological structure from velocity is hindered by the complexity of controls on the seismic response of the subsurface (Wilkens et al., 1991; Berge et al., 1992; Carlson, 2001, 2011, 2014), and a lack of models which have direct groundtruth. Even velocity models of magmatically-accreted oceanic crust, which usually exhibits a simpler, more consistent structure than tectonically-formed crust, are variably interpreted in terms of subsurface characteristics, particularly in the case of the upper ∼2 km of oceanic crust, 'seismic layer 2', and its subsidiary layers '2A', '2B' and '2C', which have been used conflictingly within different studies to determine changes in lithology, alteration or fracturing (Christeson et al., 1992; Barclay et al., 1998; Canales et al., 2005; Van Ark et al., 2007; Christeson et al., 2007). A better characterisation of layer 2 in magmatic crust, and what it represents in terms of subsurface structure, would act as a useful foundation for furthering the understanding of oceanic crust.

### 1.1.1 Lithological structure of oceanic crust

The lithological structure of the oceanic crust has been defined primarily through studies of ophiolites (Penrose Conference Participants, 1972), sections of oceanic crust uplifted and obducted onto continents, as well as detailed bathymetric surveys, submersible mapping of exposed scarps (Juteau et al., 1995; Francheteau et al., 1992), rock samples collected from the seafloor, and the drilling of boreholes in the oceanic crust (Anderson et al., 1982; Wilson et al., 2006). The currently widely accepted model of magmatic accretion proposes

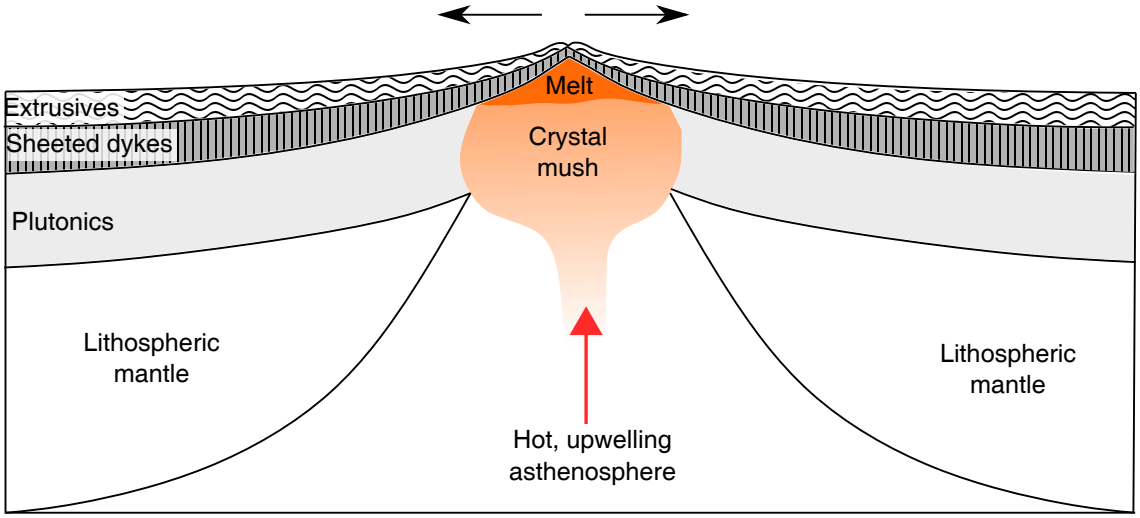


Figure 1.2: Simplified diagram of the formation of oceanic crust. Upwelling asthenospheric material forms a mush zone and melt lens(es), which erupts at the spreading ridge to form the extrusive layer through a complex of feeder dykes which cool intrusively. Melt solidifies to form the plutonic lower crust, to which mantle material accretes to create the lower oceanic lithosphere. Diagram is not to scale.

the crust, on average 6 km-thick (Grevemeyer et al., 2018b), forms from shallow magma lenses at the very top of the asthenosphere at mid-ocean ridges (Figure 1.2). Extrusive eruptions to the seabed form a top layer of primarily basaltic pillow lavas and sheet and massive lava flows. These eruptions are predominantly supplied by sets of intrusive feeder dykes, which cool to form a sheeted dyke complex beneath the extrusive layer, with dyke orientations striking parallel to the ridge axis. Beneath the basaltic layers lies a thick, massive complex of plutonic gabbroic rocks, formed either by the cooling and subsiding of the magma source chamber (the 'gabbro glacier' model, Henstock et al., 1993), or by the solidifying of a series of magma sills at different depths in the newly forming crust (the 'sheeted sills' model, Boudier et al., 1996).

If the magma supply is not sufficient to match the rate of spreading, extension must be accommodated through tectonic stretching of the lithosphere. This most often results in normal-type basement faults that dip towards the ridge axis. These faults are a characteristic feature of the oceanic crust, but most common and larger offsetting at ridges with a less robust magma supply, such as the Mid-Atlantic Ridge. High proportions of phases of tectonically-dominated accretion are more common at slow and ultra-slow spreading ridges, and can create crust with a thin or non-existent basaltic layer (Cannat et al., 2006), and with uplifted and exhumed mantle peridotites forming oceanic core complexes (MacLeod et al., 2009).

This initial diversity in new oceanic crustal structure then becomes more complicated as the crust ages and evolves: off-axis volcanism adds new magmatic material (Davis, 1982; Cooper et al., 2003); increasing thicknesses of sediments form a thick drape on the top of the igneous basement (Stein and Stein, 1992); circulating seawater causes hydrothermal precipitation and alteration of minerals (Alt et al., 1993; Carlson, 2011), and tectonic

forces close to subduction zones can result in further fracturing, deformation, hydration and alteration (Grevemeyer et al., 2018b). The resulting crust that enters trenches at subduction zones and is recycled into the mantle can, therefore, be significantly evolved from when it formed at a spreading centre. The structure and composition of this crust can have implications for the dynamics of subduction (Schmidt and Poli, 1998), and the composition and behaviour of melts which can form volcanic arcs or back-arc spreading centres (Kerrick and Connolly, 2001).

### 1.1.2 Seismic structure of oceanic crust

The primary method of mapping the structure and variability of in-situ oceanic crust is through seismic surveys. These can provide both seismic reflection images and seismic velocity models of the crust over survey regions up to hundreds of kilometres in size, and down to lateral and vertical resolutions to tens of metres, with the more recent advances using full-waveform inversion (Virieux and Operto, 2009). Early seismic studies of the crust (Raitt, 1963) characterised its velocity structure into three main layers:

- **layer 1** is characterised by low velocities of 1.6–2.5 km $s^{-1}$, and is widely assumed to correspond to the top sediment layer, which is thin or absent at ridge axes, but can be considerably thick on older oceanic crust, e.g. ∼7 km on 140 Ma Pacific crust (Shearer and Orcutt, 1986);

- **layer 2** has traditionally been characterised by velocities of 2.2–6.6 km $s^{-1}$, relatively high velocity-depth gradients (1–2 $s^{-1}$), and considerable variability in structure. It varies in thickness but is, on average, ∼2 km thick (White et al., 1992) and is commonly sub-divided into two (2A, 2B) or three (2A, 2B, 2C) layers based on changes in velocity and gradient (Figure 1.3); and

- **layer 3** is defined as having a relatively narrow velocity range of 6.6–7.6 km $s^{-1}$ (White et al., 1992) or 6.93–7.18 km $s^{-1}$ (Grevemeyer et al., 2018b), low velocity gradients (∼0.1 $s^{-1}$) and a relative lack of variability compared to layer 2. It is commonly ∼5 km thick (White et al., 1992) with its base, defined by the Mohorovičić discontinuity where seismic velocities increase to ∼8 km $s^{-1}$, interpreted as the crust-mantle boundary.

Seismic layer 2 has been traditionally associated with the basaltic upper crust and layer 3 the plutonic lower crust (Raitt, 1963). Discrepancy between the higher velocity measured in basalt samples in laboratories (∼5–6 km $s^{-1}$), and that of the in-situ upper crust is generally explained by the presence of large-scale porosity in the upper crust from fractures and void space (Spudich and Orcutt, 1980). At ridge axes, layer 2 is often divided into sub-layers 2A and 2B, traditionally associated with the more porous extrusive pillow lavas and the less porous sheeted dyke complex respectively (Houtz and Ewing, 1976; Herron, 1982; Christeson et al., 1992). For predominantly older crust off-axis, early seismic observations (Houtz and Ewing, 1976) suggested that layer 2 was partitioned into three layers, 2A, 2B

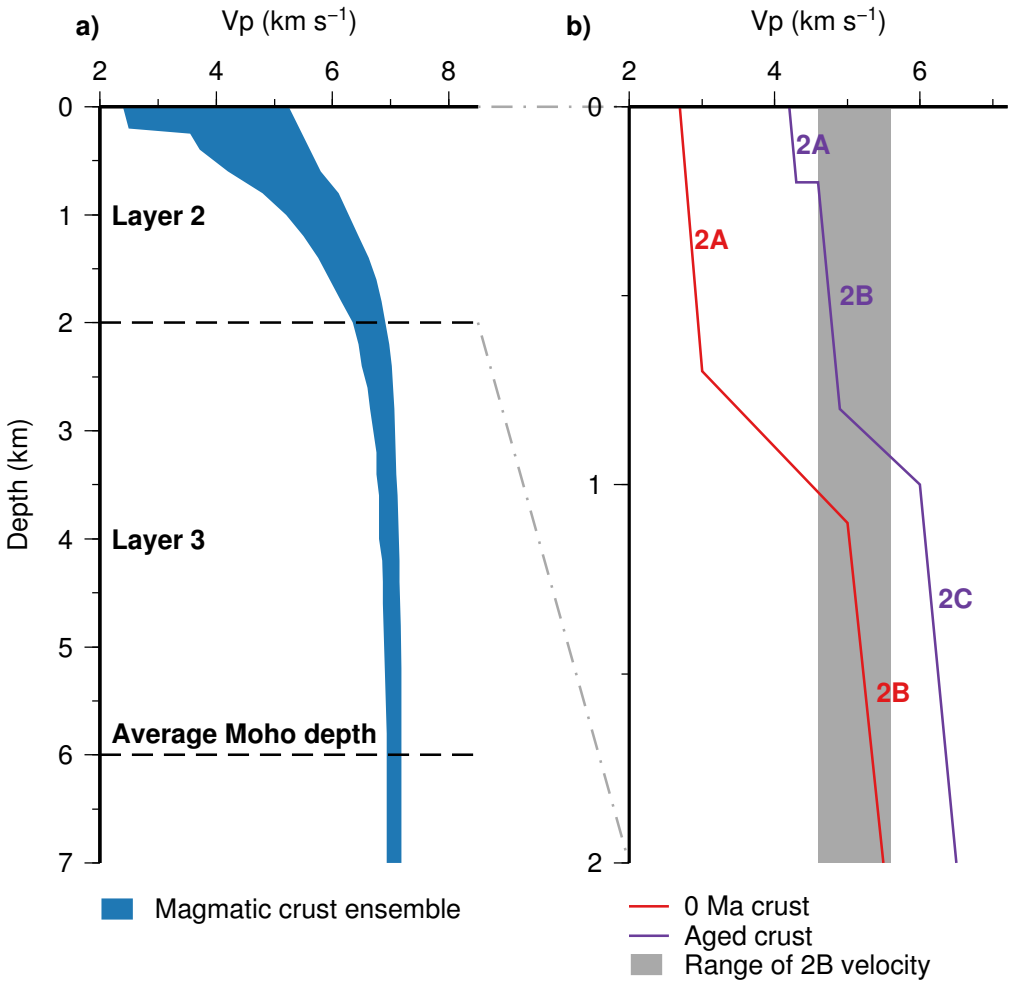


Figure 1.3: Seismic structure of oceanic crust. a) Magmatic crust ensemble compiled by Grevemeyer et al. (2018b). b) Hypothetical layer 2 seismic structure, showing a generic representation of the terminology applied on-axis to 0 Ma crust and off-axis to aged crust (after Houtz and Ewing, 1976; Anderson et al., 1982; Nedimović et al., 2008).

and 2C. In this definition, layers 2A and 2B are identified as being associated with less or more hydrothermally altered extrusive lavas, and layer 2C represents the intrusive sheeted dykes. This nomenclature disparity can create a contradiction between the lithological interpretation of the seismic layers, as on-axis layer 2B is assumed to correspond to the sheeted dykes, but off-axis to the lower, altered extrusives, with layer 2C now representing the dykes.

Although most authors agree that the predominant cause of the layer 2A/2B boundary is a reduction in crustal porosity (e.g. Carlson, 2001; Christeson et al., 2007), it is suggested that this porosity change may not be primarily due to the transition from extrusively-formed pillows and lava flows to intrusively-formed dykes, but instead to an alteration front within the crust (Christeson et al., 2007; Carlson, 2011). An increase in intensity of alteration could cause the observed increase in seismic velocity at the boundary if increased mineralisation also infills or 'seals' a higher proportion of cracks and fractures within the crust. This theory is supported by:

- early interpretations of sonic velocity logs at the deep crustal borehole 504B (Anderson et al., 1982);

- comparisons of seismic velocity structure found at other locations to laboratory analysis of oceanic rocks or results from borehole 504B (Rohr et al., 1988; Harding et al., 1989; Vera et al., 1990);

- observations of inconsistencies between the thickness of layer 2A, and the thickness of the extrusive lavas mapped at a nearby exposed scarp (Christeson et al., 2007);

- the variable mapping of the bottom of layer 2A to either the top of the lava-dyke transition zone, or within the zone, located at nearby scarps (Christeson et al., 2010);

- or modelling of downhole permeability at boreholes 504B and 1256D (Carlson, 2011).

Further studies have also proposed that the boundary may be controlled by fracturing fronts in the crust (Carlson, 2010), changes in crack aspect ratio (Carlson, 2014), or a combination of factors which change as the crust ages (Christeson et al., 2012).

Seismic layer 3, often known as the 'oceanic layer' due to pervasive observations of it during early seismic studies (e.g. Raitt, 1963), is commonly assumed to correlate to the gabbroic lower crust, due to its characteristic velocity range (White et al., 1992; Carlson and Miller, 2004), and studies of ophiolite structure (e.g. Karson et al., 1984). Usually based on this assumption, the depth, thickness and other characteristics of layer 3 are linked to the speed and dynamics of spreading at a mid-ocean ridge (Purdy et al., 1992), magma melting and crustal accretion processes (gabbro glacier vs. multiple sills - Wilson et al. (2006)), on-axis deep hydrothermal circulation regimes (Vanko, 1988), and faulting and hydration of the crust at subduction zones (Grevemeyer et al., 2018b). However, some studies argue that the layer 2/3 boundary does not represent the lithological change from basalts to gabbros, but instead represents a metamorphic front from greenschist to amphibolite facies (Christensen and Salisbury, 1975; Christensen and Smewing, 1981). Studies at boreholes 504B and 1256D have even suggested that the layer 2/3 boundary may occur within the sheeted dyke complex (Alt et al., 1996), or below the first occurrence of gabbroic rocks (Wilson et al., 2006), which may suggest that instead of representing a change from the heterogeneous, basaltic upper crust to a homogeneous complex of gabbros, the layer 2/3 boundary may also be controlled by an alteration front or porosity change unrelated to a lithology change.

These debates about how to define seismic layers within the oceanic crust, and what these layers represent in terms of lithology, make it difficult to consistently interpret seismic velocity models, and use the models to compare crust at different locations and resulting from a different spreading styles and formation mechanisms.

### 1.1.3 Hydrothermal circulation and alteration

As newly-formed oceanic lithosphere spreads away from the MOR it cools, its density increases, and the lithosphere subsides to maintain isostatic equilibrium. Half-space cooling models of the heat flow from the lithosphere (Stein and Stein, 1994; Hasterok, 2013) consistently over-predict conductive heat flow compared to measurements for crust <50 Ma on average, although the age at which the predictions and observations begin to agree varies from ∼25–75 Ma in highly to poorly sedimented crust, respectively (Hasterok, 2013). This discrepancy has been attributed to the removal of heat through advection by hydrothermal circulation (Stein and Stein, 1994). Hydrothermal circulation has been observed at ridge axes as upwellings of hot fluids (up to 400°C) through 'black smoker' vents (Spiess et al., 1980; Von Damm, 1990), as well as cooler discharge sites on ridge flanks (Kelley et al., 2001). Samples of oceanic crust obtained from dredging, drilling and from ophiolites, show evidence for extensive hydrothermal circulation through alteration at all depths within the crust. Low-temperature circulation occurs in the upper crust through downwelling seawater, resulting in the deposition of low-temperature alteration minerals such as zeolite, celadonite and and talc within porosity. High-temperature alteration is usually confined to the lower oceanic crust, and is thought to occur close to the ridge axis where cooling melt lenses can provide a high heat source. This alteration produces minerals such as albite, epidote and chlorite and, at higher pressures and temperatures deeper in the crust, actinolite, and amphibolite. Although this more high temperature, intense alteration is thought to occur close to ridge axes, the circulation of lower temperature fluids has been observed to continue on ridge flanks, suggesting that alteration continues throughout the crustal life cycle (Alt et al., 1986). Hydrothermal circulation is responsible for considerable transfer of mass and heat between the crust and ocean, having effects on crustal structure, composition and physical properties, and lithologically evolves the crust as it ages away from the ridge axis. The agreement between theoretical and observed heat flow measurements from 50 Ma has, thus, been interpreted to indicate that significant circulation within the crust ceases by this age, potentially due to the crust being sealed from the ocean by sedimentation. However, some heat flow measurements provide an agreement between theoretical and observed values at a much younger age e.g. ∼7 Ma (CRRUST, 1982), and low heat fluxes have been unexpectedly observed in highly sedimented, older crust (Langseth and Silver, 1996), suggesting that hydrothermal circulation processes are far more variable than previously thought.

The extent of hydrothermal alteration within oceanic crust of different ages has also been interpreted from changes in the seismic velocity-depth structure of the upper crust. An analysis of studies conducted between 1971 and 1994 (Grevemeyer and Weigel, 1996) demonstrates an increase in layer 2A velocity with age, regardless of spreading rate, with velocity doubling from an average zero-age velocity of 2.1 km $s^{-1}$ within 10 Ma. This observation is supported by further studies, with Grevemeyer et al. (1998) observing an increase in layer 2A velocity at the East Pacific Rise at 14°S from ∼2.9 km $s^{-1}$ at 0.5 Ma to

4.9 km $s^{-1}$ at 8.3 Ma, and Nedimović et al. (2008) observing an increase at the Juan de Fuca Ridge from ∼2.5 to 4.0 km $s^{-1}$ at the Endeavor segment over ∼5 Ma; and ∼2.3 to 3.7 km $s^{-1}$ over ∼7 Ma at the Northern Symmetric segment. The increase in layer 2A velocity has been attributed to the infilling of porosity and cracks with mineral precipitates from circulating seawater during off-axis hydrothermal circulation (Houtz and Ewing, 1976; Grevemeyer and Weigel, 1996; Carlson, 1998), with the rapid rate of up to a doubling in velocity within the first 10 Ma attributed to the primary infilling of thinner cracks and pores (Wilkens et al., 1991; Grevemeyer and Weigel, 1996). This infilling of small voids can occur relatively quickly due to the small amounts of products needed (when compared to infilling wider fractures), and as seismic velocities are sensitive to the presence of thinner cracks and pores, has a disproportionate effect on the velocity, such that only a 5% decrease in porosity can result in a doubling of the velocity. It has also been suggested that the increase in sedimentary cover over older crust may prevent significant hydrothermal circulation, which may explain why velocities tend not to apparently significantly increase past ∼10 Ma (Grevemeyer and Weigel, 1996). However, more gradual increases in velocity observed at the sediment-poor ridge flanks of the Juan de Fuca Ridge, compared with the sediment-rich flanks, lead Nedimović et al. (2008) to conclude that sediment blanketing may accelerate the evolution of layer 2A.

#### Seismic anisotropy

Extensional stresses acting at the spreading ridge as the crust forms and spreads off-axis result in a directional structural fabric, with ridge-aligned faults, fractures and small cracks . This inherited fabric results in anisotropy within the crust, where velocity varies with horizontal azimuth, which has been documented at numerous ridge axis spreading at different rates including the slow-spreading Mid-Atlantic Ridge (White and Whitmarsh, 1984), fast-spreading East Pacific Rise (Dunn and Toomey, 2001) and intermediate-spreading Galapagos Spreading Centre (Canales et al., 2014). As the crust ages, the infilling of fractures and pore spaces with mineral precipitates reduces the magnitude of this anisotropy (Fryer et al., 1989). However, the observation of azimuthal anisotropy within ∼140 Ma crust (Shearer and Orcutt, 1985) suggests that this signature is never completely erased. Thus, the magnitude, or variation in the magnitude, of anisotropy observed within the crust can act as a proxy for the pervasiveness of hydrothermal alteration, and how 'sealed' different parts of the crust have become.

## 1.2 Outstanding questions

Despite extensive seismic surveys of the oceanic crust in a diversity of settings since the 1950's, and considerable efforts to drill a deep borehole through the oceanic crust since Project Mohole over five decades ago (Bascom, 1961), its nature, variability and evolution are still not entirely understood, and neither are the interaction and linkages between

the crust and the overlying ocean through hydrothermal circulation. The interpretation of seismic layers in the oceanic crust, and indeed even how these layers are defined, is inconsistent between studies, and there is a lack of geophysical surveys with coincident groundtruth to help resolve the debate. It is also not well understood how the crust evolves due to hydrothermally driven fluid flow, and the influence that this has on the physical properties of the crust such as its seismic velocity. Does alteration occur solely close to the ridge axis, or does it continue to occur in crust up to 10 Ma, 50 Ma, or even until it is recycled during subduction? Foremost is the requirement to better understand how to interpret the seismic structure of oceanic crust, since this is the primary method of mapping its structure and variability. This understanding must extend how to relate the results of different types of seismic experiment, such as wide-angle refraction and multichannel seismic reflection acquisition, and to comprehending what causes the different recorded arrivals from the crust. This study aims to better understand how to interpret the seismic structure of the upper oceanic crust and, particularly, to address the questions:

- how should we interpret the arrivals detected during seismic surveying, and what can their modelling, undertaken in a variety of ways, tell us?,
- what controls the seismic velocity of the oceanic crust, and how can its seismic structure be consistently ascribed into lithologically meaningful layers?, and
- which processes influence velocity as the crust ages and how do these processes effect the structure and composition of the crust at different depths?

To answer these questions, seismic velocity models of the oceanic crust will be produced and, vitally, tied to coincident, sampled lithologies and physical properties. An extensive geophysical dataset acquired by the OSCAR project (Section 1.5) in 2015 (Hobbs and Peirce, 2015) at the Costa Rica Rift at DSDP/ODP borehole 504B, the deepest borehole currently drilled into the oceanic crust, provides the means to address these questions.

## 1.3 Geological setting of the Panama Basin and Costa Rica Rift

The Costa Rica Rift (CRR) spreading ridge is the eastern-most segment of the Cocos-Nazca Rift (CNR), located in the eastern equatorial Pacific (Figure 1.4). This part of the CNR lies within the Panama Basin, a deep oceanic basin enclosed to the north and east by Central and South America, and to the north-west and south by the submerged, aseismic Cocos and Carnegie Ridges, formed by volcanism from the nearby Galapagos hotspot. These barriers isolate deep water within the basin (below 2000 m) from the rest of the Pacific, apart from a few deep channels such as offshore Ecuador.

The CRR trends approximately E–W and is bounded by the Panama fracture zone to the east and the Ecuador fracture zone to the west. Similar to the other segments of the

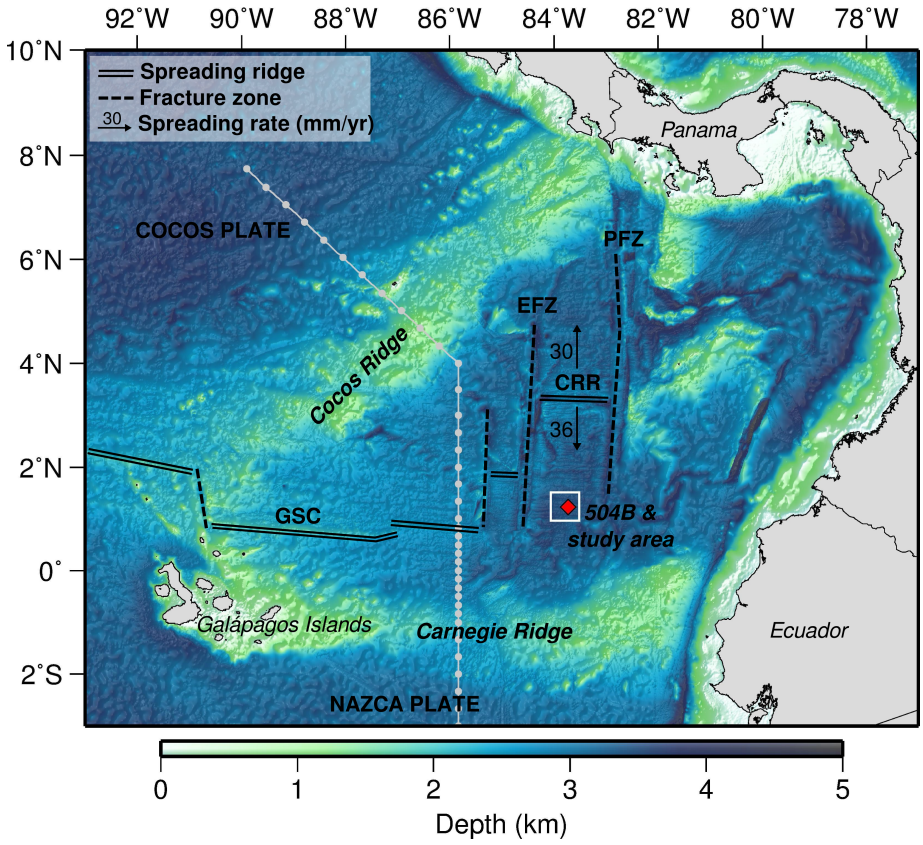


Figure 1.4: Bathymetric map of the Panama Basin and the eastern spreading segments of the Cocos-Nazca Rift, with the global location indicated in Figure 1.1. CRR=Costa Rica Rift; GSC=Galapagos Spreading Centre; PFZ=Panama Fracture Zone; and EFZ=Ecuador Fracture Zone. Borehole 504B is indicated by the red diamond, and the study area is boxed in white. The location of the World Ocean Circulation Experiment (WOCE) profile plotted in Figure 1.6 is shown by the grey circles.

CNR, the CRR is currently spreading at an intermediate rate, although asymmetrically with a half-rate of 36 mm $yr^{-1}$ to the south and 30 mm $yr^{-1}$ to the north (Hey, 1977). Tectonic reconstructions of the region suggest several spreading rate changes since the CRR formed ~15 Ma (Meschede and Barckhausen, 2000), in response to changes in absolute plate motion and other tectonic events in the wider Pacific (Wilson and Hey, 1995; Krijgsman et al., 1999; Wilson et al., 2018).

Located on the south flank of the CRR, ~230 km from the ridge axis, is deep crustal DSDP/ODP borehole 504B, which is drilled into 6.9 Ma crust. This borehole and the surrounding region are the focus for this study.

## 1.4 Existing datasets

Borehole 504B is, to date, the deepest borehole drilled into in-situ oceanic crust, penetrating to a total depth of 1.837 km into the igneous crust. Drilling was accomplished during seven legs from 1979 to 1993, providing a comprehensive series of measurements and observations of the lithological structure, composition and physical properties within the

borehole. To complement the drilling results, several geophysical studies have focussed on the borehole and surrounding area, including a previous seismic refraction experiment (Detrick et al., 1998). Borehole 504B, therefore, provides a thoroughly studied groundtruth to tie to seismic velocity models. It's use as a standard reference for oceanic crustal structure (e.g. Bratt and Purdy, 1984; Carlson and Herrick, 1990; Cudrak and Clowes, 1993; Grevemeyer et al., 1999; Harris et al., 2015; Christeson et al., 2016) , also makes it an ideal site to characterise the relationship between seismic velocity structure and the lithology of the crust.

### 1.4.1 DSDP/ODP borehole 504B

Borehole 504B was first drilled by Deep Sea Drilling Project (DSDP) legs 69 and 70 in 1979 in order to investigate geothermal processes in the oceanic crust, penetrating to a depth of 0.562 km below top basement (km bb) (CRRUST, 1982). Further DSDP drilling legs in 1981 (leg 83), and its successor the Ocean Drilling Program (ODP) in 1986 (leg 111), 1991 (legs 137 and 140) and 1993 (leg 148) deepened the borehole to its current depth of 1.837 km bb. The following summary of the downhole structure is condensed from Becker et al. (1989) and Alt et al. (1996). The borehole initially sampled 0.275 km of sediments, consisting of siliceous oozes, chert, limestone and chalk, overlying igneous oceanic crust. A 0.575 km-thick basaltic extrusive section consists of pillow lavas, massive lava flows and breccias which have undergone low-temperature alteration by the circulation of cool seawater. Below is a 0.209 km-thick transition zone, consisting of pillow lavas with an increasing proportion of dykes with depth, and containing an alteration front formed by the mixing of cool, down-welling seawater with hot, upwelling hydrothermal fluids, creating an abrupt zone of intense mineralisation and a downhole metamorphic grade change to greenschist facies mineral phases. A 1.050 km-thick complex of sheeted diabase dykes beneath the transition zone extends to the base of the borehole. This section exhibits progressively higher temperature alteration with depth, with the lower half of the dykes, from 1.3 km bb to the base of the borehole, consisting of rocks which have experienced an earlier, higher-temperature phase of alteration than the greenschist regime, and that have been leached of sulphur and metals such as zinc and iron.

Suites of downhole logs characterise the physical properties within the borehole, and show a decrease in porosity from >10% at the top of the borehole to ∼1% at the base, and increases in electrical resistivity and bulk density downhole. Sonic velocity logs characterise both the Vp and Vs of the formation, with low, highly variable velocity (Vp varies between 4–6 km $s^{-1}$) within the upper ∼0.8 km of basement, and a change to higher (Vp>6 km $s^{-1}$), more consistent velocity from this depth to the base of the borehole.

### 1.4.2 Geophysical studies

Various geophysical studies and regional seismic experiments have characterised the velocity structure at and surrounding borehole 504B (Figure 1.5). Measurements made

within the borehole itself include sonic velocity logs, a vertical seismic profile (VSP), and an oblique seismic experiment (OSE). Sonic velocity logs (Cann and Von Herzen, 1983; Becker and Sakai, 1988) are interpreted to divide layer 2 into three layers, with a thin (∼100 m-thick), highly fractured layer 2A of velocity mostly between 3.0–4.0 km $s^{-1}$, a layer 2B of velocity between 4.5–5.5 km $s^{-1}$ and a layer 2C of velocity in the range of 6.0–6.5 km $s^{-1}$ and reaching a maximum of ∼6.8 km $s^{-1}$, typical of layer 3, within 50 m of the base of the borehole (Alt et al., 1993). The OSE (Little and Stephen, 1985) produced a relatively smoothly increasing velocity-depth profile to 1.4 km bb, with no sharp velocity changes correlating to either lithological or alteration boundaries, and also suggests the presence of azimuthal anisotropy in the uppermost 50-100 m of the basement with an E–W, ridge-parallel fast direction and maximum parallel-to-perpendicular velocity difference of 0.8 km $s^{-1}$. Little and Stephen (1985) attribute the smoothness of the profile to the averaging of the velocity-depth function over a variable 8 km-wide area. The VSPs (Becker and Sakai, 1988; Swift et al., 1998b) show comparable vertical velocity to the horizontal from the OSE, within error, suggesting that there is no significant transverse anisotropy within the upper oceanic crust here. These observations also agree with smoothed sonic log measurements. A change in VSP velocity gradient at 0.875-0.925 km bb is interpreted as the seismic layer 2/3 boundary (Swift et al., 1998b), lying at the top of the sheeted dyke complex where the P-wave velocity reaches ∼6.5 km $s^{-1}$.

Larger-scale seismic experiments include a sonobuoy seismic reflection/refraction study (Hobart et al., 1985), which reports high velocity gradients in the middle crust, a 1.8 km-thick low velocity zone above the Moho, and a crustal thickness of 5 km (Collins et al., 1989). A 3D ocean bottom seismograph (OBS) seismic refraction experiment observed the upper 2 km of basement to be relatively homogeneous, with regions of faster velocity beneath basement ridges and slower velocity beneath flanking basement troughs (Detrick et al., 1998). Anisotropy of 2–4% was observed in the upper crust, with a ridge-parallel fast direction, and was attributed to aligned fractures formed at the adjacent spreading ridge.

## 1.5 OSCAR project

This study forms a part of a large, multidisciplinary experiment within the Panama Basin: the OSCAR (Oceanographic and Seismic Characterisation of heat dissipation and alteration by hydrothermal fluids at an Axial Ridge) project (Hobbs and Peirce, 2015). The objectives of this project were to investigate the evolution of oceanic crustal structure and the interaction between the crust and ocean bottom waters, using a comprehensive dataset acquired between 2014 and 2015 involving the acquisition of geophysical, physical oceanographic and heat flow data.

The dynamics of hydrothermal circulation within the oceanic crust not only has implications for the evolution of the lithosphere, but also the mass and heat balance of the deep oceans. Both focussed, high-temperature hydrothermal flow near ridge axes, and diffuse,

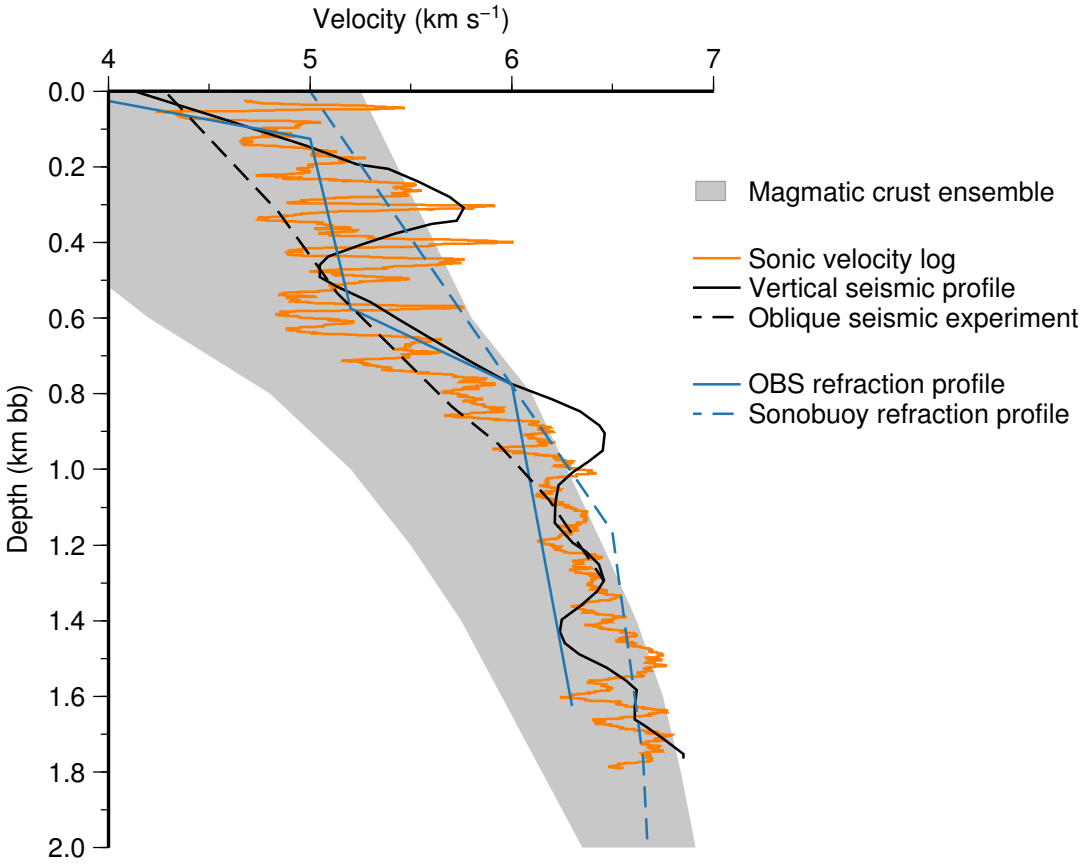


Figure 1.5: Velocity-depth profiles previously produced for borehole 504B, compared with the magmatic crust ensemble (Grevemeyer et al., 2018b). Profiles are consistent regardless of whether they were acquired within the borehole (Guerin et al., 2008), by vertical seismic profiling (Swift et al., 1998b) or oblique seismic imaging (Little and Stephen, 1985), or were regional refraction studies using sonobuoys (Collins et al., 1989) or OBSs (Detrick et al., 1998). Despite this consistency in large-scale structure however, there are significant differences in the degree of internal structure, from high variability in the sonic log, to no distinct changes in the oblique seismic profile.

cooler flow by high-volume discharge on ridge flanks, can provide a significant amount of heat to cold, abyssal ocean waters, and turbulence needed for mixing, as well as constant, conductive heat flow (Hofmann and Morales Maqueda, 2009; Barnes et al., 2018). Many ocean circulation models either disregard geothermal heating as negligible, or oversimplify the input to a global average per surface area of seafloor. However, introducing more accurate geothermal inputs, such as changing the heat flow inputs from the seafloor relative to plate age, can have a significant outcome for circulation models (Adcroft et al., 2001; Emile-Geay and Madec, 2008). The potential influence of geothermal heating on abyssal ocean waters may be seen in a profile of physical oceanographic measurements taken by WOCE in the 1990's (Talley, 2007), across the Panama Basin (Figure 1.6). This profile shows a significant increase in bottom water temperature as it crosses from the open Pacific Ocean to inside the basin, whose deep waters (below 2 km depth) are almost completely isolated from the Pacific by the Cocos and Carnegie Ridges (Figure 1.4). This temperature increase could be linked to the heat output from the oceanic spreading cen-

tres of the Cocos-Nazca boundary located within the basin, with the greatest measured temperature occurring as the profile crosses the Galapagos Spreading Centre.

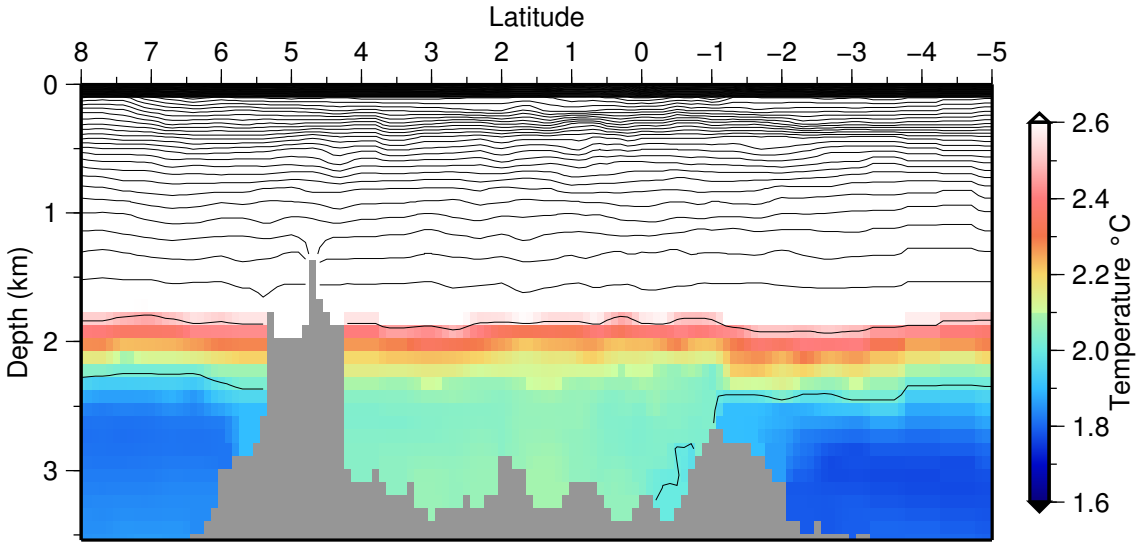


Figure 1.6: Ocean temperature from CTD measurements from the WOCE (Talley, 2007), profile P19 (location shown in Figure 1.4), passing through the Panama Basin. Abyssal waters below ∼2 km depth are warmer within the basin than in the open Pacific. Contours are plotted every 0.5°C.

The OSCAR project aimed to better understand the effects of geothermal heating on abyssal ocean waters within the Panama Basin, and the effects of heat loss and hydrothermal circulation of the structure and composition of the oceanic crust as it ages from the CRR to the location of borehole 504B in ∼7 Ma crust. The results of this study, aside from addressing the questions detailed in Section 1.2, also characterises the end-member 'aged' crust within the OSCAR project work area, and provides a link to ground-truth the seismic velocity models to the lithology sampled within borehole 504B.

## 1.6 Summary of this study

In this study a new, extensive seismic dataset acquired in the region surrounding borehole 504B is used to characterise the seismic structure of the upper crust and groundtruth it to the lithologies sampled within the borehole.

In this chapter, the background to the study has been outlined, detailing the current understanding of the seismic structure of the oceanic crust, the current debates surrounding how it may be interpreted, and the impact for seismic observations of lithology and structure of the alteration of oceanic crust by hydrothermal circulation. The wider implications of this study have been outlined, namely the understanding of the composition and evolution of the oceanic crust from mid-ocean ridge to subduction zone, but also the ocean-crust interactions and the significant influence this may have on global ocean circulation. The purposes of this work are to update our understanding of the seismic structure at the deepest borehole currently drilled into the oceanic crust, relate this to lithological

structure, and understand how the crust has been altered at this location, is addressed in the following chapters.

Chapter 2 introduces the 3D seismic dataset analysed in this study. This chapter includes the processing and results from the multichannel seismic (MCS) reflection data, alongside the initial processing of the OBS wide-angle (WA) seismic data. Chapter 3 describes the identification and picking of WA P-wave arrivals through the crust, and tomographic modelling methods and results. These methods consist of initial forward modelling in 2D, then performing 3D inversion to derive the P-wave velocity structure of the upper crust in the study area. Chapter 4 presents the methods used to test the resolution of, and uncertainties within, the 3D P-wave velocity model, to allow an informed interpretation of its structure, and any velocity anomalies within the model. Chapter 5 describes and identifies the different forms of P-wave to S-wave mode conversions recorded by the OBSs. These mode conversions are then picked, and modelled using the same 3D inversion techniques described in Chapter 3 to produce a 3D S-wave velocity model of the study area. This model is compared with its equivalent P-wave model to produce a 3D Poisson's ratio model, which can be used to appraise fracturing within the crust. Fracturing patterns are further investigated by analysis of azimuthal anisotropy, using travel time residual from both P-wave and S-wave velocity models. Chapter 6 analyses in more detail the 1D structure at borehole 504B, extracted from the 2D and 3D velocity models, and appraises methods to define the seismic layers within the oceanic crust. This structure is compared to estimates of seismic structure made from evaluating a seismic arrival recorded on long-offset MCS gathers which is commonly used to map the structure of the upper oceanic crust. These results are then compared with the lithology and physical properties sampled in the borehole, from core analysis and downhole logging, to try and understand the correlation between rock characteristics and seismic velocity. In Chapter 7, the results are synthesised, interpreted, and discussed in relation to previous studies and their wider implications drawn. Chapter 8 summarises the findings of this study, and recommends avenues for future work.

# Chapter 2

# South Grid dataset

## 2.1 Introduction

The OSCAR project (Section 1.5) conducted an active seismic experiment in the Panama Basin in 2015, primarily during cruise JC114 aboard the RRS James Cook (Hobbs and Peirce, 2015). The principal locations of data acquisition were at the Costa Rica Rift (CRR), the area around borehole 504B ∼230 km south of the CRR, and in a flowline window of crust in between (Figure 2.1). The geophysical datasets collected in these areas are called the North Grid (NG), South Grid (SG), and Synthetic Aperture Profile (SAP) datasets, respectively. Further research cruises, also part of the OSCAR project, collected conductive heat flow measurements (JC113) and physical oceanographic data (JC112 and RV Sonne cruise SO238) throughout the Panama Basin. During cruise SO238, the RV Sonne acted as a second seismic source vessel during the seismic acquisition of the SAP dataset (Section 2.4).

This study aims to characterise the oceanic crust at and surrounding borehole 504B and thus focuses on the SG seismic dataset. Multichannel seismic (MCS) data (Section 2.4) are used to investigate the seabed and basement structure and regional faulting patterns (Section 2.4.4), and also to inform starting velocity models for crustal modelling. Wide-angle refraction data (Section 2.5) are used to pick travel times of arrivals propagating through the crust for use in tomographic modelling, in order to derive velocity-depth structural models. The southern end of the SAP dataset overlaps the SG area, and as it has longer shot-receiver offsets than the SG dataset (Section 2.4), it is used in Chapter 6 in the investigation of the layer 2A/2B boundary in the upper crust.

Further datasets in this study include multibeam swath bathmetry data (Section 2.2.1) used to map the seafloor; and a selection of oceanographic measurements including conductivity-temperature-depth (CTD) casts (Figure 2.1) used to inform the water column velocity structure for all seismic modelling (Section 2.5.2).

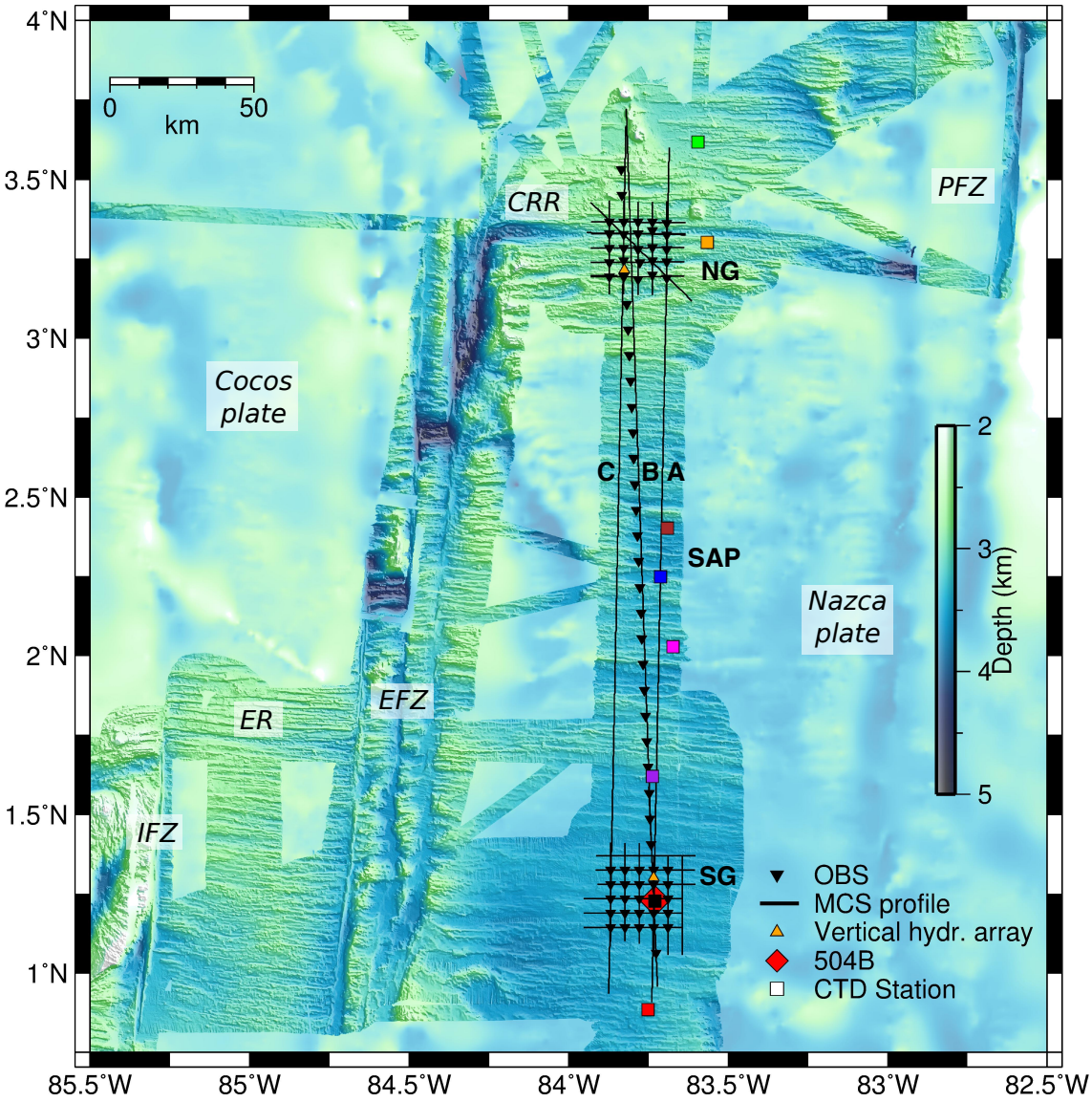


Figure 2.1: Map of the main seismic experiment conducted on research cruise JC114, shown in the context of nearby tectonic features: the Costa Rica Rift (CRR); Ecuador Rift (ER); Panama Fracture Zone (PFZ); Ecuador Fracture Zone (EFZ); and Inca Fracture Zone (IFZ). Primary acquisition regions were the North Grid (NG), South Grid (SG) and Synthetic Aperture Profiles (SAP), with SAP profiles A, B and C labelled. CTD stations are coloured according to their number (see key in Figure 2.13). Bathymetry comprises both swath data from the OSCAR cruises (full colour), along with that from the satellite-derived GEBCO 1' x 1' gridded database (paler colour).

## 2.2 South Grid

Seismic data were acquired in a 40 km x 40 km grid over the area surrounding borehole 504B, located in ~7 Ma crust (Shipboard Scientific Party, 2003b) on the south flank of the CRR. Twenty-five ocean-bottom seismographs (OBSs) were deployed at 5 km spacing to record wide-angle (WA) arrivals that propagate through the crust (Figure 2.2). Twelve multichannel seismic (MCS) profiles were acquired traversing the OBSs, using a 4.5 km-

long multichannel streamer, to produce record sections of the sediment and basement structure. OBS and MCS data were acquired simultaneously using two different seismic sources (Section 2.3). A vertical hydrophone array was also deployed within the SG to provide direct measurements of the downgoing, farfield source wavelet in the water column to inform the deconvolution stage of MCS processing. Further to the specific SG dataset, the southern end of the SAP profiles (SAP_A, SAP_B and SAP_C), comprising OBS and MCS data acquired using three seismic sources, cross the SG area, with profiles SAP_A and SAP_B being effectively coincident with profile SG_I.

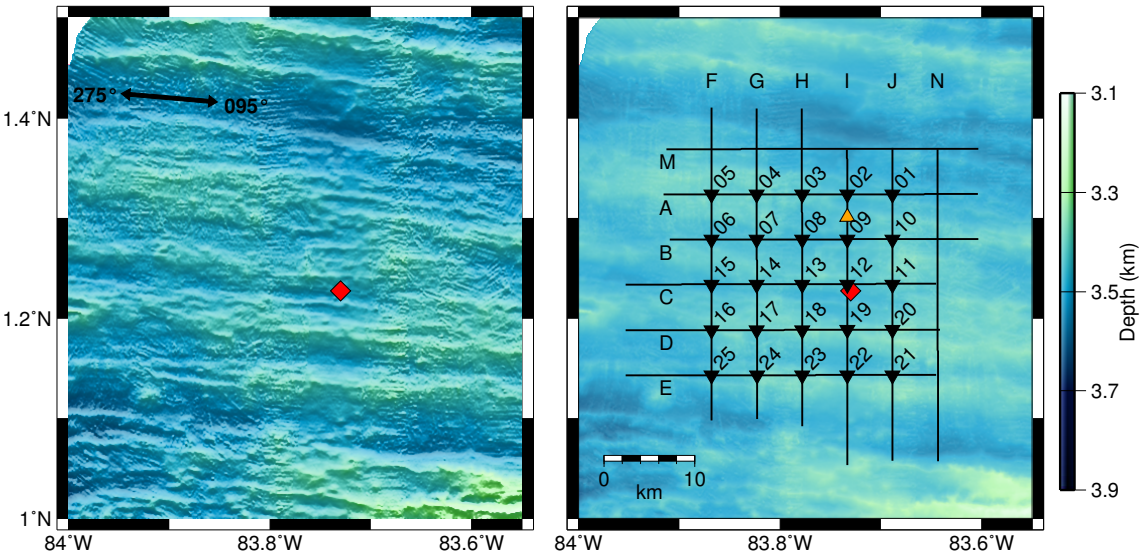


Figure 2.2: Swath bathymetry map of the SG region (left) around borehole 504B (red diamond) also showing the average abyssal hill bearing, overlain with the geometry of the SG seismic experiment (right). OBSs (black triangles) are labelled with their SG instrument number, MCS profiles (black lines) are labelled with their SG profile letter, and the SG vertical array position (orange triangle) is also shown. High frequency variations in the bathymetry are vessel motion artefacts.

### 2.2.1 SG bathymetry

Throughout the OSCAR cruises, multibeam swath bathymetry data were acquired using hull-mounted transducers to map the seafloor topography. For data acquired on the James Cook, the time measurements were converted to depth using sound velocity profiles acquired in the survey area at the start of each cruise. Swath data were cleaned onboard ship to remove the majority of spurious points (usually anomalously shallow or deep depth readings). The data from the OSCAR cruises were combined with a previous cruise of the study area, EW9416, conducted in 1994 aboard the RV Maurice Ewing, and gridded at 100 m intervals. This created a high-resolution bathymetry grid used throughout this study (e.g. Figures 2.1 and 2.2), particularly as the seabed in velocity models for 2D forward (Section 3.2) and 3D inversion (Sections 3.3 and 5.3) modelling. The contrast in resolution between the swath-derived bathymetry compared to satellite-derived

bathymetry from the General Bathymetric Chart of the Oceans (GEBCO) (IOC et al., 2003) can be seen in Figure 2.1.

The swath bathymetry grid shows that the SG area is a region of relatively smooth and constant depth seafloor (3.1–3.7 km depth) compared to the more variable bathymetry of the younger oceanic crust between the SG and the CRR, and at the ridge axis itself (2.0–5.0 km depth)(Figure 2.1). Part of this apparent smoothness is due to the ∼300 m-thick layer of sediments which drapes over the igneous basement which, to the north of the SG, is thinner and provides only intermittent coverage. Aligned abyssal hills and troughs are evident from the variation in the seabed, and trend at an average bearing of ∼095°/275° (Figure 2.2). This bearing is approximately parallel to the CRR spreading axis (which trends at ∼092°), and suggests that these E–W trending features are ridge-parallel oceanic abyssal hills formed in the vicinity of the ridge axis through either normal faulting or constructive volcanism, or a combination of these processes (Macdonald et al., 1996). The disparity between the strike of some hills, which trend closer to ∼100°/280°, and the current ridge axis trend, could suggest any of: a small change in ridge alignment over the last 7 Ma; a discrepancy between the ridge strike and the normal to the spreading direction causing oblique crustal accretion (Goff, 1991); or that rotation has occurred due to tectonic plate geometry readjustment throughout the region, or due to transtensional motion along the bounding Ecuador and Panama Fracture Zones. At the seafloor, the ridges in the SG area range from ∼40–80 m in height from peak to adjacent trough.

### 2.2.2 SG basement faults

Combining the swath bathymetry data with the interpreted sediment thickness from the MCS reflection lines enables the calculation of a topographic map of the igneous basement (see Section 3.3.5 for a detailed description of the method). Due to the relatively constant thickness of sediments, the resulting basement map (Figure 2.3) shows very similar structures and patterns to the bathymetry map (Figure 2.2), with approximately E-W trending ridges and troughs. Calculating the vertical derivative of the basement (the slope), highlights the areas of steeper basement relief, which can be interpreted in conjunction with the basement topographic map to identify and track the major faults in the study area (Figure 2.3). A total of 103 faults were identified in the region, with an average strike of 094/274° (ranging from 086/266° to 101/281°), which is consistent with the average abyssal hill (∼095°/275°) and CRR (∼092°/272°) orientations. Fault length varies from 1.3 km to 59.6 km, with a mean average length of 10.4 km. The majority of faults (74%) are northward-dipping and interpreted as normal faults, and are predominantly located on the northern side of E-W trending basement highs. This suggests that extensional faulting contributed to the construction of the basement ridges and troughs, and that they are likely both tectonic and volcanic features.

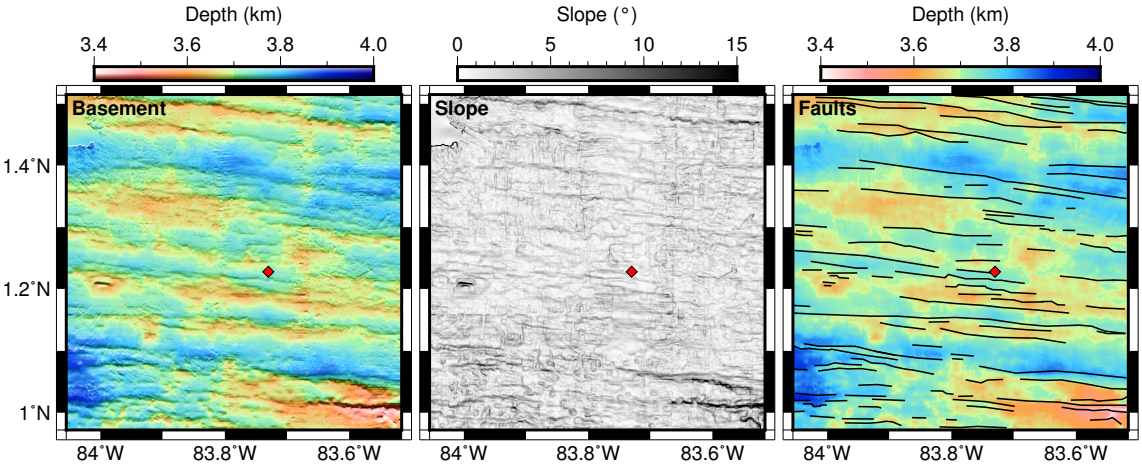


Figure 2.3: Left: basement topography map of the SG region around borehole 504B (red diamond). Centre: the maximum slope of the basement surface. Right: interpreted basement faults (black lines) overlain onto the basement topography map.

## 2.3 Seismic sources

In total, three different seismic sources were used to acquire the datasets used in this study, two for the SG area (Figure 2.4), and a third in addition for the SAP profiles:

1. **GI airgun array** - two GI airguns, each containing separate generator and injector chambers of equal volume, were towed 24 m astern of the James Cook, at a depth of 5 m. Each airgun had a total volume of 210 $in^3$ (105 $in^3$ for each chamber), and were fired with air at 2000 psi, and produced a source with a dominant frequency band of ∼24–140 Hz. GI guns are designed to suppress the bubble pulse and thus produce a less reverberative seismic signal, and in this study they are used to produce high resolution MCS images of the sedimentary section;

2. **Bolt airgun array** - an array of Bolt airguns with a total volume of 1620 $in^3$ was used to provide lower frequency energy, primarily for OBS recording of wide-angle crustal and mantle refractions, and also for MCS imaging of the basement and any visible sub-basement interfaces. This array was also fired at 2000 psi, and produced a source signature with a dominant frequency band of ∼8–40 Hz. Due to gun failures during cruise JC114 before the SG acquisition, the array set-up was changed from the six-airgun array format used to shoot the NG data. Repeated problems with rupturing of the air supply to the 500 $in^3$ airgun were incurring significant downtime for repair. For the SG this 500 $in^3$ airgun was towed independently from the rest of the array, using a wire afixed to the stern A-frame gantry. Its position in the array was filled by a 300 $in^3$ airgun. The main six-airgun array was towed at a depth of 8 m and 40 m astern, with the sole 500 $in^3$ airgun towed ∼20 m astern at a depth of ∼8 m (Figure 2.4);

3. **G-gun airgun array** - during the SAP profile shooting, a G-gun array, towed by the RV Sonne, was also fired. This array had a total volume of 4280 $in^3$, was fired at 3000 psi, and was towed at 8 m depth. This source, with its large volume and dominant frequency band of ∼4–40 Hz, provided the low-frequency, high-amplitude energy required to image long-offset crustal refractions recorded by both the OBSs and multichannel streamer.

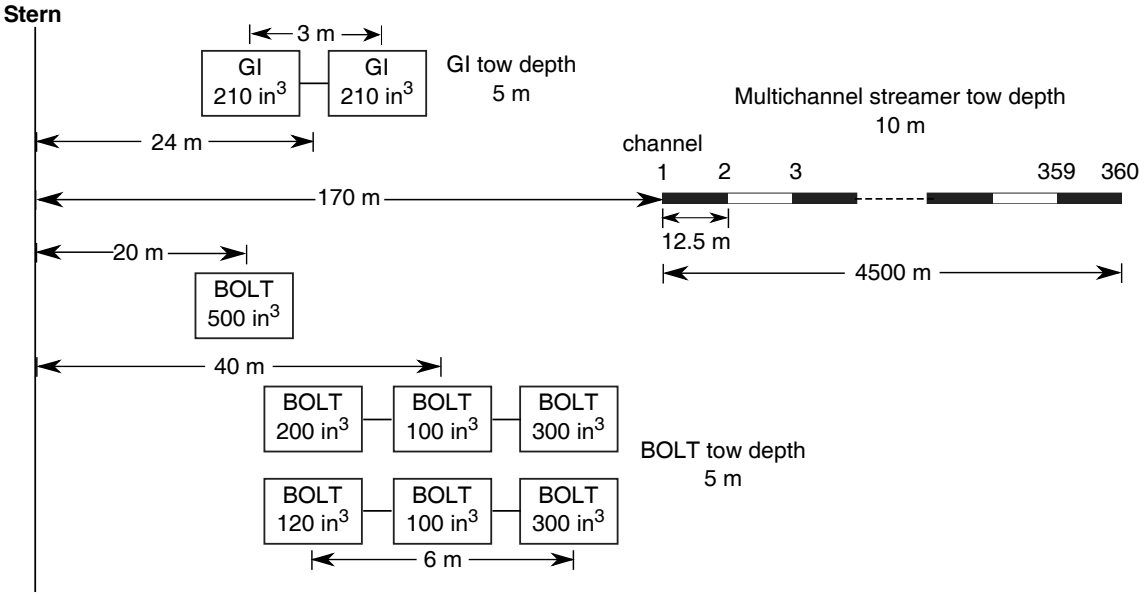


Figure 2.4: Cook seismic acquisition diagram for the setup used to acquire the SG dataset, showing the GI and BOLT main airgun arrays, along with the independently-towed 500 $in^3$ BOLT airgun, and the multichannel streamer geometry.

## 2.4 Multichannel seismic data

### 2.4.1 MCS data acquisition

The SG MCS data were acquired in a grid consisting of six E–W trending shot profiles (SG_A, SG_B, SG_C, SG_D, SG_E and SG_M) and six N–S trending shot lines (SG_F, SG_G, SG_H, SG_I, SG_J and SG_N), each with a spacing of 5 km (Figure 2.2). The profiles were defined and recorded between their 'aim' and 'end' points, although shooting into the OBSs continued between the end of one profile and the start of the next (Section 2.5.3) to add to azimuthal ray coverage. Both the GI and Bolt seismic sources were used, with the GI guns fired at *t=0 s*, and the Bolt guns at *t=6 s*. The complete firing cycle was chosen to be 30 s due to the simultaneous OBS and MCS acquisition, to allow enough time between shots for crustal refractions to reach the OBSs before the water wave from the next shot. To record the reflected arrivals, a 4.5 km-long hydrophone multichannel streamer was towed at a depth of 10 m with its first active channel 170 m astern (Figure 2.4). The streamer had a total of 360 active channels plus four auxiliary channels, with a

receiver group spacing of 12.5 m. Recorded trace lengths were 27 s for each shot with a sampling interval of 2 ms.

Synthetic-aperture acquisition (Vera and Diebold, 1994) uses two vessels with the main survey ship towing a seismic source and a multichannel streamer, and the second ship following the first at a fixed and constant offset, towing a further seismic source to provide long-offset arrivals, synthetically extending the length of the streamer. For the OSCAR project, this technique was used to record wide-angle crustal refractions on the multichannel streamer in order to constrain seismic layer 2 which, given the water depth in this location, are only incident at offsets >4.5 km. The Sonne, firing the G-gun airgun array, followed the Cook ∼8.5 km astern (Figure 2.5). The shot interval during SAP shooting was 60 s, with the GI guns fired at *t=0 s*, the Bolt guns at *t=6 s*, and the G-guns at *t=30 s*. The record length was 41 s at 2 ms sampling interval.

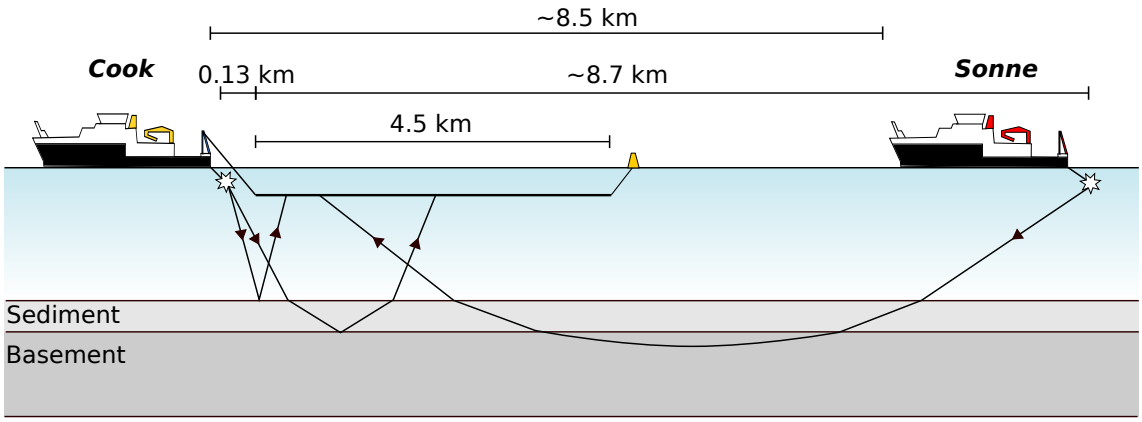


Figure 2.5: Seismic acquisition set-up during SAP shooting. Both the Cook and Sonne towed airgun arrays (white stars) firing into the multichannel streamer (thick black line) towed by the Cook. Shots from the Cook source produced reflected arrivals from the seabed, sediments and top igneous basement, whereas shots from the Sonne produced arrivals from wide-angle refractions through the upper igneous crust.

Shot gathers from the SAP profiles show arrivals from the different seismic sources (Figure 2.6). With the correct geometry applied, the long-offset shot gathers show clear crustal refractions emerging from the seabed reflection (Figure 2.6). SAP data from profile SAP_B is used in this study to analyse these wide-angle refractions from the upper crust to investigate the layer 2A/2B boundary (Chapter 6).

### 2.4.2 MCS data initial processing and brute stacks

Initially SG MCS data processing was undertaken on the two profiles which pass through borehole 504B (N–S trending SG_I and E–W trending SG_C) in order to test the geometry information and produce brute stacks. Data were processed using the *GLOBE Claritas*$^{TM}$ package, following a simple processing sequence:

1. **read *SEG-D* data -** individual *SEG-D* format shot files were concatenated to create a *SEG-Y* data file for the profile;

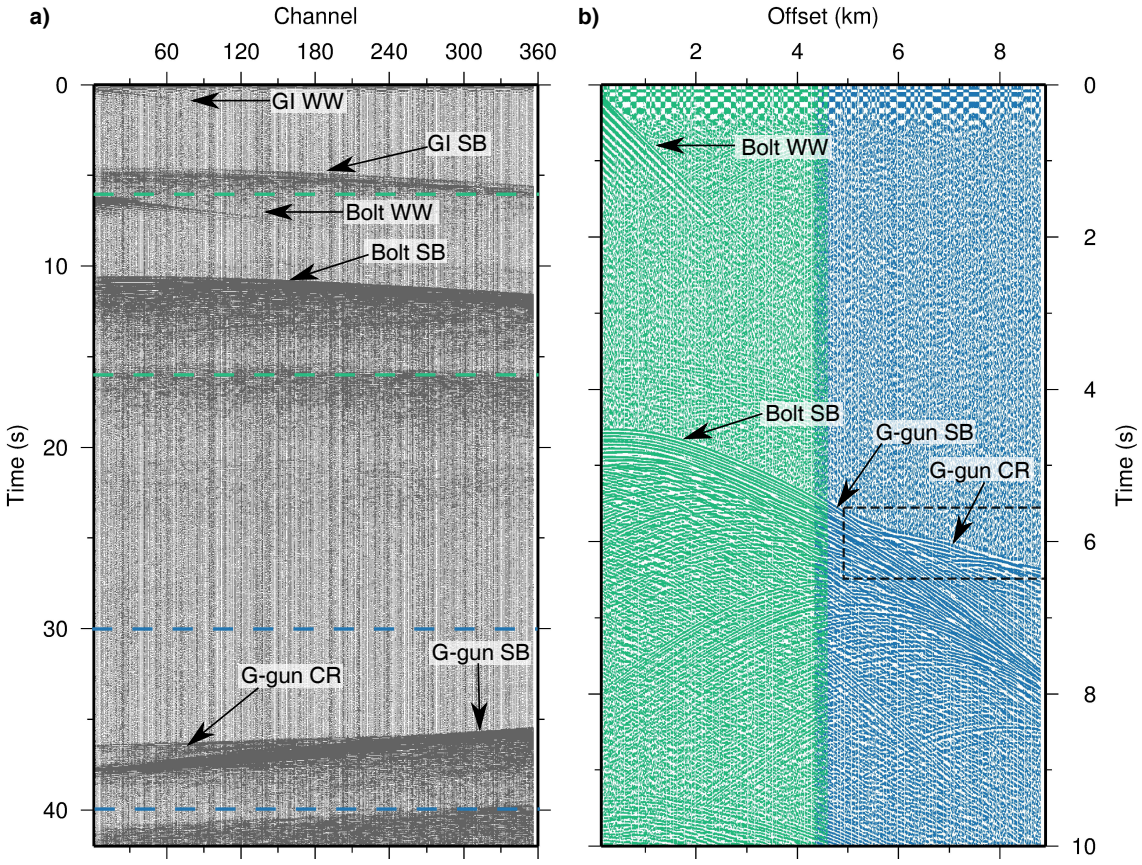


Figure 2.6: SAP shot gathers. a) Example raw shot gather from profile SAP_B, showing the arrivals from the different seismic sources (SB=seabed reflection; CR=crustal refractions; WW=direct water wave). The GI guns were fired at t=0 s, the Bolt guns at t=6 s, and the G-guns at t=30 s. Data between the green and blue dashed lines are plotted in (b) in green and blue, respectively to form the SAP gather. b) The same shot gather, split into the Bolt (green) and G-gun (blue) airgun array arrivals. Crustal refractions can be seen emerging from the seabed reflection at offsets greater than ∼4.5 km (dashed box).

2. **input geometry -** the acquisition geometry database was created using the shot locations and streamer position, and geometry information written into the data headers. Using linear common mid-point (CMP) gathers assumes that the streamer was at all times towed in a straight line behind the ship and unfeathered. The CMP spacing was 6.25 m, giving a maximum fold of ∼35. CMP numbering was defined as convention to increase from either north to south, or west to east;

3. **separate Bolt and GI data -** to process the GI arrivals, the first 8 s of data were extracted and processed. To process the Bolt data, the first 6 s of data were discarded, and a bulk static shift of -6 s was applied to the remaining data so that the Bolt firing time was at t=0 s;

4. **mute -,** front- and tail-mutes were applied to remove direct water waves and particularly noisy receiver channels were muted;

5. **CMP sort -** the data were sorted into CMP gathers;

6. **filter -** a wide, minimum-phase bandpass filter at 2/4/180/240 Hz was applied to remove low frequency noise while preserving frequencies up to the Nyquist frequency (250 Hz);

7. **NMO and stack -** a normal move-out (NMO) correction was applied at a constant velocity of 1500 m $s^{-1}$, and CMP gathers were stacked to create brute stacks for each profile.

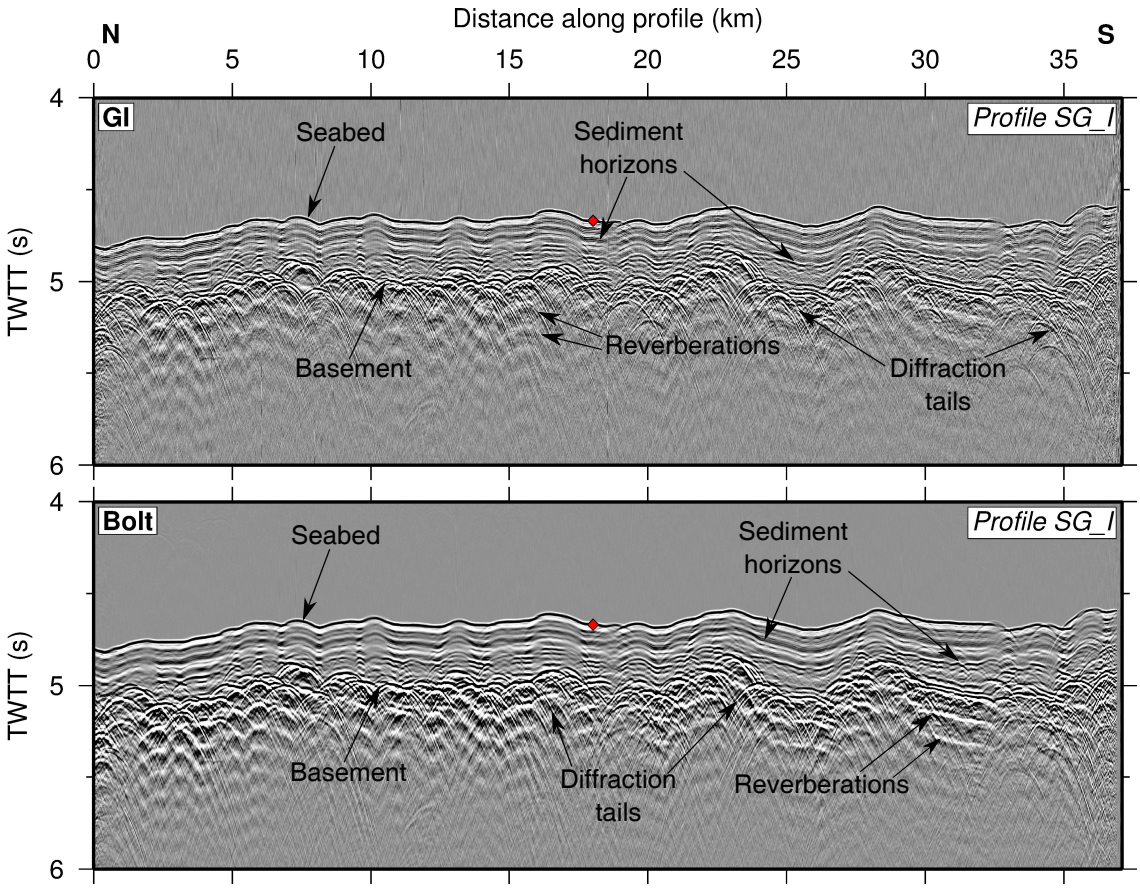


Figure 2.7: GI and Bolt brute stacks for profile SG_I, with key features labelled. Both stacks were filtered at 2/4/180/240 Hz. More detail within the sediments is visible in the higher frequency GI data. The Bolt data has a higher signal-to-noise ratio (SNR) and has more prominent reverberations due to the bubble pulse. The position of 504B is shown by the red diamond.

The brute stacks (Figure 2.7) show a coherent seabed reflection and a layered sedimentary section. The high-amplitude basement interface in both GI and Bolt stacks is characterised by rough, hummocky topography (particularly from 20–30 km along the profile), diffraction hyperbola, and a strong reverberation associated with the source bubble pulse in the case of the Bolt source. These artefacts partially mask the true onset time and geometry of the basement reflection, and may also be concealing sub-basement reflections from within the igneous crust. The prominent bubble pulse reverberations in the Bolt data also obscure the intra-sediment reflections.

### 2.4.3 MCS data full processing

The 12 SG MCS profiles were processed to final form using a more complex sequence to suppress the artefacts observed in the brute stacks, and provide highest resolution images of the seabed, sediment section and basement for picking the seabed and basement interface two-way travel times (TWTT) used to define starting velocity models (Section 2.4.5) for travel time tomography (Section 3.3) and forward ray tracing (Section 3.2), and interpreted in their own right to investigate faulting within the study area. The full processing sequence remained the same as the initial sequence until Step 5 (CMP sort), after which additional processing steps were included:

6. **filter -** a minimum-phase bandpass filter was applied at different frequencies for the GI data (4/8/140/180 Hz) and Bolt data (2/4/80/120 Hz) to minimise incoherent noise;

7. **deconvolution -** to reduce the source-generated reverberation, inverse filters were developed for the GI and Bolt sources (Hobbs, pers. comm.) using their farfield wavelets recorded at the vertical hydrophone array, and convolved with the seismic data;

8. **velocity analysis -** the CMP gathers were analysed using constant velocity analysis and semblance approaches to pick velocities every 200 CMPs, using an input Bolt brute stack (post-deconvolution) and an additional, zero-phase bandpass filter at 2/4/40/80 Hz;

9. **dip move-out (DMO) [Bolt only] -** a Kirchhoff common-offset DMO correction, using a velocity of 1500 m $s^{-1}$, was applied to the Bolt data to enhance the image of the basement interface by reducing CMP stacking-related smearing due to its significant and laterally variable dip. This did not make a significant difference to the GI data;

10. **filter -** a zero-phase bandpass filter of 2/4/40/80 Hz for Bolt data and 4/8/140/180 Hz for GI data was applied to remove white noise introduced by previous processing steps;

11. **NMO and stack -** NMO correction was applied using the stacking velocity model resulting from Step 8, and the gathers were stacked;

12. **migration -** Stolt migration at 1500 m $s^{-1}$ was applied to the final stacks to collapse diffractions and relocate dipping events to their true positions; and

13. **mute -** a seabed mute was applied for cosmetic display purposes to remove migration-related noise above the seabed reflection.

The full MCS processing sequence produces clear, high-resolution images (Figure 2.8), which are much improved on the original brute stacks (Figure 2.7). The sub-basement

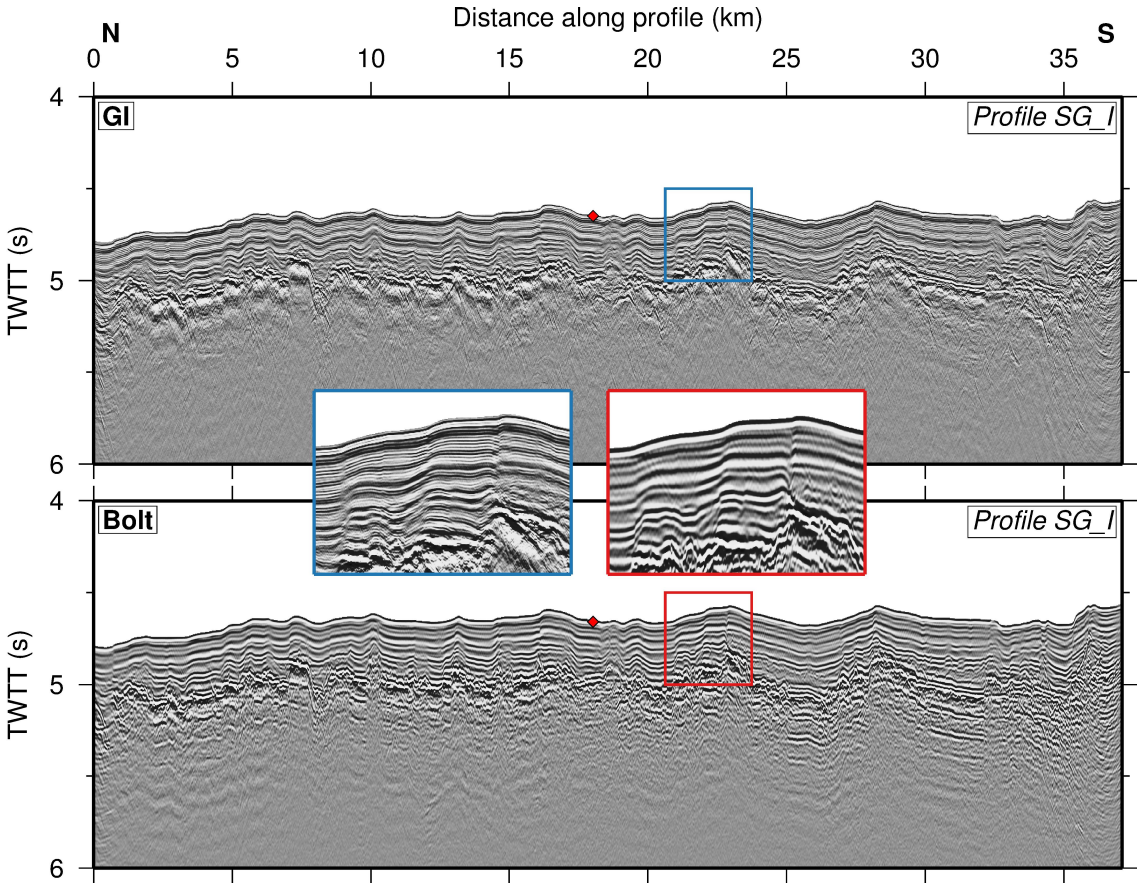


Figure 2.8: Final MCS stacks for the GI (top) and Bolt (bottom) data for profile SG_I, showing the improvement in image quality (e.g. reduction of bubble pulse, removal of diffractions) compared with the brute stacks (Figure 2.7). The zoom-in sections show the superior detail of the sediment structures achieved using the higher-resolution GI data. The position of 504B is shown by the red diamond. Colour-coded box outlines show equivalent profile locations.

reverberations caused by the bubble pulse are significantly reduced in both Bolt and GI sections due to the application of the source-derived deconvolution. DMO and Stolt migration have effectively removed the diffractions caused by the rough basement topography, producing a continuous basement reflection closer to its true subsurface position. The enlarged sections in Figure 2.8 (insets) reveal the further detail resolvable in the sediments using the higher frequency, higher resolution GI data. All 12 MCS profiles were processed for the Bolt data with the full sequence and are presented in Appendix A. Example profiles SG_C and SG_I were processed for both Bolt and GI data, and are presented and interpreted in the following section (2.4.4).

### 2.4.4 Results and initial interpretation

The final stacks for example profiles SG_I (N–S) and SG_C (W–E) (Figure 2.9) show a relatively smooth seabed and a layer of sediments covering a much rougher basement interface. The layering in the sedimentary package indicates changes in sedimentation rate or style during its deposition or later changes in composition. Drilling cores from borehole

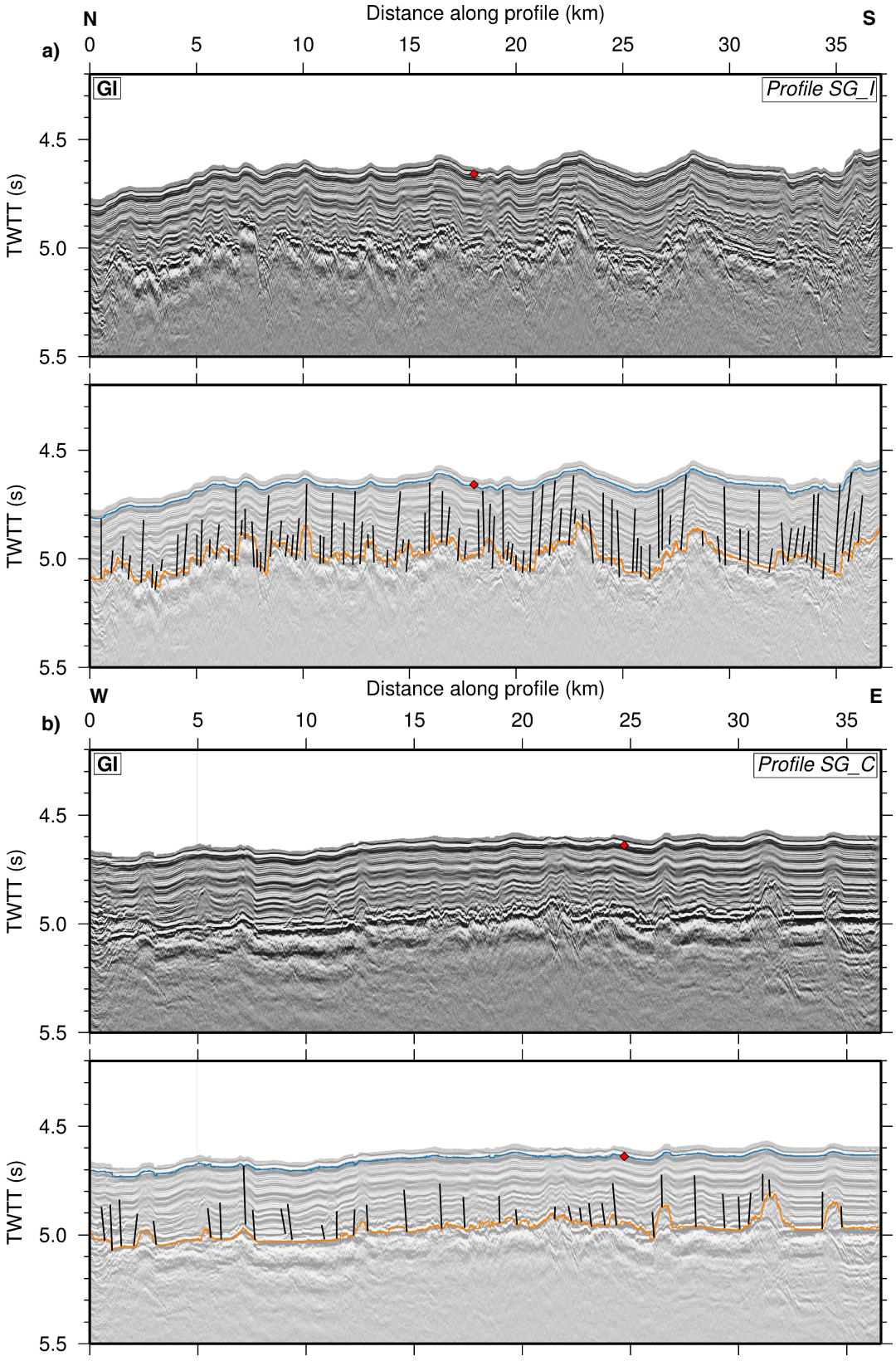


Figure 2.9: GI MCS sections along profiles a) SG_I and b) SG_C, with the lower of each pair of panels showing the traced seabed (blue) and basement (orange) interfaces, and interpreted faults (black). Note the considerable lack of faults on the SG_C section compared to the profile SG_I section. The position of 504B is shown by the red diamond.

504B sample a 275 m-thick sedimentary section consisting of unconsolidated siliceous oozes overlying diagenetically-formed chalk and layers of intercalated chalk, chert and limestone (Beiersdorf and Natland, 1983). These main units are further sub-divided due to changes in carbonate content and accumulation rate, and thin ash beds are also found throughout the core. Lateral discontinuities and vertical offsets in reflectors occur throughout the depth of the sediments in both SG_I and SG_C sections, indicating that faulting occurred at different times during continuous deposition of sediment, which suggests deformation occurred off-axis, for example, through the reactivation of ridge-related basement faults. A detailed analysis of the sedimentary packages is beyond the scope of this study.

The sedimentary sequence and basement of the SG_I flow-line section are considerably more faulted than the SG_C along-strike section. Along N–S trending profile SG_I, the majority of faults are normal and dip towards the north, suggested they are ridge-related basement faults. Faults extend from the top basement reflector up into the sedimentary section, with some faults extending to almost the seabed. The largest features in the section are two basement ridges, with their peaks at ∼23 km and ∼28 km along the profile, each with several faults which extend up into the youngest sediment layers, indicating relatively recent movement. Figure 2.10 shows the SG_I seismic section in context with the bathymetry of the South Grid, and the major basement faults interpreted in Section 2.2.2. This compilation shows that many of the largest sediment faults (e.g. at the two large basement ridges) are indeed linked to basement faults which form the large bathymetric ridges and troughs which are continuous across the study area. It also illustrates that the recent faulting indicated by the offsets in sediment horizons near the top of section represents slip along some of these major basement faults. Many of the smaller sediment faults appear unrelated to any interpreted basement faults. This may be due to the much higher resolution of the seismic section, with a CMP spacing of 6.25 m, which makes it comparatively easier to identify smaller faults when compared to the 100 m pixel-size basement topography grid used to identify the basement faults.

The E–W trending profile SG_C (Figure 2.9) exhibits mostly continuous, undisturbed sedimentary reflectors and very few large discontinuities in the basement, due to the profile running through a basement trough, parallel to tectonic fabric of the crust (Figure 2.2). However, this also results in more out-of-plane energy, which makes the profile harder to interpret with confidence. The majority of faulting present is restricted to the lower half of the sedimentary section, indicating a predominance of older faulting which has mostly ceased. Faults are predominantly normal and, on average, dip to the east, although their dip direction is less consistent than for the faults in the profile SG_I section, which is to be expected given the relative lack of directional extensional forces in an E–W direction. The largest visible basement discontinuities (at ∼26, 31 and 34 km along profile) are narrow highs up to ∼600 m-wide at their summit. These features are not always associated with large offsets of sediment reflectors, which could suggest that they were not formed tectonically, but instead constructively through volcanism at the ridge axis. Similar features are visible in the bathymetric data collected during the OSCAR

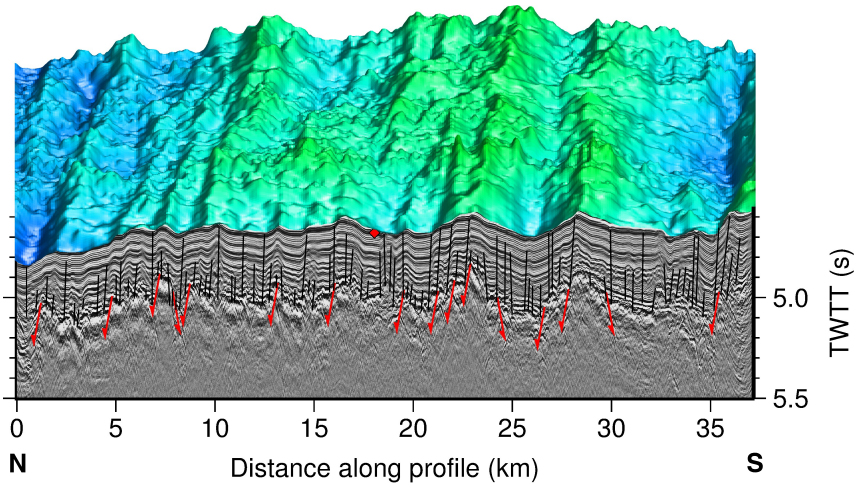


Figure 2.10: GI MCS section along profile SG_I showing the interpreted sediment faults (black), basement faults from basement slope analysis (red), and a perspective view of the swath bathymetry. The position of 504B is shown by the red diamond.

project at the CRR where there is little-to-no sediment overlying the igneous basement. These features have been interpreted as lava domes by Haughton (pers. comm., 2017).

In summary, the MCS sections indicate extensive normal faulting with a N–S direction of extension. The offsets of reflectors in the youngest sediment layers suggest that faulting has been continuous from the formation of the crust to the present day, and the relative lack of faulting in the E–W trending SG_C section suggests that the faulting is all ridge-parallel.

### 2.4.5 Seabed and basement horizons

To inform the starting velocity-depth models for both 2D forward ray-tracing and 3D inversion tomographic modelling, the seabed and basement horizons were picked from the final MCS stacks to enable calculation of the sediment thickness and basement depth (Sections 3.2.4 and 3.3.5).

The seabed and basement horizons were picked using the Bolt MCS record sections and the horizon picker tool within the *OpenDtect* software package, which tracks along a horizon seeded with points by the user. The tool was set to track along the minimum (negative) peak across the sections (the white loop in Figure 2.9), which represents the arrival time after deconvolution, and output a TWTT value for each CMP trace (Figure 2.11).

## 2.5 Wide-angle seismic data

### 2.5.1 OBS data acquisition

The SG OBSs recorded wide-angle refractions from the crust, in particular from seismic layer 2, which form the basis of travel time tomographic modelling. The OBSs

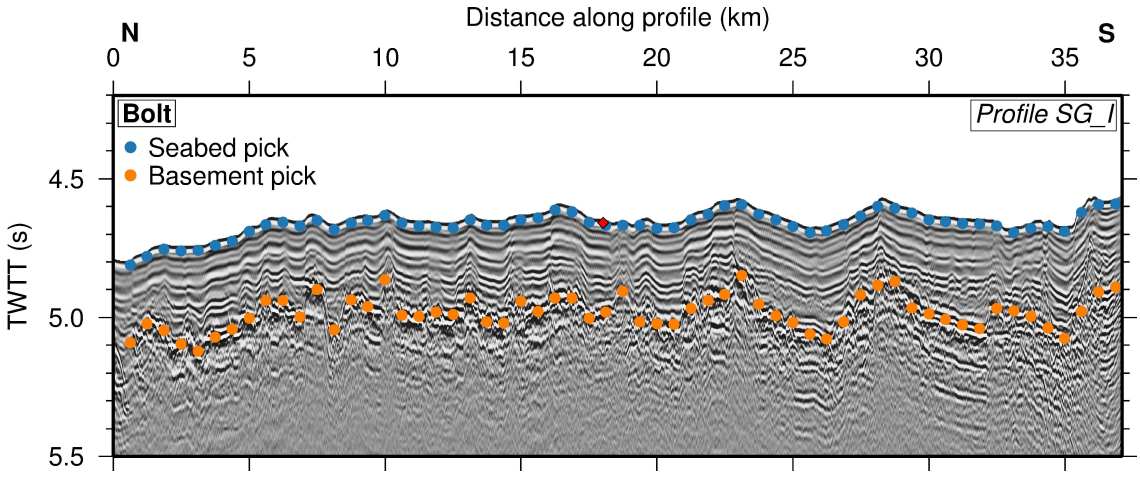


Figure 2.11: Seabed and basement horizon picks (every 100th plotted), made using the Bolt sections in the *OpenDtect* software package to enable calculation of the total sediment thickness. The position of 504B is shown by the red diamond.

were deployed in a 40 km x 40 km square grid pattern around borehole 504B to enable ground-truthing, and to provide full azimuthal coverage necessary for anisotropy analysis. Twenty-five LC-type OBSs were deployed for the SG survey (Figure 2.2), provided by the NERC's Ocean-Bottom Instrumentation Facility (OBIF). Each OBS was equipped with a hydrophone and a three-component geophone, giving a total of four data channels. Further information about the LC-type OBS sensors is included in Appendix B. The OBSs recorded shots from the GI and Bolt airgun arrays contemporaneously with the MCS profiles, at a sampling rate of 500 Hz. All 25 OBS were recovered from the seafloor, and had successfully recorded data except for SG_02, which experienced a data logging error.

The recorded data are of high quality (Figure 2.12), with high SNR on most record sections resulting in clear direct water wave and refracted arrivals. Generally, the hydrophone data have the highest SNR and the clearest arrivals. Both P- and S-wave arrivals were variously recorded by the four components. Analysis and modelling of the S-wave arrivals will be discussed further in Section 5.2.

### 2.5.2 OBS instrument relocation

An OBS's position and depth are initially defined as the deployment location, and the seabed depth at that location taken from the central beam of the swath. However, ocean currents and tides cause OBSs to drift as they sink and ascend through the water column, such that their seabed position can be significantly different from their deployment position. Therefore, it is necessary to 'relocate' each instrument to its true seabed position. This relocation is done by ray tracing through an accurate water column velocity model to match the water wave arrivals recorded by each instrument.

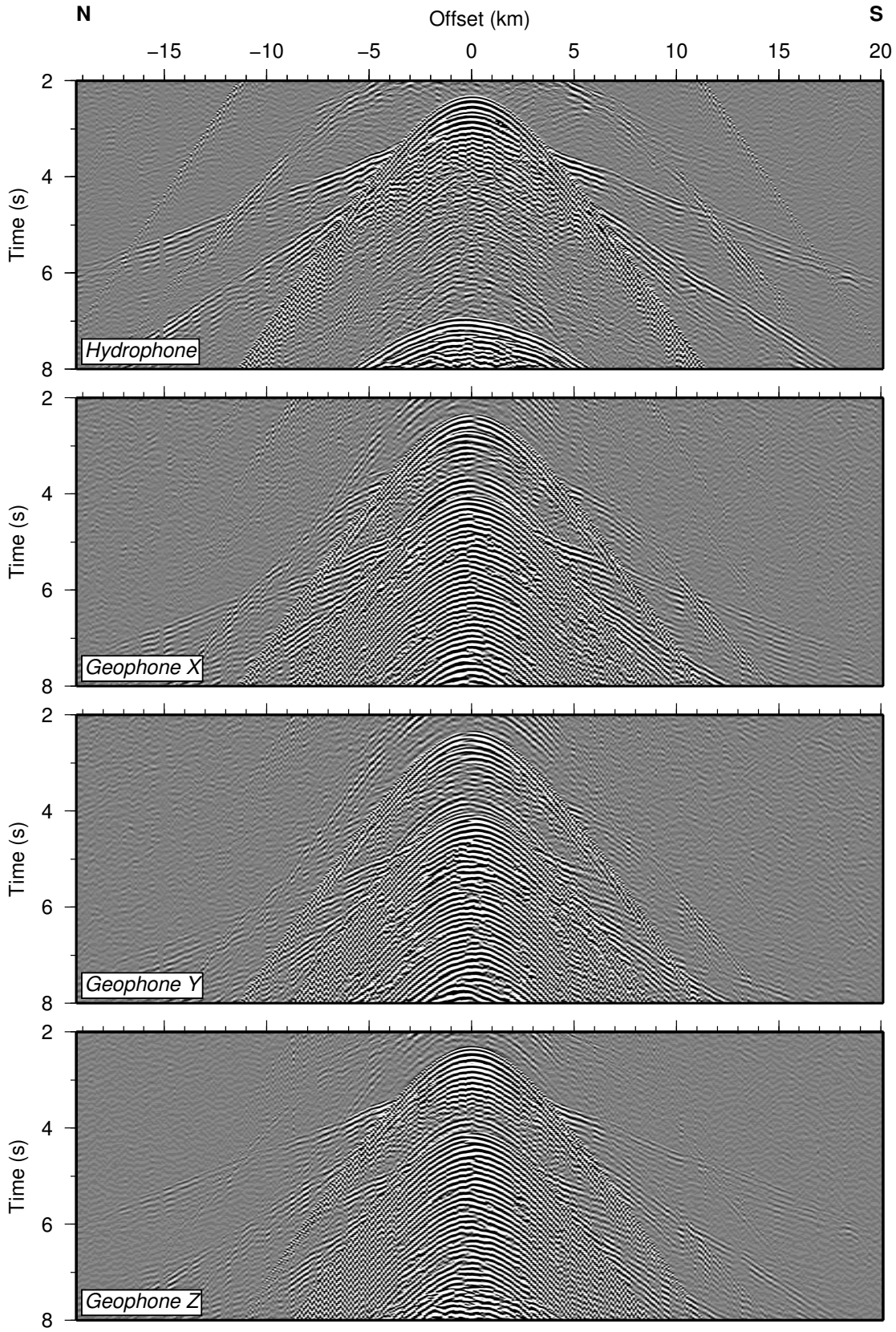


Figure 2.12: Example OBS record sections for the four components of OBS SG_12 for shot profile SG_I. The data have been filtered for clarity using a minimum-phase bandpass filter at 3/6/12/24 Hz and are plotted unreduced. These plots show primarily Bolt arrivals, although the preceding GI shot water wave and its multiple can be seen interfering with the crustal refractions. Geophones X and Y are not oriented in E–W or N–S directions.

### Water column velocity model

To model ray paths and travel times through the water column accurately, a velocity model was derived from physical oceanographic data collected throughout the Panama Basin as part of the OSCAR project. These data included measurements from a Conductivity-Temperature-Depth (CTD) instrument, which measures these properties at <5 cm intervals as it is lowered to the seabed and raised back to the vessel. The measured properties can then be used to calculate sound speed using the thermodynamic equation of seawater (IOC et al., 2010). One CTD cast (Station 11) was made at borehole 504B (Figure 2.1).

The data from Station 11 were converted to a water column velocity profile, which was then discretised into five layers, each with an assigned thickness, and top and bottom velocity (Figure 2.13). This simplified five-layer model adequately represents the full velocity-depth profile within the constraints of the modelling approach.

To test whether the velocity structure at Station 11 was a consistent feature of the study area, it was compared to seven other CTD casts made in the vicinity of the Costa Rica Rift, borehole 504B, and along the SAP profiles (Figure 2.1). These seven casts measured very similar velocity profiles (Figure 2.13), suggesting that this velocity structure is stable and consistent throughout the study area.

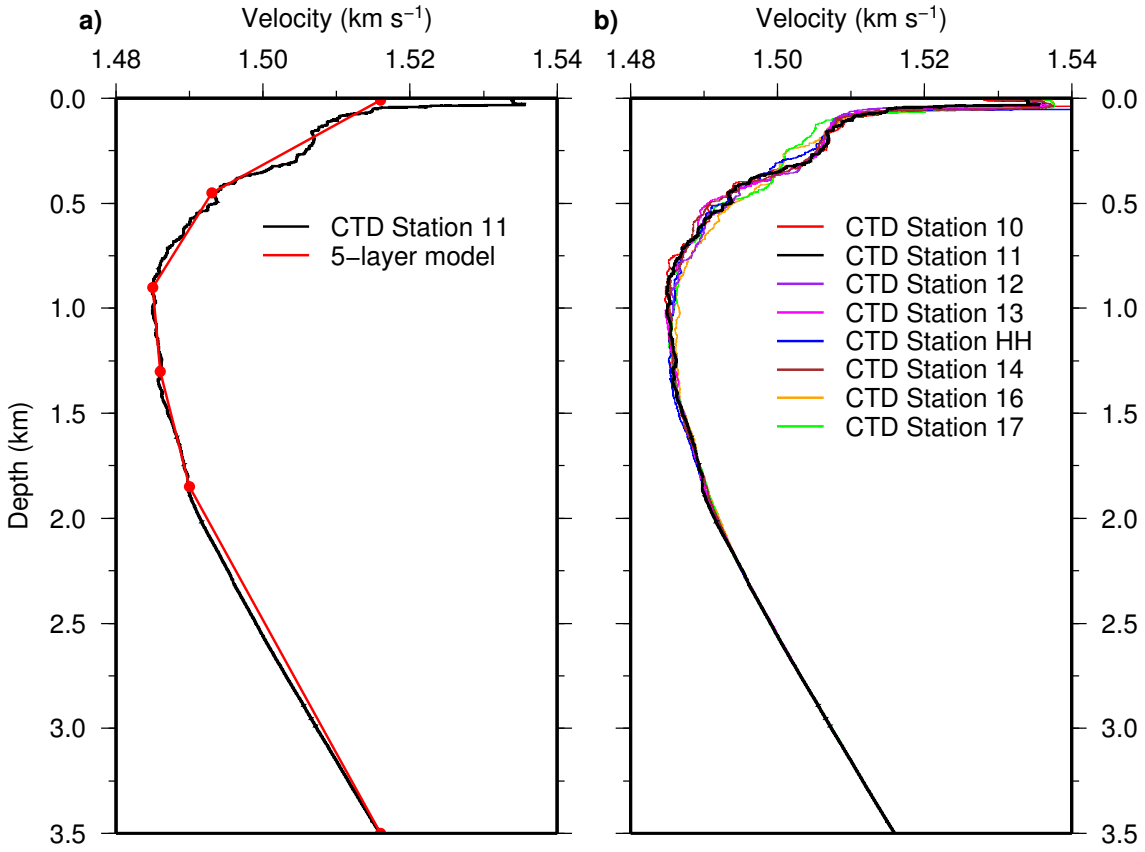


Figure 2.13: CTD-derived velocity-depth profiles of the water column. a) Profile at Station 11, situated at 504B, and the five-layer model used to calculate travel times through the water column. b) Station 11 velocity-depth profile compared to seven other CTD casts in the wider OSCAR study area. Profiles are coloured to match their position shown in Figure 2.1.

### Method

The seabed position of each OBS was found using the water wave arrivals recorded by each instrument from the N–S and E–W trending pair of shot profiles crossing each OBS. For example, for OBS SG_12, shot profiles SG_C and SG_I were used. Offset-time record sections were produced for the two shot profiles, using the known shot locations and the deployment location of the OBS to calculate the offsets. Then, theoretical water wave travel times were calculated from an array of shots to the instrument at its deployment location, using ray tracing program *rayinvr* (Zelt and Smith, 1992) and the water column velocity model derived from CTD data. The theoretical travel times were plotted as a hodochron and laid over the two OBS record sections, and compared with observed water wave travel times (Figure 2.14). Lateral misfits between the calculated and observed times were caused by an incorrect X,Y OBS location, which causes the peak of the observed water wave to be displaced from offset=0 km. Using two record sections together can provide a more accurate location for any instrument, with the E–W trending profile providing the best constraint on the X coordinate and the N–S trending profile the Y coordinate. Vertical misfits between calculated and observed travel times are caused by an incorrect instrument depth. Each OBS location was adjusted, and the offset-time sections and hodochron reproduced and re-compared until each OBS was successfully relocated (Figure 2.14). OBS deployment and final relocated positions are presented in Appendix C.

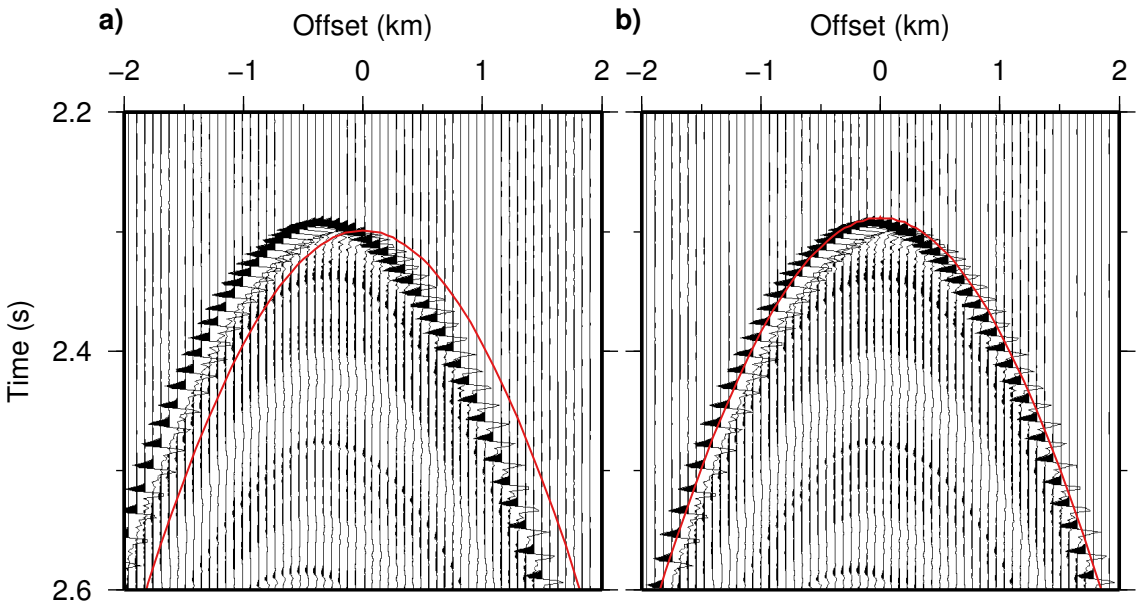


Figure 2.14: OBS relocation example. a) Offset-time record section calculated using the deployment location of an OBS, overlain with the theoretical hodochron (red line). The peak of the water wave is displaced laterally from 0 km, and the hodochron is arriving later than the real water wave, indicating an incorrect X,Y position and depth. b) Offset-time record section calculated using the final, relocated position. The water wave is now symmetrical about 0 km and hodochron crosses each trace at the first break of the water wave, correctly predicting the travel times of the arrival.

### 2.5.3 Wide-angle profiles

Wide-angle profiles, used to create OBS record sections for travel time picking, were defined differently from the MCS profiles in order to include the maximum number of shots. Profiles were chosen to include the entire length of the shooting line, ending where the ship began to turn towards the next profile. The ends of the profiles were picked using the navigation data: when shooting the straight shot lines, the ship's heading remained relatively constant, but rapidly changed when the turn began (Figure 2.15). A time was picked for the start and end of each line within the SG to the nearest 250 seconds (∼8 shots). These times were checked and adjusted to account for potential difference between the ship's heading and course by also studying the shot positions in map view, to ensure the chosen shots did not include corner shots, but extended close to the ends of the straight shooting lines. The times were adjusted to the closest real shot time (usually 10 s difference), and were then used to window the OBS data into record sections for each wide-angle profile in the SG for travel time picking (Sections 3.2.3, 3.3.4 and 5.3.2).

In this study, wide-angle profiles are labelled by the instrument and the shooting profile, for example OBS SG_01, profile SG_A. 'On-profile' record sections are those where the shooting line passes directly over the instrument. 'Off-profile' record sections are those where the shooting line is offset laterally from the OBS by 5, 10, 15, 20 or 25 km (see Figure 2.15).

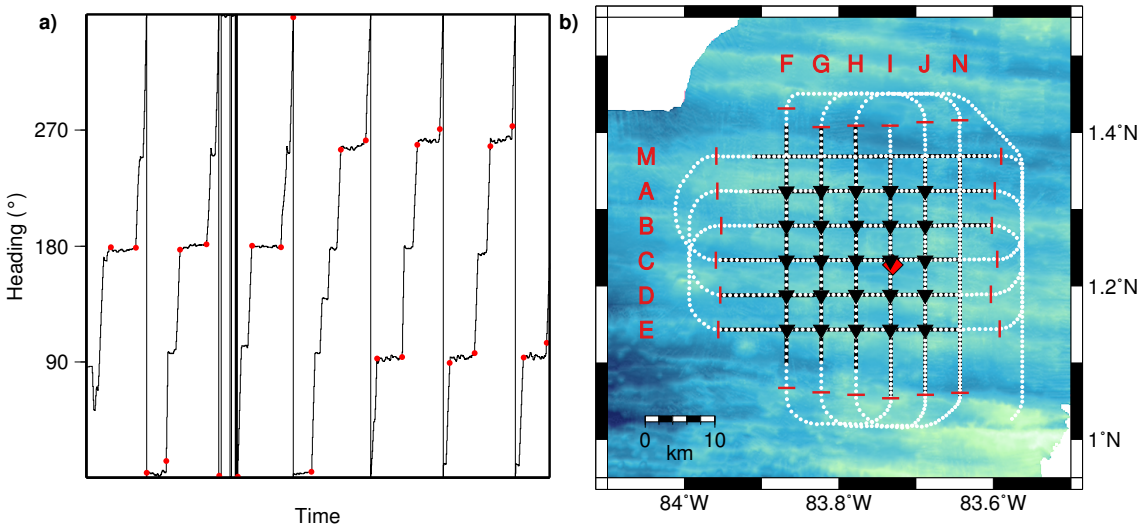


Figure 2.15: WA profile determination a) Ship's heading plotted against time for the SG survey. Horizontal regions represent times of constant heading when the ship was shooting profiles. Red dots represent the picked start and end times, after the correction using map view. b) SG acquisition map showing all shots fired in the SG survey (white dots, every 10th plotted), MCS shot profiles (black lines), OBSs (black triangles), 504B (red diamond), and the defined wide-angle profiles (capped with red bars). These are longer than the MCS profiles in order to include all possible inline shots for travel time picking.

## 2.6 Summary

An extensive geophysical and oceanographic survey in the Panama Basin, conducted by the OSCAR project in 2014 and 2015, provides a comprehensive dataset to characterise the oceanic crust around borehole 504B (the SG study area). Swath bathymetry data shows a relatively smooth seafloor when compared to that nearer the CRR, which is characterised by ridge-parallel abyssal hills and troughs. MCS profiles, acquired in a grid across the area and processed to post-stack migration, provide high-resolution sub-seabed images which show that this smoothness is due to a ∼300 m-thick layer of sediment completely covering a rougher top basement surface. The top basement is rugged and extensively faulted, with the majority of faults being normal, striking E–W, and dipping towards the ridge axis to the north. The extension of faults into the sedimentary section indicates continuous faulting from the formation of the crust ∼7 Ma to the present day. Long-offset MCS data from the SAP dataset includes refracted arrivals through the crust, which will be used to investigate upper crustal structure at 504B, primarily the layer 2A/2B boundary, in Chapter 6. Wide-angle data were successfully recorded on 24 of the 25 OBSs in the SG, and the data are of high quality. Refracted arrivals through the crust have high SNR, and will be used to pick travel times for 2D forward and 3D inversion tomographic modelling in Chapters 3 and 5.

# Chapter 3

# P-wave modelling: forward and inverse

## 3.1 Introduction

The P-wave velocity of oceanic crust has long been used to characterise its structure (Raitt, 1963; White et al., 1992; Grevemeyer et al., 2018b), and investigate its formation (Purdy and Detrick, 1986; Van Avendonk et al., 2017), evolution (Houtz and Ewing, 1976; Nedimović et al., 2008) and destruction (Spence et al., 1985; Shillington et al., 2015). The velocity of the different seismic layers within the oceanic crust, their thicknesses, and the variation in these parameters, can help to elucidate the lithological structure of the crust, its porosity, and the prevalence of alteration processes such as those caused by fluid flow. In this chapter, the P-wave velocity structure of the crust around borehole 504B is defined in two and three dimensions (2D and 3D) using travel-time tomography and both forward and inversion techniques. The velocity structure will be used to characterise the structure of the oceanic crust, in particular the upper crust (seismic layer 2), to understand the evolution of the crust since formation in terms of fracture patterns, alteration and fluid flow.

Initially, 2D forward modelling (Section 3.2) was undertaken to derive the general structure of the crust, and to provide the starting point for the subsequent 3D inversion (Section 3.3). The method of Zelt and Smith (1992) was followed (Section 3.2.1). Arrivals in the OBS wide-angle data were identified (Section 3.2.2), before the travel times were picked and their uncertainties analysed (Section 3.2.3). Starting models were constructed for six profiles, using *a-priori* knowledge such as the bathymetry and basement topography (Section 3.2.4), to produce models of the two profiles crossing borehole 504B (SG_I and SG_C), and define the outer 'box' of the study area (profiles SG_A, SG_E, SG_F and SG_J). The final 2D models are presented in Section 3.2.6, and the sensitivity of the models defined in Section 3.2.7.

3D tomographic inversion was undertaken following the method of Zelt and Barton (1998) (Section 3.3.1). The wide-angle data was processed further (Section 3.3.2) to allow

an efficient method of travel-time picking to be used for the much larger dataset utilised in 3D inversion (Section 3.3.3). The resulting pick uncertainties from this different method were then analysed (Section 3.3.4). The starting model was created using the results of the 2D forward modelling (Section 3.3.5) and inverted, before testing different starting models (Section 3.3.8 and 3.3.10) to achieve a well-fitting, unbiased final model.

Lastly, the final, preferred 3D velocity model is presented (Section 3.3.12).

## 3.2 Two-dimensional forward modelling

Forward modelling in two dimensions was undertaken to produce simple models of the general crustal structure in the study region, primarily to inform the starting point for the three-dimensional inversion.

### 3.2.1 Method

Forward tomographic modelling is a modeller-controlled, iterative process aiming to find the simplest velocity model which provides a good fit to the observed data within its uncertainties. The process involves the creation of a starting velocity model, through which synthetic rays are traced and travel times calculated. These synthetic travel times are compared to observed travel times, and the misfit analysed. The user then adjusts the velocity model and the calculations are run again. This process continues until a satisfactory fit between the calculated and observed data is reached. Misfit is analysed by calculating both the root-mean-squared (RMS) difference in travel time between synthetic and observed data pairs with equivalent travel paths, and the $\chi^2$ parameter (eq. 3.1), gives an indication of fit whilst accounting for the uncertainties assigned to each travel time pick. A $\chi^2$ of unity indicates that the model produces calculated travel time data ($t_{calc}$) which match the observed picks ($t_{obs}$) within their errors ($\alpha_{obs}$), for the number of picks analysed ($N$). These values are analysed on a phase-by-phase, instrument-by-instrument basis, and for the model overall using all instruments and all travel time picks.

$$\chi^2 = \frac{\sum^{N} \left[ \frac{t_{obs} - t_{calc}}{\alpha_{obs}} \right]^2}{N - 1} \tag{3.1}$$

To run the ray-tracing calculations, the *rayinvr* modelling package (Zelt and Smith, 1992) was used. This numerically solves the ray-tracing equations using zero-order asymptotic ray theory. A 'top-down' approach was also implemented during modelling, with the uppermost layer in the model adjusted to fit rays turning within the upper part of the model first, before progressing to the next layer down, leaving the upper model fixed. This reduces the number of free parameters when fitting the structure in the mid-to-lower part of the model, since all deeper travelling phases pass through the upper model twice along their propagation path.

### 3.2.2 Phase identification

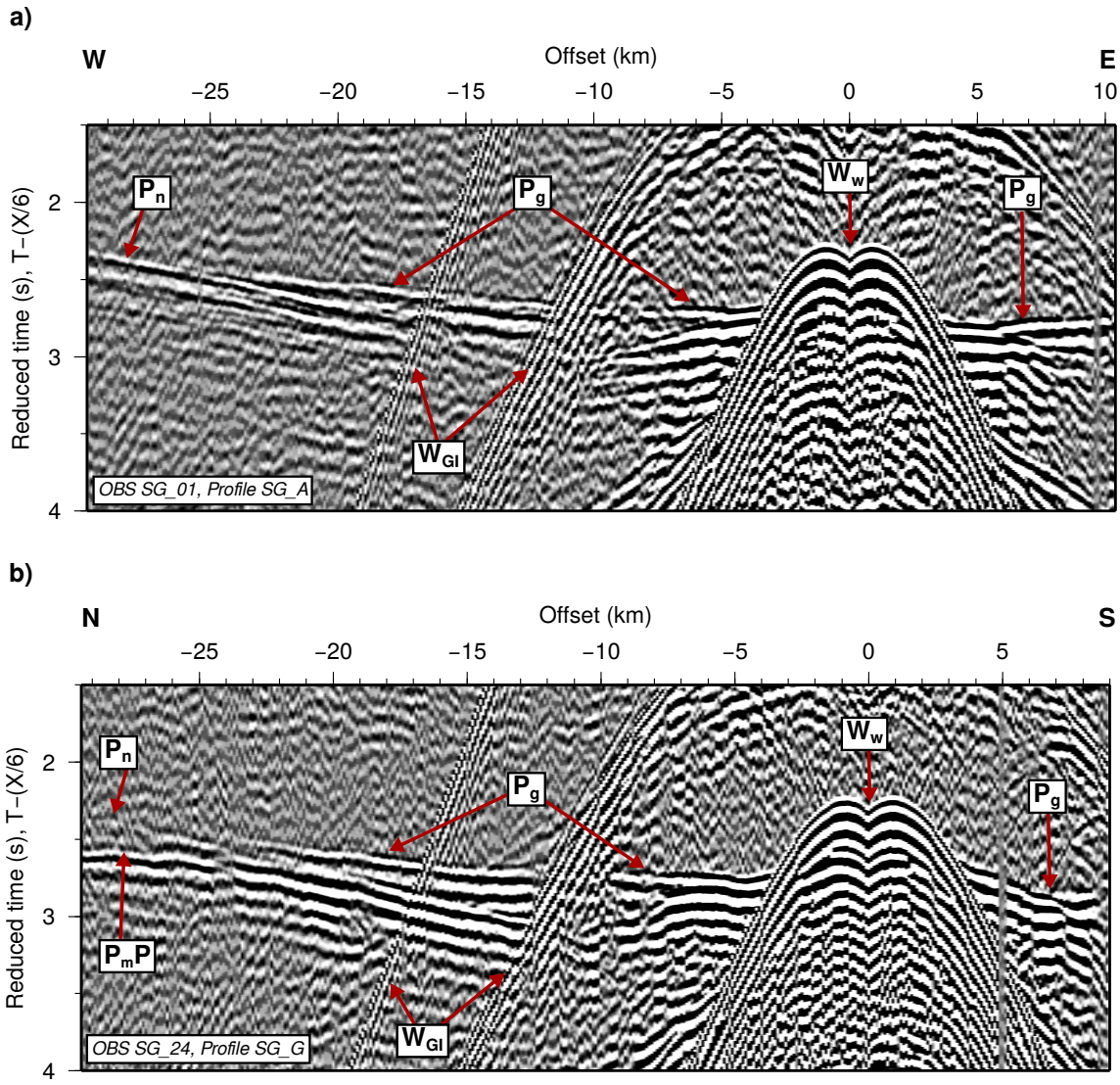


Figure 3.1: Identified P-wave arrivals on example OBS hydrophone record sections for a) OBS SG_01 for profile SG_A, and b) OBS SG_24 for profile SG_G. The data have had a minimum-phase 3/6/12/24 Hz bandpass filter applied for clarity. Arrivals labelled $W_{GI}$ are direct water wave arrivals and multiples from the preceding GI airgun array shot, which interfere with the crustal refractions from the Bolt array. See text for the other phase definitions.

Seismic arrivals which have travelled through different layers in the subsurface, or 'phases', were identified based on their offset from the instrument, their travel time, and their apparent velocity (Figure 3.1). For all P-wave tomographic modelling, arrivals were identified and their travel times picked for shots from the Bolt airgun array (as this provides the longer offset crustal refractions - Section 2.5), using the hydrophone channel (as this has the highest signal-to-noise ratio, SNR). As forward modelling was conducted in 2D, only OBS record sections with on-profile shots were used, e.g. for modelling along shot line SG_C, only OBS record sections from instruments SG_11–15 were used (Figure 2.2). At near offsets, these records have the direct water wave as the first arrival. Despite ∼300

m of sedimentary cover, no turning rays through the sediments are observed as first arrival on the sections, with crustal refractions becoming the first arrival at offsets of ∼3 km. On some records with high SNR at far offsets, mantle refractions are visible and become the first arrival at offsets of ∼26 km. The naming scheme used for the different phases is as follows:

**$\mathbf{W_w}$** — direct water wave arrivals;

**$\mathbf{P_g}$** — crustal refractions;

**$\mathbf{P_n}$** — mantle refractions; and

**$\mathbf{P_mP}$** — Moho reflections.

Further to this definition, the $P_g$ arrival is split into three distinct phases – $P_{g1}$, $P_{g2}$ and $P_{g3}$ – based on changes in the apparent velocity of the arrival at offsets of ∼4–7 km between $P_{g1}$ and $P_{g2}$, and ∼10–15 km between $P_{g2}$ and $P_{g3}$ (Figure 3.2). These changes in the velocity of the $P_g$ arrival are consistently seen on record sections throughout the dataset, and thus are not attributed to the effects of the topography of the seabed or any other interface. On average, $P_{g1}$ has an apparent velocity of 4.0–5.0 km $s^{-1}$, $P_{g2}$ 5.5–6.0 km $s^{-1}$, $P_{g3}$ 6.5–7.0 km $s^{-1}$ and $P_n$ ∼8.0 km $s^{-1}$.

### 3.2.3 Travel-time picking and error assignment

Travel-time picking was undertaken using the *zplot* package written by Colin Zelt of Rice University, Texas, which is associated with the *rayinvr* software suite. This program enables filtering and windowing of data, as well as assigning phase numbers and uncertainties to picks for use in modelling with *rayinvr*. The majority of travel-time picks made for the forward modelling were made either on unfiltered record sections, or those with a very wide, minimum phase, bandpass filter at 1/2/80/100 Hz applied. Some record sections with a lower SNR required harsher (both high- and low-cut) filtering when picking far-offset arrivals.

For travel time modelling, the uncertainty of each travel time pick needs to be defined in order to calculate statistically meaningful measures of model fit (e.g. eq. 3.1). There are a number of different sources of error in OBS data and the modelling process which contribute towards pick uncertainty:

1. *Data sampling interval.* Picks can only be made to an accuracy of one sample.

2. *OBS internal clock drift.* Drift in the time-keeping by the OBS clock.

3. *First break-to-peak delay.* Time t=0 s on each OBS record section represents the time of peak energy release from the airguns. The travel time for each arrival is picked as the first break.

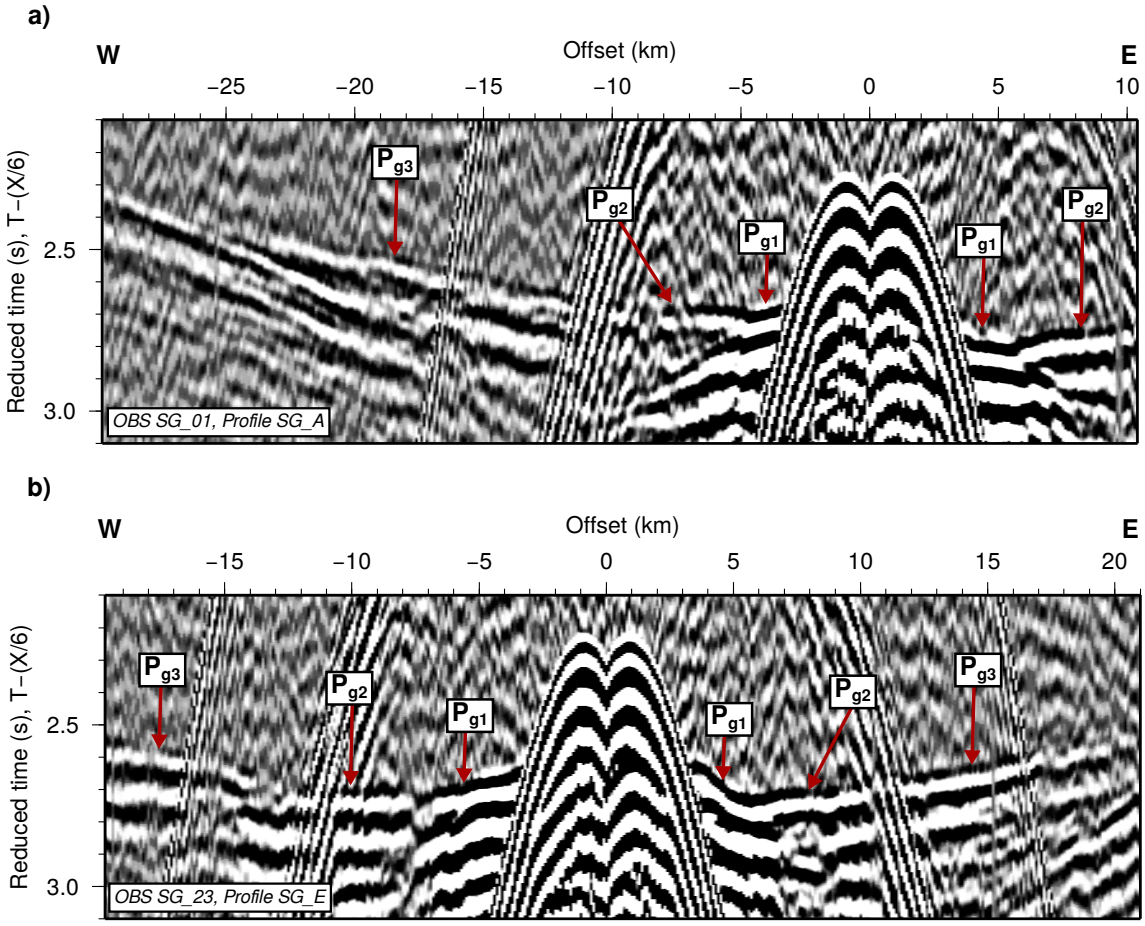


Figure 3.2: Crustal refractions are split into three separate phases on example hydrophone OBS record sections for a) OBS SG_01 on profile SG_A, and b) OBS SG_23 on profile SG_E. The data have had a minimum-phase 3/6/12/24 Hz bandpass filter applied for clarity. See text for phase definitions.

4. *Instrument location.* Uncertainty in the OBS position following its relocation from the deployment position (Section 2.5.2). Uncertainty in the OBS position influences travel time as it controls the start point of the ray path.

5. *Shot location.* Uncertainty in the shot location arises from both the error in the ship GPS position at the antenna location, and from the lateral and vertical position of the point source of the airgun array behind the vessel.

6. *Bathymetry uncertainty.* There are small discrepancies ($\leq$7 m) between the instrument seabed depths derived from OBS relocation (Section 2.5.2) and the depths from swath bathymetry data at the same location. This difference reflects the contrasting methods used to derive each depth: swath measurements are derived from beam travel times converted to depth using an input water column velocity model (Section 2.2.1), and are accurate to approximately $\pm$10% of the water depth (in this case $\pm$ $\sim$30 m); whereas the relocated OBS depths are derived from modelling water waves to a spot point, using a simplified water column velocity model (Section

2.5.2). During forward modelling, the seabed is defined using the swath data, and OBS instruments are shifted in depth to sit on the model seabed. This introduces travel time errors into the modelling process as it changes the length of path between shot and receiver.

7. *Error in picking the travel time,* $t_p$. The human error in identifying and picking the first break of each arrival. This usually increases with greater offsets and lower SNR, and is phase–dependent.

These errors were assumed to be independent and so were combined using equation (3.2) to give the total error for each travel time pick.

$$\text{Total pick error} = \sqrt{t_1^2 + t_2^2 + t_3^2 + t_4^2 + t_5^2 + t_6^2 + t_p^2} \tag{3.2}$$

The error in picking the travel time, $t_p$, varies for each phase, from ±4 ms for the direct water wave arrival, to ±30 ms for far-offset $P_n$ arrivals, giving a different total pick error for each phase (Table 3.1).

| Phase | Pick error (ms) |
|---|---|
| $\mathbf{P_w}$ | 11 |
| $\mathbf{P_{g1}}$ | 15 |
| $\mathbf{P_{g2}}$ | 23 |
| $\mathbf{P_{g3}}$ | 32 |
| $\mathbf{P_n}$ | 32 |
| $\mathbf{P_mP}$ | 32 |

Table 3.1: Total travel time pick uncertainties for each phase, calculated using Equation 3.2.

### 3.2.4 Initial model construction

2D forward modelling was undertaken for six profiles: SG_A, SG_C, SG_E, SG_F, SG_I and SG_J (Figure 3.3), in order to produce models of the two profiles crossing 504B, and the outer profiles of the data grid in order to define any long-wavelength variation across the study area. This section details how the initial model for each profile was constructed. The models were created to be the same length as the concurrent wide-angle profiles (defined in Section 2.5.3), ending where the ship began to make the turn for the next profile. This ensures that all in-line arrivals for each OBS on profile was included in the modelling procedure, and no arrivals were included from out-of-plane shots.

#### Water column

The velocity structure of the water column of the model was defined using the five-layer velocity model developed in Section 2.5.2 from CTD measurements in the study area. The

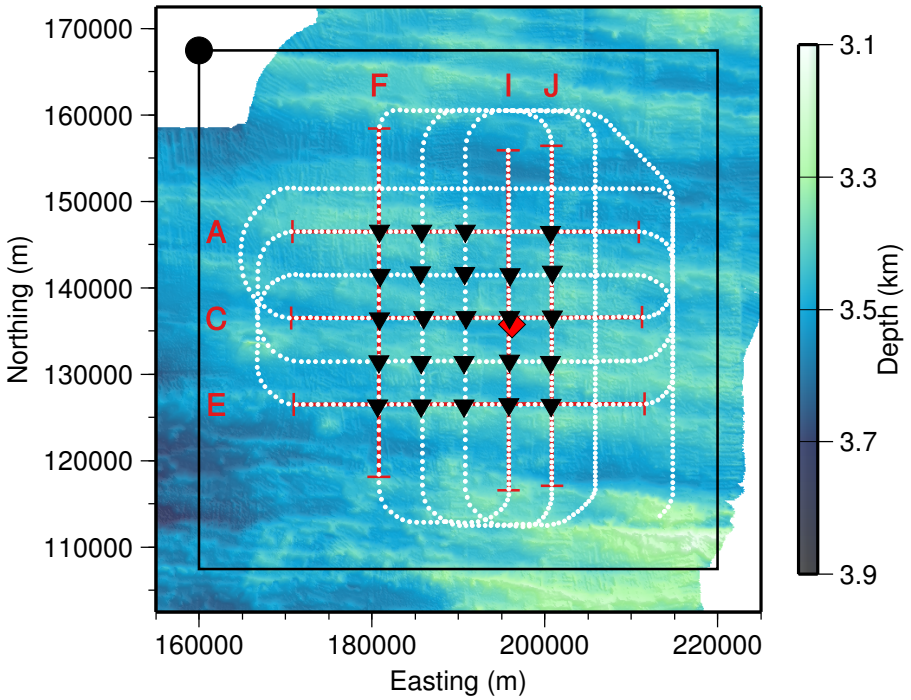


Figure 3.3: Map of the South Grid study area, showing the six profiles modelled in 2D (red, capped lines labelled with profile letter). Black triangles are OBSs, the red diamond shows the position of borehole 504B, and white circles are shot positions (every 10th plotted). The footprint of the 3D model space (black box, with its origin at the black circle), gives space around the outermost shot positions. Coordinates are relative to UTM Zone 17N.

velocity at the base of the bottom layer in the water column model varies according to seabed depth in order to maintain a constant gradient within this layer.

### Seabed

The seabed in each forward model was derived from the swath bathymetry data acquired during JC112 and JC114. Depth values were extracted from a bathymetry grid along the model line to create the seabed at an increment of 500 m.

### Basement topography and sediments

The basement topography in each forward model was derived from the coincident MCS reflection sections (Section 2.4.5). The thickness of the sedimentary package at each CMP (spaced at 6.25 m) was calculated using the TWTT of the picked seabed and basement horizons. This was then converted into a thickness using the average interval velocity picked for the sediments during velocity analysis. Basement depth is produced by summing the seabed depth and sediment thickness at each point along the profile (Figure 3.4). As the MCS profiles are slightly shorter than the model profiles due to profile navigation 'aim point' definitions (Section 2.5.3), with data gaps of up to ∼3 km at each end, the sediment thickness at each end of the MCS profile was extrapolated to the model ends.

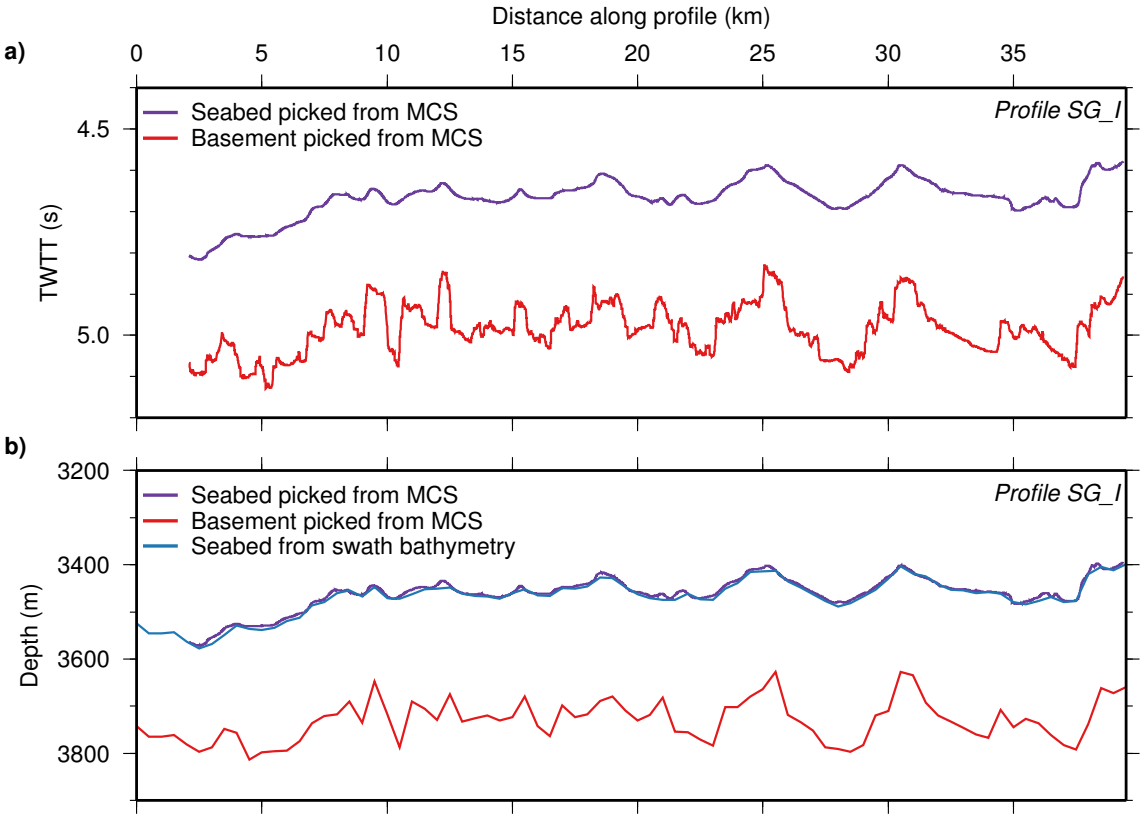


Figure 3.4: The derivation of the basement interface for profile SG_I a) Seabed and basement horizons picked from the MCS line (with CMPs spaced at 6.25 m), plotted against TWTT; b) the horizons in (a) converted to depth using water column and sediment velocities, with the seabed horizon compared with seabed sampled from the swath bathymetry file, and the basement horizon down-sampled to 500 m spacing for inclusion in the model. Note the extrapolation of the basement horizon to the model ends.

The calculated sediment thickness at borehole 504B was compared to the thickness sampled during drilling (275 m). For the profile SG_I model, the closest sample point to 504B is 358 m away, and has a calculated sediment thickness of 258 m, and for profile SG_C the closest point is 812 m away and has a thickness of 247 m. These are differences of -17 m and -28 m, respectively, which, especially considering the distances between the compared points, are within the errors in the estimation of sediment thickness: namely the velocity used for time-to-depth conversion and picking errors on seabed and basement horizons on MCS data (including the resolution of the data itself).

The velocity of the sediments in each initial model was determined using the average interval velocity from the MCS velocity analysis, adjusted to give a low gradient through the sediments as observed in sonic velocity profiles (Newmark et al., 1985) and physical properties studies of sediment cores (Wilkens and Langseth, 1983) from borehole 504B.

### Crustal structure

The velocity structure of 'average' oceanic crust was used to create the initial models [based on Searle (2013) and a previous study of the area by Detrick et al. (1998)], consisting of

a three-layer crust and mantle. This is summarised in the velocity model table below for the profile SG_I model.

| Layer | Top depth (m) | Top velocity (km $s^{-1}$) | Bottom velocity (km $s^{-1}$) | Gradient ($s^{-1}$) | Avg. thickness (m) |
|---|---|---|---|---|---|
| Water 1 | 0 | 1.516 | 1.493 | -0.051 | 442 |
| Water 2 | 450 | 1.493 | 1.485 | -0.018 | 450 |
| Water 3 | 900 | 1.485 | 1.486 | 0.0025 | 400 |
| Water 4 | 1300 | 1.486 | 1.490 | 0.0072 | 550 |
| Water 5 | 1850 | 1.490 | Variable | 0.016 | 1609 |
| Sediments | Seabed | 1.616 | 1.666 | 0.19 | 264 |
| Crust 1 | Basement | 4.500 | 5.200 | 1.0 | 700 |
| Crust 2 | Basement+700 | 5.500 | 6.500 | 0.63 | 1577 |
| Crust 3 | 6000 | 6.500 | 7.000 | 0.13 | 4000 |
| Mantle | 10,000 | 8.000 | 8.200 | 0.033 | 6000 |
| Base | 16,000 | | | | |

Table 3.2: Initial velocity model for the profile SG_I model.

### 3.2.5 Instrument positioning

OBS positions within each model were found by projecting the instrument location into the 2D profile, which was then used to calculate instrument distance along the profile. The depth of each instrument within the model was defined as the seabed depth at its position, which involved a shift from its relocated depth (Section 2.5.2). Where an instrument occurred on two different model profiles, consistent depths were used for both profiles. The maximum depth shift was 22 m and the average shift was 5 m, which corresponds to a travel time of 3 ms. This magnitude of error is already incorporated into the pick errors (Section 3.2.3), thus no corrections to travel-time picks were made to compensate for the change in depth of the instrument. In order to successfully model the ray paths for water waves and sub-surface arrivals, each OBS was positioned just above or below the seabed, respectively, for these different modelling cases. The model OBS placements were tested by modelling the water wave arrivals (direct wave and multiple) to each OBS in *rayinvr*, and checking the fit with the observed data. On all profiles modelled, the $\chi^2$ fit of the direct water wave is 1.0 or under, and for the multiple the maximum $\chi^2$ is 3.2, with the majority below 1.0.

### 3.2.6 Results

The forward modelling procedure detailed in Section 3.2.1 was followed for each of the six models, aiming to reach as close a fit to $\chi^2$=1 as possible for each phase. For the models crossing borehole 504B, SG_I and SG_C, fits of $\chi^2 \leq 1$ (Tables 3.3 and 3.4) were achieved between the observed data and the results of ray-tracing. For the remaining models, a good $\chi^2$ fit of <3 was achieved. The models for these profiles show a similar velocity structure to those for SG_C and SG_I, and are included in Appendix D.

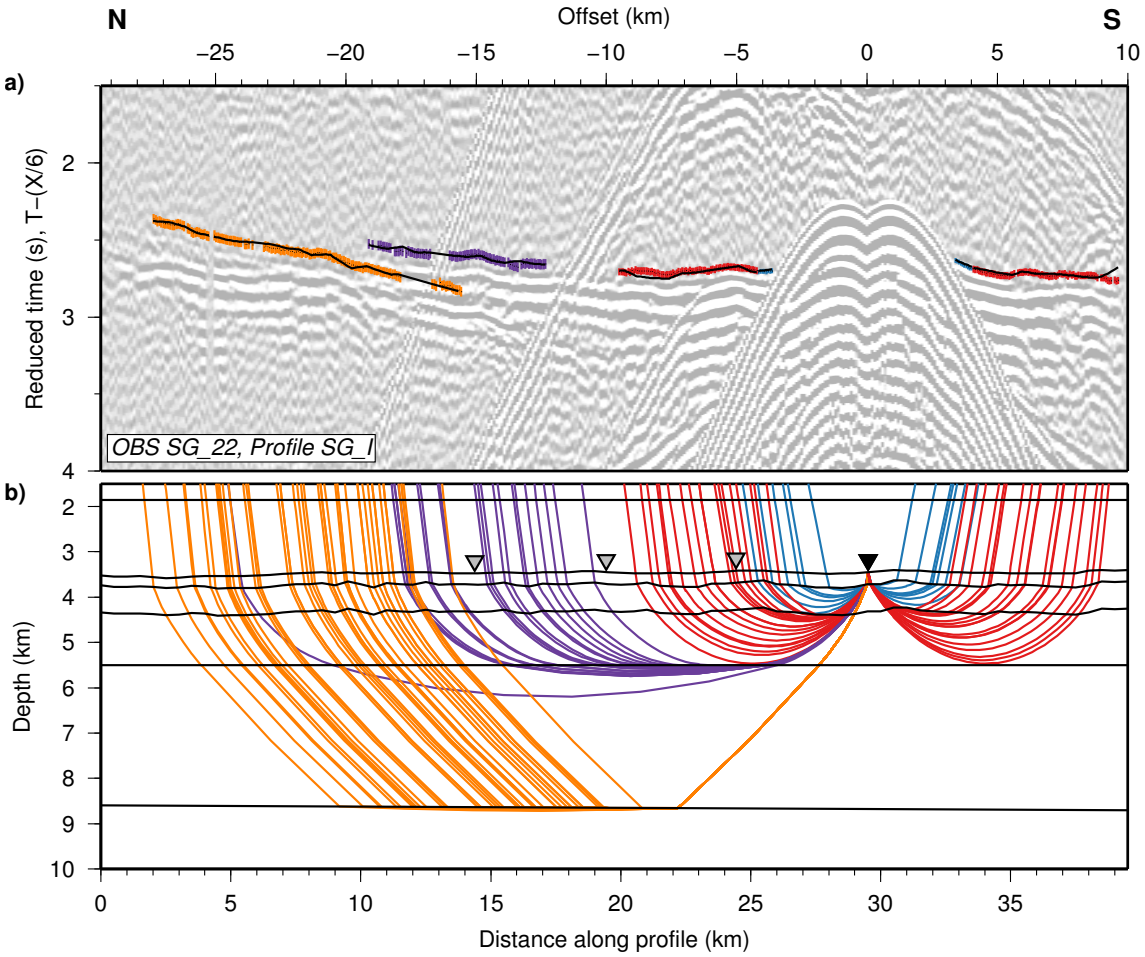


Figure 3.5: a) Picked arrivals for OBS SG_22 from shot profile SG_I (coloured bars- with the size representing the pick uncertainty) compared with modelled travel times from ray tracing (black lines), fitting with $\chi^2$=0.425. Blue=$P_{g1}$; red=$P_{g2}$; purple=$P_{g3}$; orange=$P_n$. b) Ray diagram for OBS SG_22 (black triangle), with ray paths coloured to match picks in (a).

| Phase | Uncertainty (ms) | Number of picks | RMS misfit (ms) | $\chi^2$ |
|---|---|---|---|---|
| $P_{g1}$ | 15 | 85 | 11 | 0.508 |
| $P_{g2}$ | 23 | 610 | 14 | 0.338 |
| $P_{g3}$ | 32 | 554 | 16 | 0.246 |
| $P_n$ | 32 | 374 | 27 | 0.735 |
| Total | - | 1623 | 18 | 0.425 |

Table 3.3: Final forward model fit for profile SG_I.

Many phases have a $\chi^2$ fit of below 1.0, which is regarded as an 'overfit' to the data, and results from either a good initial fit to the starting model of <1.0 for that particular phase (mostly in the case of $P_{g1}$), or a large change in fit to <1.0 from a single change to the model. The overall simplicity of the best-fit forward models for all model profiles shows that no small, unresolvable features have been introduced into the models in order

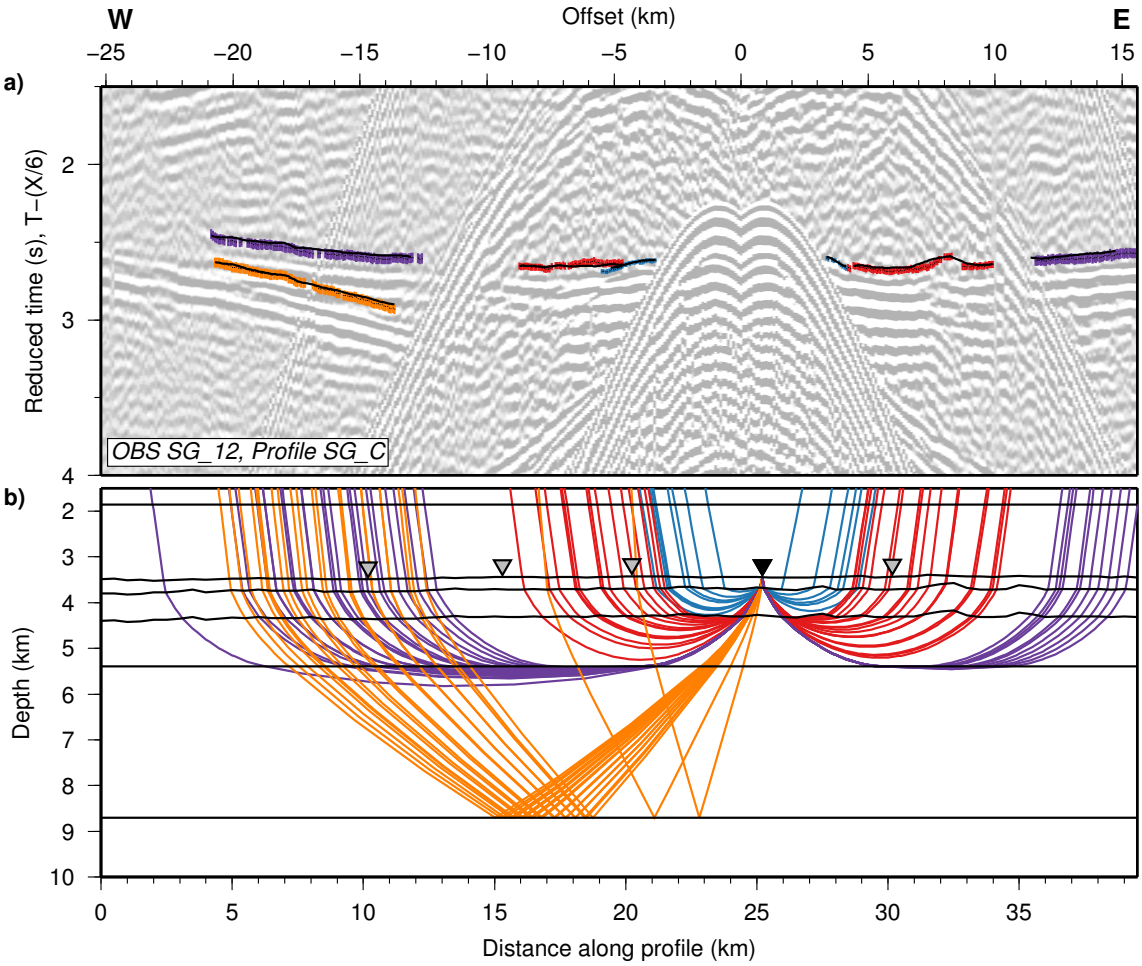


Figure 3.6: a) Picked arrivals for OBS SG_12 from shot profile SG_C (coloured bars- with the size representing the pick uncertainty) compared with modelled travel times from ray tracing (black lines), fitting with $\chi^2$=0.765. Blue=$P_{g1}$; red=$P_{g2}$; purple=$P_{g3}$; orange=$P_n$. b) Ray diagram for OBS SG_12 (black triangle), with ray paths coloured to match picks in (a).

| Phase | Uncertainty (ms) | Number of picks | RMS misfit (ms) | $\chi^2$ |
|---|---|---|---|---|
| $P_{g1}$ | 15 | 136 | 12 | 0.661 |
| $P_{g2}$ | 23 | 650 | 24 | 1.066 |
| $P_{g3}$ | 32 | 588 | 20 | 0.386 |
| $P_n$ | 32 | 419 | 30 | 0.871 |
| Total | - | 1793 | 24 | 0.765 |

Table 3.4: Final forward model fit for profile SG_C.

to produce these low $\chi^2$ values. No extra layers were required to those in the starting model to improve the fit.

The best-fit models for profiles SG_I and SG_C (Figure 3.7) show a smooth, simple crustal structure with little-to-no lateral variation. The profile SG_I model has a top crustal layer 2A that is 0.6 km-thick everywhere, increasing in velocity from 4.5 km $s^{-1}$ at the top to 5.4 km $s^{-1}$ at the bottom. Here, there is a small discrete step, or first-order

discontinuity, in velocity to the top of the second layer 2B to between 5.5 km $s^{-1}$ (at the northern-most end of the profile) and 5.6 km $s^{-1}$ (at the southern-most end), with a linear velocity transition between these end-members. This second crustal layer is, on average, 1.2 km-thick, with a base at a constant depth of 5.5 km and a bottom velocity of 6.7 km $s^{-1}$. The boundary between the second and third crustal layers is characterised by a change in gradient rather than a velocity step: the top velocity of the third layer (layer 3) is also 6.7 km $s^{-1}$, increasing to a bottom velocity of 7.1 km $s^{-1}$. The base of this layer increases from 8.6 km depth at the northern-most end of the model to 8.7 km depth at the southern-most end, giving an average layer thickness of 3.2 km. Below this is the mantle, with an top velocity of 8.0 km $s^{-1}$. The average crustal thickness is 4.9 km.

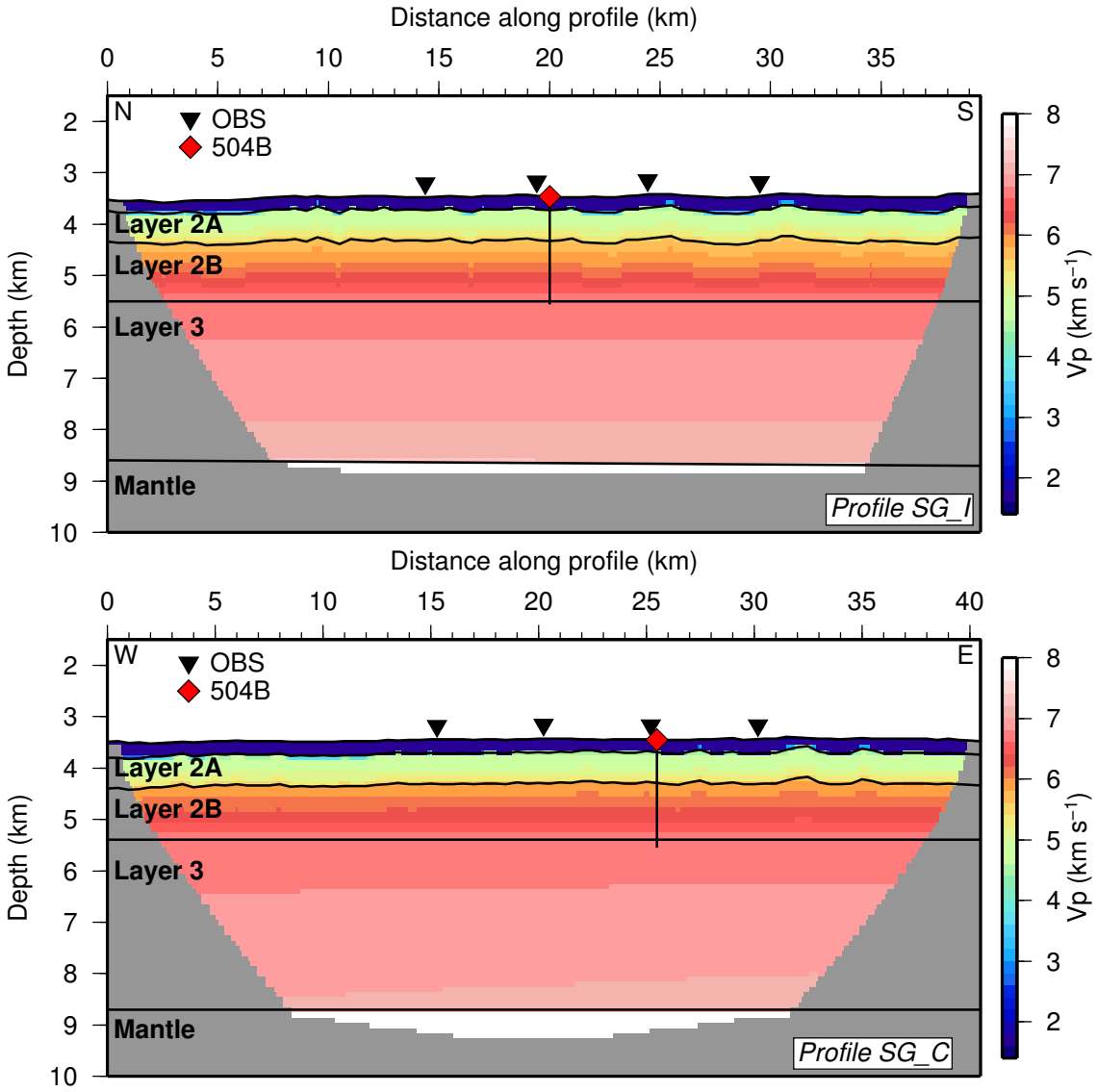


Figure 3.7: Final 2D forward models for profiles SG_I and SG_C. The black vertical line shows the depth extent of the 504B borehole.

In general, the profile SG_C model is very similar, although is slightly smoother than SG_I. This is due to the directional tectonic fabric characteristic of seafloor spreading,

which forms ridge-parallel basement faults, ridges and troughs. At the CRR, this fabric trends E–W, which results in smoother bathymetry and basement topography in the E–W direction (parallel to SG_C), and rougher bathymetry and basement topography in the N–S direction (parallel to SG_I).

The top layer of crust (2A) exhibits the same characteristics as profile SG_I, but has a larger velocity step at the bottom, from 5.4 to 5.8 km $s^{-1}$ at the top of the second crustal layer (2B). The bottom of the second layer is at a constant depth of 5.4 km, with an average thickness of 1.1 km. Both models have a consistent velocity (6.7 km $s^{-1}$) at the transition between the second and third crustal layers, although the bottom velocity of this layer in the SG_C model varies from 7.0 km $s^{-1}$ at the western-most end to 7.1 km $s^{-1}$ at the eastern-most end. The base of the crust in the SG_C model is at a constant depth of 8.7 km, producing a 3.3 km-thick third crustal layer, and an average total crustal thickness of 5.0 km.

The similarity between the SG_I and SG_C models continues throughout the other six profiles, and the general structure for the study area is found by averaging the top and bottom depths and velocities for each layer (Table 3.5).

| Layer | Top depth (km) | Thickness (km) | Top velocity (km $s^{-1}$) | Bottom velocity (km $s^{-1}$) |
|---|---|---|---|---|
| Crust 1 | 3.7 | 0.6 ±0.1 | 4.6 ±0.2 | 5.4 ±0.4 |
| Crust 2 | 4.3 ±0.1 | 1.3 ±0.2 | 5.7 ±0.3 | 6.8 ±0.2 |
| Crust 3 | 5.6 ±0.2 | 3.2 ±0.3 | 6.8 ±0.1 | 7.0 ±0.2 |
| Mantle | 8.7 ±0.2 | - | 7.9 ±0.1 | - |
| Total crust | - | 5.0 ±0.2 | - | - |

Table 3.5: Mean average crustal structure for the six best-fit forward models. Values are quoted with the errors from the sensitivity testing (Section 3.2.7), which are much greater than the standard errors associated with the mean average. The model for SG_F was excluded from the crustal thickness estimate as this profile exhibited anomalously low sensitivity for the depth parameter at the base of the crust (bottom of layer 3).

### 3.2.7 Sensitivity testing and resolution

For any type of modelling problem there are a range of different models which are able to explain the observed data to within a satisfactory fit. This range is normally defined as the maximum deviation allowed from the preferred final model, which still results in the defined 'satisfactory fit'. For every layer each forward model, there were four free parameters to test: bottom depth, top velocity, bottom velocity, and the bulk velocity (i.e. maintaining the same velocity gradient). Given that the level of fit varies between models, and between phases in each model, a satisfactory fit was defined as 1.5× the final model RMS misfit for the phase, or phases, that were used to constrain that model parameter.

These parameter tests were performed to find the average sensitivities (Table 3.6). In general, there was high sensitivity to layer boundary depth of ≤0.3 km, and particularly

for the top crustal layer (0.1 km). Sensitivity to velocity changes is also high throughout the models, with values ranging from a minimum of 0.1 km $s^{-1}$ within crustal layer 3, to 0.4 km $s^{-1}$ in crustal layer 1, although this highest value is mostly due to an unusually low sensitivity of 0.8 km $s^{-1}$ for the profile SG_E model.

| Layer | Bottom depth (km) | Top velocity (km $s^{-1}$) | Bottom velocity (km $s^{-1}$) | Bulk velocity (km $s^{-1}$) |
|---|---|---|---|---|
| Crust 1 | 0.1 | 0.2 | 0.4 | 0.2 |
| Crust 2 | 0.2 | 0.3 | 0.2 | 0.2 |
| Crust 3 | 0.3 | 0.1 | 0.2 | 0.1 |

Table 3.6: Averaged sensitivity testing results for the six forward models.

## 3.3 Three-dimensional tomographic inversion

The primary approach used to determine the structure of the oceanic crust in this study was tomographic inversion, which can produce models independent of modeller bias or preconceptions. The data acquisition geometry of the south grid has full azimuthal coverage of the survey area, and so enables 3D modelling, removing the for in-plane arrival assumption required for 2D modelling.

This section explains the 3D inversion methods used in this study and presents the resulting best-fit model.

### 3.3.1 Method

The main premise of tomographic inversion is to improve the fit between an observed set of travel time picks, and those calculated from a velocity model by automatically updating the model over a number of iterations.

The *First Arrival Seismic Tomography (FAST)* package was used to perform the inversions (Zelt and Barton, 1998), which is a regularised, isotropic, non-linear inversion code which minimises and balances both data misfit and model roughness. The primary version of *FAST* used here accepts only travel time picks from the first arrival on each trace: i.e. it does not model reflections from layer boundaries as well as refractions from layer interiors.

The forward modelling step takes a starting velocity model and calculates ray paths and travel times from given source to receiver positions. *FAST* performs these calculations using finite differencing to solve the eikonal equation, in a method modified from Vidale (1990), on a regularised node-based grid with the grid spacing chosen by the user. The calculated travel times are then compared to the observed to produce travel time residuals.

Travel time residuals and ray paths from the forward step are then used for the inverse step. Updates to the model are calculated to reduce the travel time residuals, and in the *FAST* case, also minimise model roughness. Iterations minimise a function composed of a term containing the data residual vector, and a term containing the horizontal and vertical

regularisation/smoothness matrices, with the trade-off between these two terms controlled by the parameter $\lambda$ (Section 3.3.6). The inverse step is performed on a regularised grid, usually with a larger node spacing than used for the forward step. The forward and inverse modelling steps are repeated until the fit converges to a $\chi^2$ minimum.

### 3.3.2 Filtering and deconvolution

To optimise 3D inversion, the maximum number of travel time picks, from the greatest azimuthal coverage, should be utilised. Thus, ideally, every observed first arrival from every shot within the South Grid area must be picked for every deployed instrument. For a dataset containing 10,148 shots recorded by 24 OBSs, this is a maximum possible total of 243,552 travel time picks. To optimise picking, a user-controlled automatic picking method was developed. Automatic pickers generally work by following either a first break point or peak across the data record from trace-to-trace, thus high SNR and continuity between traces is ideal. Despite its high quality, the OBS data required further processing to maximise the effectiveness of an automatic picker, particularly to suppress the masking effect of the direct water wave and its multiple from the preceding GI airgun array shot (Figure 3.8).

The data processing used to suppress the interference from the GI arrivals is outlined below:

- **deconvolution,** using inverse filter derived from direct water wave arrivals recorded by the vertical array mooring to give an estimate of the farfield seismic wavelet. This suppressed the oscillatory signature of the seismic wavelet;

- **bandpass filter,** to enhance the Bolt airgun arrivals with their peak frequency of ∼10 Hz, low- and high-frequency noise was removed by a zero-phase bandpass filter of 3/6/12/24 Hz.

- **median filter,** as the Bolt arrivals to be picked (mostly crustal refractions) have a different apparent velocity to the GI waterwave and multiple, a median filter proved an effective tool to suppress these arrivals. Crustal arrivals were flattened using a reduction velocity of 6 km $s^{-1}$, before applying a 7-trace median filter. This was effective at removing unflattened arrivals and enhancing the continuity of the crustal refractions;

- **bandpass filter** A further bandpass filter of 3/6/12/24 Hz was applied to clean up the data after the median filtering.

This processing sequence successfully suppressed the GI arrivals sufficiently cleaned up the data to allow effective automatic picking (Figure 3.8). The effect of the filtering process on the pick times was investigated post-picking in the following section (Section 3.3.3).

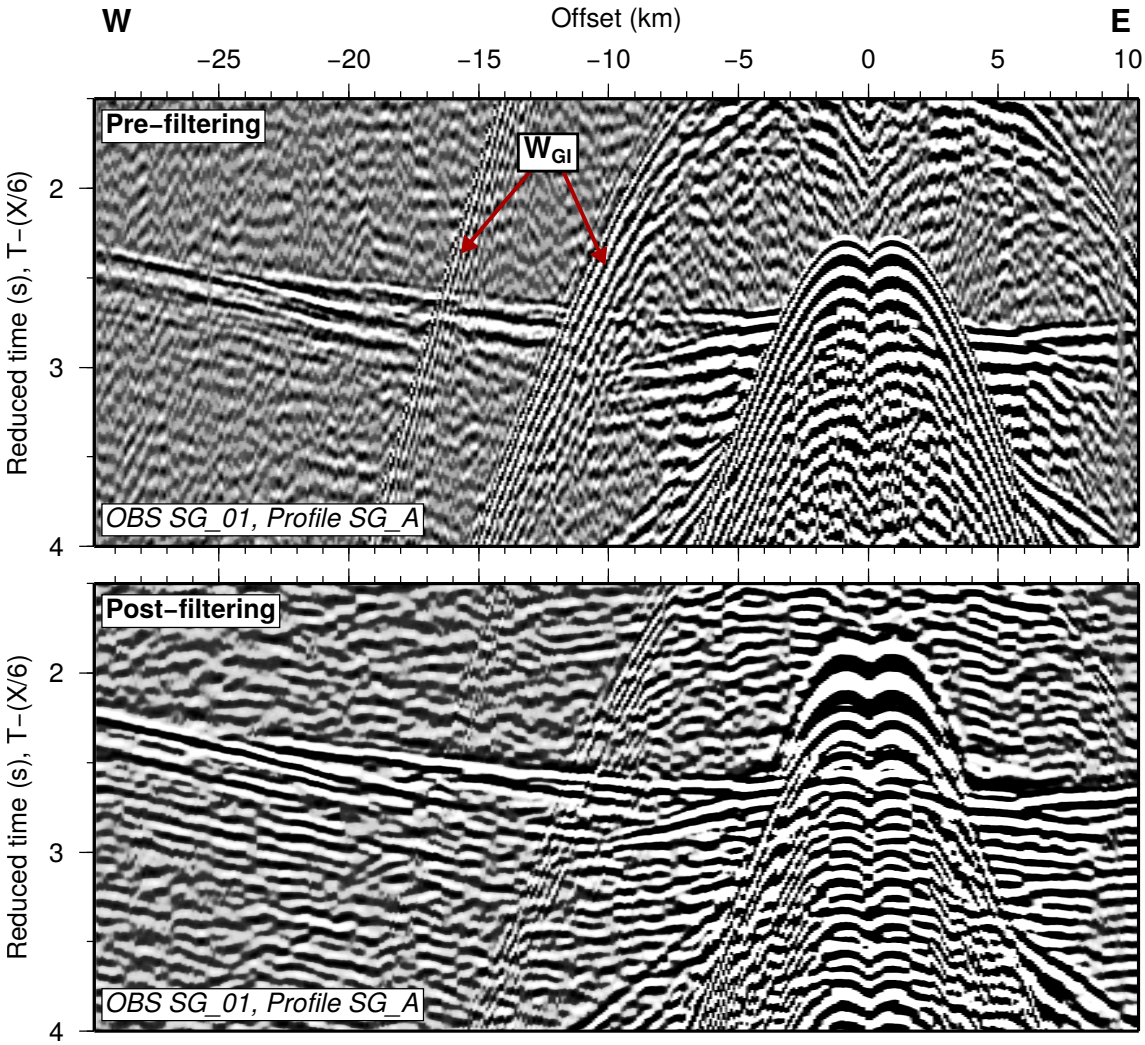


Figure 3.8: Example OBS record section showing the effect of the filtering process, most notably the suppression of the GI water wave and multiple ($W_{GI}$).

### 3.3.3 Travel-time picking

The inversion program, *FAST*, is based on a smoothed, layer-free model defined only by changes in velocity gradient. Consequently, no phase definitions are required for the input data, reducing one source of modeller bias. When picking, the resulting travel times were divided into two groups: crustal and mantle refractions, based on the characteristics described in Section 3.2.2. Arrivals identified as from the mantle were discarded as the focus of the model is the crust.

The data were picked using the 'horizon' picker provided by the GNS Globe Claritas package. Although this was designed for tracking horizons in seismic reflection stacks, it successfully traced along the relatively flat and continuous refracted arrivals in the OBS record sections (Figure 3.9). It is important to note that the high quality of data, along with the relatively smooth seabed lacking rapid bathymetric change in the study area, enabled this approach to work. The user 'seeds' the horizon with a few picks, before the

program automatically tracks the arrival across each seismic trace. The horizon tracker was set to pick the minimum peak value within a given window (i.e. the negative peak, plotted as a white loop in Figure 3.9), as this should be the pick time post-filtering, with a limited variation of 50 ms or less between adjacent traces. Horizons were smoothed with a running mix of five traces. All automatic picks were checked, and if found to be spurious, either adjusted or deleted.

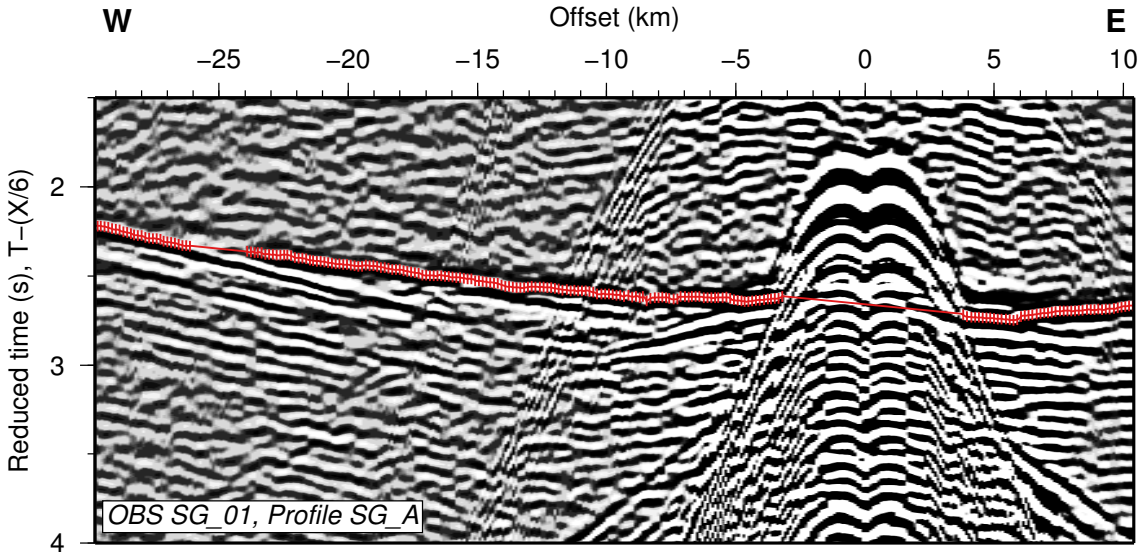


Figure 3.9: Example of a 'horizon' tracked in Claritas along the first arrival, formed of crustal and mantle refractions in this example record section. Vertical bars show the picking error and are plotted for every other pick.

To investigate whether the data processing (Section 3.3.2) had influenced the pick time, automatic picks were compared to their manual equivalents, where made as part of the 2D forward modelling. Both pick sets had similar travel times across the record sections, with an average RMS misfit between equivalent picks of 12 ms and a standard deviation of 4 ms (Figure 3.10). This misfit is within the preassigned travel time errors for the manual picks.

Arrival identification and picking was significantly easier on OBS record sections with shorter shot-receiver offsets, e.g. for the shot profiles passing directly over an OBS and the adjacent profiles (Figure 3.9). Picking on the laterally furthest offset shot profiles was challenging due to a decrease in SNR and occasionally only a few picks were made from these record sections, although many off-profile record sections still exhibited high SNR (Figure 3.11). In total, 145,181 picks were made from the 24 OBSs, with 120,794 crustal arrival picks.

### 3.3.4 Travel time error assignment

Two additional sources of error were introduced to the travel times picked using the automated method, compared to the manual method: 1. from the filtering process and use of the automatic picker, and 2. the difference in SNR between record sections from

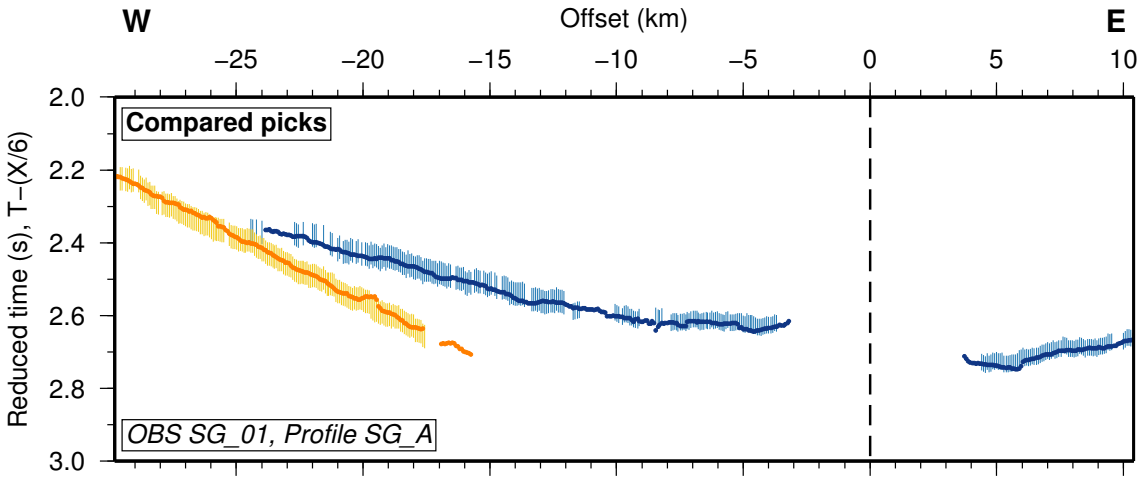


Figure 3.10: Comparison between the picks made manually for forward modelling (plotted as bars, with length equal to the pick uncertainty), and automatic picks made for the inverse modelling (plotted as circles). Crustal picks are plotted in blue, and mantle picks in yellow, with the offset=0 km point marked by the dashed line.

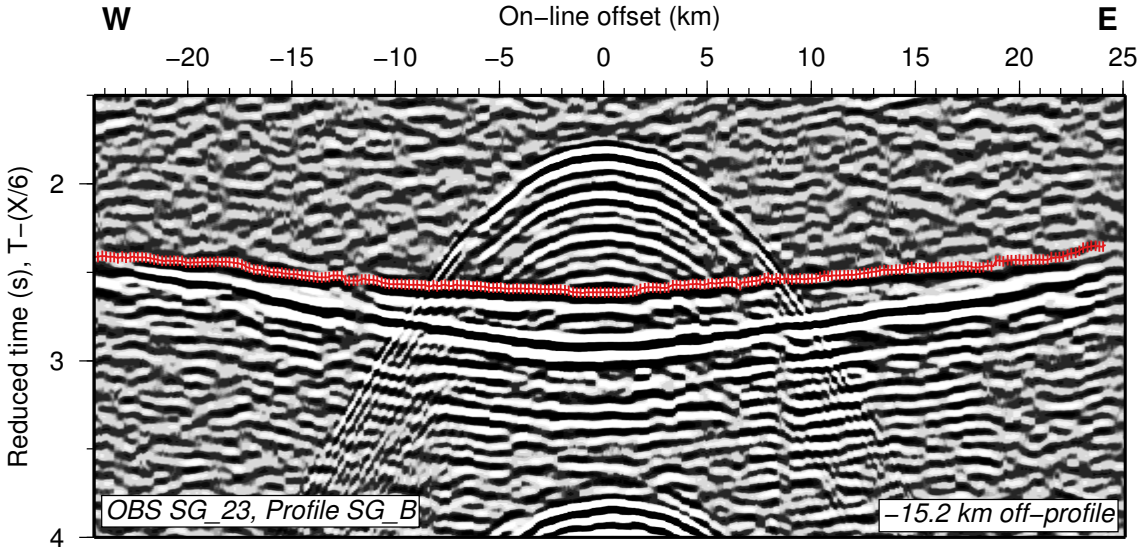


Figure 3.11: Example of a tracked horizon along the first arrival for an off-profile OBS record section which still exhibits a high SNR despite a ∼15 km lateral offset.

on-profile OBS, and off-profile OBS. To compensate for the error introduced by filtering and using the automatic picker, the average RMS misfit between automatic and manual picks, $t_m$, was included into the error equation (eq. 3.2), to give:

$$\text{Total pick error} = \sqrt{t_1^2 + t_2^2 + t_3^2 + t_4^2 + t_5^2 + t_6^2 + t_p^2 + t_m^2} \tag{3.3}$$

$t_m$ has an average value of 12 ms for crustal refractions. Since the crustal automatic picks were not sub-divided into different phases, $t_p$ for these picks was calculated as the average of $t_p$ for the $P_{g2}$ and $P_{g3}$ phases ($P_{g1}$ represents a very small number of picks so was not included in the average). Thus $t_p$ is 28 ms for crustal refractions.

As $t_p$ was only estimated for on-profile record sections, which have the smallest shot-receiver offsets and likely the highest SNR, this is too small an error for many of the other records picked for the 3D inversion. To compensate for this, the final travel time error for each record was weighted by its SNR. This was calculated following a similar method to Zelt and Forsyth (1994):

1. **calculate the energy of the arrival,** the total trace energy was calculated for a 250 ms window centred on each pick, using Seismic Unix command *supickamp* (Figure 3.12);

2. **calculate the energy of the noise,** the total trace energy was calculated for the 250 ms window immediately preceding the pick window (Figure 3.12);

3. **calculate the SNR,** the SNR was calculated as the square root of the arrival energy divided by the noise energy (Zelt and Forsyth, 1994);

4. **convert SNR to a weighting value,** to weight the travel time error, the SNR was converted to a scaling factor to apply to the minimum error value. The minimum SNR for on-profile record sections was set to be a scaling factor of 1, thus all on-profile record sections, and any others with a higher SNR, were assigned a scaling factor of 1. The maximum scaling factor was determined by studying the record sections with the lowest SNR and estimating how this influences the accuracy of picking: a value of 1.5 was determined to be appropriate (equivalent to a travel time error of 45 ms for crustal refractions). Record sections with a SNR between these two end members were designated a scaling factor between 1 and 1.5;

5. **calculate the final travel time error,** the original travel time error given by equation 3.3 was multiplied by the scaling factor for each record to give the final travel time errors used during 3D inversion.

This method gives final travel time errors of 30–45 ms for crustal refractions, and 39–59 ms for mantle refractions.

### 3.3.5 Initial model construction

The model space for 3D inversion comprised a 60 km x 60 km area covering the study region (Figure 3.3), extending to a depth of 15 km. This provided space around the edges of the outermost shots to prevent edge effects. The top-left corner of the model space in plan view (at UTM coordinates 160000,167500) was defined as the origin (X,Y model coordinates 0,0), to ensure that slices from the model plotted consistently from N–S or W–E, left-to-right across the page. This volume was parameterised on a 0.1 km x 0.1 km x 0.1 km grid for the starting inversion model and the forward calculation step, resulting in a total of 361,201 model nodes on each horizontal plane. This grid size was chosen to be able to most accurately represent the seabed interface – common features such as

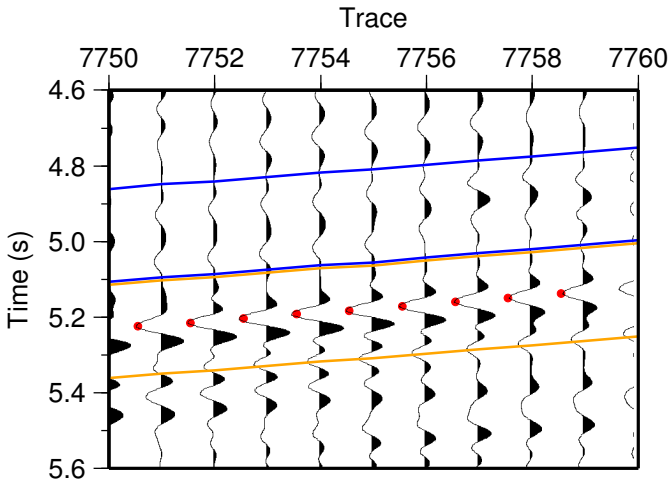


Figure 3.12: Zoom-in on an example OBS record section showing the pick times for a crustal refraction (red dots) and boundaries of the 250 ms windows used to calculate the total trace energy of the signal (yellow lines) and the noise (blue lines).

basement ridges are ∼5 km wide – whilst not making the inversions too computationally expensive.

The starting model consisted of a five-layer water column model (Section 3.3.5), a 2D seabed surface sampled from the bathymetry grid, a layer of sediments whose thickness was determined from the MCS profiles, and a crustal velocity model. A 1D velocity-depth profile was hung beneath each surface node within the model. No lateral variation was introduced into the starting model. As no arrivals from the water column or sediments were used in the inversion process, these regions could not be constrained by this method, thus were 'fixed' during inversion so all model updates occurred in the crust.

### Water column

The water column in the 3D velocity model was constructed using the same technique as the 2D forward models (Section 2.5.2), and remained constant throughout all 3D inversions.

### Seabed interface and instrument positioning

The seabed interface was first sampled from a merged bathymetry dataset (Section 2.2.1), formed from data acquired during JC112 and JC114, SO138, EW9416, and data from the GEBCO global bathymetry dataset. These data were merged to form a 'master' bathymetry file with UTM coordinates (Zone 17N), and 0.1 km grid spacing. These data were then projected on to the model node locations (Figure 3.13).

This bathymetry grid, at the OBS positions, was everywhere deeper than the relocated OBS depths (by -2 m to -23 m, with an average of -10 m). As instruments had to be relocated onto the model seafloor to model ray paths correctly, this created travel time errors. There were also discrepancies in some instrument depths compared to those used

for the 2D modelling (which had the seabed interfaces derived solely from James Cook data). Thus, from starting model number 17 onwards, a new master bathymetry file was used. This used a data source hierarchy to prioritise more accurate, reliable, and higher resolution data, with the order: 1. JC114 and JC112 data; 2. SO238; 3. EW9416; 4. GEBCO data. If data from a James Cook source was available at a grid node, then this was solely used to define the seabed depth. If not, then a Sonne data point was searched for, and so on down the hierarchy, so that the poor resolution GEBCO dataset was only utilised at nodes where no swath-derived bathymetry was available.

This new bathymetry file (Figure 3.13) had smaller discrepancies (-4 m to 21 m, with an average of 6 m) when compared to relocated instrument depths, and enabled consistent depths to be used in both the 2D forward and 3D inverse modelling. The difference between the old and new bathymetry grids follows the ship track of cruise SO238, and suggests that a different velocity profile was used to calculate seabed depth from the swath travel time measurements, resulting in, on average, a deeper seabed.

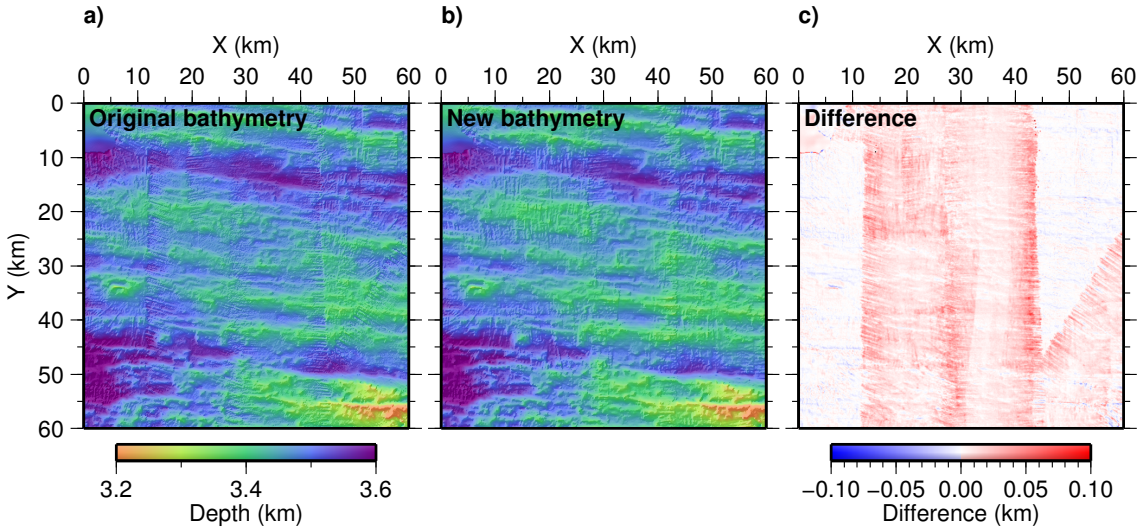


Figure 3.13: a) The original bathymetry file first used to create the 3D starting models, compared to b) the updated and improved bathymetry file made by prioritising data from the James Cook research cruises. The difference between the two files (original-new) is shown in c).

The 24 OBS were positioned on the seabed in the model, with minor adjustments (mean absolute change of 2.6 m) made to ensure consistency between the 2D forward and 3D inverse modelling. The mean absolute deviation between the consistent model depths and the original relocated depths was 5.7 m. These small deviations were already accounted for in the uncertainties calculated for the travel time picks (Section 3.2.3), thus no travel time corrections were made to the picks to account for the depth changes. The positions were checked by running the forward calculation step in *FAST* using these depths, and the majority of possible rays from all instruments traced successfully.

### Sediments and basement interface

A sediment layer of variable thickness was defined using the seabed and basement horizons picked from the 12 MCS sections in the South Grid survey area (Section 2.4.5). The sediment thickness in TWTT was calculated for each CDP position, and then converted to depth using the average interval sediment velocity from velocity analysis of the 12 profiles (1.68 km $s^{-1}$). The average sediment thickness for the survey area is 258 m. The sediment thicknesses were converted into model space coordinates, interpolated to grid nodes, and gridded to cover the whole survey area at 0.1 km grid spacing (Figure 3.14). To smoothly interpolate between the MCS profiles (5 km apart), the gridding was performed using GMT program *surface*, which 'drapes' a surface over the existing data points with a specified tension factor, before smoothing with a 5 km-wide gaussian filter. A variable basement topography surface was created by the summing of the seabed depth and sediment thickness at each node (Figure 3.14).

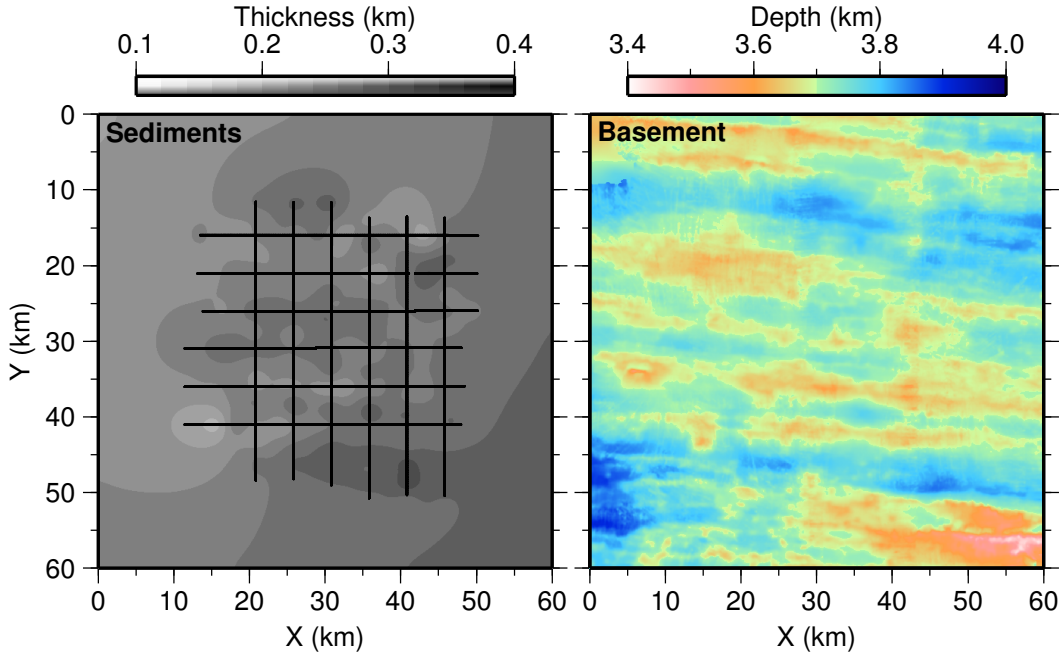


Figure 3.14: Sediment thickness layer (left), derived from the MCS profiles (black lines), and basement interface (right), derived from the sediment thickness and bathymetry interface.

### Crust

In inversion, using starting models too different from the 'true' structure can result in the inversion procedure finding a local minima or being unable to converge to any solution (Mosegaard and Tarantola, 1995) as the velocity structure also controls the propagation paths of the rays, so the initial structure can influence where model updates occur during the process. To ensure the inversion process finds the 'real' minima, prior knowledge can be used to pre-condition the model. This was done by constructing a selection of initial models using the results of the 2D forward modelling.

The average 1D profile from the 2D forward models was calculated by extracting 1D profiles through the crust at the mid-point of each of the six models with a depth spacing of 0.1 km (the same size as the 3D forward model grid spacing). The mean velocity was then calculated for each depth point within the crust to give the average profile (Figure 3.15). If necessary, the bottom layer of the 1D model (the mantle) was extrapolated downwards to the base of the 3D model, maintaining a constant gradient. The crustal profile was then smoothed using a 15-point moving average to soften the sharp layer boundaries present in the 2D forward models (Figure 3.15). The smoothed profile was 'hung' beneath the basement interface at each model node, ensuring each point had exactly the same starting crustal structure, and that velocity contours across the starting model follow the basement topography.

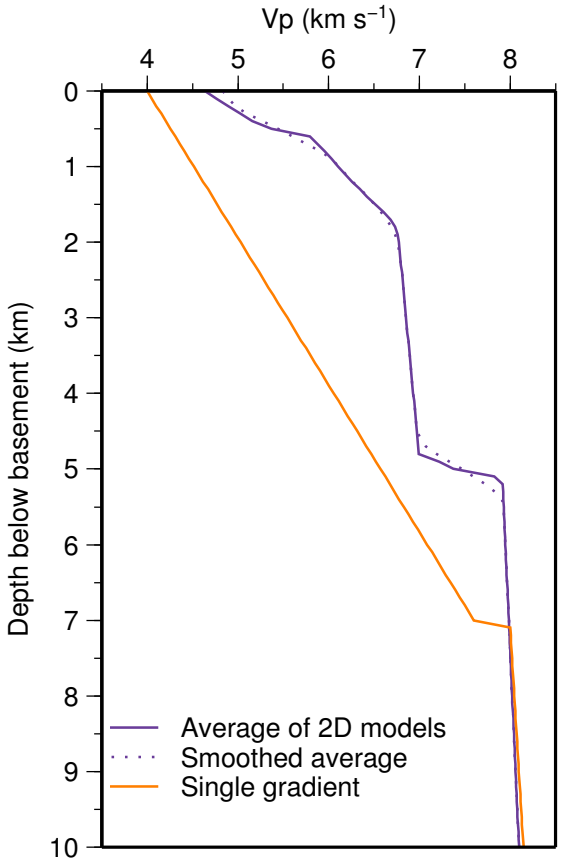


Figure 3.15: Examples of 1D velocity-depth profiles used to define the crust and mantle in the 3D starting models.

Due to the parameterisation of the model volume onto a 0.1 km grid, the sediment-basement interface cannot be created as an instantaneous increase in velocity from ~1.6 km s$^{-1}$ to >4 km s$^{-1}$ (Figure 3.16), as it is in reality. In the model this transition must instead occur over 0.1 km, from the bottom sediment-velocity node, to the top crust-velocity node, which can have the effect of artificially increasing or decreasing the given sediment thickness (Figure 3.16). This, in turn, affects travel times calculated through the model, and

thus on the velocity updates applied during inversion, particularly within the uppermost crust.

The effect of this parameterisation was investigated by performing 2D inversions in *FAST* while varying how this boundary was defined. Type 'A' models had the transition to crustal velocity occurring below the sediment layer, whereas type 'B' models had the transition included within the sediment layer (Figure 3.16). The models were created along a N-S cross-section through the 3D model, along shot line SG_C, and the inversions run with identical data and parameters. For type A models, these had a high velocity in the upper 100 m of the crust (5.0–5.5 km $s^{-1}$), and were susceptible to developing unrealistic velocity inversions and artefacts. For type B models, the final models had similar upper crustal velocities to those in the 2D forward modelling results, and more importantly, to ground-truth provided by the sonic log-derived velocities from borehole 504B (∼4.5 km $s^{-1}$). This suggests that including the velocity transition within the sediment layer gives more realistic inversion results, thus this is how this boundary was parameterised in this study.

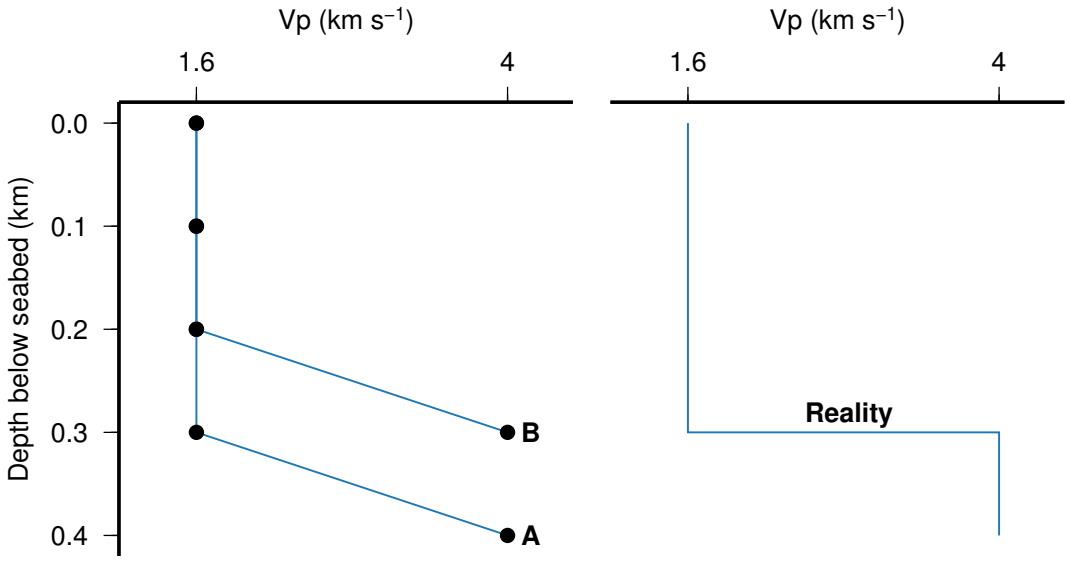


Figure 3.16: Parameterisation options tested for the sediment–basement interface, here shown for an example sediment thickness of 300 m, compared against the instantaneous velocity change in reality. The type A model begins the velocity transition below the full 300 m-thick sediment layer, whereas the type B model includes the transition within the 300 m.

### 3.3.6 Inversion parameters

Within *FAST*, the inversion process is controlled by a number of variable parameters and inputs: the starting velocity model (Section 3.3.5), the inversion cell size, smoothing parameters, 'freedom' parameter, and the observed travel time picks and their uncertainties.

### The 'freedom' trade-off parameter, $\lambda$

In *FAST*, the freedom to update the model between iterations is controlled by the trade-off parameter, '$\lambda$', with a lower value allowing larger updates to the velocity model. Within the function that calculates model updates between iterations, '$\lambda$', is a factor which weights the term conforming to the constraint equations, which maintain model smoothness, against the term which improves data misfit (Zelt and Barton, 1998). A high $\lambda$ value highly prioritises conformation to the constraint equations, and may stop the inversion making large, unrealistic updates and becoming unstable. However, this may also not allow significant enough changes to meaningfully reduce the misfit to the data, if at all. A low $\lambda$ value reduces the smoothness priority ($\lambda$<1 would prioritise reducing data misfit), and allows the inversion process to make larger updates to the model to reduce the misfit to the observed data. However, this may result in a rough and unrealistic final model. Within each iteration *FAST* tests a given number of different values of $\lambda$ (in the case of this study, 5 at each iteration), beginning with an input value chosen by the user, and reducing it by a factor of $\sqrt{2}$ (as the default) for each subsequent test. The $\lambda$ value which results in the smallest data misfit is selected.

### Smoothing parameters

Three parameters, *sz*, $\alpha$, and *sedge*, may be varied in *FAST* to control the smoothing of the velocity model during the inversion process:

- *sz* controls the importance of maintaining vertical smoothness during the inversion process, relative to the horizontal smoothness (Figure 3.17). Values range from 0 upwards, with a value of 0 resulting in no constraint on vertical smoothness. In this study, values ∼0.3 were used to enable some vertical smoothing;

- $\alpha$ is a weighting factor which controls the relative importance of fitting the smallest perturbation constraint equations, or the smoothest/flattest constraint equations. A value of 1 only uses the smoothest/flattest equations, and a value of 0 only uses the smallest perturbation equations. In this study, values of 1, or close to 1, were used to produce the smoothest models which fit the observed data. Low values of $\alpha$ (e.g. 0.1) lead to unrealistic models (Figure 3.17);

- *sedge* controls the smoothing at the edges of the model and varies from 0 upwards. It represents the weighting of the smallest perturbation constraints at the edges, with higher values (e.g. 100) causing smoothing from the edges towards the model interior (Figure 3.17). Lower values (e.g. 0.1) are often utilised to prevent smoothing from the edges where there may be little-to-no ray coverage. In this study, low values of ∼10 were used to limit this smoothing.

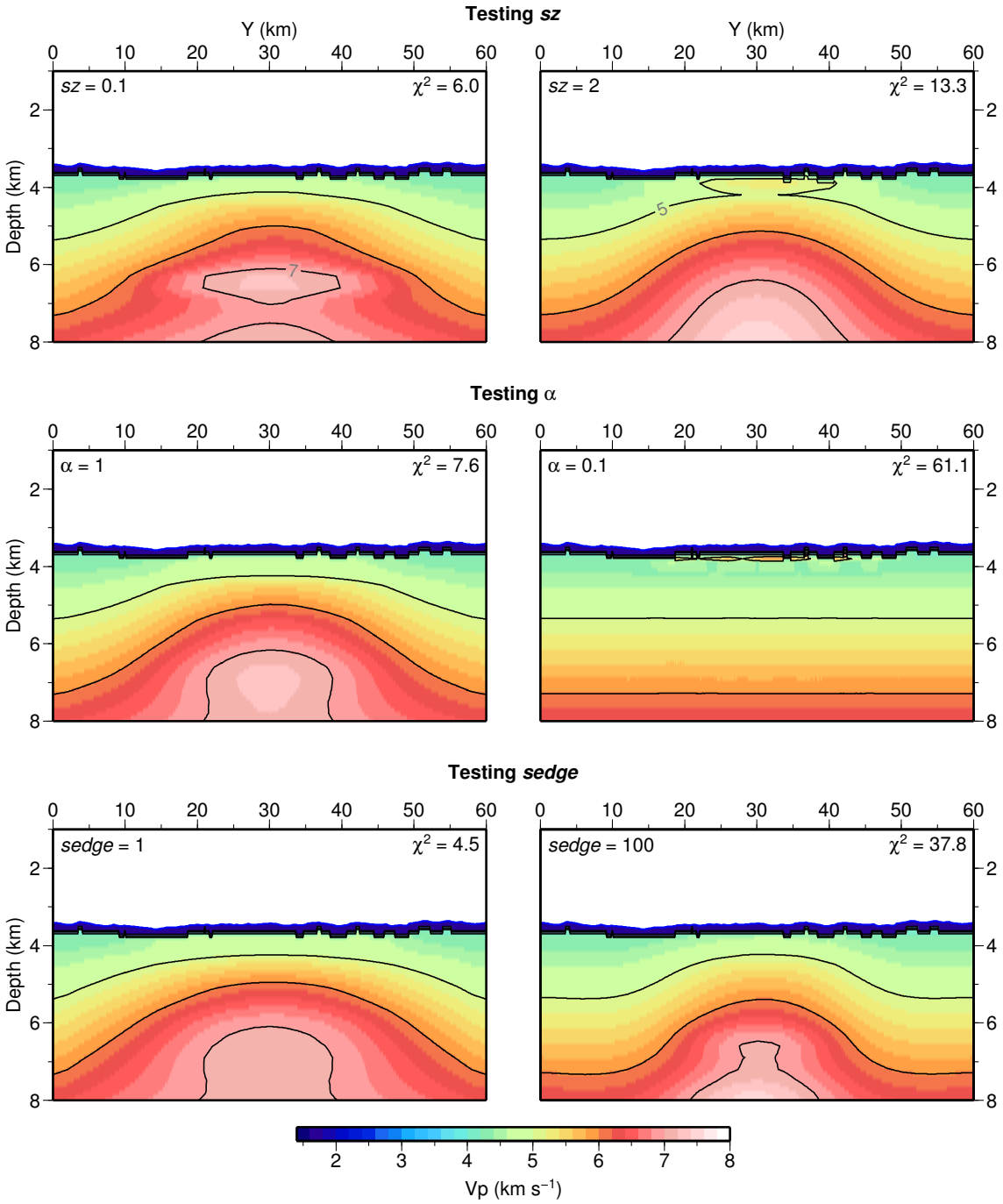


Figure 3.17: Results from inversions testing the end-member effects of the different smoothing parameters *sz*, $\alpha$ and *sedge*. All inversions were run with the observed travel time picks for five iterations using a 2 km width by 0.3 km depth cell size, and $\lambda$ value of 500. When not being tested, parameters were kept constant at *sz*=0.3, $\alpha$=1 and *sedge*=10. The panels show cross-sections oriented N-S through the location of borehole 504B (X=36.2 km) with the 3D model. Lower values of *sz* and *sedge* and higher values of $\alpha$ tend to result in smoother models with a better $\chi^2$ fit to the data.

### Inversion cell size and strategy

The cell size used for the inversion step was larger than the 0.1 km parameterisation for the forward calculation step, with different dimensions in X, Y and Z chosen to maximise

the resolution of the final model, within the errors of the observed data and its coverage. Using a larger cell size, such as 5 x 5 x 1 km, generally resulted in a smooth model with little lateral variation, and the inversion process struggled to converge to $\chi^2$ values of $\leq$1. Using a smaller cell size, such as 1 x 1 x 0.25 km, generally resulted in a rougher, better-fitting model. However, when the inversion ran for more than $\sim$5 iterations, these contained unrealistic velocity inversions and artefacts due to gaps in ray coverage. For example, faster "bulls-eye" regions surrounding each instrument.

To produce a model which was smooth and realistic from a poorly-fitting starting model, whilst optimising model resolution, a two-tier inversion process was implemented. An initial inversion run was performed with a large cell size, less freedom (high $\lambda$ value) and greater smoothing, in order to resolve the smooth large-scale structure, before running several iterations with a smaller cell size, more freedom (low $\lambda$ value) and less smoothing to resolve the small-scale variations in structure.

### 3.3.7 Results: Model A

The starting model defined above fitted the observed data well, with a $\chi^2$ value of 2.1. This was not surprising since the velocity structure of the crust in this model was built from the results of the 2D forward modelling. As the large-scale structure within the model was already providing a reasonable fit to the data, the inversion was solely run with a small cell size (Table 3.7). Within one iteration the inversion converged to a $\chi^2$ of below 1. The final model is almost identical to the starting model, only containing some minor, and smoothed changes to its velocity structure. It is fairly homogeneous with little lateral change in velocity across the model.

Although the result of this inversion provides a good fit to the observed data, the good fit of the starting model suggests that this result cannot be regarded as an unbiased method of defining the velocity structure of the study area. Within inversion studies (Mosegaard and Tarantola, 1995; Detrick et al., 1998; Dunn et al., 2005), the use of prior knowledge to precondition the model is regarded to help the process converge towards the 'true' minimum. The inversion process in this case had no opportunity, or freedom, to iterate towards a solution, as within one iteration the model became 'over-fit' to the observed data. However, the use of a starting model with a very close fit, as here, prevents the inversion process from widely sampling the potential model space, and indicates the result may be a convergence into a local minimum predetermined by the starting model.

Thus a new starting model was created to use in the inversion.

### 3.3.8 Construction of Model B

A new starting model was constructed using very little prior information. The result of such an inversion provides an independent test of the velocity structure to the 2D forward modelling, enabling the results to be compared. The new starting model was identical to Model A from the surface to the top basement interface. The crust in Model B was created

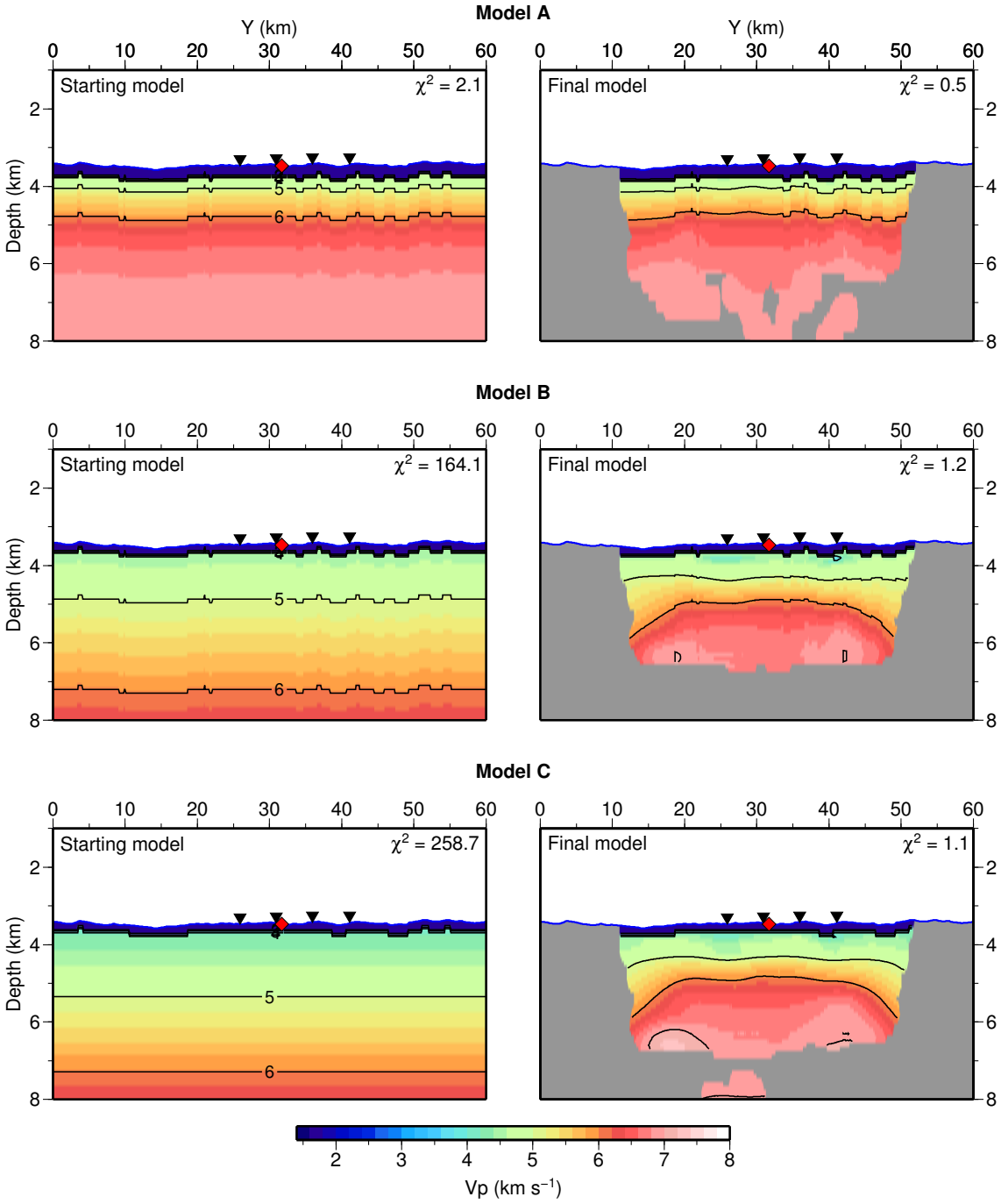


Figure 3.18: Starting (left) and final (right) models for three different 3D inversion runs. A a N–S-trending cross-section through the position of borehole 504B (red diamond) is shown for each. OBS along the profile are shown by the black triangles. The final models are masked by ray coverage. Grey regions are unsampled by rays.

| | Stage 1 | | | | Stage 2 | | | |
|---|---|---|---|---|---|---|---|---|
| | Cell size (km) | | $\lambda$ | iterations | Cell size (km) | | $\lambda$ | iterations |
| | X | Z | | | X | Z | | |
| Model A | 1 | 0.25 | 20 | 1 | | | | |
| Model B | 2 | 0.3 | 500 | 5 | 1 | 0.2 | 50 | 3 |
| Model C | 2 | 0.3 | 500 | 5 | 1 | 0.2 | 50 | 4 |
| $sz = 0.3$; $\alpha = 1$; $sedge = 10$ | | | | | | | | |

Table 3.7: Inversion parameters used in *FAST* when creating the presented models.

using a single-gradient velocity-depth profile (Figure 3.15), increasing from 4 km $s^{-1}$ at top basement to 7.6 km $s^{-1}$ at 7 km depth, which is the average thickness of oceanic crust after White et al. (1992). This profile was 'hung' beneath the top basement interface at each node in the 3D model.

### 3.3.9 Results: Model B

The Model B starting model fits the observed data with a $\chi^2$ of 354, significantly larger than the Model A starting model. The inversion was conducted following the two-stage strategy, and was initially run for five iterations with a larger cell size and high $\lambda$ value (Table 3.7) to smoothly resolve the general structure of the study area. This initial stage (Stage I) reached a plateau at a $\chi^2$ of $\sim$10, only producing very smooth models. For the second run (Stage II), the cell size and $\lambda$ value were reduced to allow smaller features to be resolved, resulting in a final velocity model with a $\chi^2$ of 1.2 within three further iterations.

The final velocity model is significantly different from the poorly-fitting starting model (Figure 3.18). It is laterally smooth and relatively homogeneous, with only slight variations in velocity laterally. This homogeneity is similar to the Model A result, however the increase in velocity from the top of the igneous crust is more gradual in Model B, with the upper >0.7 km below 5 km $s^{-1}$ compared to $\sim$0.3 km in Model A. There are also some artefacts from edge effects visible in Model B. The unsampled edges of the model remain the same as the starting model, which in the case of Model A is very similar, resulting in no change in the depth of velocity contours, but in Model B is much slower, resulting in a deepening of velocity contours towards the edges.

The method by which the starting model for Models A and B were constructed, by hanging a 1D profile off the top basement at each node in the model, creates a dependency of velocity on the basement depth within the 3D model. This dependency makes it difficult to interpret any trends in velocity that seem to be related to basement topography, which could indicate past regions of alteration or fluid flow. To investigate whether removing this dependency influence the final inversion model, a new starting velocity model was created (Model C).

### 3.3.10 Construction of Model C

The starting model for Model C was constructed from the surface to top basement in the same manner as Models A and B. The igneous crust in Model C was formed using the same 1D, single-gradient velocity profile as Model B. However, in this case, the profile was not 'hung' off the top basement at each node in the model, but instead inserted to ensure a constant velocity at each depth below the sea surface. This forms horizontal velocity contours across the model, as opposed to contours which follow the basement topography (Figure 3.18).

### 3.3.11 Results: Model C

The Model C starting model fits the observed data with a $\chi^2$ of 259, of a similar order of magnitude to the Model B starting model, and considerably greater than the Model A starting model. As such, the two-part inversion strategy was used. Stage I of the inversion ran for five iterations with a larger cell size and greater $\lambda$, and plateaued at a $\chi^2$ of $\sim$8. A reduction in cell size and smaller $\lambda$ in Stage II of the inversion enabled the $\chi^2$ to converge to a value of 1.1 after a further four iterations.

Similarly to Model B, the final model is significantly different to the starting model, with generally much faster velocities in the upper crust, and maintains a smooth and relatively laterally homogeneous structure. The features within the model are also similar to Model B, with variations in velocity of similar amplitudes in the same locations, which is visible in the depth changes in the 5 km $s^{-1}$ contour (Figure 3.18). Artefacts from edge effects are also present, due to the lack of ray coverage around the edges of the model volume, as with Model B.

### 3.3.12 Preferred model

The final model from the Model C inversion is the preferred 3D inversion result. Unlike Model A, the Model C crustal starting model was constructed based on very little prior knowledge of the velocity structure of the study area. This resulted in a large $\chi^2$ value between the starting model and the observed data which allowed the inversion the freedom to converge through several iterations to a solution (Figure 3.19). This solution can then be regarded as an independent result to the 2D forward modelling results. The advantage of the Model C result over the Model B result is that the crustal velocities in the starting model were input unrelated to the basement topography. This allows a more confident interpretation of any trends between the velocity and basement structures, which may relate to alteration and fluid flow patterns. The similarity between the Model C and Model B final models raises the confidence that any trends observed are real and are not artefacts from the model construction process.

In general, the preferred model is smooth and fairly homogeneous, with no large lateral variations in velocity structure (Figures 3.20 and 3.21). Crustal velocities increase from 4.2 km $s^{-1}$ to 4.7 km $s^{-1}$ in the upper $\sim$0.6 km of crust, before increasing more rapidly to

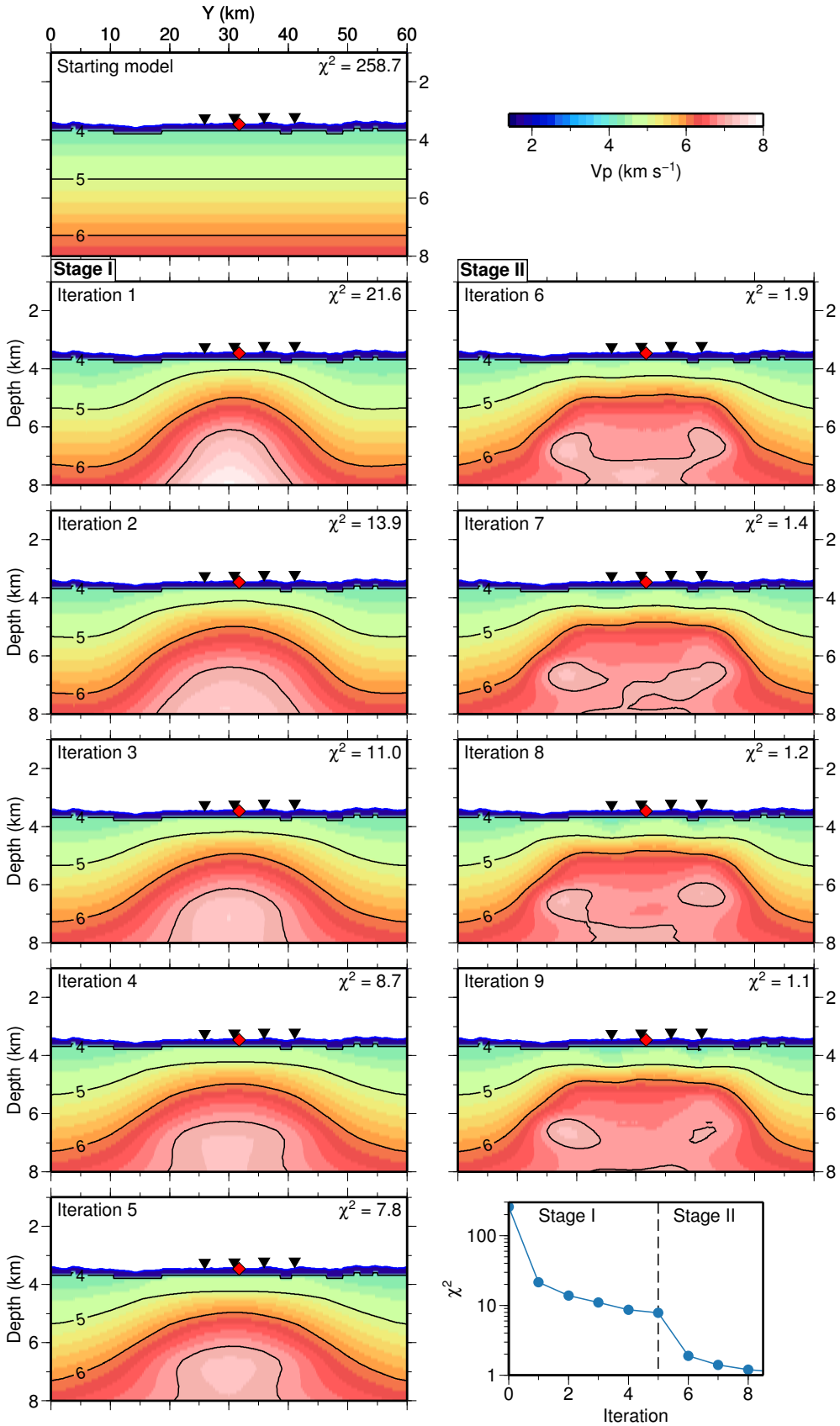


Figure 3.19: Cross-sections through the 3D model at each iteration of the inversion run for Model A, taken N–S through the position of borehole 504B. The first five iterations were conducted at a larger cell size, with the last three iterations at a smaller cell size resolving finer details in the velocity structure and achieving a closer fit.

~5.5 km $s^{-1}$ at ~1 km depth. At ~1.3 km, velocity starts to increase more gradually, from ~6.5 km $s^{-1}$ to ~6.7 km $s^{-1}$ at 2.3 km, below which ray coverage and model resolution are poor. There is generally more lateral variation in velocity in the N–S direction than the E–W direction (Figure 3.20), with the largest variations occurring with the uppermost 0.5 km of the crust, shown, for example, by the 4.6 km $s^{-1}$ contour.

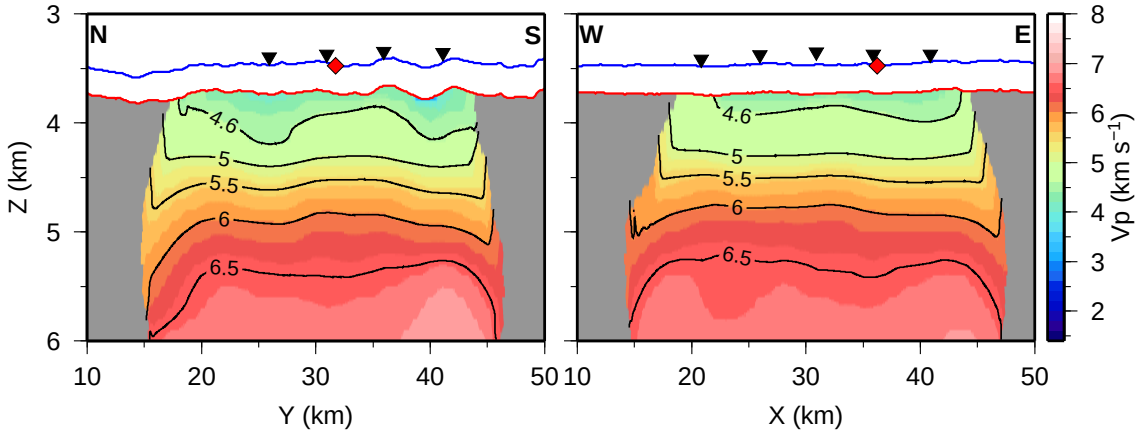


Figure 3.20: Cross-sections through the preferred final model, in N–S and E–W directions through the position of borehole 504B (indicated by red diamond), with OBS positions on the profiles shown by black triangles. The bathymetry and basement interfaces are shown by the blue and red lines, respectively. The velocity structure is masked using the semblance values from checkerboard testing, with visible structure tested to be resolvable with a 4 km-size checkerboard to semblance values of 0.7 or above. The rapid deepening and shallowing of velocity contours towards the edges of the visible model is due to artefacts from the unsampled edges of the model space.

The variations are more clearly shown by plotting the velocity anomaly (Figure 3.21), which was calculated as the difference from the mean velocity at a depth below basement. The mean was calculated from the central 400 $km^2$ of the model, to prevent bias from the outermost, unsampled areas of the model. The model slices show maximum variations of 0.4 km $s^{-1}$ in the upper 1 km of the crust, and smaller variations of below 0.2 km $s^{-1}$ below this depth. There is a large, positive velocity anomaly which extends for ~15 km in an E–W direction centred on Y=20 km, with a width of ~5 km. This anomaly is present from the top of the crust to >1.2 km depth. Two smaller velocities anomalies are centred on Y=32 km, ~5 km in length and width and extending over the same depth range. Between these two anomalies, and the larger one, is a region of negative velocity anomaly, extending in an E–W direction across the model at Y=~25 km, and again to similar depth ranges. There are also many smaller anomalies, both positive and negative, present in the model, however these appear to be related to the basement topography. These smaller anomalies may also be below the resolution of the model, which is investigated in Chapter 4.

## 3.4 Summary

In this chapter the methods used to conduct both 2D forward modelling and 3D inversion have been discussed, and the final, preferred models presented.

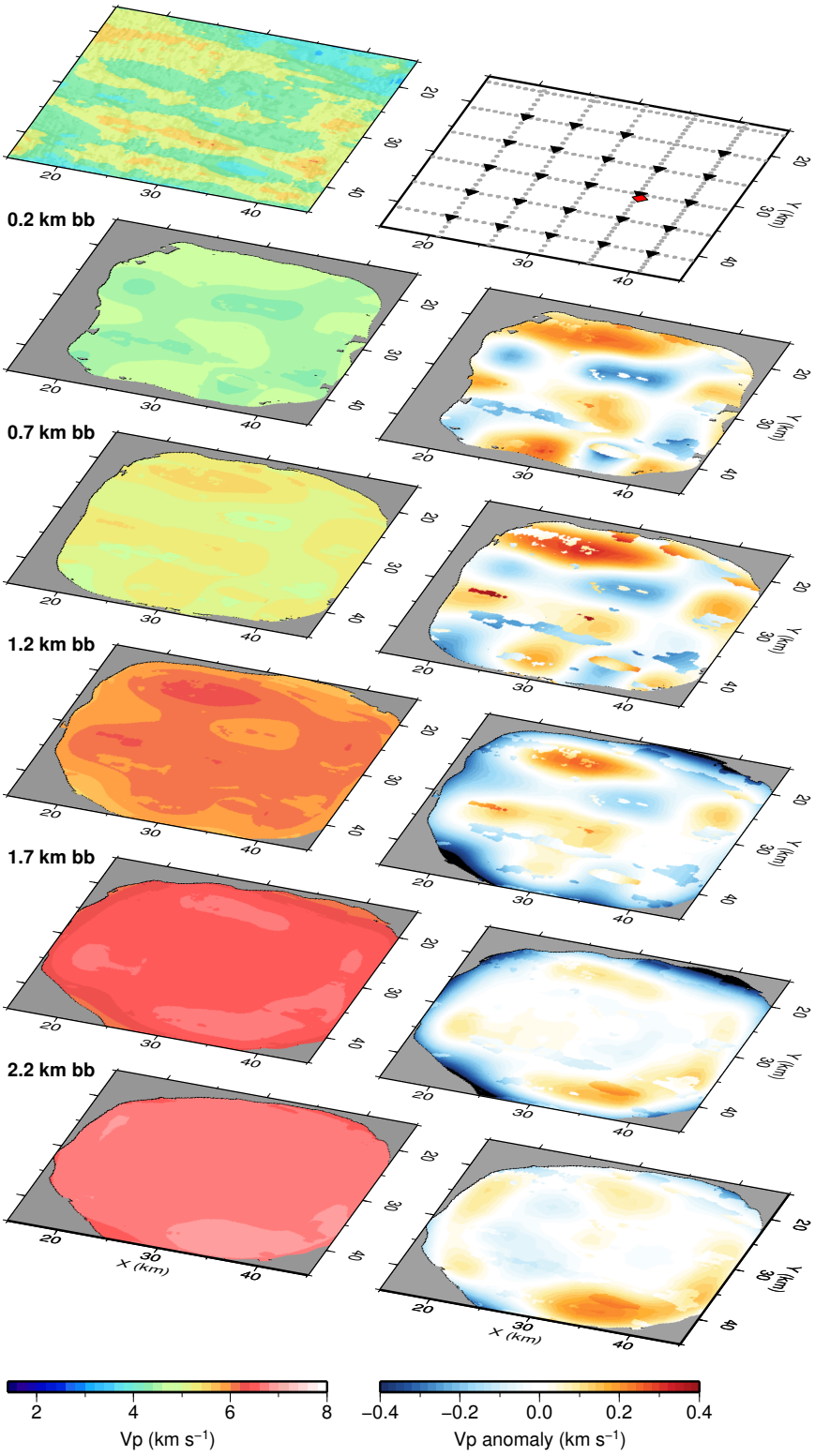


Figure 3.21: Depth-sections through preferred model at 0.5 km increments below basement (km bb). Basement topography and the experiment geometry are shown for reference at the top (black triangles=OBS; grey dots=every 10th shot position; red diamond=504B), and the depth-sections are plotted as velocity on the left, and velocity anomaly on the right. Some small anomalies are likely artefacts related to the basement structure, and the positive and negative anomalies around the edge of the visible model below 1.2 km bb are likely artefacts related to the edge effects.

The six 2D forward models exhibit very similar structure, are laterally homogeneous, and show three distinct velocity layers within the crust, which is, on average, 5.0 ±0.2 km thick. Despite their simplicity, they fit the observed data very well, and provide a good, general idea of the crustal structure in the study area. These forward models were originally used as prior information to create starting models for the 3D inversion. However, as the final preferred inversion model was created from a distinctly different starting model, the 2D models can act as independent models to compare the results to. Sensitivity testing of the models gives relatively small uncertainties on their velocities and layer boundary depths, giving confidence that these models are robust.

During the 3D inversion process a variety of different starting models were tested, as well as varying the inversion parameters, to produce an un-biased, well-fitting, and reliable result. The results provide models of the velocity structure for the upper ∼3 km of the crust. The final, preferred model was created from a starting model containing little prior information - consisting of a single gradient in the igneous crust - thus any structure in the model is a product of the inversion process. This model generally exhibits a laterally smooth and homogeneous structure, with the maximum velocity anomalies of ∼0.4 km $s^{-1}$ occurring in the upper 1 km of the crust. Velocity anomalies tend to trend E–W across the model, aligned with the tectonic fabric of the crust seen in the bathymetry and basement topography.

In Chapter 4, the resolving capability of the dataset and inversion process, along with the velocity uncertainties, are defined. Following this, the results presented in this chapter are compared with each other, and interpreted in more detail with regard to their resolution and uncertainties, in Chapters 6 and 7.

# Chapter 4

# Inversion model testing

## 4.1 Introduction

In Chapter 3, a procedure was developed to produce a robust 3D P-wave inversion model, and the final model was presented (Section 3.3.12). When undertaking modelling of any kind, it is necessary to quantify the resolution of the model, along with its errors and uncertainties, to both give confidence in the model, and prevent over-interpretation. Sensitivity testing was used to quantify velocity and depth uncertainties in the 2D forward models (Section 3.2.7), however, it is not possible to use this method for the inversion model due to the differences in their production and nature.

A common technique to investigate the lateral resolution of a model in tomographic inversion studies is checkerboard testing. This informs the user of the minimum size of anomaly, in both amplitude and area, which can be resolved using the specific experiment geometry and applied inversion procedure, in different regions of the model space. The checkerboard testing method is presented in Section 4.2.1, and the results of tests applied to the final Vp inversion model in Section 4.2.2.

Another common technique used to derive model uncertainties is a Monte Carlo search. These searches take their name from the famous casino area in Monaco, where the rules of chance and probability determine outcomes. In modelling terms, Monte Carlo searches extensively sample the possible model space, utilising random numbers and/or probability functions to assess the likelihood of a particular solution within the space. Within tomographic modelling, this type of analysis can provide estimates of velocity uncertainties within the model. One Monte Carlo method (Section 4.3), based on an algorithm initially developed by Metropolis et al. (1953), uses a controlled random walk to sample the model space, and simple probabilistic rules to control the walk. The Metropolis method is discussed more in Section 4.3.1, applied to the inversion model in Section 4.3.2, and the results presented in Section 4.3.3. To apply a general form of Monte Carlo theory to the specific inversion procedure used in this study, an alternative, simpler method was developed (Section 4.4). The methods of the Monte Carlo inversion code are detailed in Section 4.4.1, and the results presented in Section 4.4.2.

## 4.2 Checkerboard testing

Checkerboard testing, following the method of Zelt (1998), was undertaken to determine the ability of the inversion procedure and the dataset to resolve the final velocity structure. This method of testing establishes the smallest velocity anomaly that is able to be constrained in different parts of the model.

### 4.2.1 Method

The approach is to produce synthetic travel times with the same geometry as the observed, and test whether, when running an inversion with the same parameters, this synthetic data can recover an imposed pattern of velocity anomalies. The checkerboard testing procedure followed in this study is as follows.

1. Take the final inversion velocity model (Figure 4.1a), and add a known anomaly pattern. The pattern takes the form of positive and negative velocity perturbations of a given amount, following a sinusoid in two dimensions, resulting in the characteristic 'checkerboard' appearance (e.g. Figure 4.1b). This produces the 'perturbed model' (Figure 4.1c).

2. Using the same experiment geometry as the real dataset, rays are propagated through the perturbed model. This produces a synthetic dataset which samples the known anomaly pattern.

3. Add noise to the synthetic travel times based on the pick uncertainty of the observed travel time picks.

4. Perform an inversion using the synthetic travel times with the final inversion velocity-depth model (Figure 4.1a) as the starting model, using the same inversion parameters as for the original inversion procedure. This step is testing how well the inversion process and experiment geometry can recover the added checkerboard pattern.

5. Take the difference between the starting (Figure 4.1a) and final (Figure 4.1d) models from the checkerboard inversion. If successful, the recovered pattern (Figure 4.1e) should be similar to the added pattern (Figure 4.1b), with the degree of similarity being a measure of the model resolution.

6. For a quantitative measure of how well recovered the checkerboard pattern is, the semblance is calculated (Zelt, 1998). A semblance of 0.7 or above indicates a well-resolved anomaly (Figure 4.1f).

7. Repeat the above procedure for a variety of different anomaly patterns, to appraise the effect of ray path geometry versus node locations within the model. For example, shifting the pattern by half a cell size, reversing the polarity or adding an oblique pattern at a given angle $\theta$ (Figure 4.2). An average semblance for the anomaly size can then be calculated.

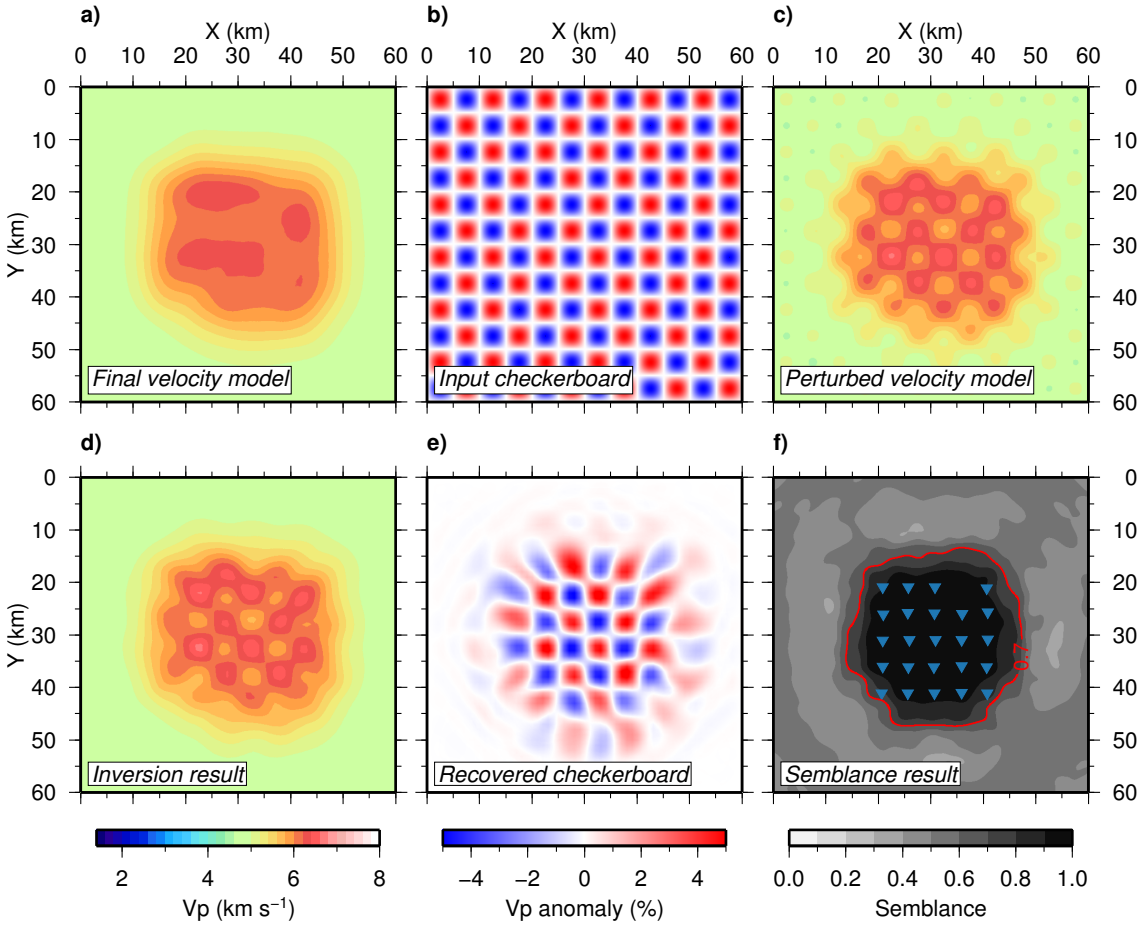


Figure 4.1: The checkerboard testing procedure, shown as horizontal slices through the 3D model volume at 5 km depth. The input checkerboard consists of a 5 km x 5 km anomaly in X and Y, with an amplitude of 5% of the velocity. A semblance of above 0.7 (red contour in (f)) is considered 'well-resolved'. OBS positions are shown for reference in (f) by blue triangles.

The noise added to the synthetic travel times in step 3 was calculated with the assumption that noise is random with a gaussian distribution. A series of random numbers were generated, normalised to values between $-3$ and $+3$, and checked for a gaussian distribution. These random numbers were multiplied by the travel time uncertainty to calculate the amplitude of noise to add to each synthetic travel time, with the range shown in Figure 4.3.

Zelt (1998) suggests that 3D travel time tomography is mostly concerned with determining lateral variations in velocity, and thus the checkerboard testing should be focussed on determining lateral resolution. Thus, the checkerboard pattern in the method of Zelt (1998) is only two-dimensional, i.e. in a 3D model, forms 'columns' of positive and negative polarity perturbations, with the pattern visible in plan view. The vertical resolution of an inversion model is determined mainly by the background model, along with the ray coverage (controlled by the vertical velocity gradients), and thus is tied to the methods used to constrain the background model, for example, supplementary data or 1D or 2D travel time analysis (Zelt, 1998). However, to obtain an independent constraint on vertical

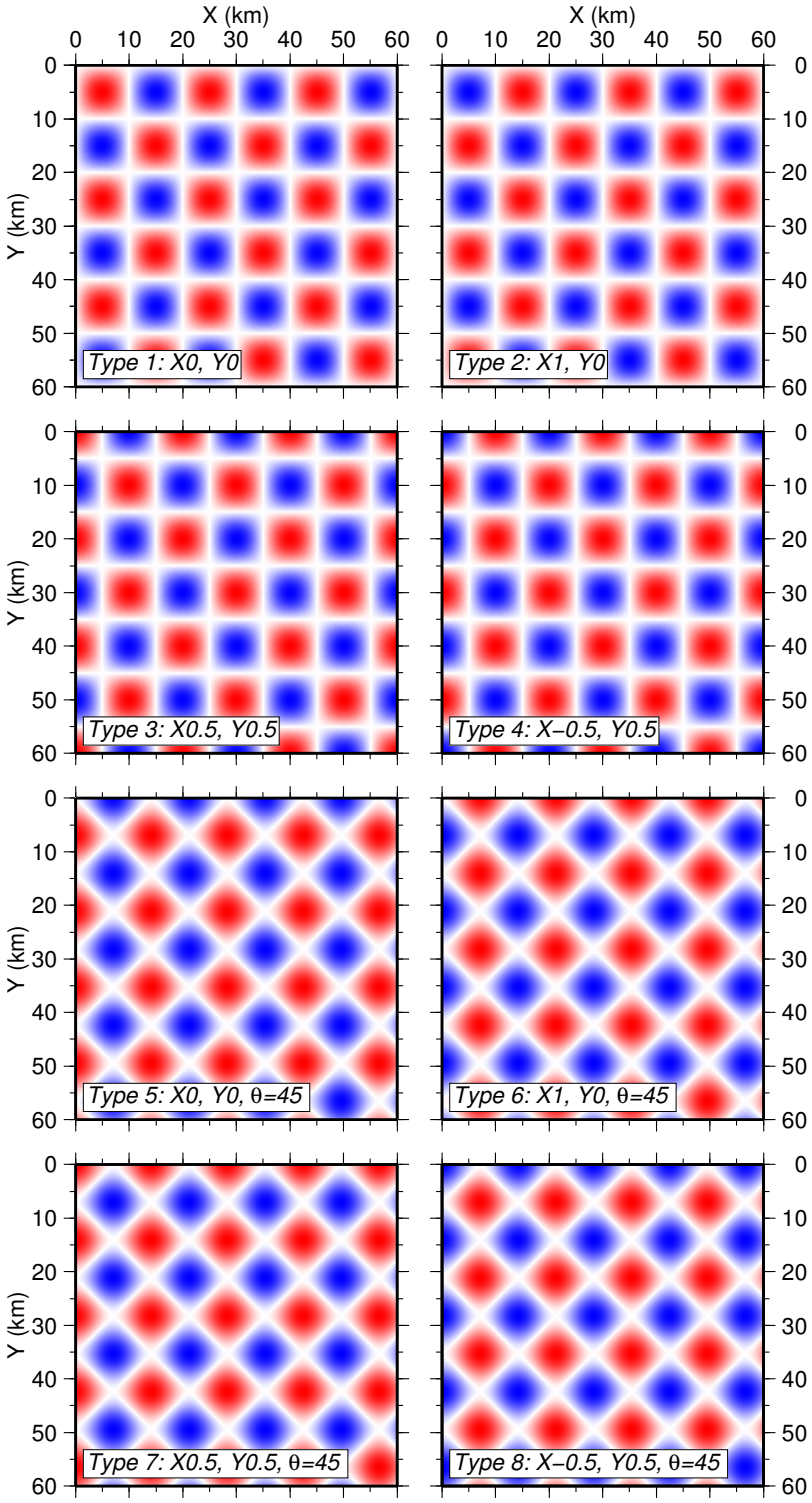


Figure 4.2: Eight checkerboard pattern variations for a 10 km x 10 km anomaly, shown as horizontal slices through the 3D model volume at 5 km depth. The checkerboard was shifted by a whole, or half a cell size in X and Y, and also made oblique by varying the $\theta$ parameter.

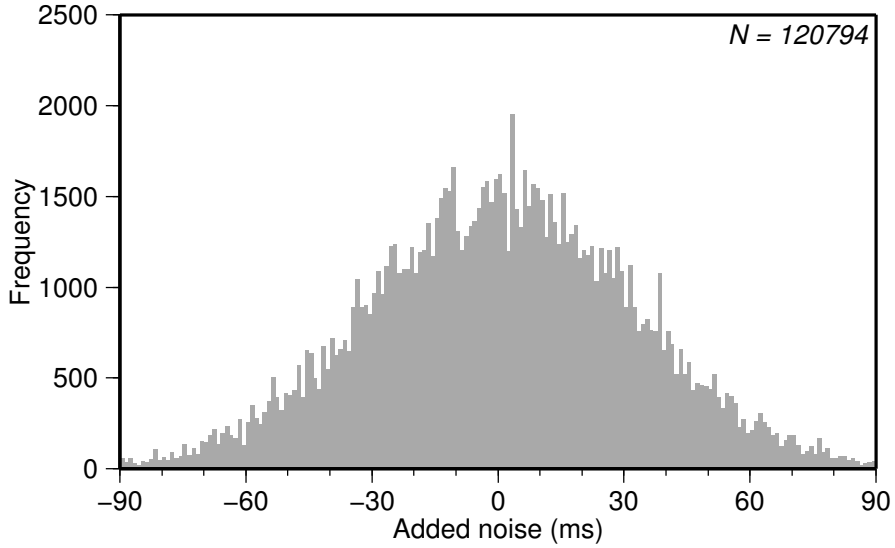


Figure 4.3: The gaussian distribution of noise values added to the population of synthetic travel time picks produced while checkerboard testing.

resolution, the *FAST* program suite, which produces the checkerboard perturbations (via its *anomaly6* program in this case) was modified to vary the pattern in the third dimension (Z), producing anomaly 'cubes' as opposed to 'columns' (Figure 4.4). The inversion procedure outlined above was then followed using these new 3D checkerboard patterns, alongside the traditional 2D patterns.

### 4.2.2 Results

Checkerboard testing results for the final preferred Vp model (Figure 4.5) show that the best lateral model resolution, for a 5% amplitude anomaly, is 3 km. The 0.7 semblance contour shows that this resolution applies to the central section of the 3D model from Y∼20–40 km and X∼20–40 km, and from the top basement to ∼6.5 km depth below the sea surface, equivalent to ∼2.8 km bb. The smallest resolvable cuboid checkerboard size is 5 x 5 x 2 km throughout the model, although it is not fully-resolved in the upper 0.5 km of basement.

These results show that the primary anomalies within the preferred model, described in Section 3.3.12, are of resolvable sizes and magnitudes, and confirm that the smaller anomalies are indeed below the lateral resolution.

## 4.3 Monte Carlo uncertainty analysis I: Metropolis algorithm

In conjunction with analysing the ability of the modelling procedure and travel time dataset to resolve velocity anomalies to give an understanding of the lateral resolution of the model, it is useful to define the uncertainty in the velocity structure. These uncertainties cannot be attained through checkerboard testing, and were instead investigated

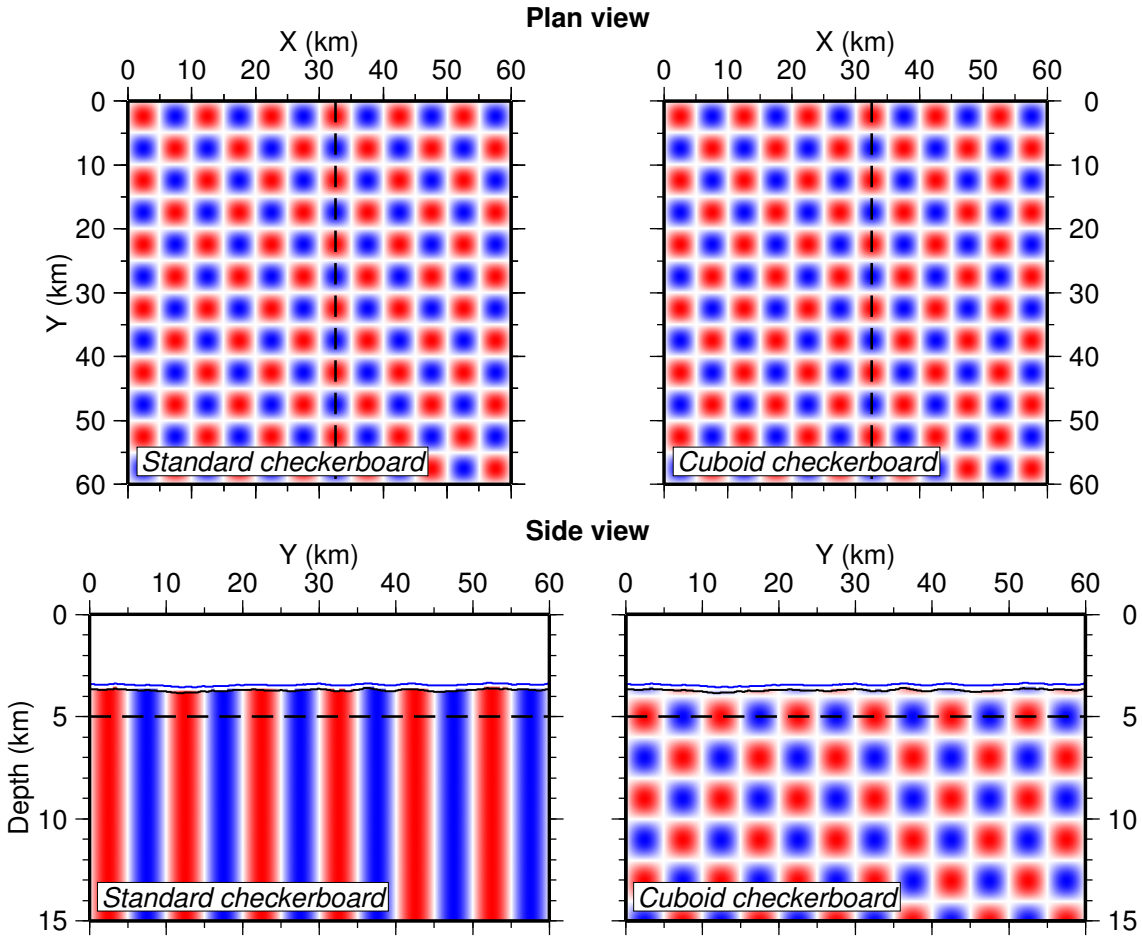


Figure 4.4: A comparison of a 5 km x 5 km standard checkerboard pattern as used by Zelt (1998) (left), which forms columns when viewed side-on, and a 5 km x 5 km x 2 km cuboid anomaly pattern produced after modifying the *FAST* code (right). The black dashed lines show the relative positions of the slices at 5 km depth and 32.5 km offset in X.

through Monte Carlo-style tests. In a general sense, this involves testing a number of randomised models in order to define the distribution of models which solve the problem to a satisfactory level. Two different techniques were implemented:

1. a modified version of the Metropolis Monte Carlo search algorithm, which uses *rayinvr* to test the models (Pearse, 2002); and

2. a Monte Carlo inversion code to test large numbers of randomised starting models using *FAST*.

### 4.3.1 Theory

The Metropolis code (Pearse, 2002) produces probability-density functions to analyse the uncertainty of a tomographic model. It is based on theory presented in Mosegaard and Tarantola (1995), and Metropolis et al. (1953). The code produces an array of different starting velocity models using a random walk method. Beginning with a given input model, a random update is applied to the previous model to create the new model for

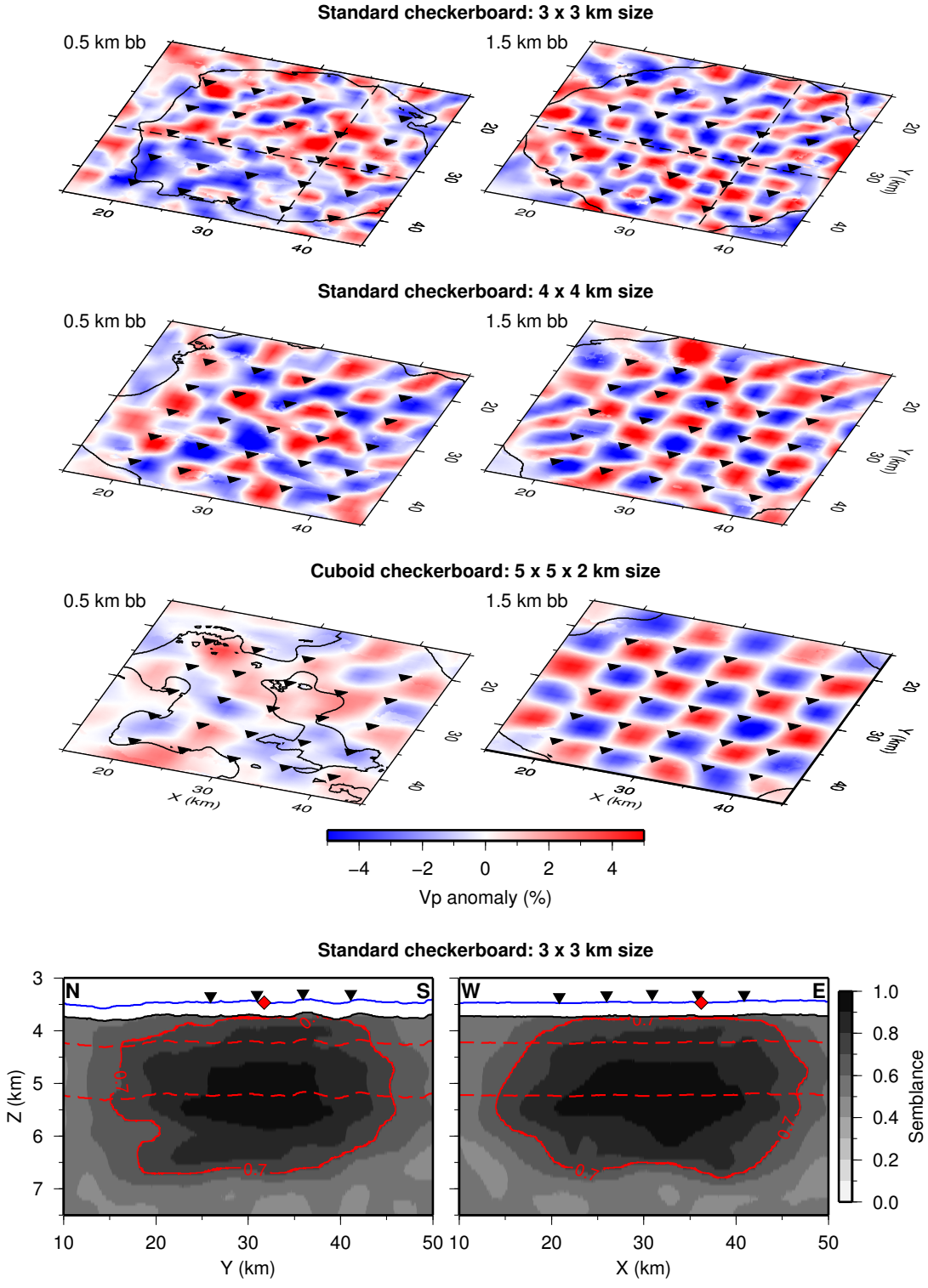


Figure 4.5: Checkerboard testing results for the preferred model, shown as depth-sections at 0.5 and 1.5 km bb. All tests were run with a 5% velocity anomaly input checkerboard. The solid black line shows the 0.7 semblance contour - within this contour the checkerboard is considered 'well-resolved'. The bottom two plots are N–S and E–W cross-sections through the 3D semblance model for the 3 x 3 km-size checkerboard test (their positions are shown as black dotted lines on the top depth-sections), with the 0.7 semblance contour shown in red to delineate the depth-limit of model resolution. The relative positions of the depth-sections to these plots are shown with red dotted lines. OBS locations (black triangles) and the position of 504B (red diamond) are shown for reference.

each iteration. The maximum size of these updates, or the 'freedom' of the code, is chosen by the user. To try and prevent bias due to the choice of input model, a 'burn-in' cycle takes place at the start of each run of the code. This carries out a series of 200 updates to the given model, accepting each updated model regardless of the criteria detailed below, to shift the beginning of the random walk away from the input model. During each iteration 'burn-in', the newly created model is tested for its fit to the observed travel times using *rayinvr*, and the model is accepted or discarded based on two different criteria:

1. the model is accepted if it produces a better fit to the data than the previous model (i.e. the models are converging on a solution). The value of fit is determined both by the $\chi^2$ value, and a term representing the number of observed travel times which are successfully ray traced through the model, $P$; and

2. the probability function of the current model is calculated with respect to the input model, using the equation:

$$Probability = \exp[-0.5((\chi^2_{current} + P_{current}) - (\chi^2_{input} + P_{input}))], \tag{4.1}$$

   giving a value between 0 and 1. A random decision whether to accept the model is then made, with the model accepted if the calculated probability value is greater than a random number produced between 0 and 1.

The method to choose the 'best-fitting' model from the results was modified from the original code. Originally, the model with the highest probability function, relative to the input model, as calculated using Equation 4.1 was chosen. This, however, was viewed as unnecessarily complicated, and thus the method was changed to choose the 'best-fitting' model based solely on its own fit to the data, calculated as its 'probability' (Equation 4.2). This depends on the fit ($\chi^2$) of the model to the data, and the proportion of rays reaching their destinations (i.e. the number of rays tracing successfully through the model), given by term $P$:

$$Probability_{current} = \exp[-0.5(\chi^2_{current} + P_{current})] \tag{4.2}$$

Once an array of accepted models has been found, the probability-density distribution is calculated. The two-dimensional model space (velocity vs. depth) is divided into regularised cells. The number of accepted models which sample each cell (the 'hit count'), normalised by the total number of accepted models, gives the probability of the cell being part of the 'correct' solution.

### 4.3.2 Implementation

The Metropolis code was run using several different 2D starting models (Figure 4.6), different values of freedom, and for varying numbers of iterations from 1000 to 80000. All starting models were constructed along an east-west-trending cross-section through the 3D model volume, along shot line SG_C, and had identical structure through the

water column and sedimentary sections. The crustal structure varied between the starting models (Figure 4.6), based on:

1. **2D forward model average -** the crustal structure was defined using the average profile of the six 2D forward models. This input model fit the data very well ($\chi^2 = 0.8$, technically 'overfit'), which made it difficult for the code to converge to any other solution;

2. **single-gradient model -** the crustal structure was defined using a single-gradient velocity increase from 4.5 to 7.5 km $s^{-1}$, based on the single-gradient starting models used for 3D inversion. This resulted in a very poor initial fit to the observed data ($\chi^2 = 60.9$), which caused the code to fail to converge to any solution; or

3. **previous studies -** a previous tomographic experiment of the study area produced a 1D velocity profile for borehole 504B (Detrick et al., 1998), which was used to create the input crustal velocity model. This input model fit the observed data with a $\chi^2$ value of 2.5, which allowed the code to run stably and converge upon solutions without becoming 'lost'.

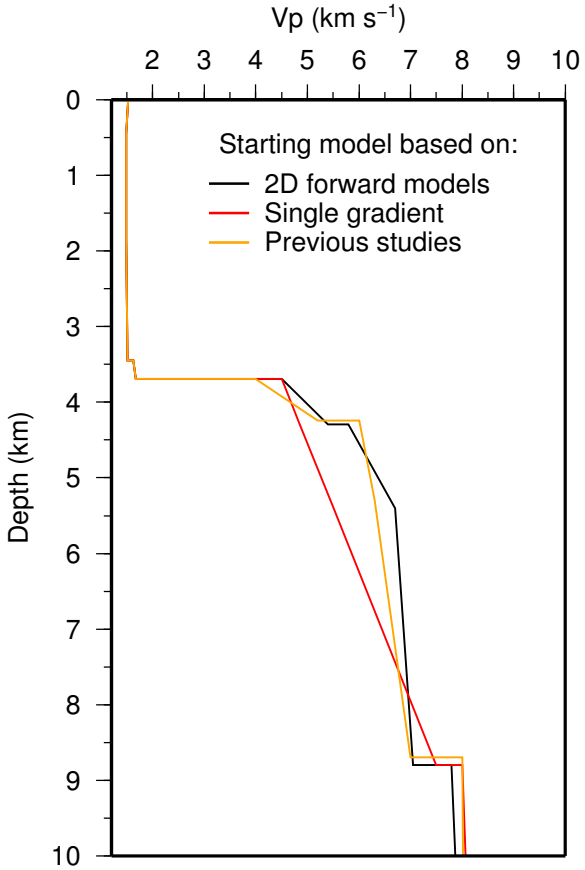


Figure 4.6: 1D profiles used to create the various 2D input models for Metropolis uncertainty analysis. The model based on previous studies (Detrick et al., 1998) produced the best results from the algorithm.

All starting models were created using the same number of model layers, with four layers defining the crust and mantle. Observed travel times from shots from line SG_C recorded by on-line OBSs (instruments 11–15) were used to calculate the fit of each model. An update to the model could take the form of a perturbation in one of three parameters: the average velocity of a layer, the velocity gradient of a layer, or the thickness of a layer (in two-way travel time). The maximum allowable degree of model updates, or 'freedom', was defined as a percentage of the previous value for each parameter for each layer. Throughout all tests, the water column layers remained fixed (i.e. had a freedom of 0%). The seabed depth was assigned a small amount of freedom (1%), to account for errors in the swath bathymetry data, and the sediment layer parameters, including basement depth, assigned a freedom of 4% to account for errors in the sediment thickness and velocity. Freedom values used for below-basement crustal layer parameters varied between 2–12% to test the effect on the Metropolis algorithm, and appraise the number of models which fulfilled the criteria to be accepted. Tests were conducted with the aim of a model acceptance percentage of ∼33%.

### 4.3.3 Results

The results from the Metropolis modelling (Figure 4.7) were produced using a starting model based on previous studies of the area (version 3), crustal freedom values of 4%, and 80,000 iterations. The range of accepted models fits a relatively narrow band of increasing velocity with depth. Calculating the mean and standard deviation at each depth in the 2D model space gives 95% confidence boundaries for the velocity structure. Probabilities of above 0.04 (light blue and green in Figure 4.7), delineate a three-layer crustal model, consisting of an upper layer from the top basement to ∼4.5 km depth (0.8 km bb) with velocities of ∼4.5–5.5 km $s^{-1}$, followed by a velocity increase to a middle layer with velocities of ∼5.8–6.5 km $s^{-1}$ which extends to ∼5.4 km depth (1.7 km bb), where there is a gradient decrease to a lower layer with velocities of ∼6.5–6.8 km $s^{-1}$. The 'best-fit' model found by the code is similar to the 2D forward model result in the upper crust, although it contains a slower middle layer and a large first-order discontinuity at the interface between the middle and lower layers at 5.4 km depth, as opposed to a gradient change. This first-order discontinuity is interpreted as an unusual feature of this particular model, as the velocity-depth range with the highest probability in Figure 4.7 suggests that a gradient change, with no discontinuity, is more likely at this depth. Its velocities are, in general, slower than the sonic velocity log from downhole logging of borehole 504B (Guerin et al., 2008), though is faster than the final 3D inversion result at the location of the borehole.

This method produces uncertainties for velocity structure derived from 2D, layer-based models and, thus, complements the sensitivity testing (Section 3.2.7). However, these same characteristics make the method less appropriate to use to define uncertainties for velocity structure derived from smoothed tomographic inversion models. The inversion models in this study were produced using the *FAST* code, with no defined layers or phase-defined

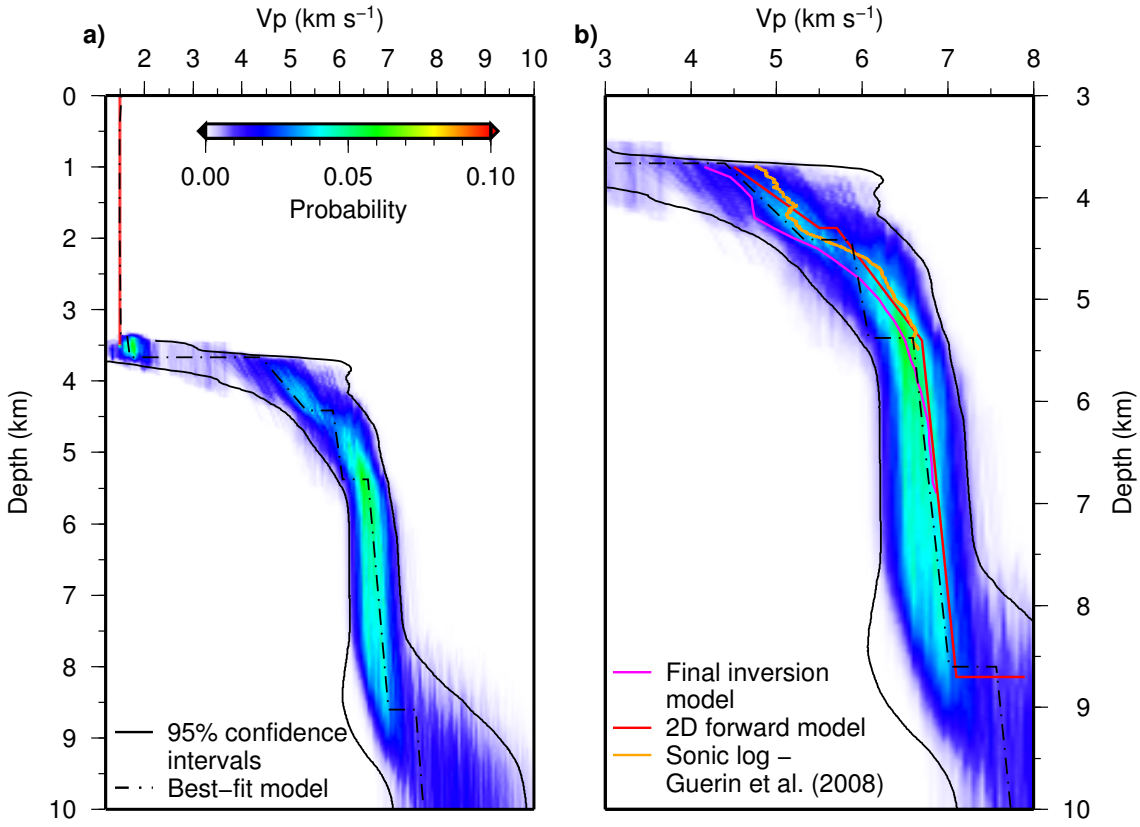


Figure 4.7: Metropolis uncertainty analysis results. a) Full probability-density distribution, also showing the best-fit model. b) Zoom-in on crustal depths for comparison with other velocity profiles from this study and borehole 504B.

travel time picks, and so are not directly comparable to the results of this uncertainty analysis produced using the *rayinvr* code.

## 4.4 Monte Carlo uncertainty analysis II: inversion code

### 4.4.1 Method

To undertake uncertainty analysis more appropriate for the 3D inversion model, a Monte Carlo inversion code which used *FAST* was developed. The code produced a number of random starting models, performed inversion on each one using the same procedures and parameters as for the 3D inversions, and accepted or rejected each final model based on its fit to the observed data. In this code each starting model is created randomly, as opposed to the Metropolis algorithm which aims to progressively improve fit by altering the previously accepted model in a 'random walk'. To save computational time, these tests were only run in 2D, which means they do not test uncertainty caused by 3D variations in structure, and do not make use of the entire travel time dataset to constrain the result. They also cannot provide individual uncertainties for each node in the 3D model, however, due to the general homogeneity within the inversion model result (Section 3.3.12), and consistency in lateral resolution (Section 4.2), velocity uncertainties are also likely to be

similar across the model space. To account for the effects of azimuthal anisotropy, the code was run separately for two starting models: one created in the N–S direction, and the other in the E–W direction.

The 2D starting models were built as cross-sections through the 3D model volume, running through the position of 504B (i.e. along shot line SG_C for E–W models, and shot line SG_I for N–S models). The water column, seabed, sediment and basement structure were constructed as for the 3D models. The crustal velocity structure was different for each starting model, and comprised a 7 km-thick layer of a single gradient with randomly assigned top and bottom velocities. The top velocity of the crust was randomly assigned a value from 2.0–5.9 km $s^{-1}$, and the bottom a velocity with a minimum value of the top velocity (to ensure a positive gradient and a maximum of 7.9 km $s^{-1}$.

Each starting model was run through a full 2D inversion using *FAST*, using the same procedure (e.g. number of iterations run at larger and smaller cell sizes), and same parameters as the 3D inversion. The observed data used for inversion comprised crustal travel time picks from the coincident shot line to the on-line instruments. The final model from the inversion run was accepted if the $\chi^2$ fit was below a chosen threshold. A $\chi^2$=3 was considered an appropriate upper bound, as final inversion models were generally accepted if they had a fit better than a $\chi^2$=2. This produced an array of accepted models, which satisfy the observed data to within the chosen fit condition (Figure 4.8). The 'best' model from a run was chosen as the final model with the best fit to the observed data (i.e. the lowest $\chi^2$).

The code was run to test 1000 models in both the N–S and E–W directions. The accepted models were first cut to exclude parts not sampled by rays during the inversion. The arrays of accepted models were then analysed to find the mean average velocity and standard deviation at each 0.1 km depth (Figure 4.9), to give the 68% and 95% confidence boundaries. To account for the differences between the results from each direction, the two arrays were merged, and the boundaries re-calculated to give the final uncertainties to apply to the 3D inversion model.

### 4.4.2 Results

The results from the Monte Carlo inversion modelling code (Figures 4.8 and 4.9) show a total of 403 accepted models out of 1000 tested from N–S starting models, and 415 accepted models from E–W starting models. The 1D profiles from the accepted models, extracted at the position of borehole 504B, follow similar velocity-depth patterns, particularly in the upper crust above ∼5 km depth. There is a greater number of accepted models in the E–W array which fit with a $\chi^2$ ∼1, which is most likely due to the relatively smoother and flatter seabed and basement topography in this direction, and less variation in the velocity structure of the crust, enabling the inversion process to converge to a solution more easily. The 95% confidence boundaries from the E–W and N–S accepted model arrays (Figure 4.9) are very similar above ∼5.5 km depth. The divergence below this depth is likely due to

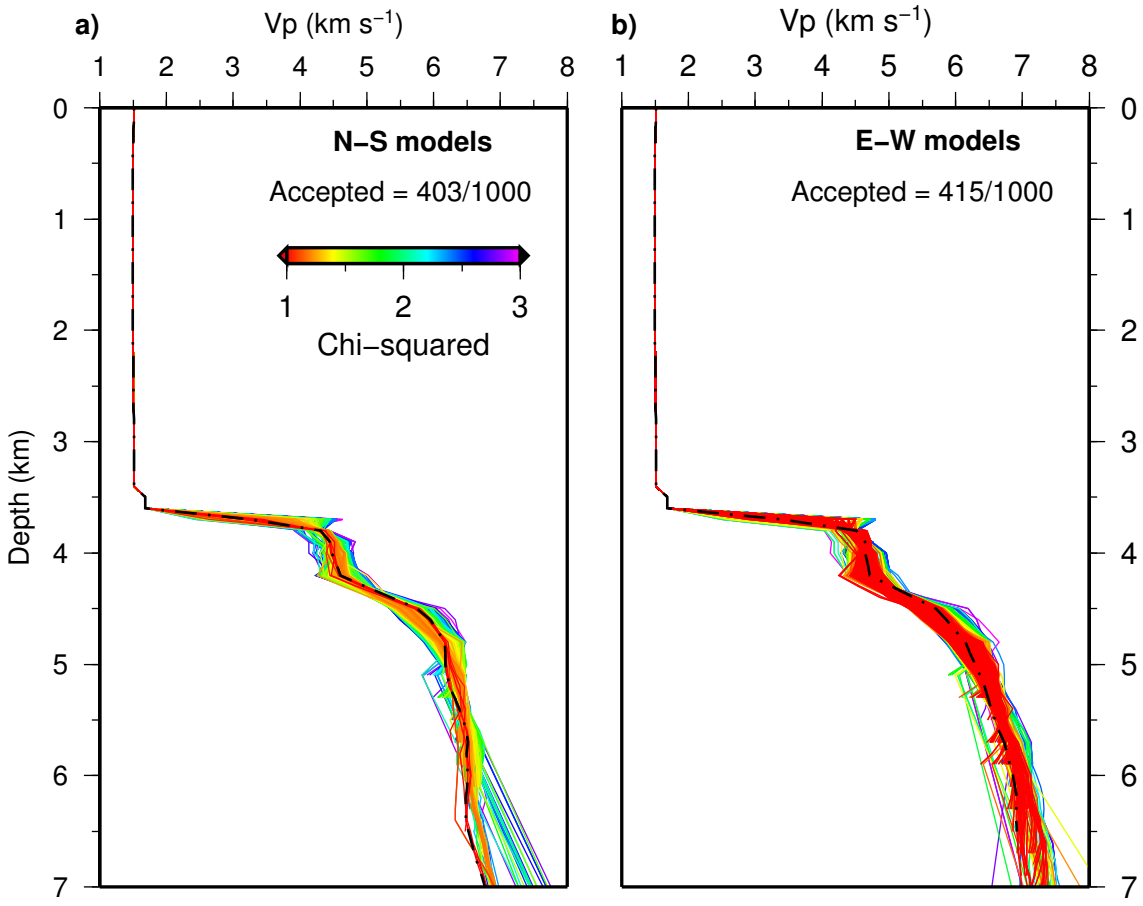


Figure 4.8: 1D profiles extracted from the accepted models for two runs of the Monte Carlo inversion code. a) Array of accepted models from N–S trending starting models. b) Array of accepted models from E–W trending starting models. The profile from the 'best-fitting' model from each run is shown by the black dotted line. 1000 models were tested in each run, and the models were accepted if the $\chi^2$ value was less than 3. The 1D profiles were extracted at the position of borehole 504B, and masked where there was no ray coverage.

a lack of ray coverage preventing the models from resolving the velocity structure (Section 4.2.2). The 'best-fit' models from each array are also relatively similar, and both consist of a clear upper layer extending from the top basement to 4.2 km depth with velocities of ~4.3–4.7 km s$^{-1}$, and a rapid increase in velocity to >5.5 km s$^{-1}$ overlying a second layer with a gradually decreasing velocity gradient. The merged confidence boundaries show a relatively narrow ranges at both 68% and 95% confidence, with average 95% uncertainties of ±0.3 km s$^{-1}$ from top basement to ~5.5 km depth.

Comparing these confidence boundaries, derived from 2D inversions, to the 1D profile at 504B extracted from the 3D inversion model shows that they are consistent with one another, with the 3D inversion profile lying just within the 68% confidence boundaries, and comfortably within the 95% boundaries. Thus, the confidence boundaries produced using this 2D Monte Carlo inversion method are able to provide valuable estimates of velocity uncertainty for the 3D model profile. Figure 4.9 also shows the 2D forward modelling result at borehole 504B from this study, and the smoothed sonic velocity profile (Guerin

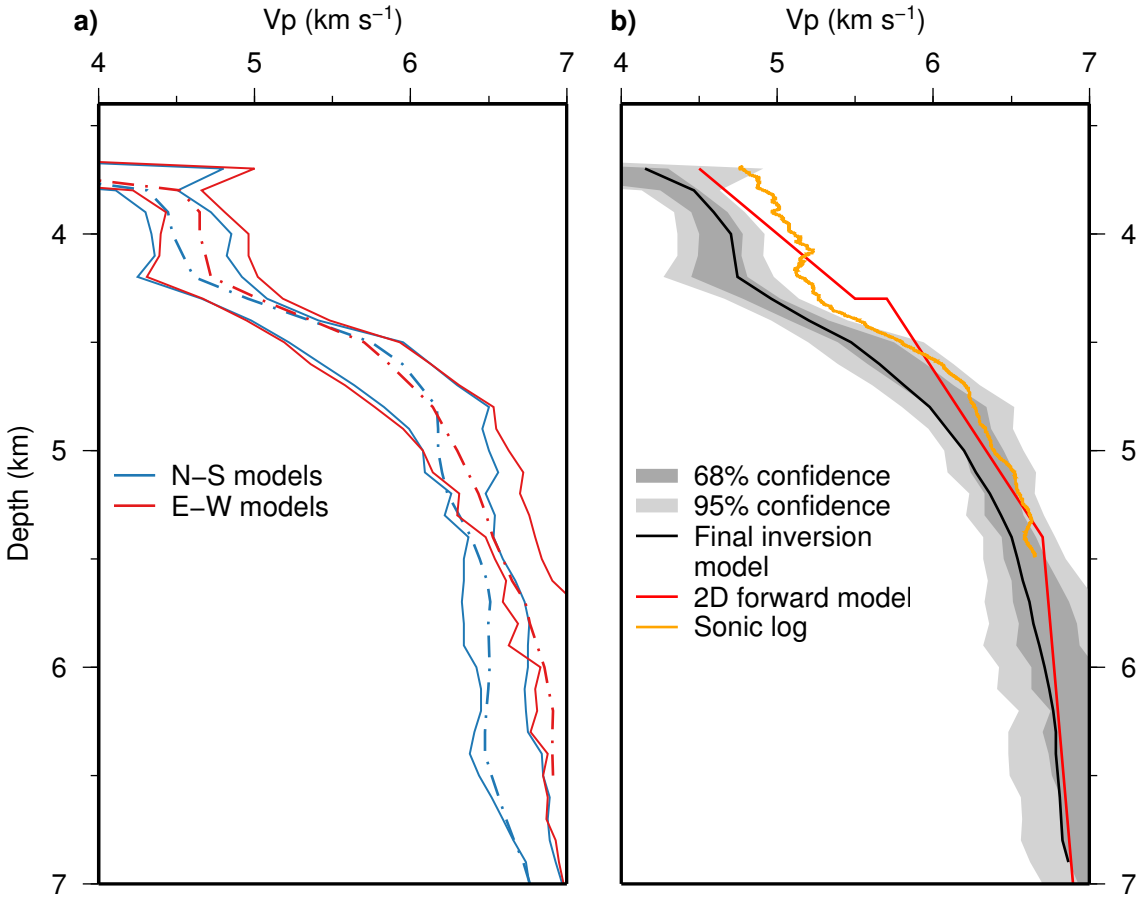


Figure 4.9: Confidence interval boundaries from the Monte Carlo inversion code results. a) 95% confidence interval boundaries (solid lines), and 'best-fitting' models (dashed lines), calculated separately for the N–S and E–W directions. b) 68% and 95% confidence boundaries for the merged dataset, compared to the final 3D inversion model at 504B, 2D forward model at 504B, and the downhole sonic log (Guerin et al., 2008).

et al., 2008) from downhole logging in the borehole. Within the uncertainty imposed by the inversion model cell size (0.1 km), the seismic velocity patterns closely mirror that of the downhole sonic velocity log, with a low gradient upper layer from the top basement to ∼4.2 km depth, followed by a rapid increase in velocity to ∼4.5 km depth, and a gradually reducing gradient in the layer below. The 2D forward model, however, exhibits a simpler structure, with a first-order discontinuity at 4.3 km depth separating two distinct layers. The differences in absolute velocity, which in the upper layer are outside the inversion confidence boundaries, are attributed to contrasts in measurements scale and method. The sonic log measures only in the vicinity of the borehole wall whereas seismic data samples, and provides the combined response of, a much large volume of rock surrounding the borehole. The forward modelling approach has no embedded restrictions on the depth specification of interfaces, discretises the crust into layers of constant velocity gradient, and favours the production of the simplest model which fits the observed data. In contrast, inversion modelling is discretised at the cell size, which in this study is 0.1 km in depth, and has the imposed condition that the 3D velocity model is smooth such that a step

in velocity becomes spread over the cell height. This manifests itself by the inversion underestimating the actual measured velocity by ∼10% above 4.2 km depth, and to a lesser extent below this depth.

## 4.5 Summary

In this chapter, the resolution and uncertainties of the velocity models presented in Chapter 3 were defined.

The resolving capability of the dataset and inversion process was investigated using checkerboard testing. The best lateral resolution within the preferred model is 3 km. This applies within the central part of the model from X∼20–40 km and Y∼20–40 km, and from top basement to ∼6.5 km depth. Below this depth the velocity structure is unresolvable.

Velocity uncertainties at particular depths were tested using two different Monte Carlo approaches, the first using forward ray tracing and the Metropolis algorithm (Metropolis et al., 1953), and the second producing a large population of possible 2D velocity models through inversion. The first method provides uncertainties which are more appropriate to apply to 2D, discretised models produced using ray tracing programme *rayinvr*. The second method, which utilises the *FAST* code to produce smoothed final models, provides uncertainties which can be applied to the 3D final inversion model, also produced using *FAST*. These show that the 1D velocity profile at borehole 504B, extracted from the 3D inversion model, can characterise the upper crustal velocity structure to within ±0.3 km $s^{-1}$. Uncertainties increase to approximately ±0.5 km $s^{-1}$ at 6.5 km depth, below which the checkerboard testing results show that the velocity structure is poorly resolved.

The velocity models presented in Chapter 3 are interpreted and further discussed, with respect to their resolution and uncertainties defined in this chapter, in Chapters 6 and 7.

# Chapter 5

# S-wave modelling and seismic anisotropy

## 5.1 Introduction

Faults and fractures within the oceanic crust, that mostly form at the ridge axis when the crust is created, act as fluid flow pathways and influence the type and patterns of alteration within the crust (Fisher, 1998; Fisher and Becker, 2000). These fractures affect the physical properties of the crust, such as its density and seismic velocity. Therefore, velocity can be used to determine the extent and characteristics of fractures within the oceanic crust, especially when S-wave velocity (Vs) is considered in conjunction with P-wave velocity (Vp). The modes of propagation of these two wave types results in a difference in the material properties that they are particularly sensitive to. For example, Vp is more sensitive to the bulk velocity of the material, whereas Vs is more sensitive to the presence of small (or thin) discontinuities, such as narrow fractures (Shearer, 1988). In this chapter, S-wave arrivals are identified (Section 5.2) and picked from the dataset, before being inverted in 3D (Section 5.3) to create an equivalent Vs model to the Vp model presented in Chapter 3. The resolution and uncertainties in the Vs model are discussed in Sections 5.3.6 and 5.3.7. In order to directly compare the Vp and Vs 3D models, and variations in their relationship across the study area, a 3D Poisson's ratio model is also calculated and interpreted (Section 5.4).

Further, fractures with a predominant orientation which potentially control the direction of fluid flow within the crust also result in seismic anisotropy (Section 5.5.1). Anisotropy analysis, conducted using the travel time residuals from the Vp and Vs 3D models (Section 5.5.2) is conducted and the results discussed (Section 5.5.3) to understand both the alignment and aspect ratio of cracks in the crust, and variations in these parameters laterally and vertically.

## 5.2 Phase identification

Wide-angle refractions which have travelled as S-waves through the crust or mantle were identified on the OBS record sections by their slower apparent velocity (∼3.5 km $s^{-1}$) than the P-wave arrivals (∼6.0 km $s^{-1}$) (Section 3.2.2). This energy must have travelled through the water column as a P-wave, and the upper basement as an S-wave, and thus are a form of P-S mode conversion. Record sections from the four different components of each OBS [hydrophone, horizontal geophones (X' and Y'), and vertical geophone (Z)] exhibit different mode conversions with different arrival travel times (Figure 5.1). For the geophones, a set of mode conversions are recorded with arrival travel times 1.5-2 s later than the set recorded by the hydrophone. This indicates the type of wave the arrival travels as during the final part of its path: as to be recorded on the hydrophone (positioned in the water column), the energy must be a P-wave, whereas the geophones can record incident S-waves as they are directly coupled to the seabed. To determine these different P-S mode conversion types, they were modelled synthetically using *rayinvr* (Zelt and Smith, 1992).

### 5.2.1 Two-dimensional ray-tracing

#### Method

The 2D modelling to identify the different P-S mode conversions was performed by ray-tracing through a model constructed along shot profile SG_I (Figure 3.3). When using the *rayinvr* program (Zelt & Smith) to model S-waves, the user must supply a layered P-wave velocity model alongside a Poisson's ratio for each layer, and define the conversion points from P-S or S-P for each modelled phase. The final Vp forward model for shot line SG_I (Section 3.2) was used as the input P-wave velocity model. Poisson's ratio ($\sigma$) is a property of a material defining how it deforms (Christensen, 1996), and is defined using the P-wave (Vp) and S-wave (Vs) velocities by:

$$\sigma = \frac{V_p^2 - (2V_s^2)}{2(V_p^2 - V_s^2)}. \tag{5.1}$$

Within the oceanic crust, $\sigma$ can generally range from 0.20–0.48 (Shaw, 1994; Collier & Singh, 1998), with lower values indicating a smaller difference between Vp and Vs. A $\sigma$ of 0.5 indicates that S-wave cannot travel in the material (i.e. Vs=0 km $s^{-1}$), such as in fluids. Here, a $\sigma$ value of 0.28, characteristic of ridge-flank oceanic crust (e.g. Christeson et al., 1997; Collier and Singh, 1998), was chosen to apply to the model below top basement.

When tracing ray paths through the model all possible arrivals to each instrument were calculated, regardless of shot point location. The arrival travel times were then overlain on the OBS record sections to determine the phase identification of the observed arrivals, and the P-S or S-P conversion points within the model. This was conducted as an iterative process, adjusting the P-S conversion points within the *rayinvr* model, and the $\sigma$ value of each layer, if necessary, until a match was found.

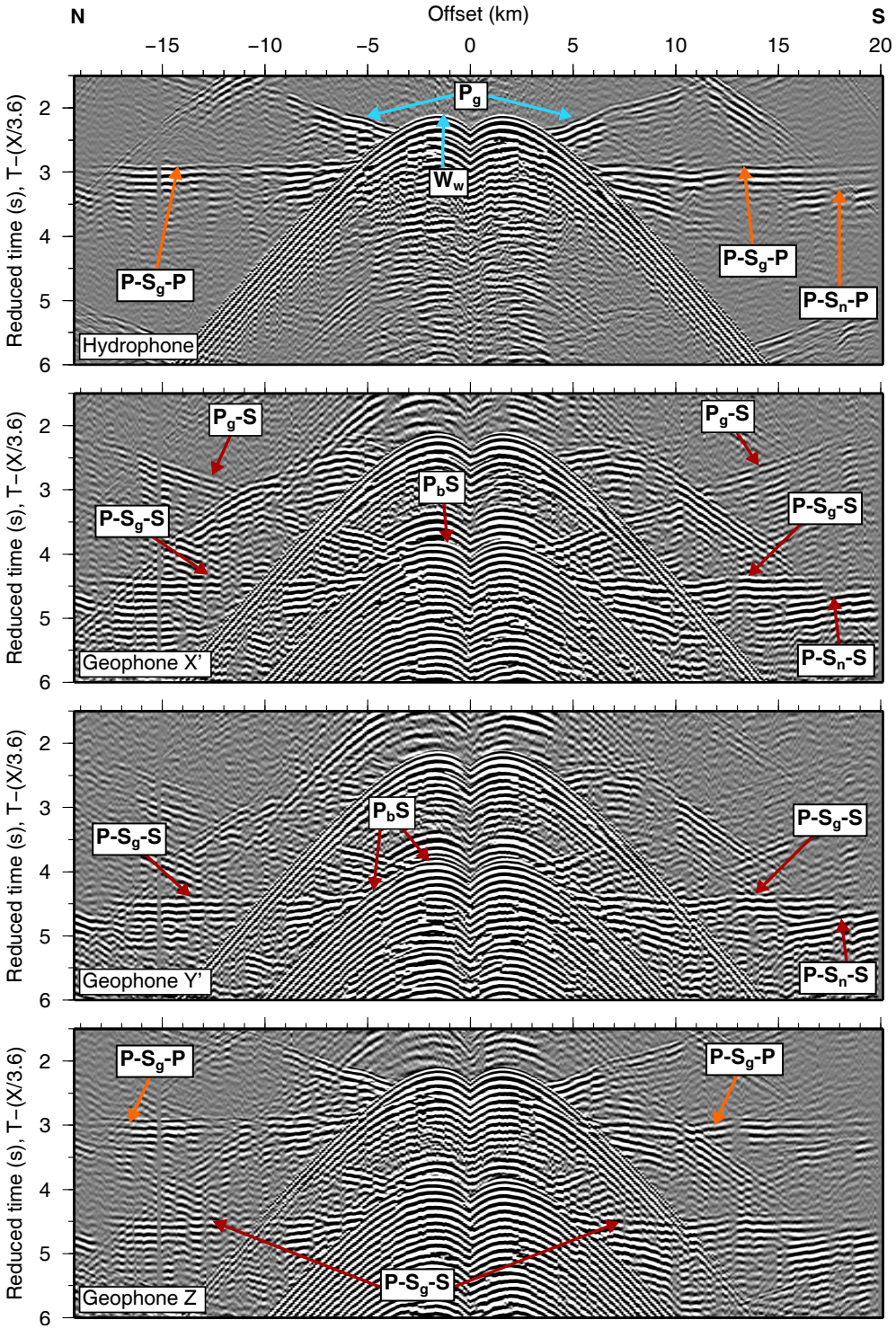


Figure 5.1: Record sections for the four components of instrument SG_12 for shot profile SG_I, plotted against time reduced at 3.6 km $s^{-1}$ in order to flatten arrivals which have travelled through the crust as S-waves ($S_g$). Pure P-wave arrivals are indicated by blue arrows, and P-S converted arrivals by orange or red arrows, with orange indicating the arrival reaches the OBS as a P-wave, and red indicating that the arrival reaches the OBS as an S-wave. Arrivals are labelled with their phase determined through modelling. Not all arrivals are labelled on each record for clarity. Geophones X' and Y' are the horizontal geophones, and Z is the vertical.

### Results

The most likely boundary for the conversion of P-S or S-P is the sediment-basement interface, which is the most significant velocity change in the model (Vp increases from ∼1.6 km $s^{-1}$ to >4 km $s^{-1}$). The P-S conversions observed on the hydrophone and vertical geophone record sections are well-matched by synthetic rays which convert at the basement both on the down-going path from the seismic source (P-S), and on the up-going path to the instrument (S-P), travelling through the rest of the crust as S-waves (Figures 5.2 & 5.3).

These arrivals are identified as:

**P-$S_g$-P** — crustal refractions;

**P-$S_n$-P** — mantle refractions;

**P-$S_m$S-P** — Moho reflections.

Sub-phases are identified within the crustal refractions based on their offset and changes in the apparent velocity. P-$S_{g1}$-P has an apparent velocity of ∼3.0 km $s^{-1}$, P-$S_{g2}$-P ∼3.4 km $s^{-1}$, P-$S_{g3}$-P ∼3.8 km $s^{-1}$, and P-$S_n$-P ∼4.2 km $s^{-1}$.

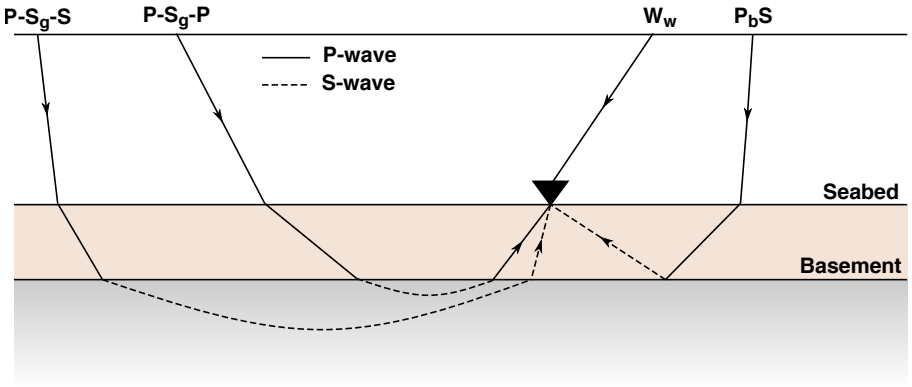


Figure 5.2: Example ray paths of the different P-S mode conversions, showing the conversion points from P-waves to S-waves and vice versa. The OBS is represented by the black triangle.

The P-S conversions observed on the horizontal geophone record sections (and the second set arriving at the vertical geophone) arrive later than these modelled phases by ∼1.5–2.0 s. The absence of these delayed arrivals on the hydrophone channel indicates that they arrive at the instrument as S-waves. These arrivals are well matched (Figure 5.3) by synthetic rays with a single conversion point from P-S at the basement interface on the down-going path, and the energy travelling as an S-wave through both the crust and the sediments on the up-going path to the instrument (Figure 5.2). The delayed arrival with the same shape as the water wave (labelled P-S: $W_w$ in Figure 5.1) is well-matched by a reflection from the basement interface, which occurs close to the instrument (Figure 5.3). The energy travels as a P-wave on the down-going path through the sediments, converts as its reflected, and travels up to the instrument as an S-wave (Figure 5.2). These arrivals are defined as:

**$P_bS$** – basement reflection;

**P-$S_g$-S** — crustal refractions;

**P-$S_n$-S** — mantle refractions;

**P-$S_m$S-S** — Moho reflections.

To produce the required delay of 1.5–2.0 s and match the observed arrivals, the model requires a high $\sigma$ within the sediment layer of 0.495. This gives a low S-wave velocity in the sediments of $\sim$0.16 km $s^{-1}$.

## 5.3 Three-dimensional tomographic inversion

After the P-S mode converted arrivals were identified, the dataset was inverted to derive an equivalent 3D Vs model to the final 3D Vp model presented in Section 3.3.12. The inversion process followed the same procedures, where possible, used to derive the Vp model for two reasons: 1) as this method had already been found to be fit for purpose, through extensive testing, to result in a reliable final model; and 2) to ensure that the two final models were comparable, and any differences between them would not be a result of a difference in the method used to derive them.

When using *FAST* (Zelt and Barton, 1998) the user cannot define the phases of the arrivals. This can be considered as an advantage, as it reduces the potential for user bias and wrongly-identified phases to influence the inversion result. However, the user then cannot define whether a particular arrival is travelling as a P-wave or an S-wave in a particular layer, nor input, as possible when using *rayinvr*, both Vp and $\sigma$ values for the model. In order to model P-S mode conversions, the velocity model must be created with layers in Vp (where the arrivals must always travel as P-waves), and layers in Vs (where the arrivals must always travel as S-waves). This precludes the use of the second, delayed set of P-S mode conversions observed on the geophone record sections (e.g. P-$S_g$-S), which travel through the sediment layer both as a P-wave (on the down-going path) and as an S-wave (on the up-going path). Thus, the travel times input into *FAST* as the observed data were picked from the P-S mode conversions observed on the hydrophone record sections (e.g. P-$S^g$-P), as these arrivals only travel as S-waves below the basement interface. As the P-wave inversion modelling procedure did not utilise travel times from the mantle, these were not included in the Vs modelling.

### 5.3.1 Data filtering

To ensure consistency between the picking process of the P-wave and mode converted arrivals, the OBS data were filtered before picking using the same processing sequence (described in Section 3.3.2). In this case, the data were reduced at a velocity of 3.6 km $s^{-1}$ as opposed to 6.0 km $s^{-1}$ prior to applying the median filter in order to flatten, and therefore

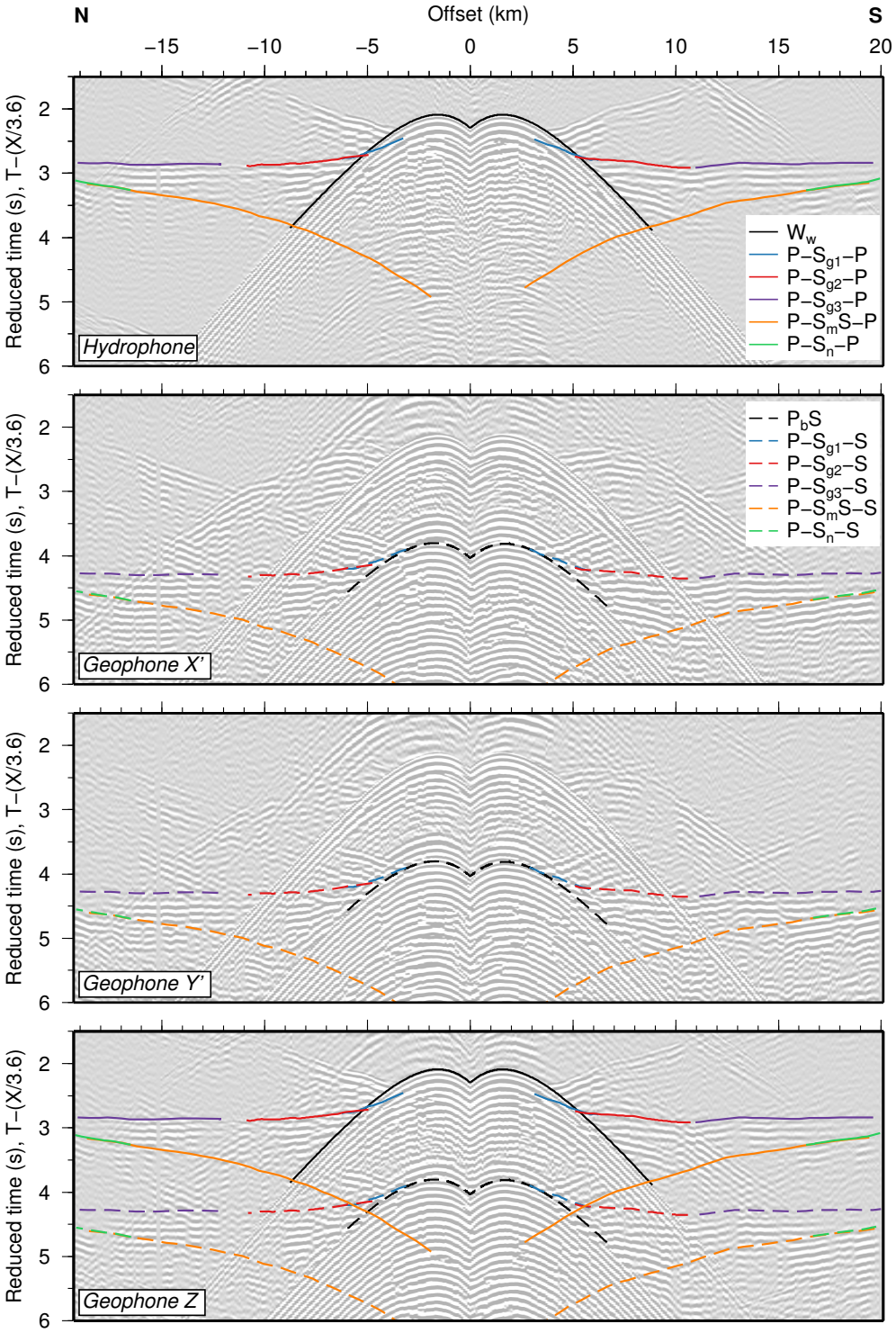


Figure 5.3: Arrivals modelled using *rayinvr* overlain on top of the record sections from Figure 5.1 (OBS SG_12, shot profile SG_I), using $\sigma$=0.28 for the crust and mantle, and $\sigma$=0.495 for the sediments. Energy arriving at the OBS as a P-wave is plotted using solid lines, and as an S-wave using dashed lines. Not all arrivals are overlain on each record section for clarity.

preserve, the mode converted arrivals rather than the P-wave arrivals. The filtering process also reduced the interference from the GI airgun water wave and its multiple with the mode converted arrivals, and improved their coherence across the record sections (Figure 5.4). The effect of the filtering process on the travel times picked from the records is discussed in the following section.

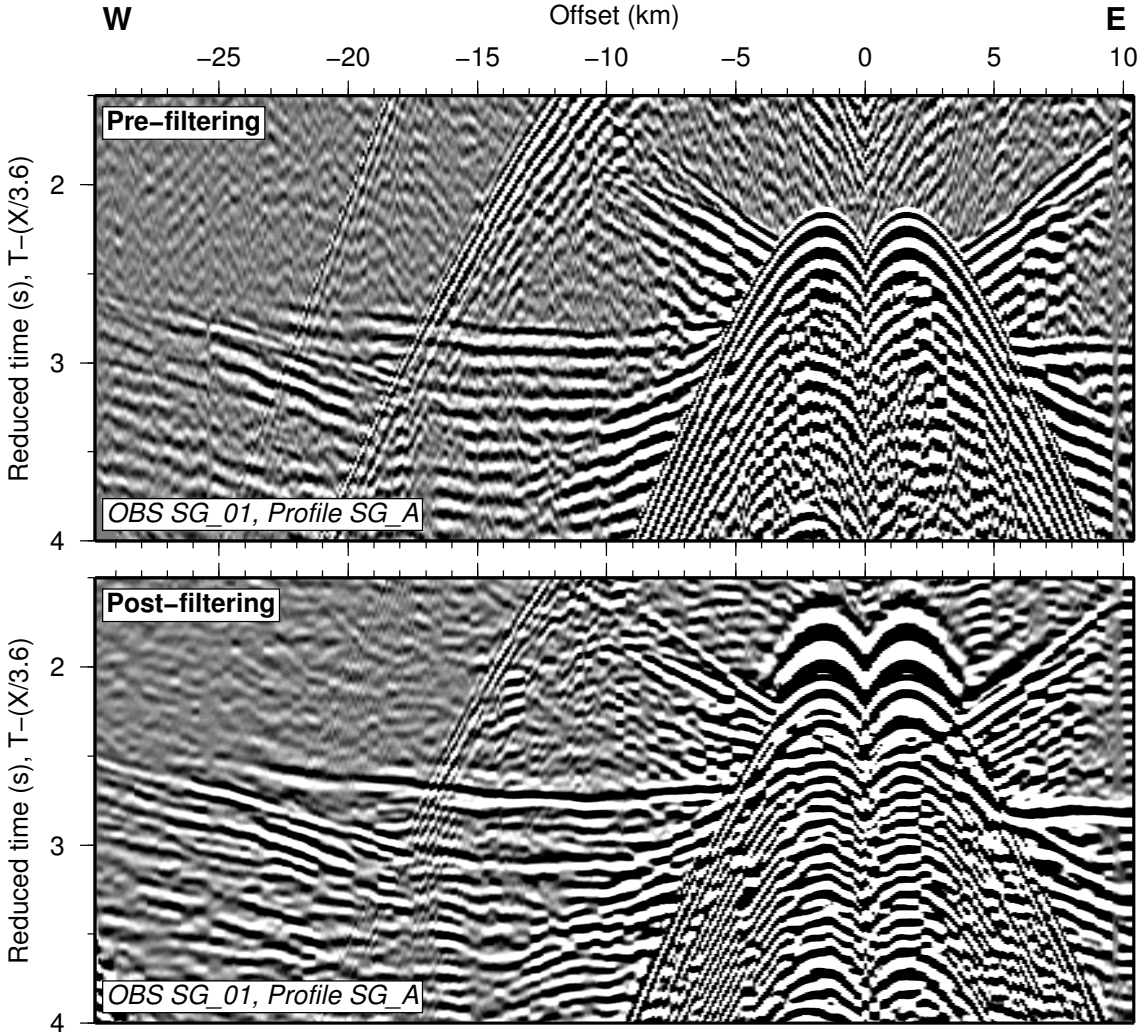


Figure 5.4: Record sections showing the effects of data filtering on the clarity of the P-S mode conversions. The pre-filtering record section has a minimum-phase bandpass filter applied at 3/6/12/24 Hz for plot clarity; and the post-filtering record section has had deconvolution, a zero-phase bandpass filter at 3/6/12/24 Hz, and a median filter applied (Section 3.3.2).

### 5.3.2 Travel time picking and errors

Travel times for the crustal mode converted arrivals were picked using the semi-automatic horizon tracker feature within the *Claritas* software package (Figure 5.5), following the same method used to pick the P-wave arrivals (Section 3.3.3). A total of 101,696 wide-angle crustal refractions were picked from the 288 record sections of the dataset.

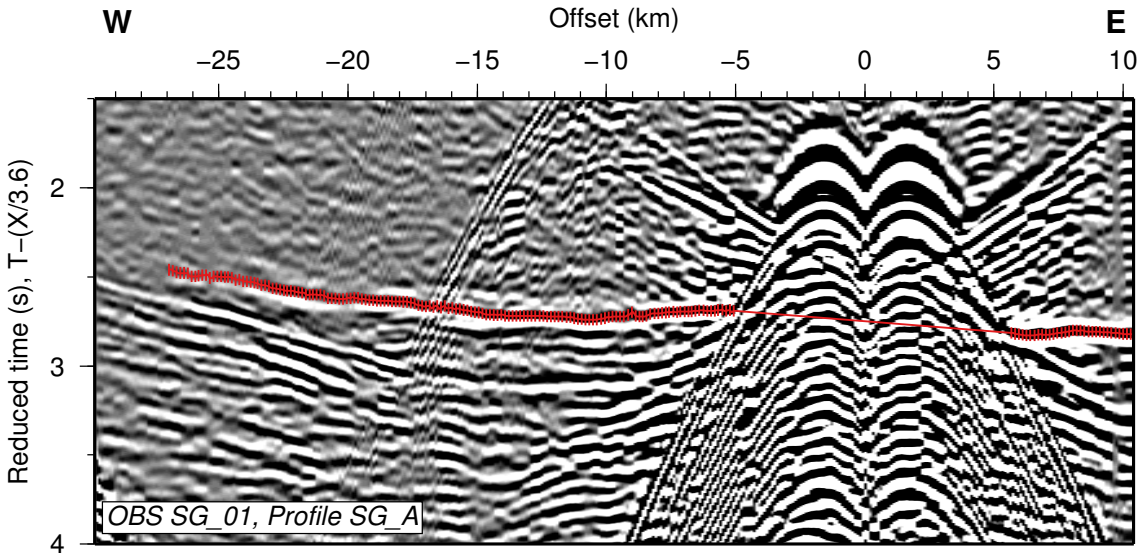


Figure 5.5: Example of the horizon tracker within *Claritas* tracing along the crustal first arrival (red line). Vertical bars show the pick uncertainty (plotted for every other pick).

The effect of the data filtering procedure on the arrival travel times was investigated to prevent this from influencing the inversion result. For 20 OBS records sections the mode conversion travel times were picked manually on unfiltered data using the *zplot* package. When picking using the unfiltered data, picks were made at the first break of the arrival, with the first following peak positive in polarity. When picking using the filtered data, the picks were made at the peak of the positive (black in Figure 5.5) loop of the zero-phase filtered arrival. A comparison between the unfiltered data picks and the picks made within *Claritas* using the filtered data revealed a mean average difference of -20 ms (i.e. the filtered picks were delayed relative to the unfiltered), with a standard deviation of 5 ms. To correct for this delay, a bulk shift of 20 ms was applied to each pick, which successfully decreased the travel time difference to within the defined uncertainties, with an RMS average misfit of 7 ms (Figure 5.6).

To determine the uncertainties of the travel time picks, the method described in Section 3.3.4 was used. This method combines sources of error in the data with the filtering and picking errors for each phase, before weighting the uncertainty using the SNR of each OBS record section. For the P-S mode converted crustal arrivals (P-$S_g$), the picking error, $t_p$, is 30 ms, and the average misfit found between the corrected picks and the picks made on unfiltered data, $t_m$, is 7 ms. Thus the overall initial uncertainty on the travel time picks is 32 ms, which is then weighted by a factor between 1 and 1.5, determined by the SNR of each record section, to give a final uncertainty between 32 and 48 ms.

### 5.3.3 Initial model construction

The starting model for the Vs 3D inversion was created using the starting model that resulted in the preferred Vp inversion model (Section 3.3.5), with a variable sediment layer, single-gradient profile through the crust, and constant velocity laterally across the model

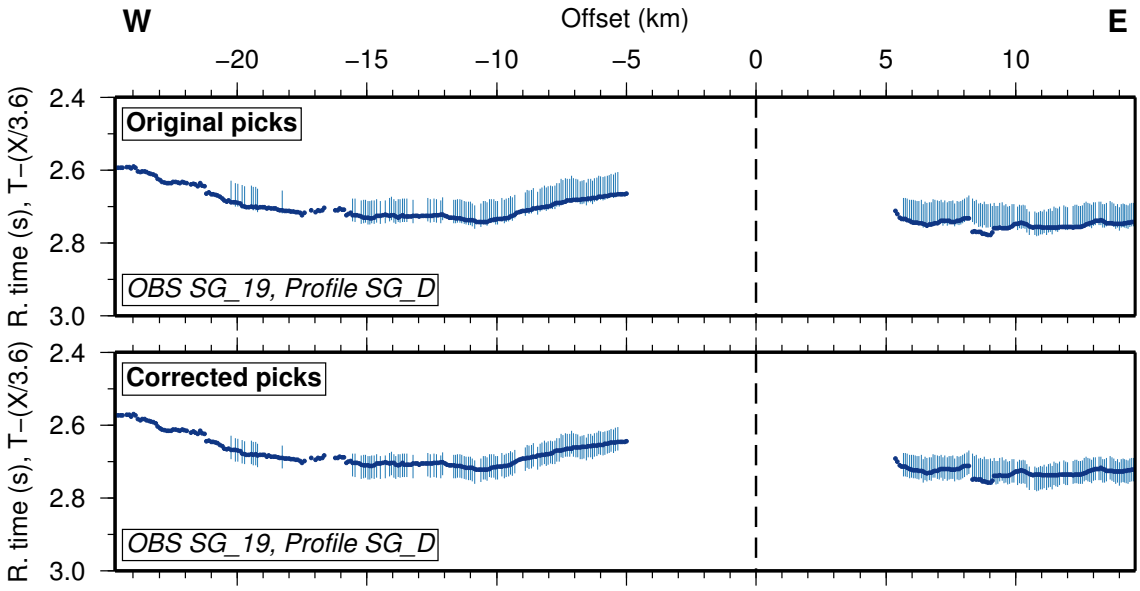


Figure 5.6: Demonstration of the ∼20 ms offset between the travel time picks made using the filtered data in *Claritas* (blue circles), and picks made manually using unfiltered data (bars, where the size of the bar is the uncertainty of the pick). A bulk shift of 20 ms corrects the majority of the picks to lie within the data uncertainty. The picks shown are from a crustal first arrival, and are plotted at reduced time (R. time).

to reduce bias towards the basement structure. The Vp starting model was converted to a mixed-velocity model to match the P-S and S-P conversion points of the picked arrivals. The water column and sediment layer remained as Vp, and the crust and mantle were converted from Vp to Vs using a constant Poisson's ratio of 0.28 (Figure 5.7) (Christeson et al., 1997; Collier and Singh, 1998), by rearranging Equation 5.1:

$$V_s = \frac{V_p^2(2\sigma - 1)}{\sqrt{(2\sigma - 2)}}. \tag{5.2}$$

The model coordinates of the OBSs remained the same as those used for the preferred Vp inversion (Section 3.3.5), along with the horizontal interfaces that were used both to create the initial model (e.g. seabed and basement), and to limit the inversion updates to the crustal part of the model (basement).

This starting model has an initial $\chi^2$ fit to the data of 912, which is significantly, but not unreasonably, greater than the initial fit of the Vp starting model to the P-wave arrivals of 253.

### 5.3.4 Inversion parameters

To produce a comparable Vs model to the Vp preferred model, the Vs inversion was initially run using the same inversion parameters (cell size, freedom parameter $\lambda$, and smoothing parameters *sz*, $\alpha$, and *sedge* - described in Sections 3.3.6), given in Section 3.3.7. The two-stage inversion procedure was also implemented, consisting of an initial inversion (Stage I) with a larger cell size and greater value of $\lambda$, followed by a secondary

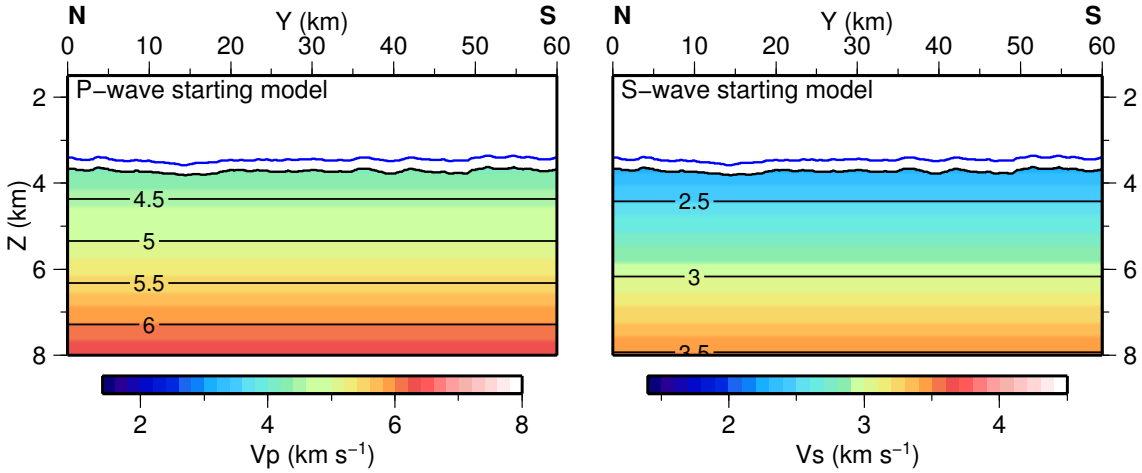


Figure 5.7: S-wave starting model (right), shown as a N–S trending cross-section along profile SG_I. This was created by converting the crust below the basement interface (black line) in the P-wave starting model (left) from Vp to Vs using a Poisson's ratio of 0.28. The blue line is the seabed.

inversion (Stage II), with a smaller cell size and reduced $\lambda$. In general, these parameters resulted in a stable inversion process that was able converge to a solution. However, due to the larger $\chi^2$ of the initial model (912 compared with 253), in order to reach a $\chi^2$ of close to one during the second stage, a lower $\lambda$ value (300 compared with 500) was needed to be used during Stage I. This allowed the inversion process to make larger updates to the model to reduce the data misfit, resulting in a similar $\chi^2$ after the first five iterations (5.5 compared with 7.6), to take forward to the Stage II.

### 5.3.5 Results

The final preferred Vs model was determined, as detailed above, following an almost identical procedure to that used for the preferred Vp model. The first five iterations of the inversion (Stage I) were performed with a larger cell size and less freedom (Table 5.1), culminating in a laterally smooth model with a $\chi^2$ fit of 5.3 (Figure 5.8). Stage II of the inversion was performed with a reduced cell size and more freedom for the inversion process to update the model (Table 5.1), and reached a final $\chi^2$ of 1.0 within four iterations (iterations 6–9) (Figure 5.8).

| | Stage I | | | | Stage II | | | |
|---|---|---|---|---|---|---|---|---|
| | Cell size (km) | | $\lambda$ | iterations | Cell size (km) | | $\lambda$ | iterations |
| | X | Z | | | X | Z | | |
| Preferred model | 2 | 0.3 | 300 | 5 | 1 | 0.2 | 50 | 3 |
| $sz = 0.3$; $\alpha = 1$; $sedge = 10$ | | | | | | | | |

Table 5.1: Inversion parameters used with *FAST* to create the preferred Vs model.

The final model exhibits a homogeneous and smooth structure, with little variation laterally (Figure 5.9). This is especially evident from the E–W section, which follows the

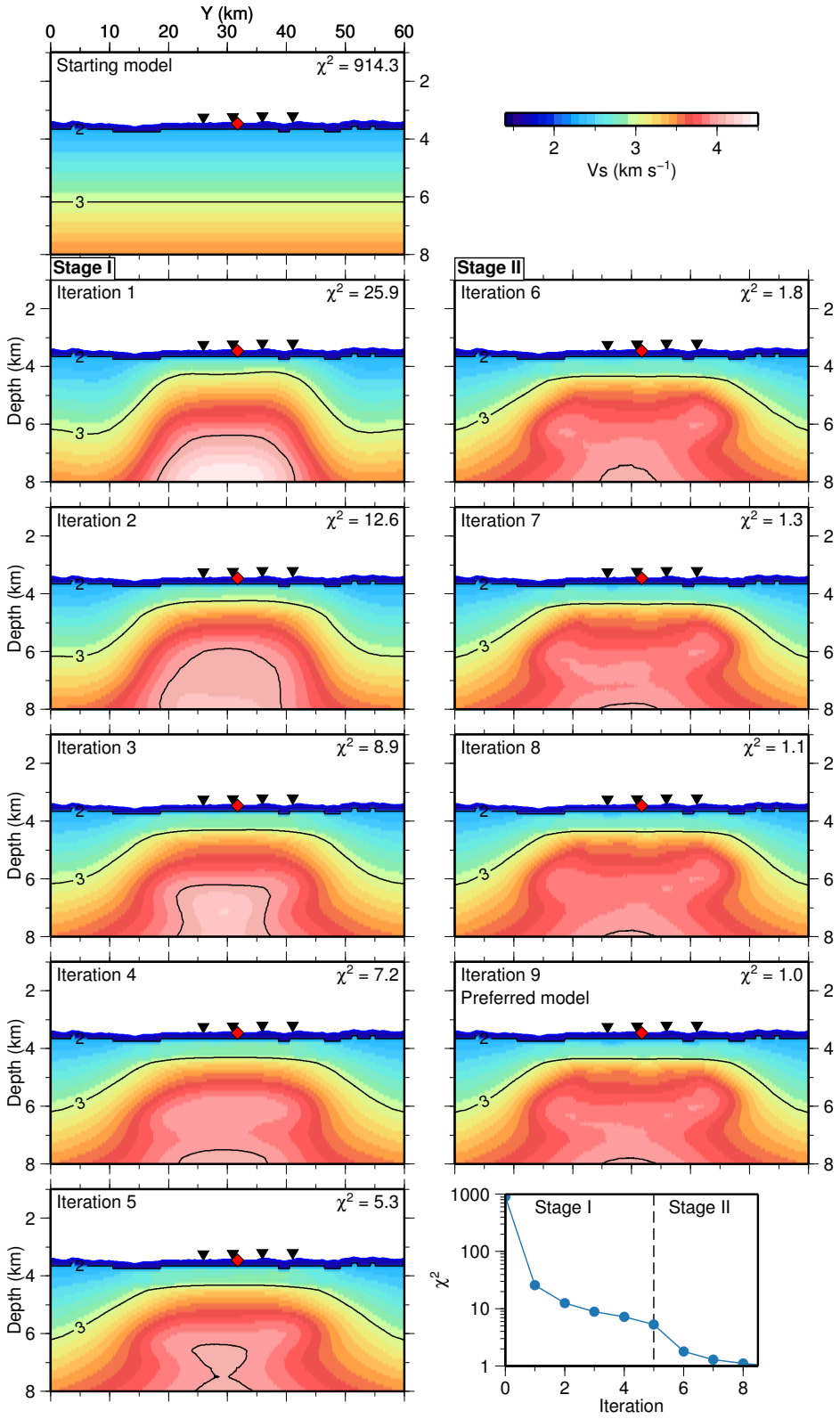


Figure 5.8: Inversion sequence for the preferred Vs model (bottom right), from the starting model (top left), shown as N–S trending cross-sections through the position of 504B (position indicated by red diamond), along profile SG_I. OBS positions along profile are shown by black triangles. The 'edge' effects are notable within regions of ~15 km from each edge. The $\chi^2$ value for each iteration is shown in the graph and illustrates the effect of separating the inversion into Stages I and II with different parameters.

tectonic fabric of the crust, where velocity contours are almost horizontal. Across the model, velocity increases from ~2.5 km $s^{-1}$ at the top of the basement to ~2.7 km $s^{-1}$ at to 0.5 km depth. Velocity then increases more rapidly to ~3.3 km $s^{-1}$ over the next 0.3 km, before reaching ~3.5 km $s^{-1}$ just over 1 km below top basement (km bb). From this depth the velocity increases more gradually to ~3.7 km $s^{-1}$ at 1.5 km bb. Velocity appears to decrease towards the edges of the model in both the N–S and E–W directions. These decreases are interpreted as "edge effects"- artefacts from the ray coverage of the model space caused by the poor sampling of the edges of the model by ray paths. This means that velocity updates during inversion tend not to occur in these edge areas, and as the starting model is slower than the final model, these areas retain a lower velocity than in the centre of the final model.

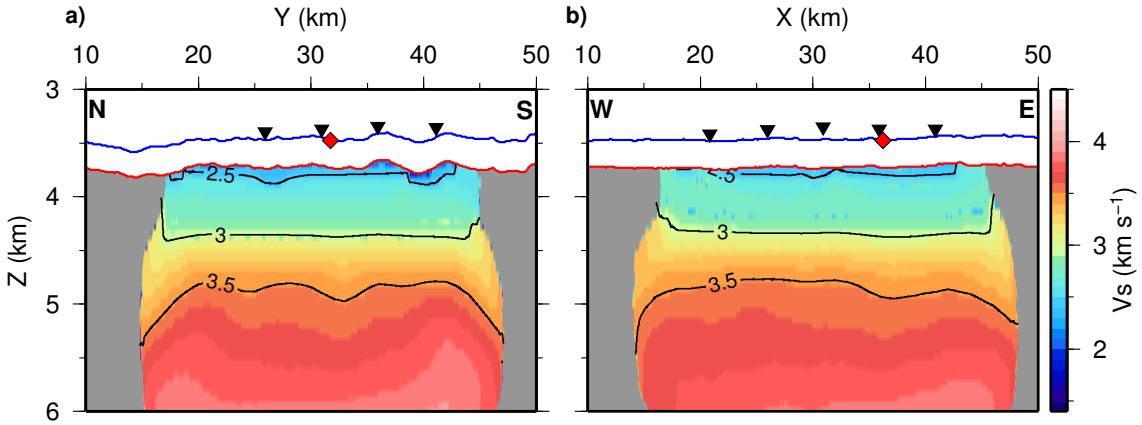


Figure 5.9: Cross-sections through the final model at the position of borehole 504B (red diamond), trending a) N–S along profile SG_I and b) E–W along profile SG_C. Seabed and basement interfaces are shown by the blue and red lines, respectively. The model is masked using the 0.7 semblance contour from checkerboard testing with a 4 km x 4 km size checkerboard.

Depth sections through the 3D volume (Figure 5.10) show the variation across the model space more clearly than the cross-sections. However, the variation remains low, with relatively small velocity anomalies with a maximum amplitude of ~0.2 km $s^{-1}$ in the upper 1 km of the crust, and below 0.1 km $s^{-1}$ below 1 km. The larger, circular anomalies around the edges of the model below 1.7 km bb are interpreted as artefacts from the edge effects.

In general, the velocity anomalies exhibit an E–W trending pattern within the upper 1.5 km of the basement, similar to the patterns in basement topography. At the top of the igneous crust (0.2 km bb) there are two positive velocity anomalies between Y=30–35 km of ~0.1 km $s^{-1}$, extending approximately 5 km E–W, and ~4 km N–S. These anomalies extend downwards and merge, and are still visible as low amplitude anomalies (~0.05 km $s^{-1}$) at 1.2 km bb, although this is likely to be below the resolution of the model. A lower amplitude positive anomaly (<1 km $s^{-1}$) spreads E–W across the north of the model at Y=~20 km, featuring small regions up to ~1 km $s^{-1}$. This anomaly also extends down to over 1 km into the crust, although remains at low amplitude. The most prominent negative velocity anomaly in the model occurs as a thin (<3 km-across) E–W

trending band from Y=∼35 km in the west to Y=∼38 km in the east, visible from 0.2–1.2 km bb and varying in amplitude from 0.05–1.5 km $s^{-1}$. Further negative anomalies centred on model X,Y coordinates 40,32 and 35,25 are most prevalent at 1.2 km bb, with a maximum amplitude of ∼1 km $s^{-1}$. Smaller anomalies, both positive and negative, occur throughout the upper 1 km of the crust, although these are interpreted to most likely be artefacts caused by the influence of the basement topography, and are also below the resolution of the dataset and inversion procedure.

### 5.3.6 Checkerboard testing

Checkerboard testing was applied to the final model to test the lateral resolution and identify areas of the model which are poorly resolved. This followed the same procedure as the checkerboard testing applied to the Vp model (Section 4.2): different anomaly patterns were added to the model, with the inversion process attempting to recover them using the experiment geometry and same inversion process as the final model. These tests were run with both the standard, columnar pattern, and the cuboid pattern (Section 4.2).

The checkerboard testing results show that 3 km-size anomalies are resolvable for the majority of the central model space, to ∼6.0–6.5 km depth below the sea surface, equivalent to ∼2.3–2.8 km bb, with the limit of 'well-resolved' anomalies shown by the 0.7 semblance contour (Figure 5.11). Tests using cuboid anomaly patterns indicate that 5 x 5 x 2 km-sized anomalies are mostly well-resolved in the central model area in the upper 0.5 km of the basement, and well-resolved over a wider area at 1.5 km bb. The results from both the standard and cuboid checkerboard tests suggest that the final model has a similar lateral resolution to that of the Vp model, which also has 3 km lateral resolution within the crust to ∼2.8 km bb, and 5 x 5 x 2 km resolution when defined using a cuboid pattern. This is to be expected given the similar number of picks from the same experiment geometry, and the use of the same inversion procedure and almost identical parameters. These resolution results suggests the primary anomalies within the Vs model, discussed above, are large enough to be interpreted, and that the many smaller, high amplitude anomalies present, particularly at 0.7 km bb, are below the resolution of the model and their interpretation needs to be treated with caution.

### 5.3.7 Monte Carlo uncertainty analysis

To calculate the uncertainty in the velocity at different depths within the model, the results were analysed using Monte Carlo methods (Section 4.4.1). These uncertainties are particularly useful for the interpretation of 1D velocity-depth profiles extracted from the 3D model volume. This analysis used the Monte Carlo inversion code described in Section 4.4.1, which performs inversions in 2D using randomly-generated starting models to produce an array of possible velocity models with an 'acceptable' level of fit (chosen by the user). The 2D starting models were created along shot profiles SG_I (N–S trending) and SG_C (E–W trending), and the inversions run using the same parameters as the 3D

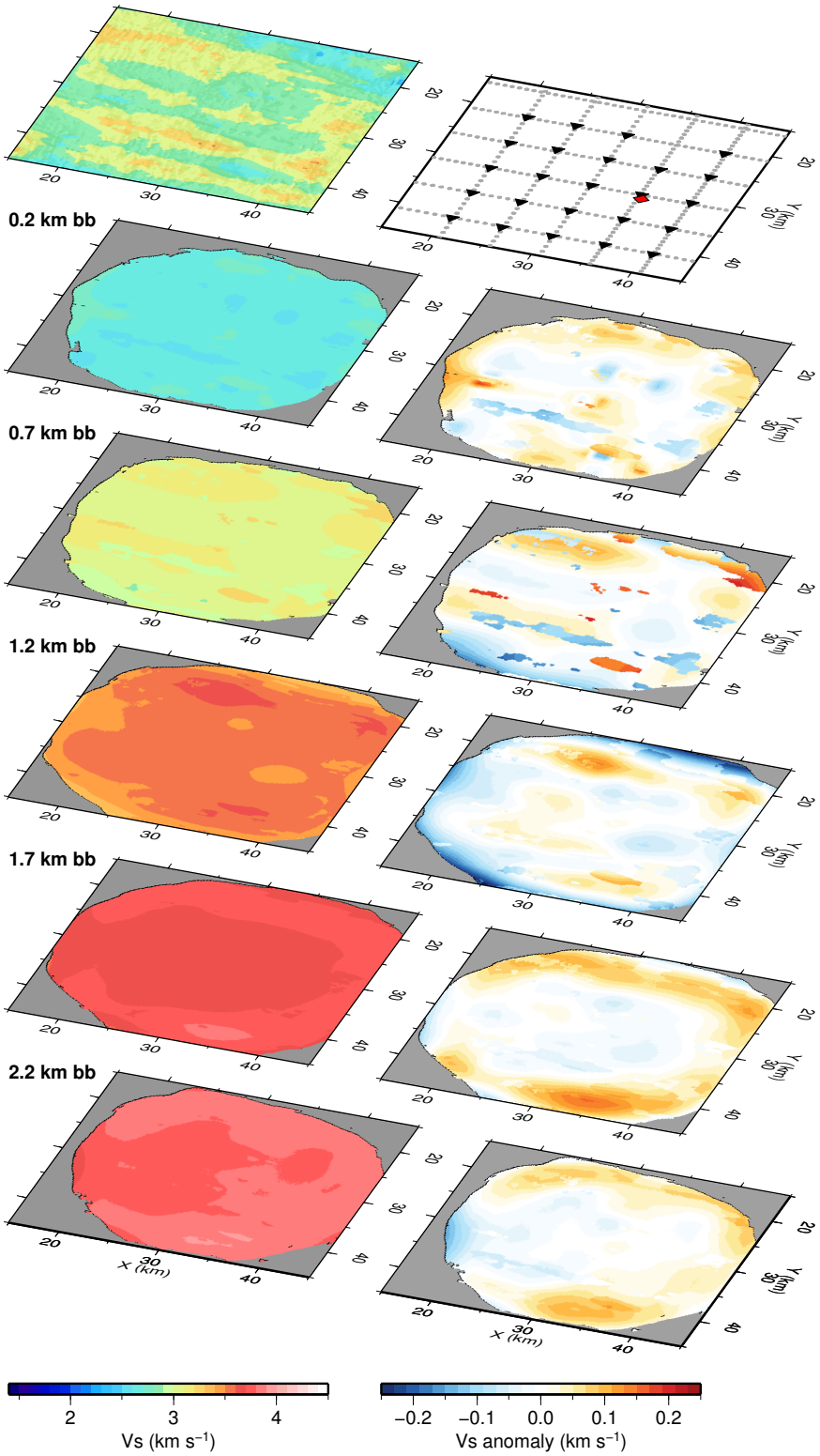


Figure 5.10: Depth sections through the final 3D Vs model, with depth calculated as km below basement (km bb), shown as velocity (left), and velocity anomaly (right). The model is masked using the 0.7 resolvability contour from checkerboard tests of a 4x4 km size anomaly. Basement topography (top left) and the acquisition geometry (top right) are shown for reference, with OBSs represented by black triangles, shot points by grey circles (every 10th plotted), and borehole 504B by the red diamond.

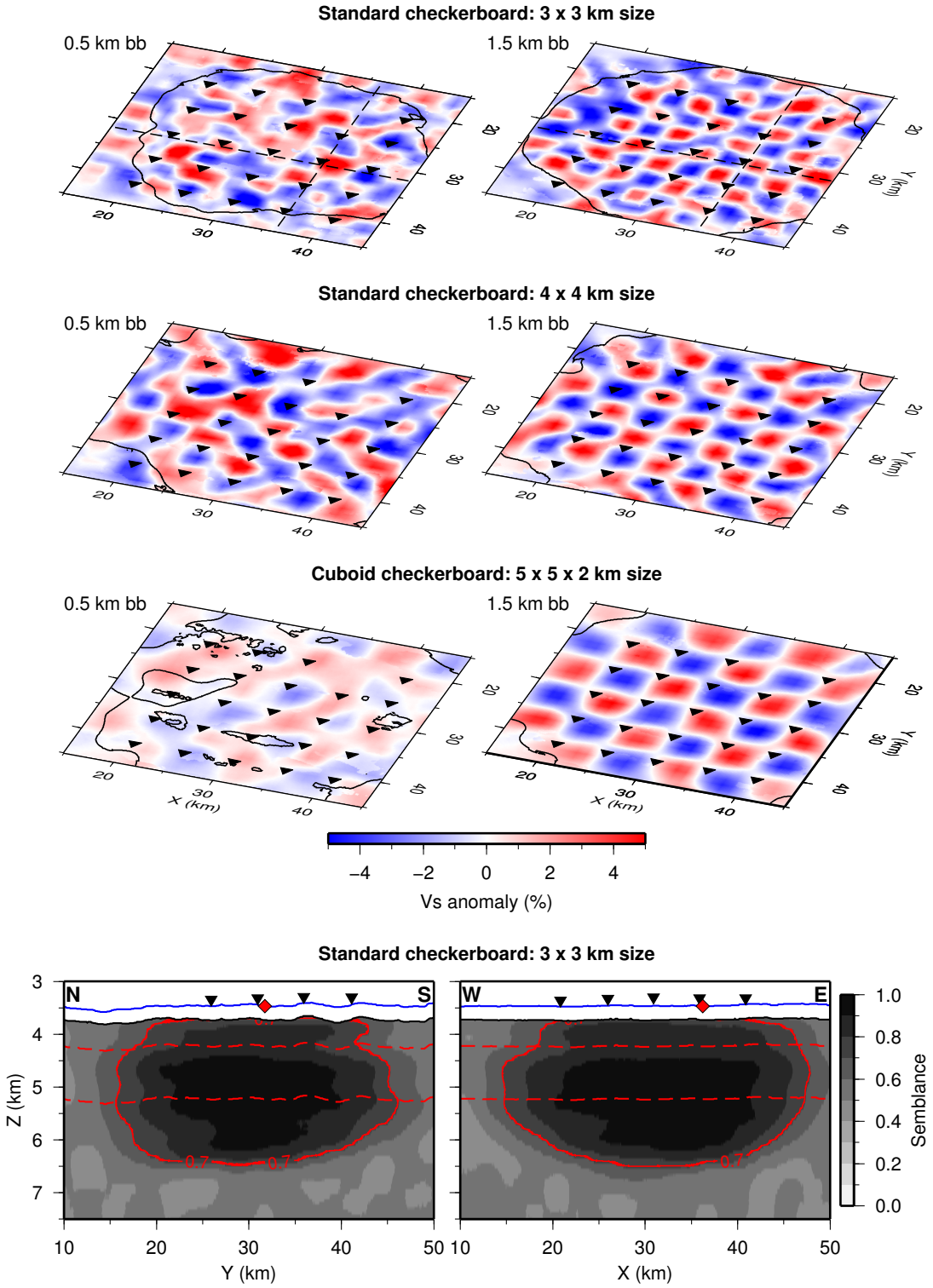


Figure 5.11: Checkerboard testing results for the final S-wave model, shown as depth-sections in km below basement (km bb). An example recovered checkerboard is plotted, along with the 0.7 (solid line) semblance contour calculated from an average eight checkerboards for the same anomaly size. All checkerboard tests were performed using a 5% velocity anomaly. The bottom two plots show N–S and E–W cross-sections through the 3D semblance model for the 3 x 3 km-size checkerboard test, and show the depth limits of resolvability with the 0.7 semblance contour (red line). Respective positions of the depth-sections and cross-sections are shown with dashed lines. Positions of OBSs (black triangles) and 504B (red diamond) are shown for reference.

inversion. The observed data used comprised shots from each profile to the in-line OBSs: 09, 12, 19, 22 for SG_I; 11, 12, 13, 15, 15 for SG_C. The code was run for 1000 iterations in both the N–S and E–W directions, and models accepted if they fit the observed data to a $\chi^2$ of 3.0 or smaller. This resulted in arrays of 447 N–S accepted models and 511 E–W accepted models, which are further analysed by extracting a 1D velocity-depth profile from each model at the location of borehole 504B (Figure 5.12).

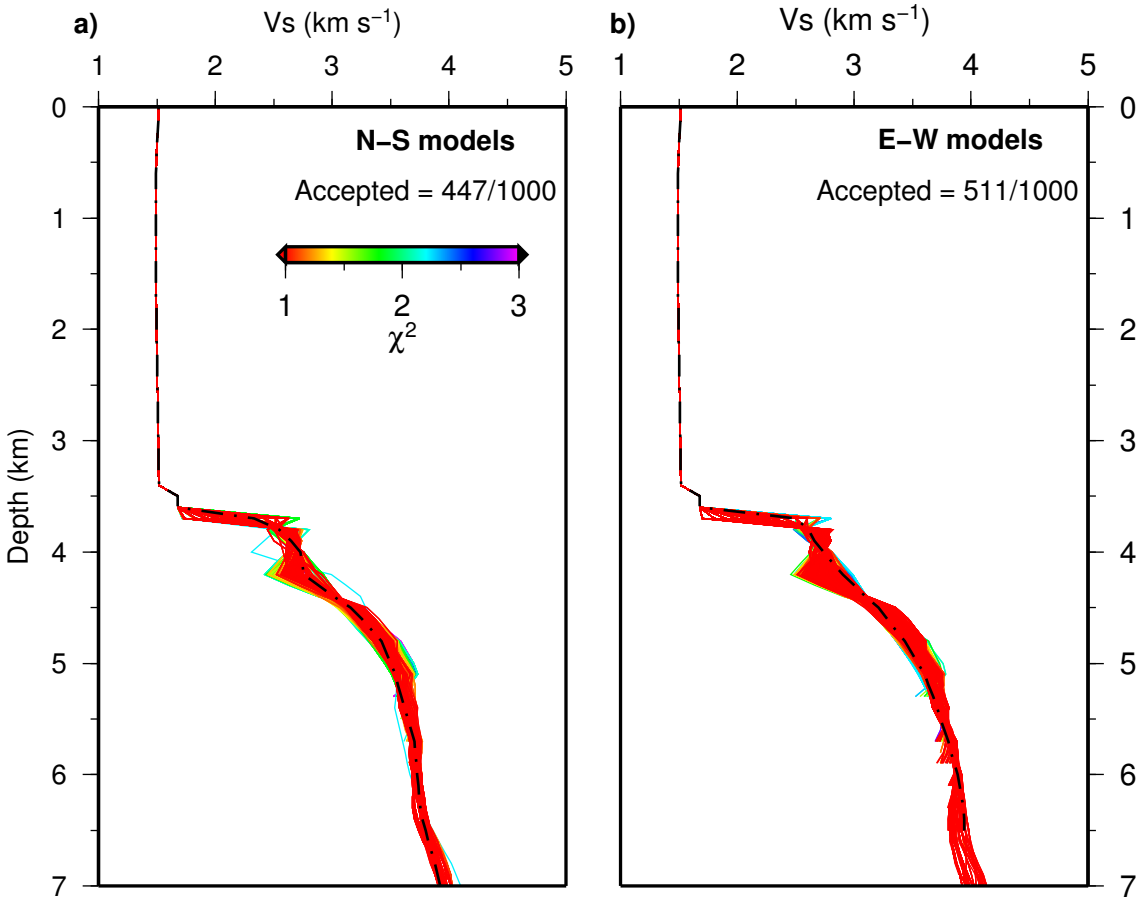


Figure 5.12: Monte Carlo inversion code results. 1D profiles through the N–S (a) and E–W (b) accepted models at the position of borehole 504B. The best-fitting model (lowest $\chi^2$) from the tests is shown by the dashed-dotted line, and lies near the centre of the range of accepted profiles.

Using the 1D profiles extracted from the populations of accepted models, the 68% (one standard deviation) and 95% (two standard deviations) confidence boundaries at each depth were calculated (Figure 5.13). The best-fit E–W model is slightly faster than the N–S best-fit model throughout the entire crust, although also only by a maximum of ~0.1 km s$^{-1}$, which is below the resolution of the models. Merging the two populations of accepted models and calculating the confidence boundaries provides non-directional (or isotropic) velocity uncertainties for a 1D profile at the position of borehole 504B (Figure 5.13). The confidence boundaries are wide at the very top of the crust, where the velocity increases rapidly from the low velocity sediments into the igneous basement. The remainder of the upper ~2.5 km of the basement has relatively narrow confidence

boundaries, with a 95% confidence of approximately ±0.15 km $s^{-1}$. These confidence boundaries agree well with the 1D profile at 504B extracted from the 3D Vs model, and relatively well with the sonic velocity log from borehole 504B, especially above ~0.8 km bb (4.5 km depth below sea surface).

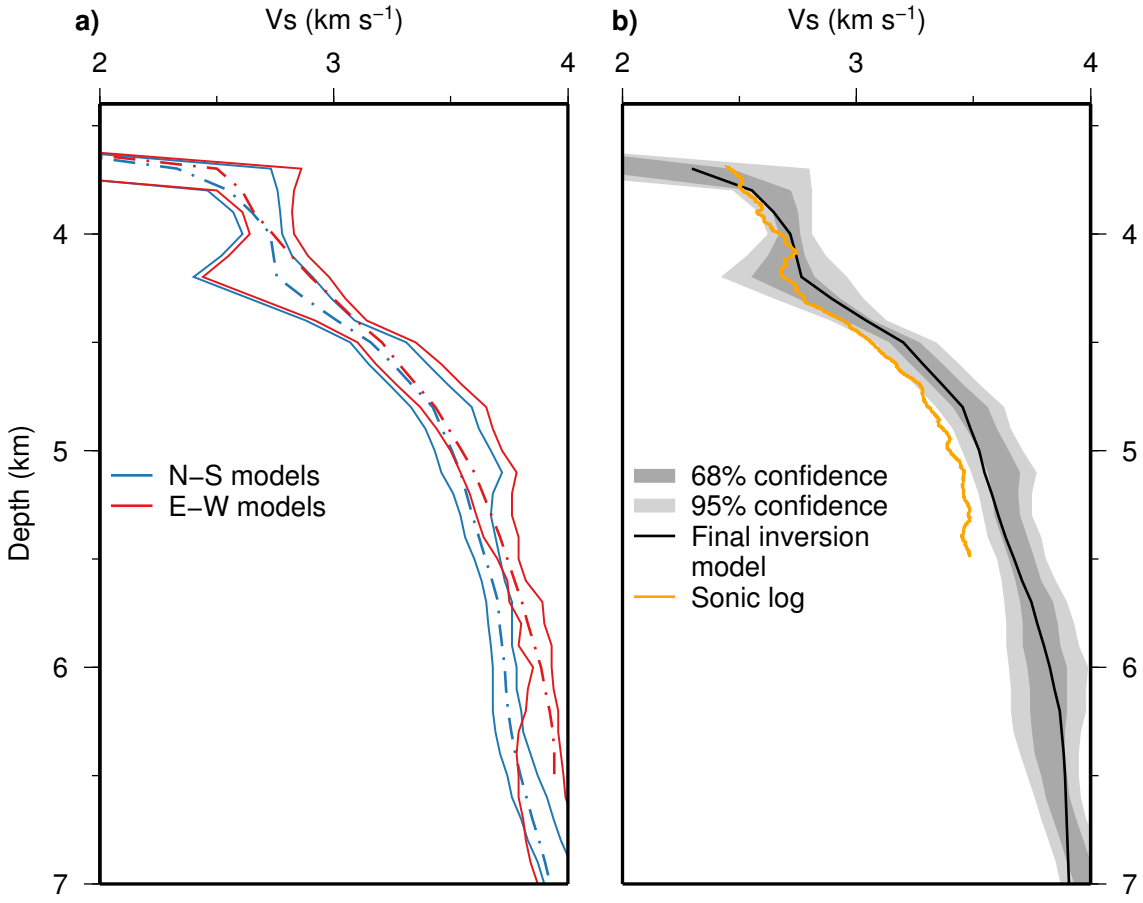


Figure 5.13: Statistical confidence limits calculated from the Monte Carlo inversion code results. a) 95% confidence boundaries for the E–W and N–S model populations are similar (solid lines), although the E–W models tend to be slightly faster, as is the E–W best-fitting model (dot-dash line). b) Merged confidence boundaries are relatively narrow throughout the crust, and fit well with the 1D profile at borehole 504B extracted from the final Vs inversion model, and reasonably well with the downhole sonic log from the borehole (Guerin et al., 2008), although become ~0.1 km $s^{-1}$ faster below 4.5 km depth in the model (equivalent to 0.8 km bb).

## 5.4 Poisson's ratio model

Vp and Vs models can be directly compared by calculating the Poisson's ratio, $\sigma$, (Equation 5.1). Changes in $\sigma$ within the same material indicate disproportionate changes in Vp and Vs, which can be caused by changes in the shape or types of cracks and voids in the crust (Shearer, 1988):

- S-wave velocities are generally more sensitive to thinner, low aspect ratio cracks (<0.005, calculated as the width divided by the length), thus a prevalence of these will disproportionately reduce Vs and increase $\sigma$;
- P-wave velocities are generally more sensitive to thicker, higher aspect ratio cracks (0.05–0.5), and so a greater proportion of these will primarily reduce Vp and so decrease $\sigma$.

The Vp/Vs ratio is often calculated instead of $\sigma$ (e.g. Grevemeyer et al., 2018b), and exhibits the same relationship with fractures, with values commonly varying from 1.7–2.0. Both the $\sigma$ and Vp/Vs ratios have been previously used to ascertain changes in fracture density and shape in the oceanic crust at the East Pacific Rise (Christeson et al., 1997; Collier and Singh, 1998), Juan de Fuca Ridge (Barclay and Wilcock, 2004) and Mid-Atlantic Ridge (Barclay et al., 2001), with values as high as 0.48 in the uppermost layer (2A) of the igneous oceanic crust. These parameters are also sensitive to the water content of materials, and have been used to map hydration in the mantle (Moscoso and Grevemeyer, 2015), distinguish between serpentinised peridotite and gabbro (Prada et al., 2016) and determine the degree of serpentinisation of the oceanic lithosphere at subduction zones (Grevemeyer et al., 2018b).

In this study, Poisson's ratio is calculated to investigate the fracturing patterns within the crust to better understand fluid flow pathways and the effects of hydrothermal alteration.

### 5.4.1 Method

Poisson's ratio, $\sigma$, was calculated from the final Vp and Vs inversion models using Equation 5.1 (Figure 5.14). To reduce the number of artefacts and anomalies which are below the model resolution in the $\sigma$ model, the Vp and Vs models were both smoothed before the calculation. Smoothing was performed using a Gaussian-weighted function with a lateral filter width determined by the best lateral resolution indicated by the checkerboard testing results (Sections 4.2 & 5.3.6), which was 4 km. The smallest well-resolved cuboid anomaly pattern was 5 x 5 x 2 km in size, so vertical cross-sections were filtered with a diameter of 2 km.

To determine which areas of the model are 'well-resolved' and can be interpreted as geological in origin, the final semblance results from the Vp and Vs models were combined. 'Well-resolved' areas were defined as having a semblance value of 0.7 in both Vp and Vs models, as calculated from a 4 km-sized standard checkerboard test (Section 4.2). Areas with a semblance of below 0.7 in either the Vp or Vs model were masked.

### 5.4.2 Results

In general, $\sigma$ does not vary widely throughout the model, with values mostly between 0.22 and 0.28 (Figure 5.14). The main anomalies visible in cross-sections appear to be

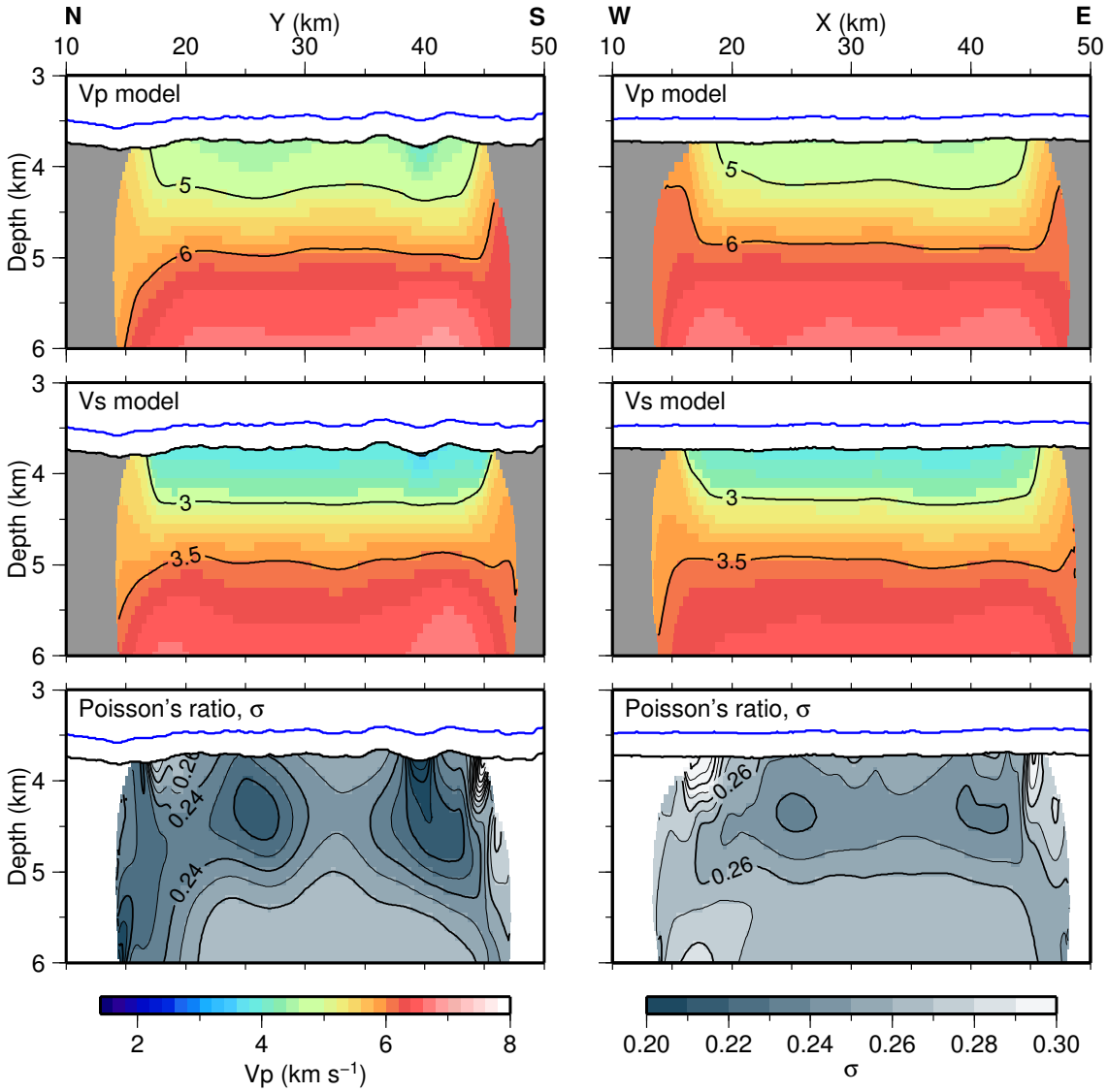


Figure 5.14: Cross-sections through the Vp, Vs and $\sigma$ final models along profiles SG_I (N–S) and SG_C (E–W), after smoothing with a 2 km-wide filter. Coloured areas of the $\sigma$ model have Vp and Vs model semblance values $\geq$0.7, calculated from standard checkerboard tests run with a 4 km-sized anomaly pattern. Seabed=blue line, top basmenet=black line.

lows from 0.5-1.0 km bb, which extend across the model, and up to the top basement in localised areas. These are more prominent in the N–S cross-section than the E–W cross-section. Below these lows, $\sigma$ increases with depth to values $\sim$0.26 across the whole model.

The depth-sections (Figure 5.15) also show average values of $\sigma$ ($\sim$0.26) within the upper 0.2 km of the igneous crust, with localised low anomalies of $\sim$0.22. These anomalies become larger in size at 0.7 km bb, spreading E–W across the model forming parallel bands of high and low $\sigma$. Below 1.2 km bb $\sigma$ remains relatively uniform across the model with high average values of 0.27. These changes with depth could indicate a mix of low and high aspect ratio fractures at the very top of the crust, evolving into a dominance of

thicker cracks between 0.5-1.0 km bb. Below 1.2 km bb, thinner, low aspect ratio cracks become dominant, increasing $\sigma$.

The $\sigma$ anomaly is calculated for each depth-section by finding the difference between each value and the mean average in the model at that depth (Figure 5.15). The average is calculated only using values from the central 400 km$^2$ to limit the influence of the outer, poorly sampled and resolved edges of the model. The upper 1.2 km of the basement shows significant lateral variation in $\sigma$ across the model, with clear, E–W trends. Positive $\sigma$ anomalies extend E–W across the model at Y=20 km and Y=30 km, are apparent in depth slices from 0.2–1.2 km bb, and are of highest amplitude at 0.7 km bb (>0.03). These are divided by bands of negative anomaly extending across the model at Y=25 km and Y=40 km, with similar amplitudes to the positive anomalies. Below 1.2 km bb little lateral variation is observed. These patterns could suggest that there are variable fracture populations in the upper ∼1.2 km of the igneous crust, alternatively dominated by either thick or thin cracks. Deeper in the crust fracture density and shape become almost homogeneous across the model.

## 5.5 Azimuthal anisotropy

Seismic anisotropy, the variation of seismic velocity with direction, has been frequently observed within the oceanic crust at mid-ocean ridges (e.g. Tong et al., 2004; Dunn et al., 2005; Canales et al., 2014) and also in older oceanic crust (Shearer and Orcutt, 1985; Detrick et al., 1998). Seismic anisotropy is primarily caused by a preferential alignment of fractures or layering within the subsurface. The predominant form of anisotropy present in the oceanic crust is *azimuthal anisotropy*, caused by the alignment of vertical fractures within the crust along a particular horizontal azimuth. Seismic waves travel more quickly in homogeneous media, i.e. if they do not have to cross fractures within the crust. Where fractures are present, seismic waves travelling parallel to the fracture alignment will travel faster, as the void space within fractures is normally filled with water or another material with a lower seismic velocity than the host rock. This forms a 'fast' direction, parallel to the fracture alignment, and a 'slow' direction, perpendicular to the fracture alignment. Azimuthal anisotropy analysis can, therefore, indicate the presence of aligned fractures within the crust and the direction of that alignment. The 'strength' of anisotropy, or the difference in velocity between the fast and slow directions, can then indicate the density of aligned fractures.

In this study, the full azimuthal coverage of the model space due to the acquisition geometry allows azimuthal anisotropy to be used to analyse fracturing within the crust, and whether this may vary laterally across the model or change with depth within the crust. This analysis will complement the Poisson's ratio model discussed in Section 5.4 and enable a better understanding of the potential fluid flow pathways and alteration patterns in the study area.

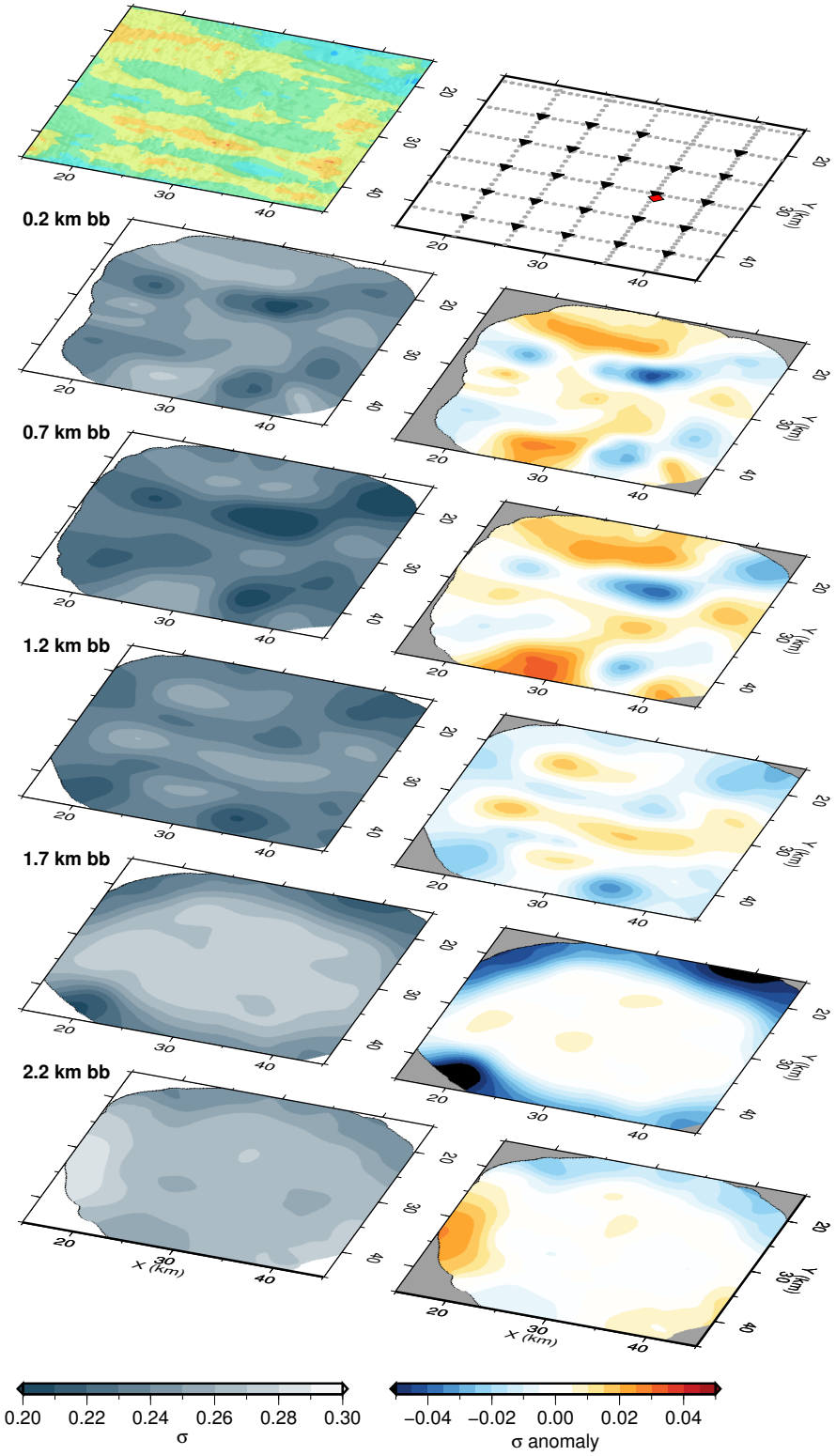


Figure 5.15: Depth sections taken at 0.5 km increments below basement (km bb) through the $\sigma$ model. The $\sigma$ anomaly was calculated as difference from the mean average value at each depth. Basement topography and the experiment geometry are shown at the top of the figure for reference.

### 5.5.1 Theory

Azimuthal anisotropy is analysed by comparing the seismic velocity with azimuth, $\theta$, (Figure 5.16), measured as a bearing in degrees from North, or from the bearing of a feature, such as the axis of a spreading centre, to investigate anisotropy relative to that particular feature.

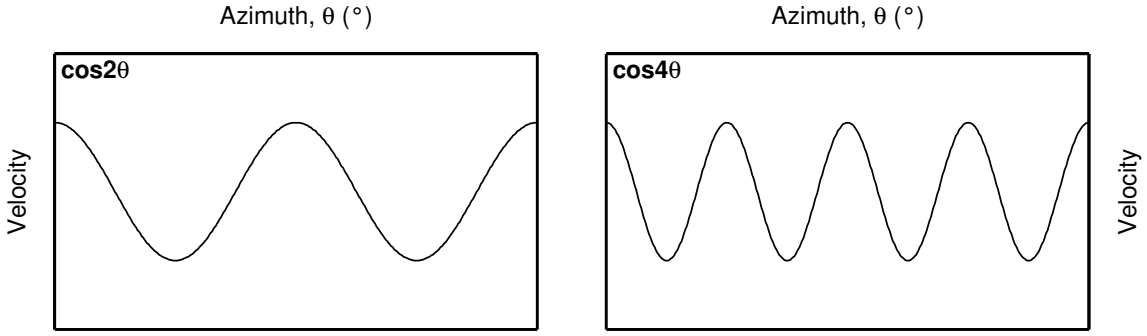


Figure 5.16: Example cos2$\theta$ patterns between azimuth and P-wave velocity (left), formed by aligned, open fractures within the crust, while aligned, closed fractures form cos4$\theta$ patterns (right). Aligned fractures of all aspect ratios form cos2$\theta$ patterns between azimuth and S-wave velocity.

Theoretical studies by Hudson (1981) and Crampin (1984), further expanded on by Shearer and Orcutt (1986) and Crampin (1993), show that the presence of open, aligned fractures within the crust results in a cos2$\theta$ pattern of P-wave velocity (Figure 5.16). The presence of aligned fractures of any aspect ratio is shown to form a cos2$\theta$ pattern of S-wave velocity. The peaks and troughs of the wave indicate the slow and the fast directions, respectively, and the amplitude of the function gives an indication of the strength of anisotropy. The relationship between Vp (but not Vs) and azimuth is shown to be dependent on the aspect ratio of the fracture population, with thin, closed fractures resulting in a cos4$\theta$ pattern as opposed to the cos2$\theta$ pattern (Figure 5.16). Shearer & Orcutt (1986) suggest aspect ratios <0.001 result in almost entirely 4$\theta$ patterns, and thicker cracks with aspect ratios between 0.01 and 0.1 yield predominantly 2$\theta$ variations. With a pure cos4$\theta$ wave, the velocity peaks occur at azimuths both parallel and normal to the fracture alignment, so it may be difficult to deduce the true alignment without other observations. Aspect ratios between 0.001 and 0.1, or a combination of more open (thicker) and closed (thinner) fractures, result in a more complex pattern, which can be described by the equation:

$$A_{2\theta}cos(2\theta + \alpha) + A_{4\theta}cos(4\theta + \beta). \tag{5.3}$$

The relative strengths of the cos2$\theta$ and cos4$\theta$ patterns, calculated as $\frac{A_{4\theta}}{A_{2\theta}}$, gives an indication as to the dominant aspect ratio of the fractures (Tong et al., 2004), or the relative prevalence of open versus closed fractures, with a value of one indicating equal prevalence, and below one a dominance of open fractures. The values of $\alpha$ and $\beta$ are the phase shifts, and so determine the fast and slow velocity directions. For S-wave azimuthal

anisotropy, the cos4$\theta$ term is not needed, thus the pattern is described by the equation:

$$A_{2\theta}cos(2\theta + \alpha). \tag{5.4}$$

### 5.5.2 Method

Azimuthal anisotropy was analysed separately for the Vp and Vs models, due to the different relationships between the velocities and azimuth. As the inversion code used in this study, *FAST*, cannot resolve seismic anisotropy and produces isotropic models, the velocity in any area in the final model is an average of the range of velocities sampled in that area by ray paths. Similarly, the travel time calculated through an area in the final velocity model is an average, with some observed travel times from the dataset larger (indicating a slower velocity), and some smaller (indicating a faster velocity). If the material is anisotropic, the residual misfit between an observed travel time for a shot-receiver pair, and its equivalent travel time calculated through the final velocity model along an identical ray path, will vary systematically with shot-receiver azimuth (Figure 5.17). Thus, in effect, the travel time residuals can act as a proxy for velocity when investigating azimuthal anisotropy. In this study, the azimuth ($\theta$) is defined as the shot-receiver azimuth relative to North.

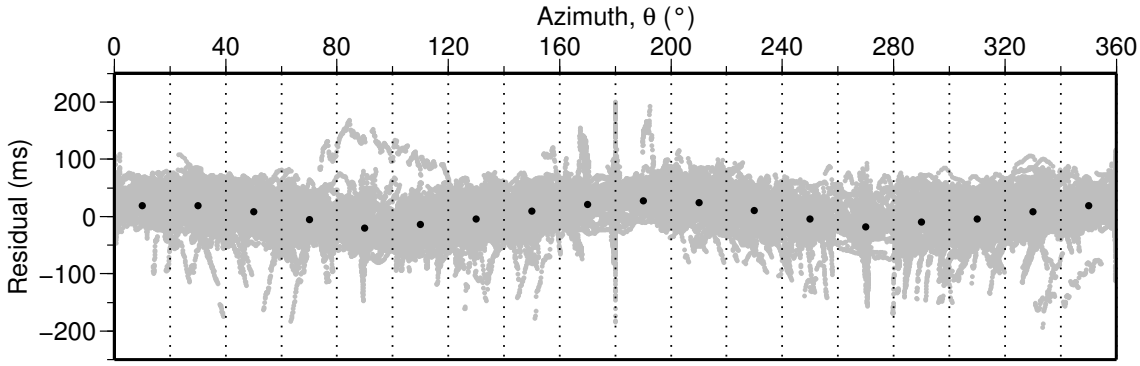


Figure 5.17: All travel time residuals (observed–calculated) for the Vs final model plotted against shot-receiver azimuth in degrees from north (grey circles), which show the full azimuthal coverage of the dataset. The data were divided into 20° bins (dotted lines) and the average residual calculated for each bin (black circle), in order to analyse the overall pattern in the data.

Following the method of Canales et al. (2014), the whole population of travel time residuals for the Vs or Vp final model was divided into 20° bins, and the mean average residual calculated for each bin (Figure 5.17). The standard error was calculated for each mean average residual. In this case, due to the large number of samples within each bin, the standard errors are very small. A curve is then fitted to the mean values using a robust least-squares method, defined by an adaptation of Equation 5.3 (Tong et al., 2004) for the Vp dataset and Equation 5.4 for the Vs dataset:

$$A_0 + A_{2\theta}cos(\frac{2\theta\pi}{180} + \alpha) + A_{4\theta}cos(\frac{4\theta\pi}{180} + \beta). \tag{5.5}$$

$$A_0 + A_{2\theta} cos(\frac{2\theta\pi}{180} + \alpha). \tag{5.6}$$

The inclusion of the $A_0$ term compensates for a non-zero average misfit, such as if all observed travel times at all azimuths are larger than the calculated travel time. The goodness-of-fit of the curve to the data was defined using the $R^2$ value. The fast and slow directions for Vp and Vs, and $\frac{A_{4\theta}}{A_{2\theta}}$ for Vp, were then found from the coefficients of the best-fit curve, if its fit to the data was significant. Travel time residuals were firstly analysed for both the entire Vp and Vs datasets, and subsequently for sub-sets of the data, split by either lateral space, or depth below top basement. The data were split by depth to investigate changes in fracturing with depth in the crust, and spatially to determine any changes in fracturing which could help explain lateral variations in lateral in the area (Swift et al., 1998a) . When splitting the data spatially, for example into east and west halves, both the shot and receiver of a ray path were required to be in the same spatial area, e.g. the east section, to be included in the dataset for that area. This means that there were no ray paths included which sample, for example, both halves of the model being compared. The data was split by depth using the ray turning depths (which is the deepest point sampled by the ray path), as this should represent the depth at which the ray was travelling laterally in the crust and be most affected by azimuthal anisotropy. *FAST* can output this depth information, as an indexed binary file containing the depth for every ray traced through the model, by changing the *nwrite* parameter in the *ray.par* parameter file to one, and re-running the forward calculation and ray tracing programs. The ray turning depths are output by *FAST* as the total depth within the model, and in this study these were then converted to depth below top basement.

### 5.5.3 Results

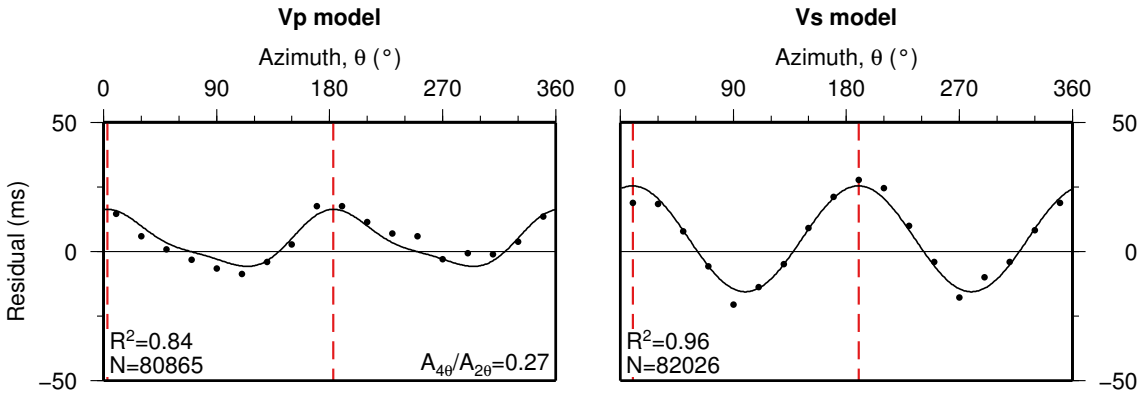


Figure 5.18: Travel time residual (observed–calculated) versus shot-receiver azimuth for the Vp and Vs final velocity models for rays turning in the upper 2.5 km of the basement. Best-fit curves were calculated using Equation 5.5. Mean averages for each 20° bin are plotted (black circles), and standard error bars for each mean are too small to be plotted. The slow direction for each dataset is shown by the red dashed line.

The results for both Vp and Vs models show evidence of azimuthal anisotropy for both entire travel time datasets (Figure 5.18). The Vs dataset exhibits a strong cos2$\theta$ pattern, with a slow direction of 190°, and a $A_{2\theta}$ of 20 ms. The Vp dataset exhibits a combined cos2$\theta$ and cos4$\theta$ pattern, with a slow direction of 183°, an $A_{2\theta}$ of 10 and an $\frac{A_{4\theta}}{A_{2\theta}}$ of 0.3. This indicates that the upper basement (from 0.0–2.5 km bb) has significant anisotropy caused by aligned fractures, with a greater influence on the S-wave velocity than the P-wave velocity. The average slow direction, which is normal to the fracture alignment, is 187°. This results in an alignment direction of 097°, very similar to the current CRR ridge-alignment of ∼090°, thus the fractures are 'ridge-parallel'. The $\frac{A_{4\theta}}{A_{2\theta}}$ of 0.3 of the Vp dataset indicates that open fractures dominate the overall crack population.

The residual datasets were then split into 0.5 km depth intervals based on ray turning depth (Figure 5.19). Most depths do demonstrate an anisotropic pattern, although the fit to the data varies from $0.22 \leq R^2 \leq 0.93$. Despite the variation in fit, both the Vp and Vs depth-divided datasets show a relatively consistent slow direction from 0–2.5 km below basement, with the Vp direction varying from 180°–207° (207° results from a poorly-fitting curve), and the Vs from 184°–196°, with an overall average of 190°. This suggests a consistent fracture alignment of 100°, similar to the strike of the CRR, and that this alignment direction does not change with depth. However, both the Vp and Vs datasets show significant variations in the strength of anisotropy with depth and also, for Vp, in $\frac{A_{4\theta}}{A_{2\theta}}$ values.

The top 0.5 km of basement shows a well-fitting anisotropic pattern in the Vp dataset, with a dominance of closed fractures ($\frac{A_{4\theta}}{A_{2\theta}}$=1.3), although a relatively poorly-fitting ($R^2$=0.35) anisotropy pattern in the Vs dataset. From 0.5–1.0 km bb, $\frac{A_{4\theta}}{A_{2\theta}}$ reduces significantly, although the anisotropy pattern is relatively poorly-fitting to the Vp dataset. The Vs dataset shows a slightly stronger and better-fitting anisotropic pattern over this depth interval. These trends may indicate that the upper 0.5 km of basement contains more randomly-oriented fractures, and those that are aligned are predominantly of a low aspect ratio (i.e. closed or thin), and below this depth both alignment and aspect ratio increase. However, in general the residual misfit ($A_0$) is relatively large from both 0.0–0.5 km bb and 0.5–1.0 km bb, the errors on the bin averages are large, and the number of sample points is small, so these trends should be interpreted with caution.

Between 1.0 and 2.5 km bb both Vp and Vs datasets exhibit stronger cos2$\theta$ patterns with increasing depth, with low $\frac{A_{4\theta}}{A_{2\theta}}$. This indicates a high density of aligned fractures within the basement with generally high aspect ratios (i.e. open or thicker cracks).

The residual datasets were then split spatially: firstly into east and west halves of the model (along X=30 km), and secondly into north and south halves (along Y=30 km) (Figure 5.20). Similar to the depth-divided datasets, the slow direction of all the anisotropy patterns is relatively consistent, varying from 182°-186° in Vp and 188°-191° in Vs, with an overall average of 186°. Anisotropic patterns in the western half of the model space indicate aligned, open fractures, with high $A_{2\theta}$ values, although the trends are generally poorly-fitting. Conversely in the eastern half, the anisotropic trends fit the data very well,

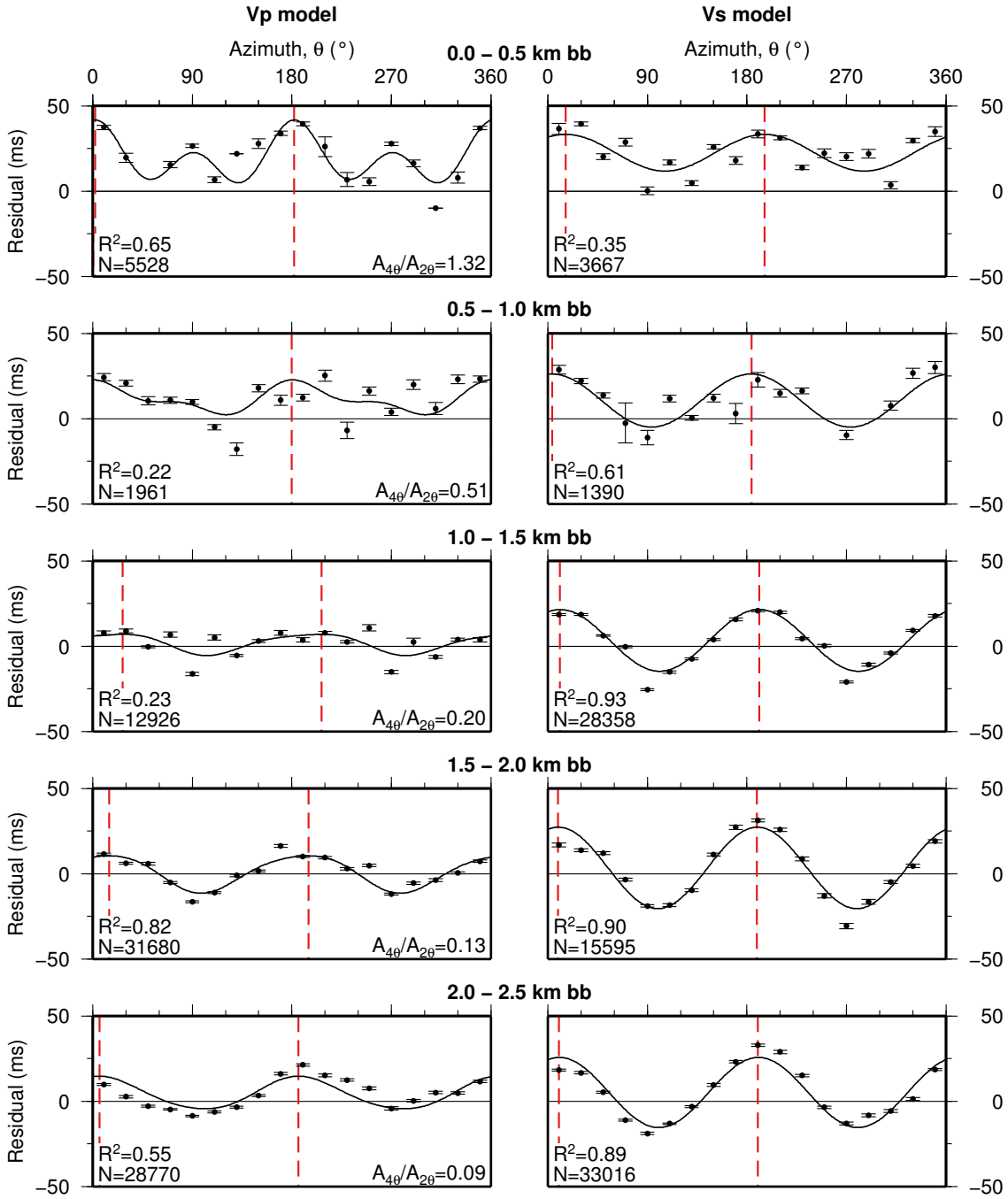


Figure 5.19: Travel time residuals for the final Vp and Vs models plotted against azimuth, divided into 0.5 km depth intervals based on the ray turning depth below basement (km bb). The mean average for each 20° bin is plotted with error bars representing the standard error in the mean. The slow direction for each data sub-set is shown by the red dashed line.

also indicating aligned, predominantly open fractures, although with a weaker strength of anisotropy (lower $A_{2\theta}$). This could indicate, perhaps, a higher fracture density in the west, causing higher amplitudes of anisotropy, but a more consistent alignment of fractures in the east, resulting in less scatter about the general trend. Splitting the data spatially into north and south areas shows a slightly more significant difference in the Vp anisotropy pattern. The northern portion of the model space exhibits trends in both Vp and Vs, with a higher $\frac{A_{4\theta}}{A_{2\theta}}$ of 0.9 suggesting a population of aligned, both thin and thick, fractures, although the Vp fit is not excellent. In the south the Vs trend remains similar, although with a slightly higher amplitude, however the $\frac{A_{4\theta}}{A_{2\theta}}$ value in the Vp trend reduces significantly to 0.1. This could indicate a change to more open fractures in the south.

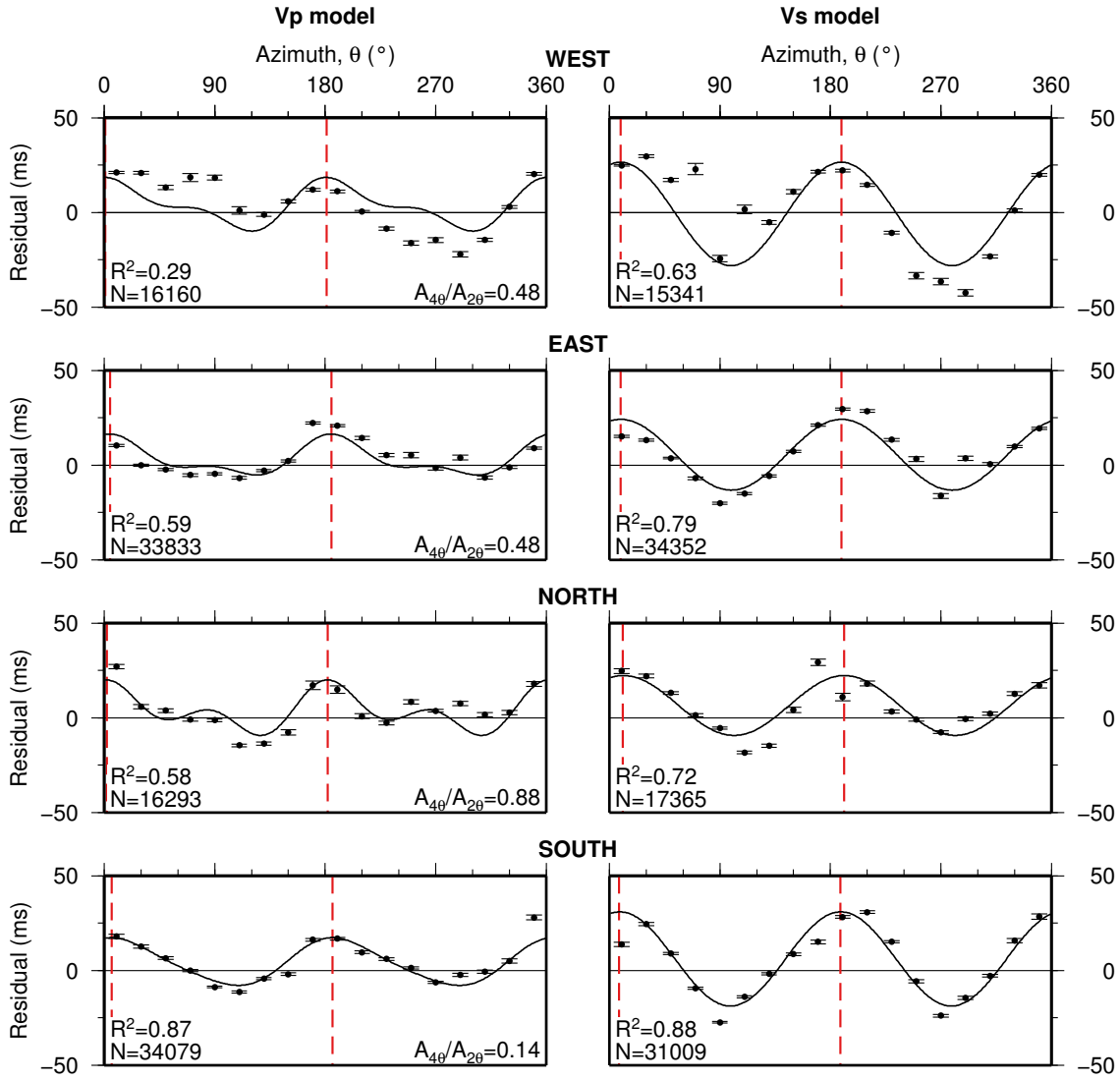


Figure 5.20: Travel time residuals for the final Vp and Vs models plotted against azimuth, divided into west and east halves, along Y=30 km; and north and south halves, along X=30 km. Black circles are the mean average for each 20° bin, error bars represent the standard error in the mean, the slow direction is indicated by the red dashed line.

## 5.6 Summary

In this chapter, different methods and results have been presented which aim to ascertain fracturing patterns within the oceanic crust, and any variations in these across the study area and with depth in the basement. The methods used comprised: 3D S-wave velocity inversion modelling; the calculation of a 3D Poisson's ratio model; and azimuthal anisotropy analysis using travel time residuals.

The final preferred 3D Vs model was produced following the same procedure as the 3D Vp model, and resolves the upper 2.5 km of the basement with a lateral resolution of 3 km. The model is smoother and more laterally homogeneous than the Vp model presented in Chapter 3. Velocity anomalies are a maximum of 0.2 km $s^{-1}$, with the most variation in the upper 1.2 km of the basement, and are generally elongated in the E–W direction, showing similar patterns to the basement topography.

The 3D Poisson's ratio ($\sigma$) model, calculated from the final Vp and Vs models, also does not show particularly large variation in general, with values ranging from 0.22–0.28. However, there are trends visible in the model. The lowest $\sigma$ occurs between 0.5-1.0 km in the basement, with higher values at the top of the basement, and the highest $\sigma$ occurring with little variation below 1.2 km bb. The generally low values throughout the basmenet, compared to values >0.4 found in younger oceanic crust (e.g. Collier and Singh, 1998), could indicate that a general lack of thinner fractures (and predominance of thicker cracks) is characteristic of this area. The areas of lower $\sigma$ in the mid-crust (0.5-1.0 km bb) suggest anomalous regions potentially containing higher densities of more open, wider fractures. The most prominent $\sigma$ anomalies occur in the upper $\sim$1 km of the basement, with positive and negative variations extending E–W across the study area in a similar pattern to the S-wave velocity anomalies and the basement topography, suggesting more variation in fracturing occurs within the upper basement than the lower basement.

Azimuthal anisotropy is shown to be prevalent across the entire study area, and suggests a population of aligned fractures trending at 097°, parallel to the current spreading axis of the CRR, with a range of aspect ratios. There is some variation in the anisotropy patterns with depth in the basement, with less defined anisotropy in the upper 0.5 km suggesting a relative lack of aligned fractures, and well-defined anisotropy caused by predominantly open fractures from 0.5–2.5 km bb. Although some of these trends do not have particularly good fits to the data, or are derived from small sample sizes, they are consistent with the $\sigma$ results which suggest a predominance of more open, wider fractures throughout the basement. Spatial variations in azimuthal anisotropy potentially suggest a higher density of fractures, although less consistent alignment, in the west than the east of the study area, as well as a predominance of thinner, closed fractures in the north compared to open fractures in the south, but these differences are not particularly significant.

The results presented in this chapter will be further discussed and synthesised with each other, and the 3D Vp model results, in Chapters 6 and 7.

# Chapter 6

# Layer 2 structure

## 6.1 Introduction

The P-wave seismic structure of the upper igneous crust (layer 2) is commonly used to infer its geological characteristics and the dynamics of processes such as crustal emplacement, hydrothermal alteration and fracturing (e.g. Houtz and Ewing, 1976; Hooft et al., 1996; Van Avendonk et al., 2017). To interpret the seismic models presented in Chapters 3 and 5, it is first necessary to understand which factors influence the seismic velocity structure of the crust. Layer 2 is commonly interpreted as the basaltic layer with its subdivisions, layers 2A and 2B, are traditionally associated with the more porous extrusive pillow lavas and lava flows, and the less porous sheeted dykes, respectively (Houtz and Ewing, 1976; Herron, 1982; Christeson et al., 1992). Some studies, however, interpret the boundary between layers 2A and 2B primarily as a porosity front (e.g. Carlson, 2011), controlled by either the position of a hydrothermal alteration front within the crust (Anderson et al., 1982; Christeson et al., 2007), or fracturing patterns superimposed onto lithological structure (Carlson, 2010). In addition, for predominantly older oceanic crust off-axis, early seismic observations suggested that layer 2 was instead partitioned into three layers, termed 2A, 2B and 2C (e.g. Houtz and Ewing, 1976). In this definition, layers 2A and 2B are associated with less or more hydrothermally altered extrusive lavas, and layer 2C represents the intrusive sheeted dykes. The ambiguity in this interpretation, and the introduction of layer 2C off axis, is a direct consequence of basing layer nomenclature on the absolute seismic velocity, rather than, for example, velocity contrast.

In this chapter, an alternative definition, based on the change in velocity or velocity-depth gradient, is proposed and applied to each seismic velocity model (Section 6.2). This approach is then compared with a frequently applied method of stacking the layer 2A caustic in MCS gathers, to better understand what, lithologically, this technique images (Section 6.3). Both methodologies are applied to the seismic models and the results compared to the geological structure and physical properties observed in borehole 504B (Section 6.4) to understand what each seismic layer represents in this specific locality in

terms of lithology and alteration. This comparison is made with a view of developing a more generally applicable approach for interpreting the structure of oceanic crust.

## 6.2 Velocity-depth gradient

The inconsistency between dividing layer 2 into either two or three subsidiary layers, together with the observed increase in the seismic velocity of the upper crust with age (Houtz and Ewing, 1976; Nedimović et al., 2008), results in difficulties when trying to reconcile the ageing of oceanic crust from ridge (2A, 2B) to mature (2A, 2B, 2C). For example, immature sheeted dykes at the ridge axis have a seismic velocity comparable to that of older extrusive basalts that have been hydrothermally altered, and where precipitates have infilled the associated porosity. The result is that the same layer term (2B) is applied to two different lithologies, since on-axis layer 2B likely comprises sheeted dykes while, off-axis, it likely comprises altered extrusive pillow lavas and flows under the 2A/2B/2C approach. Thus defining layers using their absolute velocities can introduce inconsistencies in nomenclature from ridge axis to ridge flank and hinder studies of how the crust is modified as it spreads off axis.

Irrespective of the age and spreading rate, however, a relatively high seismic velocity gradient region is widely observed in the upper 2 km of the crust (Christeson et al., 1992, 2012). This region separates an upper low gradient section from a moderate gradient section, and is often interpreted as the layer 2A/2B transition (Harding et al., 1993; Grevemeyer et al., 1998). This transition zone is commonly located within layer 2A, and has been referred to as the high gradient region within layer 2A in some studies (Christeson et al., 1994). Therefore, calculation of the velocity-depth gradient may act as a better proxy for seismic layer definition.

### 6.2.1 Method

The velocity-depth gradient of the 3D inversion models is calculated throughout the study area. The 1D velocity profile at each surface node is extracted, and the gradient at each point in depth calculated as the rate of change between that point and the point below. The model node interval, or depth spacing between points, is 0.1 km. The 1D gradient profiles are then merged to form a 3D volume, to enable lateral variations in vertical gradient to be investigated. The 1D gradient-depth profile at the position of borehole 504B is extracted separately for comparison to geological groundtruth provided by the borehole logs. The average velocity-gradient structure at borehole 504B is also calculated from the 2D forward models that intersect the borehole, to enable a comparison of modelling approaches.

### 6.2.2 Results: 1D

The Vp and Vs 1D velocity-depth profiles at the position of 504B, extracted from the 3D inversion models, show similar patterns to one another (Figure 6.1). Vp increases from

4.2 km $s^{-1}$ at the top of the igneous crust to 4.7 km $s^{-1}$ at 0.5 km bb. A more rapid increase to 5.5 km $s^{-1}$ occurs over the subsequent 0.3 km, followed by a more gradual increase to reach a velocity of 6.6 km $s^{-1}$ by 2.0 km bb. The Vs profile shows a similar pattern, increasing from 2.3 km $s^{-1}$ to 2.7 km $s^{-1}$ from the top basement to 0.5 km bb, before a more rapid increase is observed between 0.5-0.8 km bb to 3.2 km $s^{-1}$. Poisson's ratio ($\sigma$) shows little variation, with slightly lower values of ~0.25 within the upper 0.8–1.0 km of basement, compared to up to ~0.27 from 1.0–2.0 km bb. The Vp structure from the 2D forward models is slightly faster overall than the inversion model profile, and exhibits three distinct layers, separated by a first-order discontinuity of 0.2 km $s^{-1}$ at 0.6 km bb and a change in gradient at 1.7 km bb.

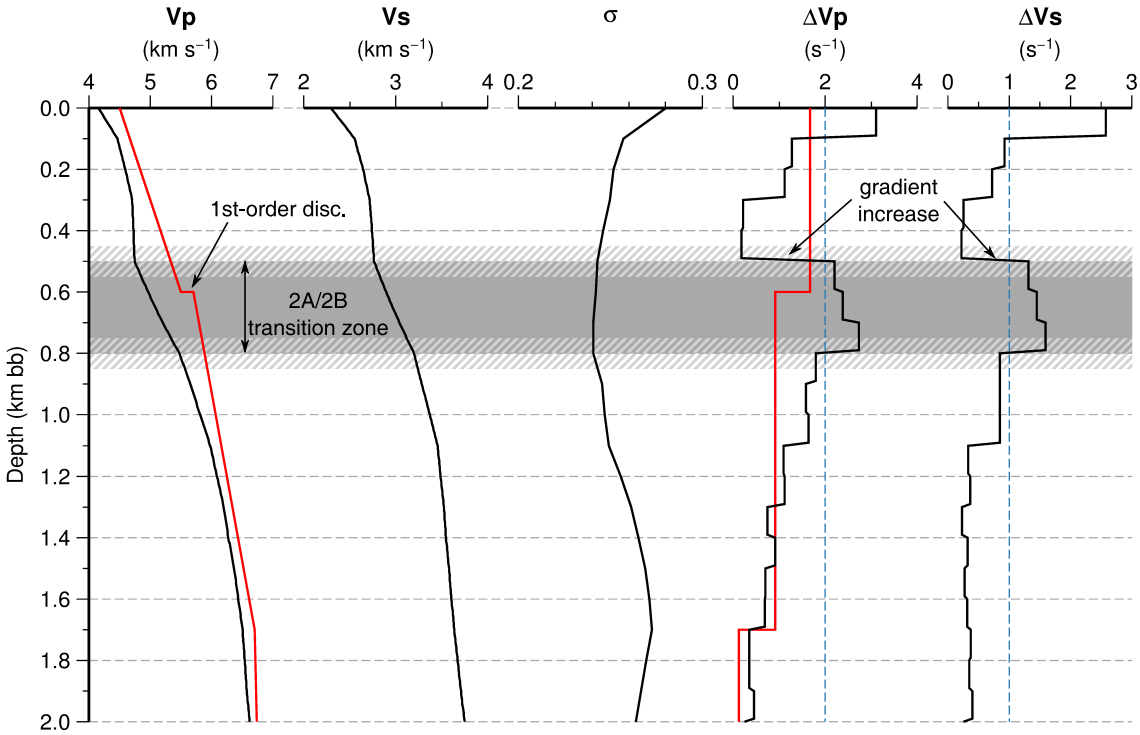


Figure 6.1: Velocity-depth profiles extracted from the 3D Vs and Vp inversion models at the position of 504B (black lines), $\sigma$, and the gradient-depth profiles (ΔVp and ΔVs). The high gradient region, interpreted as the layer 2A/2B transition zone, is shown by the dark grey band, with the light grey stripes showing the errors (0.1 km) in depth due to the cell size within the inversion models. The blue dashed lines represent the threshold gradient values for the 2A/2B boundary. Also shown are the Vp and ΔVp profiles for the average 504B profile from 2D forward models (red) that intersect.

The Vp-depth gradient profile (ΔVp in Figure 6.1) shows moderate (<1.5 $s^{-1}$) and low (<0.5 $s^{-1}$) gradients in the upper 0.5 km, before a sharp increase at 0.5 km bb to match the rapid velocity increase observed in the Vp profile. The high gradient, >2 $s^{-1}$, is sustained for 0.3 km before a drop in gradient to values <2 $s^{-1}$. Below this depth, the gradient steadily decreases to reach values <0.5 $s^{-1}$ at 1.7 km bb. The Vs-depth gradient profile shows a similar trend, with a large gradient increase at 0.5 km bb to >1.0 $s^{-1}$ before a decrease in gradient to <1.0 $s^{-1}$ at 0.8 km bb. The velocity-depth gradient

profiles delineate the region of rapid velocity increase from 0.5-0.8 km bb. This region is interpreted as the layer 2A/2B transition zone, characterised by Vp gradients of >2.0 $s^{-1}$ and Vs gradients of >1.0 $s^{-1}$. As the transition zone in usually included in the thickness of layer 2A (Christeson et al., 1994), this gives a total 2A thickness of 0.8 km. The simpler 2D forward model ΔVp, together with its Vp profile, suggests that the 2A/2B transition in discretised forward models is represented by a first-order discontinuity, which separates two layers with different gradients. The absence of any further significant changes in the inversion model Vp gradient below the base of the 2A/2B transition zone provides no basis to introduce a layer '2C' and, thus, layer 2 is defined here with only two subsidiary layers. The position of the bottom of layer 2 is discussed in Chapter 7.

### 6.2.3 Results: 3D

The ΔVp and ΔVs 3D models are laterally smooth and homogeneous in both N–S and E–W directions (Figure 6.2), similar to the velocity models presented in Sections 3.3.12 and 5.3.5. The edges of these models are affected by inversion edge effects, and thus the changes in structure within ∼5 km of the lateral edges are artefacts. The ΔVp model exhibits the same gradient pattern as the 1D profile through 504B, with high gradient values (1–2 $s^{-1}$) in the initial 0.1-0.2 km bb, before ∼0.3 km of low gradient (<1 $s^{-1}$). This is followed by a 0.3 km-thick region of high gradient (>2 $s^{-1}$) extending laterally at the same depth across the model in both N–S and E–W directions. The continuity of this high-gradient region representing the layer 2A/2B transition, suggests that any variations in its depth across the study area are less than the vertical cell size of the 3D inversion models (0.1 km). There is some minor variability in ΔVp within the upper portion of layer 2A, with slightly higher gradients (>2 $s^{-1}$) at the top of the crust close to the two basement ridges at Y=37 km and Y=32 km. Low gradients (<0.5 $s^{-1}$) are reached consistently across the model at ∼5.3 km depth below the sea surface, approximately 1.6 km bb.

The ΔVs 3D model also exhibits a similar structure to the 1D profile through 504B, with moderate gradients of >1 $s^{-1}$ near the top of the crust and in a ∼0.3 km-thick region from ∼4.2–4.5 km below sea surface (∼0.5–0.8 km bb). Low gradients (<0.5 $s^{-1}$) are observed in the remainder of the upper 2 km of igneous crust. There is less variability in gradient within layer 2A in the ΔVs model than the ΔVp model.

These results indicate that, apart from some small variability in the upper part of layer 2A, the structure of layer 2 is remarkably consistent across the study area, comprising a ∼0.8 km-thick layer 2A, containing a 0.3 km-thick high gradient region at its base which forms the layer 2A/2B transition. Layer 2B, with lower gradients, extends below this. The position of the bottom of layer 2B, the layer 2/3 interface, is discussed in Chapter 7.

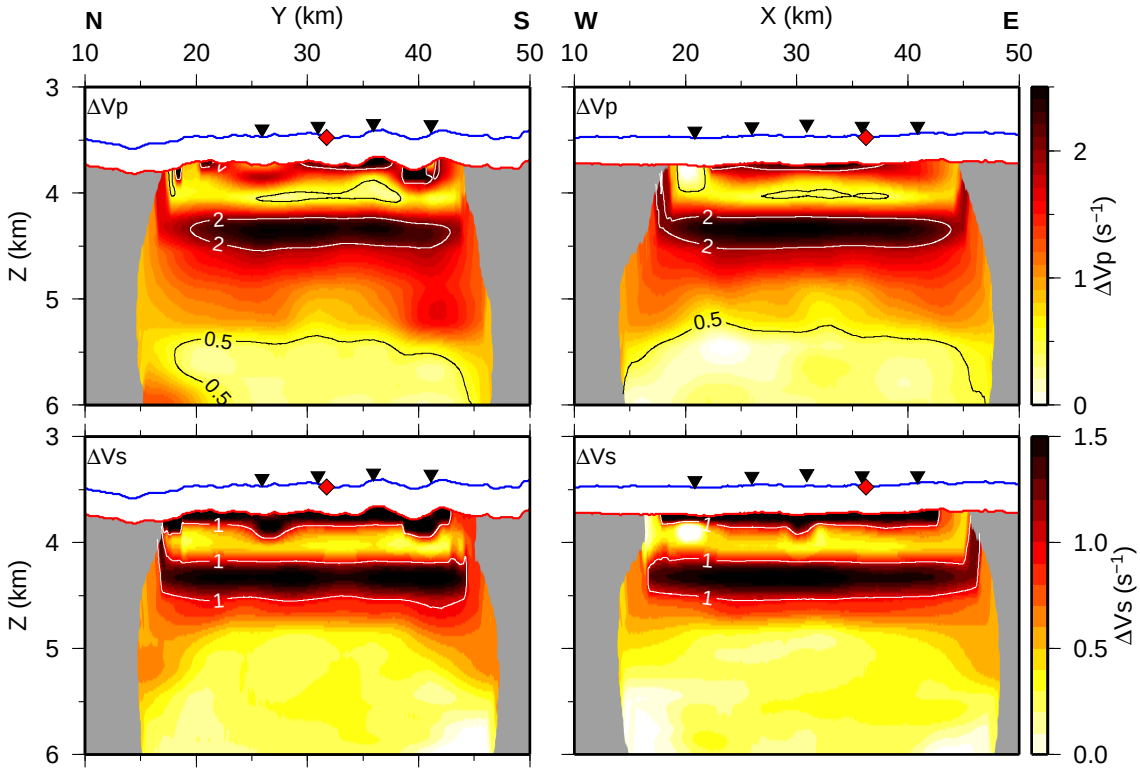


Figure 6.2: Cross-sections from the 3D gradient models, in N–S and E–W directions through the position of 504B (red diamond). OBS positions along profiles proximal to the cross-sections are shown by black triangles, and the seabed and basement interfaces are shown in red and blue, respectively. Contours mark specific high and low gradients discussed in the text. The ∼5 km closest to the edges of each cross section contain artefacts due to edge effects during inversion.

## 6.3 The 2A caustic

The structure of oceanic crust is commonly investigated using wide-angle refraction data and either forward or inverse modelling because the gradational lithological and porosity changes do not produce seismic reflections visible in MCS data, such that the crustal structure cannot be imaged in conventional MCS stacks. However, regions of high velocity gradient can focus incident, turning energy to form caustics, which may be recorded by MCS surveys. Such an arrival, termed the layer 2A caustic, has been observed in MCS studies and used to investigate the layer 2A/2B transition (Harding et al., 1993; Christeson et al., 2010). The arrival is commonly treated as a reflection, flattened and stacked into MCS images, and interpreted as representing the position of the layer 2A/2B boundary (e.g. Van Ark et al., 2007; Nedimović et al., 2008). However, as the 2A caustic is not a true hyperbolic reflection event, this approach should be treated with caution and the images interpreted accordingly.

To complement the velocity-gradient analysis of the structure of layer 2, this alternative method is applied to the South Grid dataset to provide an additional constraint on the characteristics of the layer 2A/2B transition. Due to the long shot-receiver offsets required to record the caustic arrival in the study area given the water depth, data from shot profile

SAP_B, acquired using the synthetic aperature profiling technique to increase shot-receiver offsets (Section 2.4), are used to analyse the 2A caustic here. The southern end of profile SAP_B samples the South Grid area, and is coincident with SG shot profile SG_I (Figure 2.1).

### 6.3.1 Identification

The 2A caustic is observed as a high amplitude arrival in CMP gathers at the near-offsest end of the layer 2B refraction branch and is formed by the focussing of energy turning at the base of the high gradient 2A/2B transition zone (Harding et al., 1993). If the 2A/2B transition was a sharp interface, the arrival would represent the critical range of the reflection from the boundary. The caustic arrival is flattened and stacked to appear as a "horizon" in MCS images. This requires a dataset specific processing sequence, which can vary from developing a stacking velocity model to flatten both the caustic and regular reflection events, to stacking the caustic separately, and 'pasting' it onto a conventionally-processed image as a final step (e.g. Nedimović et al., 2008). To identify the time-offset range to expect the 2A caustic arrival in the long-offset SAP MCS CMP gathers, both 2D synthetic ray tracing and finite-difference modelling are applied to a model representing layer 2 at borehole 504B.

#### 2D ray tracing

A layered 1D velocity model was constructed from the 1D velocity profile extracted at the position of 504B from the smoothed inversion model. For ray tracing program with *rayinvr* (Zelt and Smith, 1992), the smoothed model was discretised into a series of constant gradient layers (Figure 6.3) consisting, in the upper crust, of separate layers for layer 2A, the 2A/2B transition, and layer 2B. Rays were then traced through the 1D model from a seismic source positioned at 10 m depth in the water column, to a series of receivers across the model at 10 m depth in the water column to simulate a long-offset MCS survey (Figure 6.3). The results show a focussing of rays turning within the high gradient 2A/2B transition at offsets of 5.5–6.0 km, forming a triplication between the 2A refraction, the 2A/2B gradient zone, and the 2B refraction travel-time branches, called a caustic. This caustic appears on the synthetic CMP gather as a ∼0.3 km-wide arrival just outside the seabed reflection, at the point of convergence between the layer 2A and 2B refractions, and the theoretical pre-critical reflection from the base of the transition (Figure 6.4).

#### Finite difference modelling

Ray tracing provides an estimate of the offset-time window in which to expect the 2A caustic, but it does not effectively predict the different amplitudes of arrivals. To model synthetic waveforms and amplitudes, and investigate the expected relative amplitude of the 2A caustic arrival, synthetic finite difference elastic waveform modelling was undertaken using *sofi2D* (Bohlen et al., 2016).

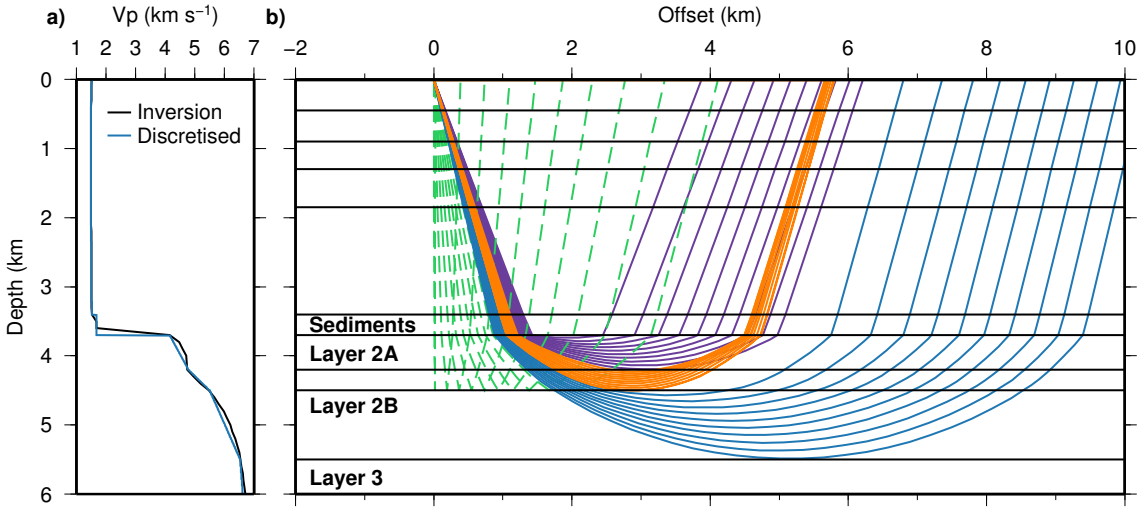


Figure 6.3: Ray trace modelling of the 2A caustic. a) The 1D P-wave velocity profile extracted from the inversion model at 504B and its discretised version used as input to *rayinvr*. b) Ray tracing through the velocity model from a shot at 0 km offset, showing refractions through layer 2A (purple), layer 2B (blue) and hypothetical reflections from the base of the 2A/2B transition (green dashed). Refractions from the 2A/2B transition zone (orange) focus as a caustic at a narrow offset range.

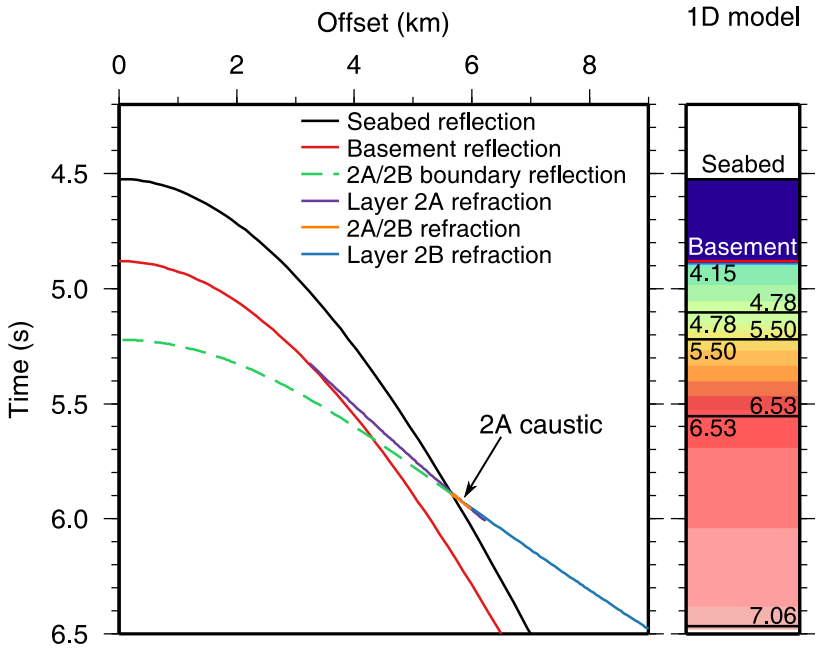


Figure 6.4: Synthetic CMP gather from calculating ray tracing through the 1D velocity model (numbers represent top and bottom P-wave velocities for each layer in km $s^{-1}$). The gather shows the narrow arrival region of the 2A caustic (orange), just outside the seabed reflection (black) and at the confluence between the 2A (purple) and 2B (blue) refractions, and hypothetical base 2A/2B boundary reflection (green dashed).

The same 1D velocity profile from the inversion model was used to create a laterally homogeneous 2D velocity grid with a node spacing of 10 m. Arrivals were then propagated through the velocity model from a seismic source to an array of receivers, to simulate the long-offset MCS experiment. The resulting CMP gather (Figure 6.5) shows the variable

amplitudes of the arrivals, with the highest amplitude energy arriving as the seabed reflection, the basement reflection, and the layer 2B refraction. Overlying the synthetic traced rays shows that the caustic arrival sits in a region of high amplitude at the onset of the 2B refraction which extends over a offset range of ∼1.5 km. The larger offset range of this region of high amplitudes, compared to the offset range of the ray traced caustic arrival, suggests that the width of the caustic may be highly sensitive to the velocity structure of the crust, which is slightly different between the 2D grid used for the finite difference modelling, and the discretised model used for ray tracing.

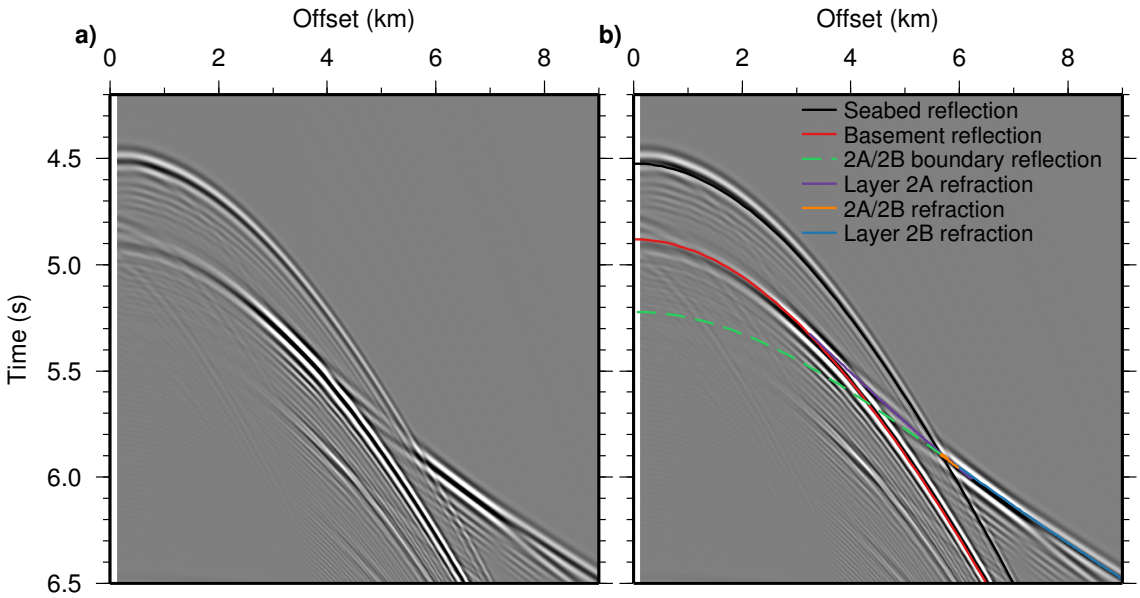


Figure 6.5: Finite difference modelling. a) Synthetic CMP gather calculated from a 1D velocity model using *sofi2D*, overlain in b) by the ray traced arrivals shown in Figure 6.4. The main regions of higher amplitude are within the basement reflection from ∼3–6 km offset, and at the onset of the 2B refraction, where it diverges from the 2A refraction and also meets the seabed reflection and hypothetical 2A/2B transition base reflection (which is not generated by the finite difference modelling).

### MCS gathers

Merged CMP gathers (Section 2.4) from shot profile SAP_B (Figure 6.6), where it intersects the SG area, were analysed to locate the 2A caustic arrival. Consistently across the profile there is a high amplitude arrival seen at the onset of the crustal refraction, which is identified as the 2A caustic (e.g. Figure 6.7). The caustic arrival is highly variable across the profile, appearing at offsets ranging between 4.5–6.5 km, both inside and outside the seabed reflection (Figure 6.7). Its amplitude varies from similar to the basement reflection (e.g. CMP 10998), to significantly larger than any other observed arrivals (e.g. CMP 10960). The arrivals in CMP 10986 also display a later region of high amplitude within the 2B refraction branch, which may indicate a secondary, deeper, zone of high gradient at this location. This variability could indicate that the depth or characteristics of the 2A/2B transition (i.e. its thickness, top or bottom velocity, or gradient) change along

profile. Also, it is likely that the basement and seabed topography influence the position and amplitude of the arrival, either focussing or dispersing it depending on the geometry.

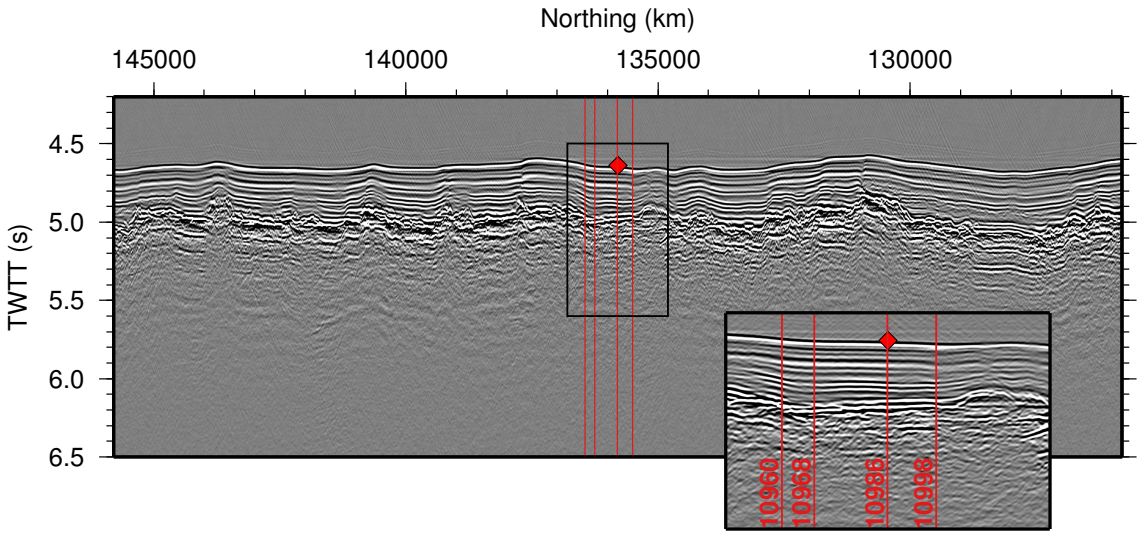


Figure 6.6: A 'conventional' stack of shot profile SG_I (coincident with SAP_B), showing a 20 km section centred on borehole 504B (red diamond). 504B is laterally offset by 304 m (to the east) from the shot profile. No arrivals are seen below the top basement horizon. Red lines represent the positions of SAP_B CMPs plotted in Figure 6.7, with their CMP number shown in the zoomed inset.

### 6.3.2 Processing methods

To stack the 2A caustic arrival into MCS images of profile SAP_B, a tailored processing sequence was developed. The key step in achieving a stack containing both the conventional reflection horizons and the 2A caustic horizon is building the stacking velocity model. Velocities of ~1.5 km $s^{-1}$ are required to flatten the seabed, intra-sediment, and basement reflections using an NMO correction. However, a faster velocity (>2.0 km $s^{-1}$) is necessary to flatten the 2A caustic. To ensure that the position of the 2A caustic horizon on the stacked section is consistent with the premise underpinning MCS images (that the TWTT of a visible horizon can be related to the depth of the interface), the caustic was flattened at the same velocity that also flattens the theoretical reflection from the bottom of the 2A/2B transition zone. This velocity, ~2.2 km $s^{-1}$ (Figure 6.8), varies along the profile. Thus, the TWTT of the caustic on the stacked section is a proxy for the base of the transition zone and the top of layer 2B.

The SAP_B shot profile was formed of composite gathers derived from both Bolt and G-gun sources (Section 2.4), which must be separated, have the correct geometry applied, and re-merged to form the composite gathers. The processing sequence consisted of:

1. **separate data -** the Bolt and G-gun arrivals were separated, and bulk shifts of 6 s and 30 s applied, respectively, to correct the shot time to t=0 s;

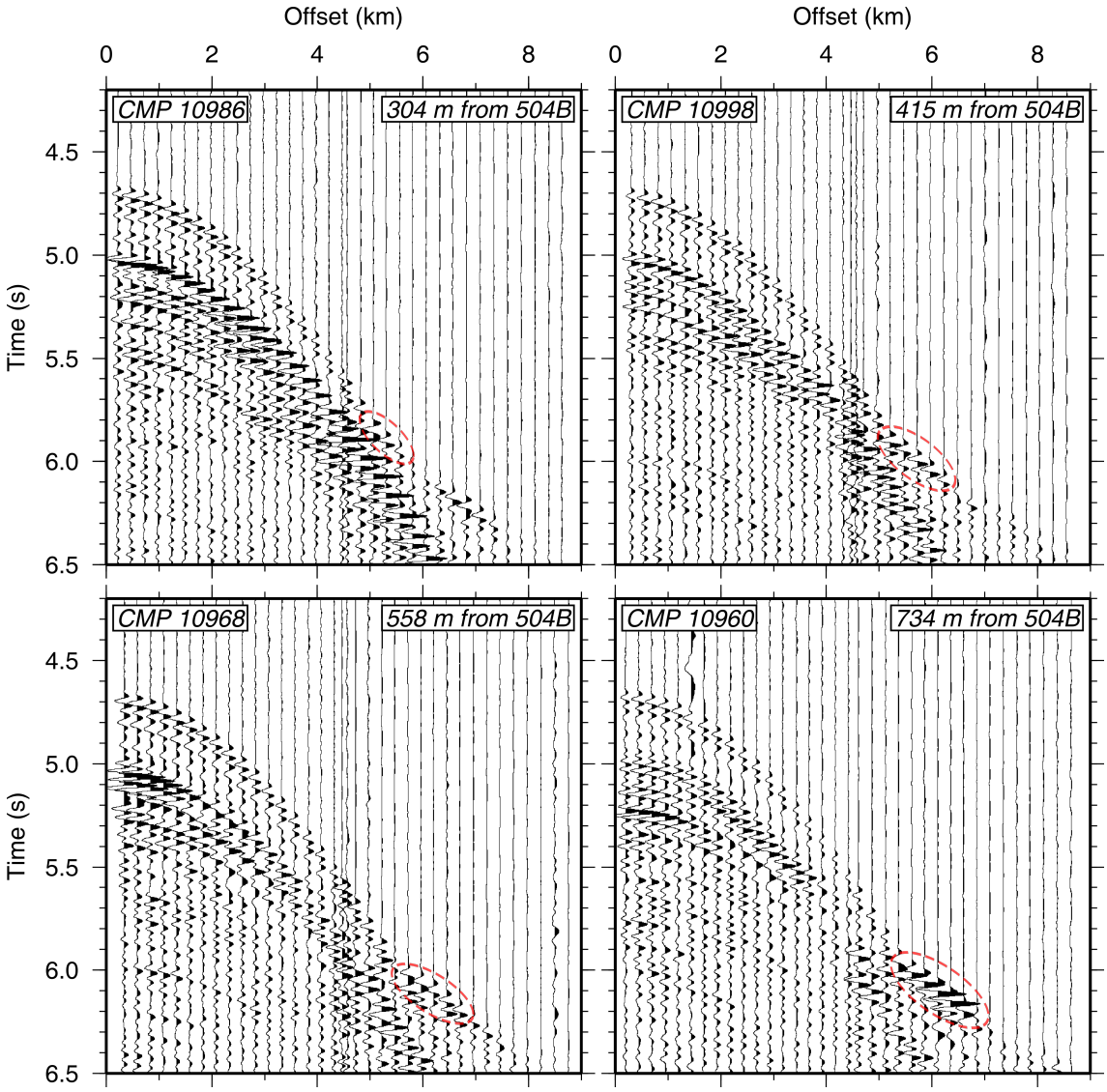


Figure 6.7: Example CMP gathers proximal to borehole 504B (locations shown in Figure 6.6), plotted with a minimum-phase bandpass filter of 2/4/24/32 Hz. The 2A caustic is visible on each gather (shown within red dashed ellipses) although varies in its offset extent and amplitude along profile.

2. **input geometry -** a linear CMP geometry was calculated and written into the headers prior to sorting to CMP gathers of 25 m bin spacing to give a maximum fold of 137;

3. **deconvolution -** Bolt and G-gun arrivals were deconvolved separately using filters derived from their respective source wavelets recorded at the vertical hydrophone array, to a common zero-phase wavelet with frequency characteristics of 2/4/16/24 Hz;

4. **CMP sort and merge -** the traces in each file were sorted into CMP gathers for each source type, prior to merging to form full-offset CMP gathers;

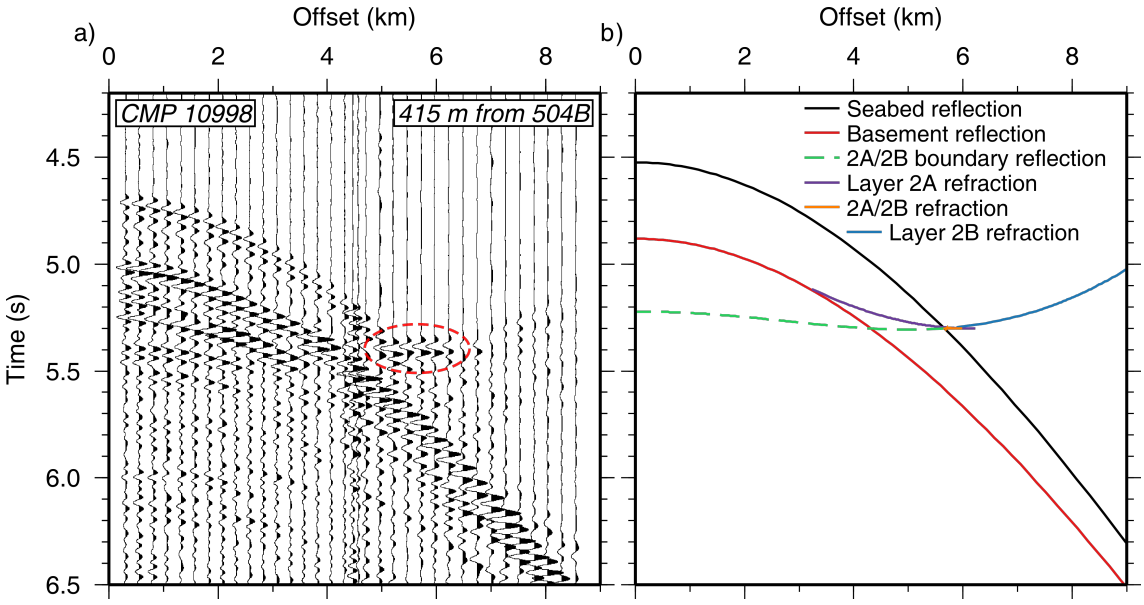


Figure 6.8: Flattened 2A caustic. a) CMP gather 10998 with an NMO correction applied at 2.2 km $s^{-1}$, flattening the caustic (within red dashed ellipse). b) Synthetic rays traced through the 1D velocity model (Figure 6.4) with the same NMO correction applied, causing the caustic arrival to stack at the same TWTT as the hypothetical reflection from the base of the 2A/2B transition zone (green dashed line).

5. **filter -** the data were filtered with a zero-phase bandpass filter of 2/4/16/24 Hz, to remove both low and high frequency noise, and to enhance 2A caustic arrival which has a dominant frequency range <16 Hz;

6. **trace sum -** due to the geometry of the acquisition and the chosen bin size, the CMP gathers consist of a series of groups of approximately four traces with similar offsets (with a difference of 12.5 m between each trace), separated from each other by ∼300 m. To regularise the trace spacing and also improve the SNR, each group of traces were stacked together, and the new CMP traces re-numbered;

7. **velocity analysis -** stacking velocities were picked every 100 CMPs for the seabed and basement reflections and the 2A caustic, using semblance and common velocity analysis. The resulting stacking velocity model increases from ∼1.5 km $s^{-1}$ to >2.0 km $s^{-1}$ in the region after the basement reflection and before the caustic arrival, to ensure that the stacking velocity for the arrivals was not affected by interpolation;

8. **NMO correction -** an NMO correction was applied to the CMP traces, using the velocity model derived from velocity analysis, to flatten the reflections from the seabed to the basement, and the 2A caustic;

9. **mute -** the effect of the NMO correction on the 2B refraction branch causes it to interfere with the seabed, sediment and basement reflections at offsets $\gtrsim$4 km. An asymmetrical offset-mute removed this part of each CMP gather to reduce this interference;

10. **offset weighting -** trace amplitudes were adjusted using the trace offset as the scaling factor, to increase the relative amplitude of the 2A caustic arrival (incident at greater offsets) relative to reverberations from the basement reflection at near offsets, which would otherwise mask the arrival post-stacking;

11. **stack -** the gathers were stacked into CMP traces;

12. **filter -** a zero-phase bandpass filter was applied at 2/4/16/24 Hz;

13. **trace mix filter -** to suppress artefacts in the stacked section a 15-trace running mix was applied.

The final stacked section (Figure 6.9) shows the stacked 2A caustic, creating a consistent sub-basement horizon arrival ∼0.3 s TWTT after the basement interface observed at ∼5.3 s TWTT.

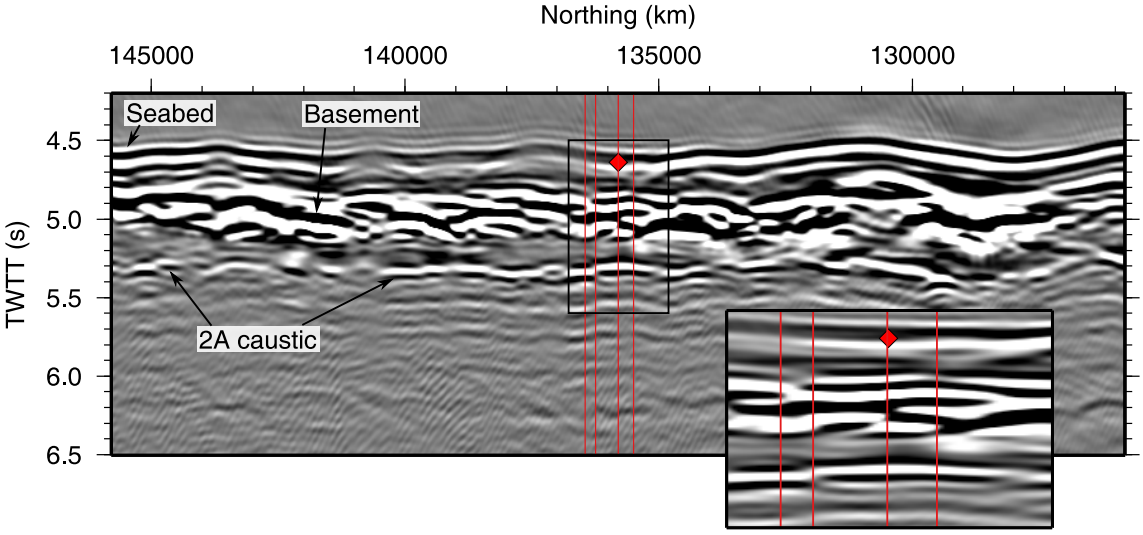


Figure 6.9: The final caustic stack of a 20 km section of SAP_B centred on 504B (red diamond). See Figure 6.6 for the equivalent conventional stack. The seabed and basement horizons are imaged along with the 2A caustic arrival appearing ∼0.3 s TWTT below the basement interface across the entire image. The relatively low resolution of this section results from the high-cut bandpass filters applied to enhance the 2A caustic arrival since that is the primary processing goal. Red lines represent the positions of the CMPs plotted in Figure 6.7. CMP numbers are the same as labelled in Figure 6.6.

### 6.3.3 Depth estimation

The inversion model characterises the 2A/2B transition as a 0.3 km-thick region of high velocity gradient occurring, at borehole 504B, from 0.5–0.8 km below the top basement. Synthetic ray tracing (Section 6.3.1) predicted that this transition zone would produce a caustic arrival within long-offset CMP gathers. The 2A caustic arrival is observed on the CMP gathers in the real data, however, its character and position is not identical to that synthetically calculated. To estimate the depth and other characteristics of the 2A/2B

transition at borehole 504B from the observed position of the 2A caustic, 1D forward modelling was undertaken using *rayinvr*. This modelling was undertaken to produce an independent 1D velocity model that fits the observed caustic arrival in the real CMP gathers, and provides an alternative approach to characterise the nature of the transition, such that it can be compared to the inversion model.

**Travel time picking**

The composite CMP gather used for the forward modelling was CMP 10998 (Figure 6.7), as it is one of the closest CMP gathers to borehole 504B (located 415 m away), and has a prominent caustic arrival. Travel times were picked for the first breaks of the seabed and basement reflections ($P_sP$ and $P_bP$), the 2A caustic arrival ($P_{2A/2B}$) and the 2B refraction ($P_{2B}$). Travel time uncertainties were assigned considering the manual picking error for each arrival ($P_sP$=5 ms; $P_bP$, $P_{2A/2B}$, $P_{2B}$=20 ms), the data sampling interval (2 ms), the peak-to-first-break delay (see Section 3.2.3 - 5 ms), and error in the shot location (5 ms). A further error of 25 ms results from the four-trace summing in terms of trace offset within gathers, as the offset of the new trace is set to be the offset of the first trace in the mix. This creates a maximum offset error of 37.5 m (the offset difference between the first and fourth traces in the sum). Assuming a horizontal travel path and velocity of 1.5 km $s^{-1}$, this gives a maximum travel time error of 25 ms. Assuming the individual errors are independent, a total travel time error of 27 ms for $P_sP$ and 33 ms for $P_bP$, $P_{2A/2B}$ and $P_{2B}$ results.

**Forward modelling**

To produce a final 1D model independently from the inversion model, the starting model was created from the results of 2D forward modelling (Section 3.2.6). The model layers were constructed using the average structure of six 2D forward models, with the seabed and basement depths adjusted to match those at the position of CMP 10998 found from the swath bathymetry and sediment thickness grids (Figure 6.10). In this starting model, the 2A/2B transition is inserted to simulate a discrete interface by creating a layer of negligible thickness (10 m) with the same velocity as the bottom of layer 2A. Ray tracing with *rayinvr* through this model results in low $\chi^2$ fits of $\leq$1.0 of the seabed, basement and 2B arrivals. However, no 2A caustic arrival is modelled. Forward modelling was then undertaken to create a model which produces a 2A caustic arrival with a good fit to the observed arrival. The sediment and water column layers were left fixed during this stage.

**Result**

The final, best-fitting forward model produces a 2A caustic with a $\chi^2$ fit of 0.3 to the observed arrivals, occurring over a similar offset range (Figure 6.10). The $\chi^2$ fit of the 2B refraction branch is also 0.3. The 'overfit' $\chi^2$ values (<1.0) resulted from ensuring that the modelled caustic arrival occurred over a similar offset range to the observed caustic, as

well as fitting the travel time picks. The model consists of a 0.470 km-thick low velocity gradient region, interpreted as the upper part of layer 2A, a 0.3 km-thick high velocity gradient 2A/2B transition zone, and a low velocity gradient layer 2B (the bottom of layer 2B was not constrained during this modelling). Comparing this 1D model to the 1D profile extracted from the inversion model at the position of 504B (Figure 6.10) shows that they are similar in structure. The depth of the top of the 2A/2B transition is slightly shallower (by 31 m), and the top and bottom velocities slightly faster (by 0.12 and 0.2 km $s^{-1}$, respectively), but both of these changes are uncertainty. The thickness (0.3 km) of the 2A/2B transition zone is the same and the velocity gradient (2.7 $s^{-1}$ vs 2.4 $s^{-1}$ in the inversion model) is very similar. Layers 2A and 2B are also remarkably similar between the models. This similarity shows that the depth of the high gradient region causing the 2A caustic observed on the long-offset MCS gathers is the same as the high gradient 2A/2B transition zone in the inversion model. These results also show the sensitivity of the amplitude and width of the 2A caustic arrival. The original synthetic ray tracing, undertaken with a discretised form of the inversion model, predicted a narrow, ∼0.3 km-wide, caustic arrival (Figure 6.4). The synthetic finite difference modelling, undertaken using a gridded form of the inversion model, predicted a ∼1.5 km-wide caustic arrival. The final forward model, which is very similar to the inversion model, produces a ∼0.8 km-wide caustic arrival from ray tracing. This sensitivity most likely explains the variability in the appearance of the caustic between different CMP gathers close to 504B (Figure 6.7), and does not indicate significant changes in the thickness or velocity gradient of the 2A/2B transition. Significant changes in the depth to the top of the transition zone, however, would be expected to change the incident time of the caustic arrival, and thus its location on a stacked image.

### 6.3.4 Results

The identification of the 2A caustic arrival on CMP gathers throughout the SG portion of the SAP_B profile indicates that a high gradient 2A/2B transition zone is consistently present in layer 2 of the crust. The caustic appears as a horizon on the stacked section (Figure 6.9) ∼0.3 s below the basement interface across the entire profile, suggesting that the bottom of the transition (and top of layer) 2B remains at a generally constant depth below the top basement along the profile. Small local variation in the TWTT topography of the horizon indicates that the depth of the transition does vary slightly along the profile.

1D forward modelling used to determine the depth and character of the 2A/2B transition at a CMP gather close to borehole 504B, suggests that the high gradient region causing the 2A caustic begins 0.47 km below the top basement, and is 0.3 km-thick with a velocity gradient of 2.7 $s^{-1}$. This forward model is in agreement, within the uncertainties, with the inversion model at borehole 504B.

In summary, the analysis of the 2A caustic suggests that the arrival is formed by turning rays within a high gradient region in layer 2, that this region, at 504B, is located ∼0.5–

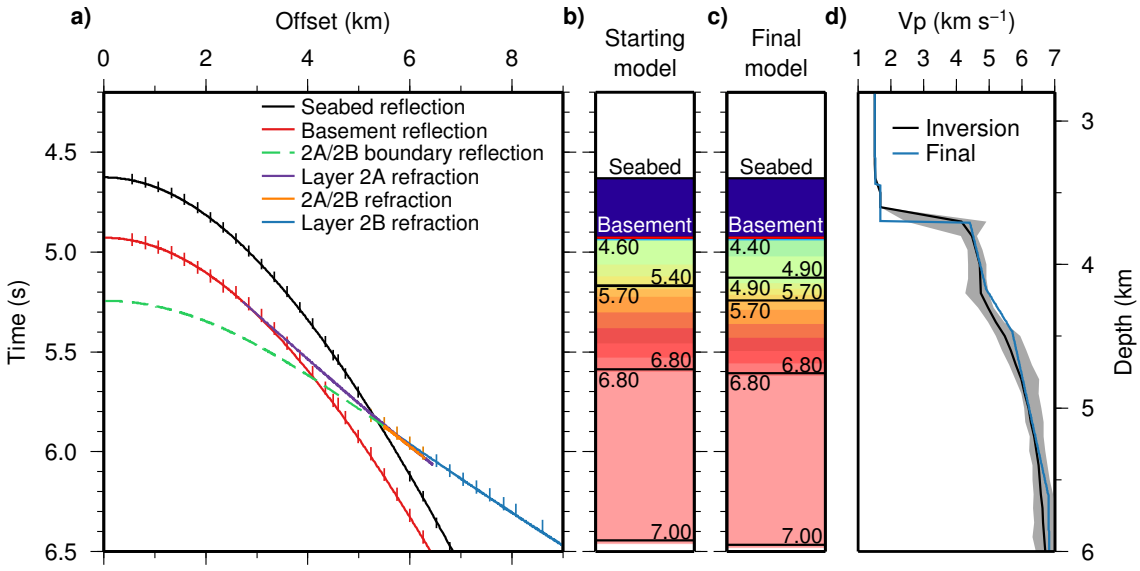


Figure 6.10: Forward modelling of the 2A caustic. a) Results show the close fit between the traced arrivals (solid lines) and the travel time picks (bars, with length of bar equal to pick uncertainty). The main difference between the starting model (b) and the final model (c) is the introduction of the high gradient layer between layer 2A and 2B to generate the caustic arrival. Numbers on the models represent the top and bottom layer velocities. d) The 1D profile through the inversion model at borehole 504B with 95% confidence boundaries (grey shaded area), and the final 1D forward model. To facilitate the comparison of layer 2 structure, depths have been adjusted so that the top basement occurs at the same depth in both models. NB: (d) is plotted against depth whereas (a), (b) and (c) are all plotted against time, so the axes are not comparable.

0.8 m below the top basement, and that its depth, thickness and gradient are generally constant along a N–S profile through the SG. Thus, by inference, also throughout the SG, as the inversion models show the structure to be effectively invariant.

## 6.4 Borehole 504B logs

During the seven stages of drilling borehole 504B, conducted from 1979–1993, suites of downhole logs were acquired, alongside laboratory core sample analyses. In this study, the most recent, and complete, downhole logs and core data are used to analyse the lithology and physical properties for comparison with the seismic results (Figure 6.11). This comparison aims to elucidate the primary controls on the seismic structure of the upper crust, and how best to interpret it in terms of geological structure in all modes of seismic surveying.

### Sonic velocity

Sonic Vp and Vs logs acquired down 504B during the last drilling leg in 1993 (Leg 148) were reprocessed by Guerin et al. (2008). These logs provide measurements every 15 cm from the top of the igneous crust to 1.786 km bb, ∼50 m above the base of the borehole at 1.837 km bb. It was not possible to measure to the very bottom of the borehole due

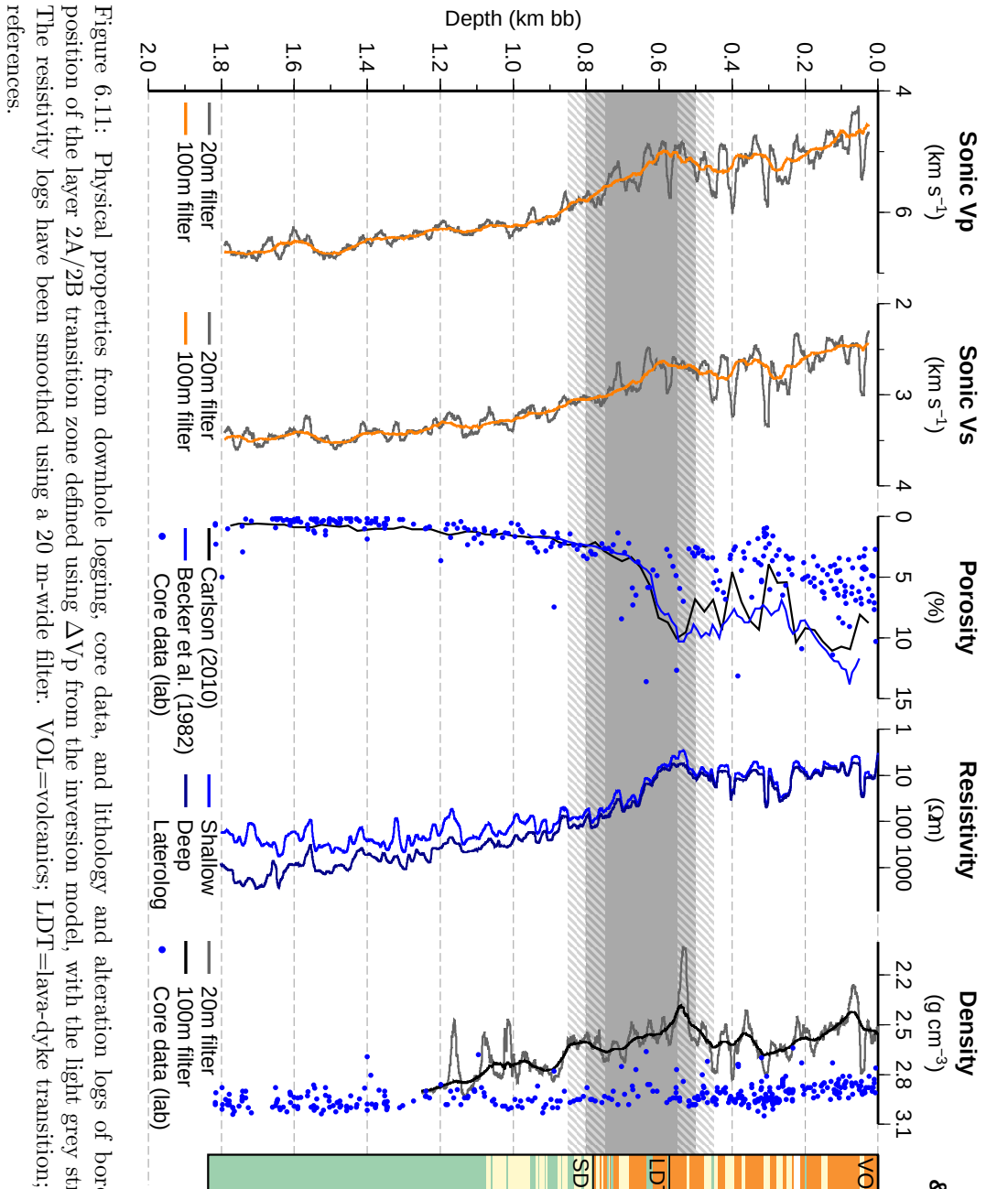


Figure 6.11: Physical properties from downhole logging, core data, and lithology and alteration logs of borehole 504B. The dark grey bar shows the position of the layer 2A/2B transition zone defined using $\Delta$Vp from the inversion model, with the light grey stripes showing the errors (0.1 km) in depth. The resistivity logs have been smoothed using a 20 m-wide filter. VOL=volcanics; LDT=lava-dyke transition; SDC=sheeted dyke complex. See text for references.

to an obstruction at 1.809 km bb and the position of the sonic log tool in the logging tool string (Alt et al., 1993). These measurements were subsequently filtered using a 100 m filter to suppress the large scatter in the values, and to make the logs, with their small sampling interval, more comparable to the seismic velocity models. Smoothed sonic Vp increases gradually from ∼4.5 km $s^{-1}$ at the top of the basement to ∼5.2 km $s^{-1}$ at 0.3 km bb, where it remains relatively constant for a further 0.3 km. This upper 0.6 km is characterised by high, short-period variability in the unsmoothed sonic log, from ∼4.2–6.0 km $s^{-1}$. A decrease in velocity at ∼0.53 km bb is attributed to the inferred presence of a fault within the borehole. From 0.6 km bb, Vp increases more rapidly to reach a velocity of ∼6.0 km $s^{-1}$ by 0.9 km bb. From 0.9–1.5 km bb velocity increases gradually and with much less variability to ∼6.5 km $s^{-1}$. Below 1.5 km $s^{-1}$, sonic Vp is relatively constant. The sonic Vs profile exhibits a similar pattern, although the rapid increase in velocity beginning at 0.6 km bb in sustained over a thinner region of 0.1–0.2 km.

### Porosity

Apparent fractional porosity profiles down the borehole were calculated by Becker et al. (1982) and Carlson (2010) using Archie's law (Archie, 1942) and resistivity logs from Legs 83 and 148, respectively. In both cases, the authors assumed the constant a=1 and the exponent m=2, and calculated the resistivity of the pore fluid by using the temperature-sensitive resistivity of seawater and borehole temperature profiles to give:

$$\phi = [\rho(3 + T/10)]^{-\frac{1}{2}}, \tag{6.1}$$

where $\phi$ is the apparent fractional porosity, $\rho$ is the measured downhole resistivity of the formation, and T is temperature in °C. The porosity of core samples was also measured in shipboard laboratories after coring during all drilling legs (Shipboard Scientific Party, 1988, 1992, 1993; Ocean Drilling Program, 2005). The calculated apparent porosity profiles are very variable in the upper 0.6 km of the igneous crust, with the highest values (7–14%) in the top 0.2 km, and values mostly between 5% and 10% from 0.2–0.6 km bb. Laboratory measurements of porosity from core samples average at ∼5%, but the data exhibit considerable scatter. The discrepancy between the average core porosity and the apparent porosity calculated from the resistivity logs suggests pervasive networks of faults, fractures or void space within the formation which are larger than core samples analysed in the lab. Beginning at 0.5–0.6 km bb the porosity rapidly decreases from ∼8% to <3% at 0.8 km bb, and below this gradually decreases to reach lows of ∼1% at the base of the borehole. Below 0.8 km bb, measured core porosities exhibit very little scatter and are, on average, only slightly lower than the apparent velocity (by ∼1%), indicating a relative lack of large fault and void space in the formation.

### Resistivity

Shallow and deep laterolog measurements were made down the length of the borehole during the last drilling leg (Leg 148) to provide a measure of electrical resistivity. These measurements were filtered with a 100 m filter to compare with the seismic velocity models. Shallow measurements penetrate ∼10 cm from the borehole wall, measuring within the invaded/saturated zone, and give an indication of the resistivity of the drilling fluid, which is seawater in this case. Deep laterolog measurements penetrate 1 to 2 m within the formation and give a measurement of the resistivity of the formation itself, which is dependent on its porosity and the composition of the pore fluid, which in the case of oceanic crust is likely to be similar to seawater. The low resistivities of the upper 0.6 km of the basement and the close match between the shallow and deep measurements indicate that this portion of the crust is highly fractured and of high porosity, containing similar volumes of fluid as the fractured and invaded zone at the borehole wall. The rapid increase in both resistivity logs from 0.6–0.8 km bb suggests a rapid decrease in the amount of pore space. Below ∼0.9 km bb, the shallow and deep resistivity measurements begin to diverge, with the deep measurements becoming progressively greater, indicating a reduction of pore space within the formation with depth, assuming correlation between porosity and permeability.

### Density

Downhole density measurements were made during drilling Leg 111 in 1986 using a Lithodensity Tool. These measurements were filtered with a 100 m filter to suppress data scatter and enable comparison with the seismic velocity models. The density of samples was also measured on recovered core during all drilling legs (Shipboard Scientific Party, 1988, 1992, 1993; Ocean Drilling Program, 2005). The downhole density measured during logging exhibits high variability, from ∼2.0–2.8 g $cm^{-3}$ throughout the measured portion of the borehole. When smoothed with a 100 m-width filter, the downhole density averages at ∼2.5 g $cm^{-3}$ in the upper 0.5 km of the basement, and then begins to increase steadily to reach ∼2.8 g $cm^{-3}$ at 1.2 km bb. Lab measurements of core sample bulk density increase slightly from ∼2.80 g $cm^{-3}$ to ∼2.95 g $cm^{-3}$ at 0.5 km bb, and remain at that density, with little scatter, to the base of the borehole at 1.837 km bb. The higher density measured in the core samples, compared to density from downhole logging, suggests large-scale void space within the crust which is not evident at core sample scale. The gradual reduction in the discrepancy below ∼0.5 bb indicates a downhole reduction of formation void space, and the convergence of downhole and core density at or just below ∼1.2 km bb suggests there is negligible large void space remaining, and any porosity or fractures within the crust are small enough to be observed in core samples.

### Lithology and alteration

Logs of sampled downhole lithology, alteration and features of interest were compiled from reports from all drilling legs (Shipboard Scientific Parties of Leg 68 (Site 501) Leg 69 and Leg 70, 1983; Adamson, 1985; Shipboard Scientific Party, 1985; Alt et al., 1996). Lithology was subsequently grouped into one of five types: massive flows and basalts; sheet flows and fragmented flows; pillow lavas and thin flows; breccias; and dykes to enable comparison to analysis of borehole 1256D in Chapter 7 (e.g. Harris et al., 2015). Units described as massive flows or basalts within the sheeted dyke complex are likely to also be diabase dykes (Adamson, 1985), and breccias are noted within the pillow basalts units in the 504B logging records. The 0.572 km-thick volcanic section at the top of the basement comprises 57% pillow basalts (including 9% of breccia material), 22% massive units, 17.5% thin flows and 3% minor dykes, when analysing recovered core (29.8% in the volcanics) (Alt et al., 1996). However, as core recovery is biased towards massive units, the volcanic section is likely comprised of closer to 70% pillow basalts (including up to 17% breccias), 13% massive units, 13% thin flows and 4% dykes (Alt et al., 1996). The low recovery rate also adds uncertainty to the location of boundaries between different units. The top 0.1 km of basement forms an lateral aquifer which is currently exchanging fluids with bottom seawater through the borehole, and fluid circulation is active in the uppermost ∼0.3 km of the basement which may currently be undergoing alteration and cementation (Alt et al., 1996). This forms a zone in the upper volcanics of low-temperature, oxidising alteration, also containing a zeolite-rich interval from 0.254–0.289 km bb likely caused by a focussing of fluid flow. The lower volcanics are closed to hydrothermal circulation and have experienced, low-temperature alteration under reducing conditions. The presence of a fault at 0.525 km was inferred from a change in the magnetic inclination, which could be caused by tilting of the volcanic section, low values in density, resistivity and sonic logs, high apparent porosity, and evidence for small-scale offsets from slightly deeper rocks (Alt et al., 1993).

At 0.572 km bb dykes become more common (three dykes were sampled within 5 m), and the following 0.209 km represents the lava-dyke transition zone (LDT), with no further pillows recovered below the bottom of the zone. The top of the LDT has experienced similar alteration to the lower volcanic section, however at 0.624 km bb there is an abrupt appearance of hydrothermally altered rocks, which characterise the remainder of the LDT and consist of greenschist facies mineralogy, indicating temperature conditions of <350°C. Between 0.636–0.654 km bb, a mineralised stockwork-like zone occurs in a brecciated and fractured pillow basalt, potentially suggesting fluid pressure fracturing and subsequent mineralisation of the zone.

A sheeted dyke complex extends from 0.780 km bb to the bottom of the current borehole, comprising mostly massive diabase with some chilled margins evident. The upper dykes (from 0.780–1.225 km bb) exhibit similar alteration to the transition zone (with maximum temperatures of 350–380°C), although with variable intensities due to variable

fracturing and permeability within the rocks. Less fractured rocks have experienced only slight alteration, whereas dykes with a higher porosity are highly recrystallised and contain numerous veins. A temperature increase from 1.075–1.225 km bb results in a greater extent of pyroxene alteration and proportion of actinolite (a higher temperature alteration product) compared to plagioclase alteration. The lower dykes (1.225-1.836 km bb) have undergone an earlier, higher temperature period of alteration (>400°C) and have been leached of sulphur and metals such as copper and zinc. These dykes would have acted as a source of these elements for hydrothermal vent fluids and sulphide deposits, and could be the source for an increased abundance of these metals within the mineralised transition zone. Variations in alteration intensity within the lower dykes also correlate with fracture density and porosity, with relatively unfractured regions less altered, and highly fractured areas more affected by later hydrothermal circulation and seawater recharge. The observation of fracturing and slickenlines in rock samples before the penetration of pulverised material in the bottom 7 m of the borehole may indicate the presence of a zone of microfaults above a fault core. However, a re-evaluation of core samples and the electrical logs suggests that the microfaults could have been induced by drilling.

**Summary**

The top 0.5–0.6 km of the basement comprise relatively high porosity, fractured pillow basalts and breccias, leading to low downhole density, low resistivity, high porosity and low and variable sonic velocity. These rocks have mostly experienced alteration by cool, downwelling seawater, with active circulation present in the upper ∼0.3 km, and seawater flowing downhole and laterally into a 0.1 km-thick aquifer at the very top of the basement. The beginning of the lava-dyke transition zone at 0.572 km bb, compounded by an abrupt change to higher temperature alteration and significant mineralisation at 0.624 km bb, leads to a period of rapid change in the physical properties beginning between 0.5–0.6 km bb. Over 0.2–0.3 km there is a significant increase in velocity, resistivity and density, and decrease in porosity. Below 0.780 km bb, in the more homogeneous sheeted dyke complex, physical properties change more gradually and become less variable. Sonic velocity, resistivity and density increase, and porosity decrease suggests a reduction in fracturing and pore space with depth within the sheeted dykes. The convergence of downhole and core density occurs close to the upper boundary of the high-temperature altered lower dykes section, and may indicate a loss of larger-scale porosity or fracturing controls the extent of this alteration. Below ∼1.4 km bb, within the lower dyke section, physical properties are relatively constant.

### 6.4.1 Comparison with seismic results

In order to compare the borehole logs with the seismic structure at 504B derived from velocity gradient-depth profiles, the vertical depth-derivatives of the borehole logs were calculated. In this case, 100 m-wide smoothing filters were applied to the downhole logs

to remove the small-scale variation and to match the 100 m cell size present in the 3D inversion models.

The inversion model Vp and Vs gradient-depth profiles correlate remarkably well with the sonic velocity gradient-depth profiles, with the sharp increase in gradient marking the 2A/2B transition beginning at the same depth and being maintained over the same thickness, within the errors of the inversion model, in both the Vp and Vs sonic logs. A significant characteristic of both Vp and Vs gradient-depth profiles (Figure 6.12) is the correlation of their features with those of similar profiles calculated for the density and resistivity borehole log data in the vicinity of 0.5 km bb. Comparing with borehole lithology, this depth marks the top of the transition from the pure extrusive, low alteration lava sequence (0.572 km bb) into the sheeted dyke, greenschist facies sequence (0.780 km bb). In the middle of this transition, mirrored by the abrupt change in gradient (and first-order discontinuity shown in Figure 6.1) in the forward model, is the mineralised zone representing the low-to-high temperature alteration front (0.625 km bb). Velocity, resistivity and density gradient-depth profiles all show a positive change at the onset of this transition, while the porosity gradient-depth profile shows a significant negative change. Thus, at 504B, the 2A/2B boundary manifests as a transition zone of increased Vp gradient ($>2.0$ s$^{-1}$) from 0.5–0.8 km bb, and the correlation with changes in physical properties indicates that the cause of this velocity increase is a significant reduction in open porosity (from 10% to 3%), regardless of whether that is caused by pore infilling through hydrothermal alteration of the increasing dominance of low permeability dykes within lava-dyke transition zone. A negative gradient change in both Vp and Vs at 0.8 km bb marks the base of the $\sim$0.3 km-thick high velocity gradient zone. This marker mirrors the lithological transition from a mix of lavas and dykes to a predominance of dykes, although does not equate to corresponding gradient changes in the porosity, resistivity and density profiles. From these contrasting features, it is likely that, at 504B, the base of the 2A/2B transition zone, and start of layer 2B, represents the end of a transitional change in lithology, i.e. the depth at which dykes become predominant over pillow or sheet lava flows.

## 6.5 Summary

At borehole 504B, the inversion model shows that layer 2 consists of a low gradient upper 0.5 km section, underlain by a 0.3 km-thick region of high gradient ($\Delta$Vp$>2.0$ s$^{-1}$) which forms the layer 2A/2B transition zone, and a layer 2B with decreasing gradient with depth. Low gradients ($\Delta$Vp$<0.5$ s$^{-1}$) are reached from 1.7 km bb. 2D forward models characterise the 2A/2B transition as a first-order discontinuity at 0.6 km bb. Analysis of the 2A caustic arrival observed at borehole 504B indicates that the position and extent of this arrival is consistent with the inversion model velocity structure. When compared to the lithology sampled in the borehole, the upper part of layer 2A consists of porous pillow lavas affected by low-temperature alteration. The layer 2A/2B transition represents a significant porosity decrease and the progression from lavas altered by cool downwelling seawater, to the

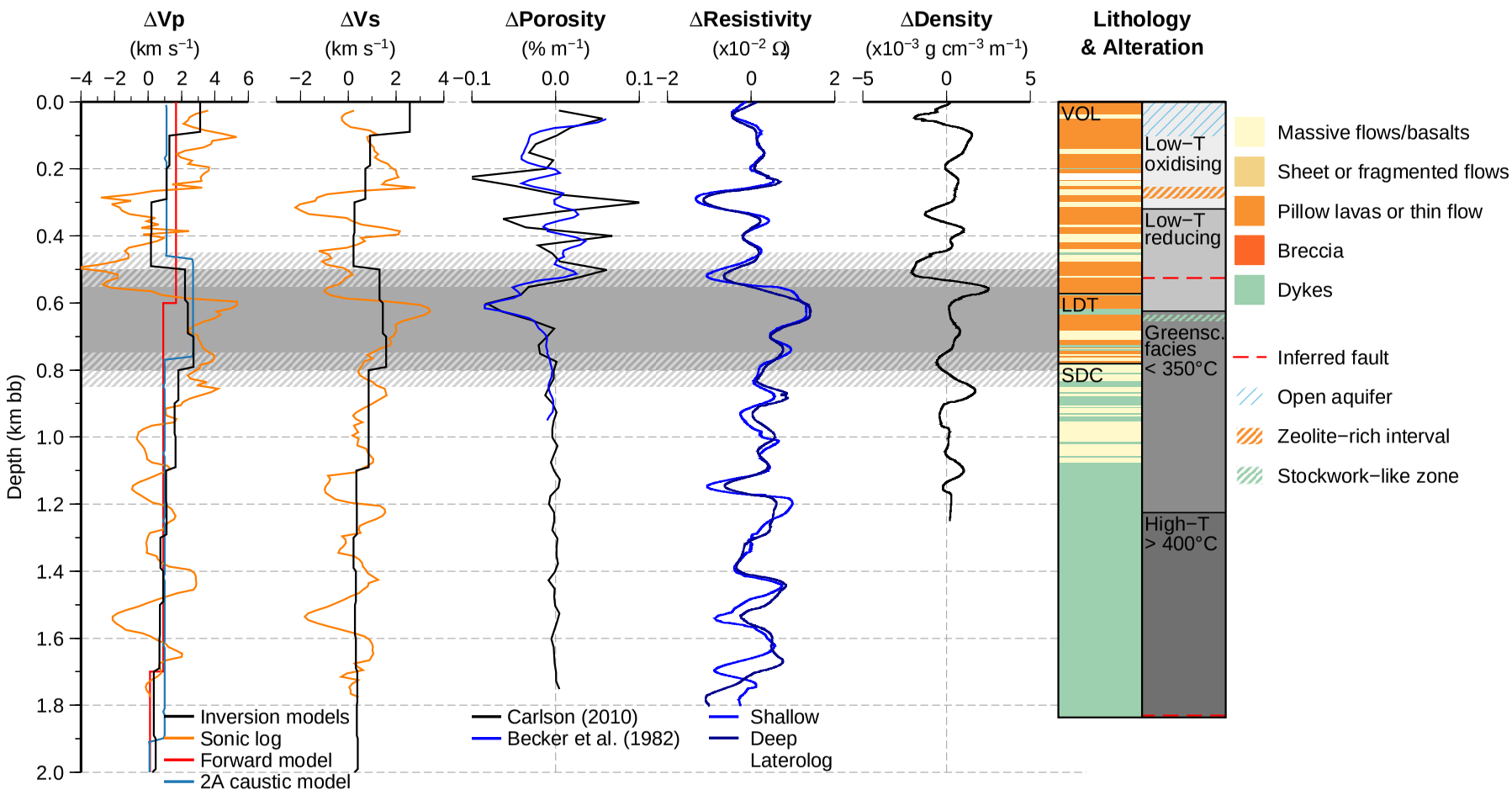


Figure 6.12: Gradient-depth profiles of the Vp and Vs inversion models, Vp forward model, and 2A caustic model at 504B, compared to gradient-depth profiles of measured and derived downhole physical properties, and summarised lithology and alteration logs. See text for references. The dark grey bar represents the 2A/2B transition zone, with the light grey stripes showing the errors (0.1 km) in depth due to the cell size within the inversion models. VOL=volcanic section, LDT=lava-dyke transition, SDC=sheeted dyke complex.

sheeted dyke complex which has experienced high temperature, greenschist-facies alteration by upwelling hydrothermal fluids. The first-order discontinuity within the forward models occurs at the point of greatest change within the crust, where the abrupt alteration front occurs within the lava-dyke transition, forming a zone of intense mineralisation.

The consistency of the velocity-depth gradient structure across the 3D models (Figure 6.2), and the consistency of the depth of the 2A caustic in the SAP_B stack (Figure 6.9), both suggest that the general structure of layer 2 varies very little in the study area. The most variation observed occurs in the upper section of layer 2A. This consistency suggests that the significant porosity change which controls the 2A/2B transition occurs at a similar depth across the study region, indicating that the thickness of the extrusive lavas, sheeted dykes, and the transition between them is relatively homogeneous throughout this portion of ∼6 Ma oceanic crust.

# Chapter 7

# Interpretation and discussion

## 7.1 Introduction

The results presented in Chapters 3, 4, 5 and 6 characterise the seismic structure of the upper crust at borehole 504B and in a 40 x 40 $km^2$ area around it. Firstly, the velocity structure at borehole 504B will be discussed and interpreted in terms of the geological structure of the crust and its physical properties. This analysis aims to improve understanding of how seismic velocity models should be interpreted, through the unique opportunity to ground-truth a series of models, derived using a variety of seismic acquisition and data analysis approaches, to a coincident deep borehole. Here, a particular focus is placed on understanding the geological origin, or cause, of the seismic layer 2A/2B and layer 2/3 boundaries.

The relationships and conclusions drawn from the comparison to borehole ground truth can then be applied to interpret the general structure of 7 Ma crust of the 3D model volume as a whole, in relation to how the oceanic crust may have evolved as it aged. Finally, variations found in the structure of the upper crust of the 3D models are summarised and discussed in relation to what they may indicate in terms of alteration and fluid flow.

## 7.2 Velocity structure of the upper crust at borehole 504B

In Chapter 6, the 1D velocity structure imaged at borehole 504B was presented, by extracting a 1D profile from the 3D inversion models at the location of the borehole. The Vp model characterises the structure as consisting of a 0.8 km-thick layer 2A, divided into a low-gradient 0.5 km-thick section where the velocity increases from 4.2 km $s^{-1}$ to 4.7 km $s^{-1}$, overlying a 0.3 km-thick region of high gradient where the velocity increases to 5.5 km $s^{-1}$. Layer 2B decreases in velocity gradient with depth, reaching a velocity of 6.5 km $s^{-1}$ by ∼1.7 km bb. The Vs profile exhibits a similar pattern, meaning the 1D Poisson's ratio is relatively constant, with slightly lower values (∼0.24) in layer 2A increasing to values ∼0.26 in lower layer 2B, and decreasing again below ∼1.7 km bb.

Analysis of the 2A caustic within long-offset MCS gathers suggested that this arrival is caused by turning rays within the high-gradient region, consistent with the prediction of the inversion velocity model.

As discussed in Chapter 1, the seismic layer 2A/2B model of oceanic crustal structure at the ridge axis has been historically extended off-axis to include a layer 2C to accommodate the observation of three distinct velocity layers from simple analysis of legacy seismic data (Houtz and Ewing, 1976; Houtz, 1976), and furthered by the interpretation of sonic velocity logs as opposed to seismic velocity models (Salisbury et al., 1985). The 2C terminology has resulted in a seismic model vs. borehole log interpretation challenge in terms of consistent lithological identification, and in how to describe the consequences of progressive porosity closure with distance off-axis as an indicator of the oceanic crustal ageing process, or of fluid and heat flow. More recent studies (e.g. Christeson et al., 1992, 2007), using more sophisticated seismic modelling and data processing approaches, still do not agree as to what the seismic layers actually represent and what terminology should be used. In this study, using the modern definition of layer 2A (Christeson et al., 1994), and defining the layer 2A/2B boundary as the observed region of a high velocity gradient, there is no requirement to introduce a third sub-layer within layer 2.

Calculation of velocity-depth gradient profiles and their comparison with the lithology and physical properties sampled within borehole 504B, suggested that the upper part of layer 2A corresponds to the low-temperature altered extrusive lavas, the high-gradient region to the lava-dyke transition zone, and layer 2B to the sheeted dykes which have undergone greenschist facies alteration. These correlations suggest that gradient-depth profiles may help locate the boundary between extrusive and intrusive basalts within the oceanic crust, which could be a useful tool to apply to seismic velocity models in locations without a coincident borehole. In order to investigate the validity of this method and what it may tell us about the nature of the 2A/2B boundary, it is first necessary to consider the different factors which influence the seismic velocity structure of the crust, and then test the method at another deep crustal borehole, ODP/IODP Hole 1256D.

### 7.2.1 What controls the seismic velocity of the crust?

As was discussed in Chapter 1 (Section 1.1.1), studies of the oceanic crust over the past 55 years have variously interpreted its seismic structure in terms of lithology (Raitt, 1963; Christeson et al., 1992), fracturing regimes (Carlson, 2010), a porosity front (Carlson, 2011) or an abrupt change in alteration (Anderson et al., 1982; Christeson et al., 2007). This disagreement is due to the numerous possible geological controls on seismic measurements which researchers use to investigate the oceanic crust. Figure 7.1 illustrates the complex relationship between the geological and geophysical observations using a conceptual diagram, whereby a change in rock characteristics (such as the lithology, porosity, fracturing regime or alteration) modifies the physical properties of the rock (e.g. the P- and S-wave velocity and density). These characteristics are inter-dependent. For example,

a change in fracturing will influence the porosity. Characteristics will also vary in importance, or dominance, depending on the particular setting. For example, within a highly fractured region, a change in lithology may not have a significant effect.

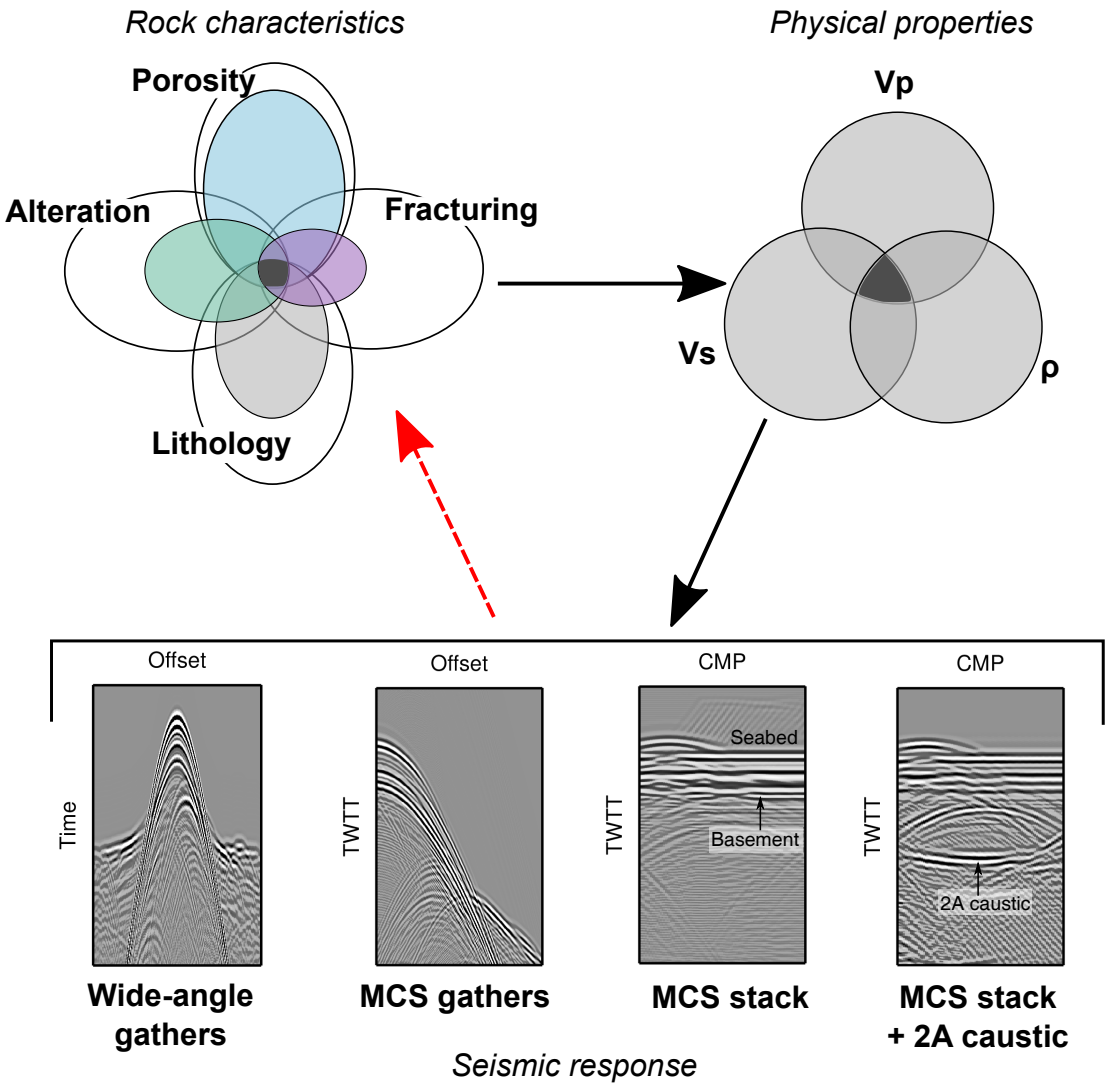


Figure 7.1: Conceptual illustration showing the interplay between controlling influences of rock properties (porosity, fracture density and geometry, lithology, and alteration) on the seismic response of the subsurface. Combinations of changes in these properties control the velocity (Vp, Vs) and density ($\rho$) response and, thus, define seismic image characteristics. The strongest seismic response results from a coincident change in all properties, although how they combine and their relative degree of influence is setting and crustal process specific. The seismic response is most commonly observed and quantified from wide-angle refraction and reflection travel-time modelling and MCS stacked images. Using the gradient-depth profile can directly assist in relating seismic response to changes in the underlying rock properties (red dashed arrow).

If it is assumed that porosity is the fundamental defining property of the crust at the time of its formation at a mid-ocean ridge, then any change in this porosity (e.g. between the extrusive lavas and intrusive dykes) provides a consistent framework to explain the subsequent evolution of the oceanic crust with age. As a hypothesis, it is likely that a

combination of changes in lithological characteristics will occur around the same location and that when they do, they tend to reinforce a matching change in the physical properties.

Using results from this study and DSDP/ODP data, this hypothesis can be tested. The change in lithology from extrusive lavas to intrusive dykes over the 2A/2B boundary transition zone observed at 504B (Section 6.4) is a region where permeability and porosity also decrease, hence it also marks the transition zone from high volume, low temperature seawater-dominated flow to low volume, high temperature hydrothermal circulation, with a corresponding change in alteration regime. The combined effect on Vp, Vs and density results in the high gradient zone observed in seismic refraction and reflection imaging and modelling methods.

It should be noted that, even based on this simplified conceptual diagram, this is an underdetermined problem due to the greater number of unknowns than measured properties (seismic velocity). Thus, although it may be possible to suggest the dominant controls on the measured seismic velocity structure, it is not possible to use inversion models to absolutely define the characteristics of the subsurface without other constraints.

### 7.2.2 Application of the gradient-depth profile

In Chapter 6 the gradient-depth profile was shown to be an effective way to locate and identify seismic layers within the oceanic crust within models. Carlson (2001) attributes a low Vp gradient ($<0.1$ s$^{-1}$) to the compressional effects of lithostatic loading. Hence any significant change in gradient above this value should indicate that other factors (see Figure 7.1) are influencing the velocity, and cause the widely-observed high gradient zone in the upper 2 km of the oceanic crust which characterises the layer 2A/2B boundary. Thus, the gradient-depth proxy may be more effective in locating and characterising the 2A/2B boundary transition zone, and potentially other seismic layer boundaries, than comparing absolute velocity alone (e.g. Grevemeyer et al., 2018b), especially as velocity varies not only with crustal age (e.g. Nedimović et al., 2008), but also between different mid-ocean ridges spreading at different rates. Further, the absolute velocity structure may vary depending on both the acquisition geometry and the chosen modelling/inversion strategy. The overall similarity in gradient-depth profiles between those derived from the seismic models and sonic logs (Section 6.4) provides confidence that the gradient-depth profile can be used to quantitatively analyse datasets acquired at different dimensional scales to localise the boundary, or transition zone, between the lower velocity layer 2A and the higher velocity layer 2B and hence estimate the associated rock characteristics.

For example, at 504B, the inversion model characterises layer 2A as an 0.8 km-thick layer with velocity increasing from $\sim$4.0 km s$^{-1}$ to $\sim$5.7 km s$^{-1}$. These velocities are higher than those observed within oceanic crust at ridge axes (e.g. Sohn et al., 2004; Canales et al., 2005), but within the expectation for sedimented, $\sim$7 Ma crust (Nedimović et al., 2008) such as that found at 504B. Although the absolute velocities may differ depending on setting, the gradient profile characterisation of layer 2A, comprising both a layer of

low gradient (0-1 $s^{-1}$) lying over a high gradient region (>2 $s^{-1}$), is shown to be a general characteristic of crust of various ages (Christeson et al., 1992, 2012).

### 7.2.3 Comparison to borehole 1256D

To ascertain the applicability of the gradient-depth approach, the methodology is applied to a refraction profile at the only other borehole to drill through the lava-dyke transition and has a suite of downhole logs. IODP borehole 1256D (Figure 7.2) penetrated through ~0.250 km of sediments and 1.257 km of basement rock in ~15 Ma crust formed at the East Pacific Rise during a period of super-fast spreading (Wilson et al., 2006). This borehole samples 0.284 km of off-axis lava flows, 0.470 km of on-axis extrusive lavas, a 0.057 km-thick lava-dyke transition zone, and 0.346 km of sheeted dykes before the first occurrence of gabbro at 1.157 km bb (Expedition 309 and 312 Scientists, 2006, Figure 7.3). Alteration changes observed downhole include a stepwise increase in metamorphic grade at the top of the lava-dyke transition zone, from low temperature phases to higher temperature greenschist facies mineralogy (Alt et al., 2010).

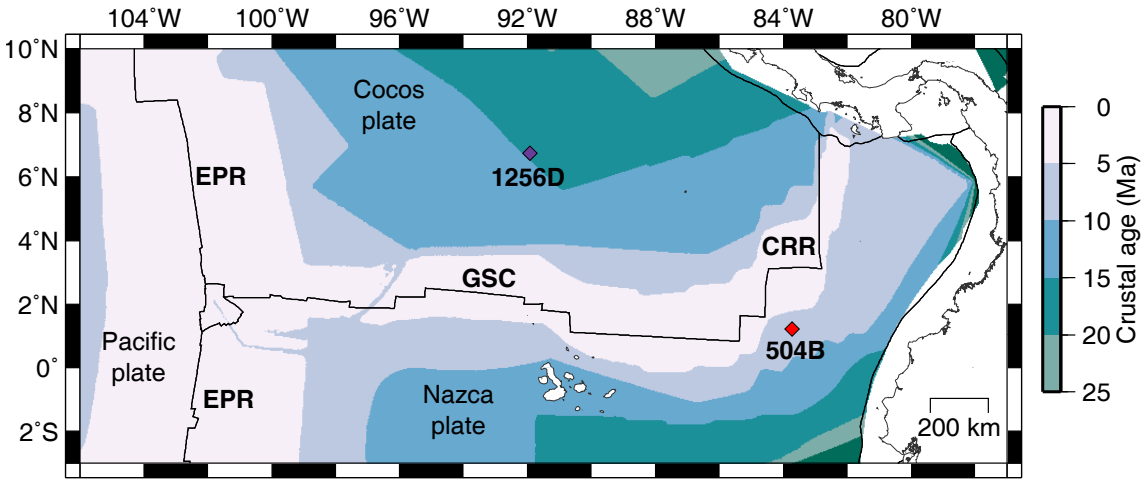


Figure 7.2: Map of crustal age in the eastern equatorial Pacific, from Müller et al. (2008), showing the positions of boreholes 504B and 1256D. Black lines show plate boundaries (Bird, 2003), with the Costa Rica Rift (CRR), Galapagos Spreading Centre (GSC) and East Pacific Rise (EPR) spreading ridges labelled.

To apply the gradient-depth method to borehole 1256D and compare the results with those from borehole 504B, downhole logs, core data and lithology and alteration information were compiled from drilling results from the four visits to the site: ODP Leg 206 and IODP Expeditions 309, 312 and 335 (Wilson et al., 2006; Teagle et al., 2006; Alt et al., 2010; Guerin and Zakharova, 2011; Harris et al., 2017). Further information on the detailed lithological structure was sourced from Tominaga et al. (2009) and Harris et al. (2015). Vp and Vs sonic logs from Expeditions 309 and 312 were reprocessed by Guerin et al. (2008). Apparent porosity was derived using Archie's law (Archie, 1942) following the same approach adopted for 504B (Becker et al., 1982, Section 6.4) and using the downhole resistivity and temperature logs from Expedition 312 (Teagle et al., 2006).

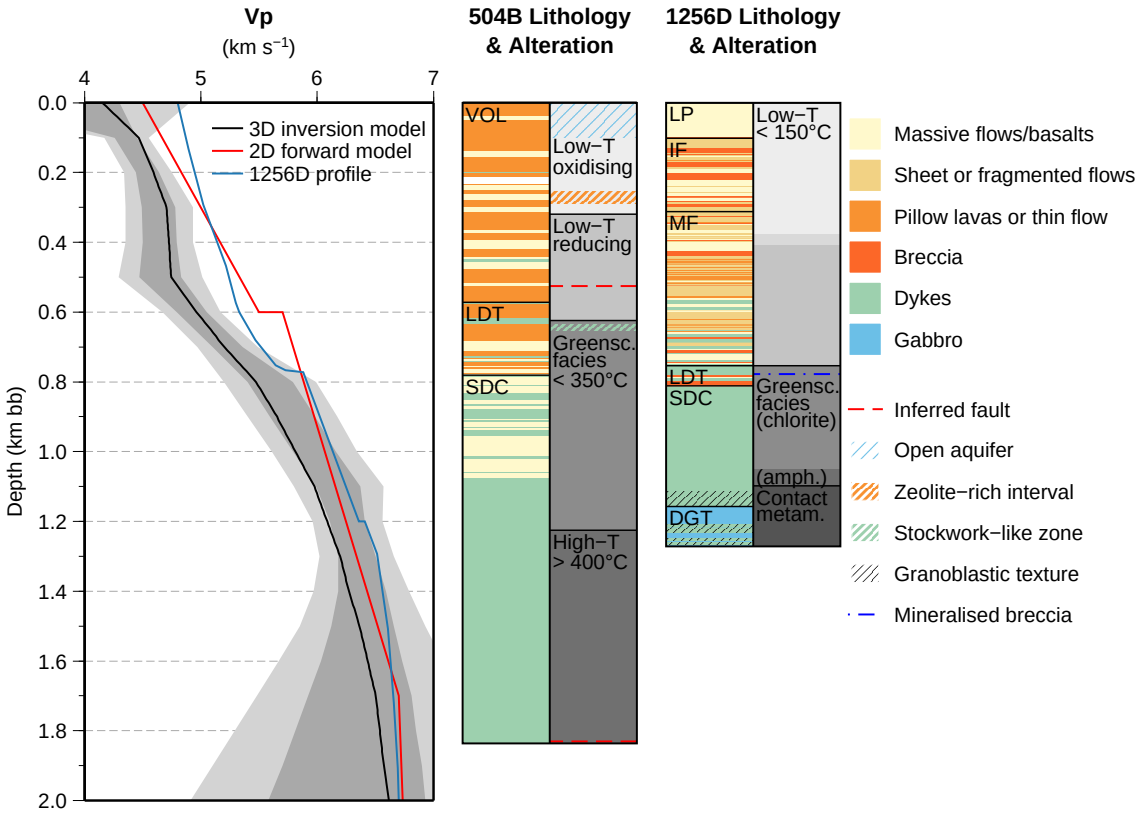


Figure 7.3: Refraction velocity-depth profile for 1256D from the site survey (Shipboard Scientific Party, 2003b) compared to the 1D extracts from velocity models at borehole 504B. Grey and dark grey bands represent the 98% and 65% confidence intervals, respectively, for the 504B inversion model. Lithology and alteration logs for Holes 504B and 1256D are also shown for comparison. Note the higher variability within the extrusive section in Hole 1256D and the thinner lava-dyke transition zone. Lithology labels: VOL=volcanics; LDT=lava-dyke transition; SDC=sheeted dyke complex; LP=lava pond; IF=inflated flows; MF=massive and sheet flows; DGT=dyke-gabbro transition. A section of lower dykes in Hole 1256D are altered to amphibole (amph.) facies, and the lowermost dykes and DGT have experienced contact metamorphism (contact metam.).

Although no extensive, 3D, active-source seismic experiment has been conducted over borehole 1256D, a pre-drilling seismic site survey of Site 1256 (Wilson et al., 2003), acquired both reflection and refraction data. A 1D inversion of the ocean-bottom hydrophone refraction data (Shipboard Scientific Party, 2003a) resulted in upper layer 2 velocities of ~4.8–5.7 km $s^{-1}$, with a first-order discontinuity at ~0.770 km bb to 5.9 km $s^{-1}$ (Figure 7.3). This velocity-depth profile is similar to that of the forward model at Hole 504B and was produced using a comparable defined-layer approach to that adopted here, as opposed to the smoothed approach inherent in inversion.

The gradient-depth profile of the Site 1256 refraction model (Figure 7.4) shows a rapid and significant change (henceforth termed peak) in gradient at 0.770 km bb, which is interpreted to be the layer 2A/2B boundary characteristic equivalent at Hole 1256D. However, the downhole log gradient-depth profiles from Hole 1256D are different to those from Hole 504B (Figure 7.3), with large variation within the volcanic section due to considerable variability in extrusive style, from off-axis lava ponds to on-axis inflated flows and sheet

flows. In contrast, at Hole 504B, the volcanic section is predominantly formed from pillow lavas (∼70% by volume) and thin sheet flows (∼13%) (Alt et al., 1996). The Site 1256 seismic refraction gradient-depth profile exhibits little of the variability seen in the downhole logs, maintaining a relatively constant low gradient until the large peak at ∼0.75 km bb, identified as the layer 2A/2B boundary, which is coincident with similar features in the corresponding sonic log-derived gradient-depth profile. The variable gradient-depth patterns of the downhole logs through the extrusive layer are most likely caused by local structure with considerable lateral variability, as evidence in another borehole, Hole 1256C, drilled just 30 m away from Hole 1256D which shows significant variation in the extrusive stratigraphy (Tartarotti et al., 2009). These local features are not detectable by seismic tomography methods as they are below their resolution, and only manifest themselves as seismic amplitude variations (Christeson et al., 2012).

At ∼0.8 km bb, the sonic log peak gradients (3.0 $s^{-1}$ in both Vp and Vs) have similar values to those at ∼0.5 km bb at Hole 504B (5.0 $s^{-1}$ in Vp and 3.5 $s^{-1}$ in Vs). These peaks align with a decrease in porosity and an increase in resistivity, again with similar peak amplitudes to the changes observed in Hole 504B (-0.1% $m^{-1}$ in porosity gradient and 1.5 x $10^{-2}$ Ω in resistivity gradient). In the lithology log, these changes at or near 0.75 km bb correspond to the start of the lava-dyke transition zone, with the depth of the peak gradients in the logs close to that of the low-to-high temperature alteration front identified in the borehole.

Comparing the thickness of the zones of high gradient between boreholes suggests that it is related to the distance over which physical parameters change. At Hole 504B, both the inversion model and sonic log exhibit a high gradient over approximately 0.3 km, with changes in porosity and resistivity over 0.2-0.3 km, and the lava-dyke transition occurring over 0.209 km. At Hole 1256D, the sonic log exhibits a high gradient over <0.1 km depth, a similar length scale to the observed peaks in porosity and resistivity, and the thin, 0.057 km-thick lava-dyke transition.

Christeson et al. (2012) used full-waveform inversion to derive velocity models of the ridge flanks at the Juan de Fuca Ridge and East Pacific Rise which both have high gradient zones 0.23–0.28 km-thick, compared to proximal tectonic escarpments with lava-dyke transitions varying from ∼0.7 km at the Blanco Transform Fault (Juan de Fuca Ridge) to ∼0.15 km at the Hess Deep (East Pacific Rise). Although full-waveform inversion techniques provide a higher model resolution than travel-time tomography, they are sensitive to the choice of starting model and, in these cases, cannot be rigorously appraised for correlation between derived velocity models and lithological structure or physical properly measurements since there are no boreholes coincident with the seismic profiles.

### 7.2.4 Nature of the 2A/2B boundary

The analysis of both Holes 504B and 1256D suggests that the layer 2A/2B boundary observed in many seismic studies of the oceanic crust (e.g. Houtz, 1976; Harding et al.,

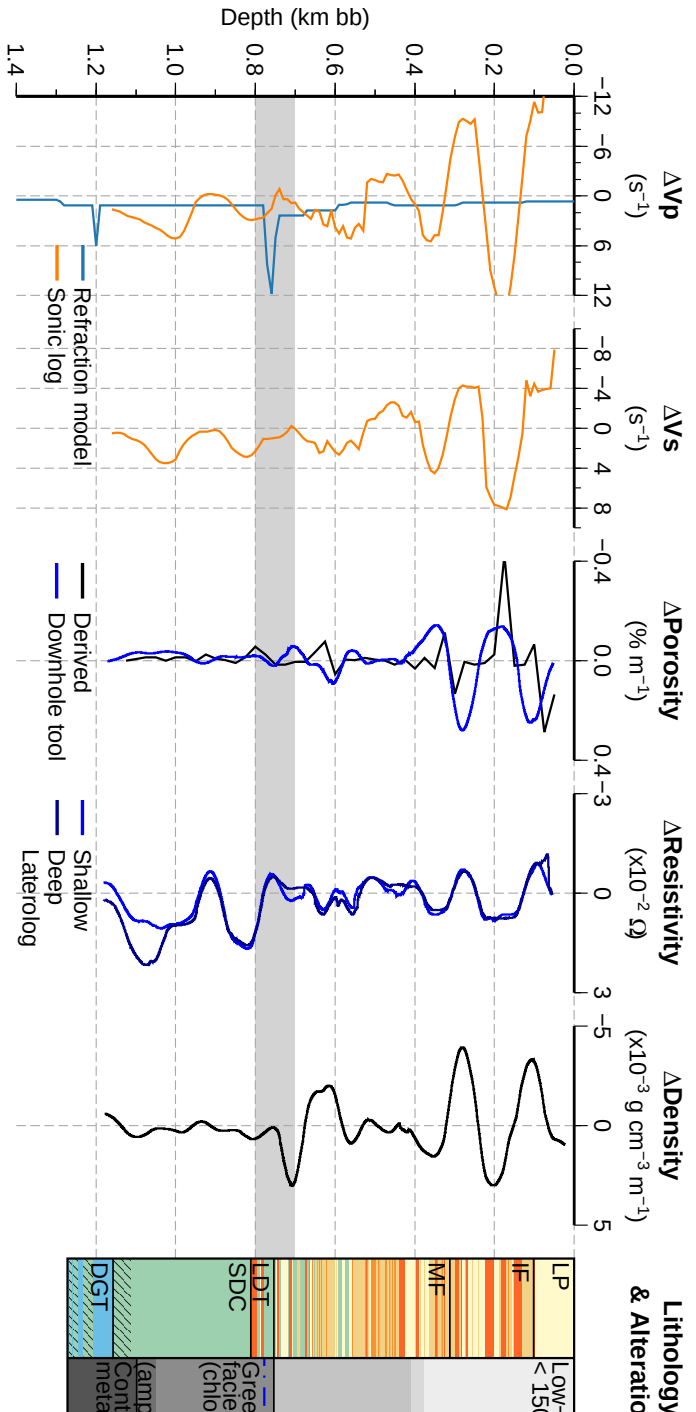


Figure 7.4: Gradient-depth profile derived from the 1D refraction profile at Site 1256 (Shipboard Scientific Party, 2003b), compared to gradient-depth profiles of measured and observed downhole physical properties, and summarised lithology and alteration logs from Hole 1256D (after Tominaga et al., 2009; Harris et al., 2015). These logs show much larger variation than those from borehole 504B and, hence, are plotted at different scales cf. Figure 6.12, although the vertical scale remains the same. A gradient peak at ∼0.75 km depth bb in the site survey refraction profile is coincident with peaks in the two sonic profiles and they share similar amplitude gradient increases to those at 0.5 km bb in Hole 504B. These peaks correspond to the top of the lava-dyke transition zone, and changes in porosity, resistivity and alteration. Here the thickness of the high gradient zone is much smaller than at Hole 504B, corresponding to a thinner lava-dyke transition zone. LP=lava pond; IF=inflated flows; MF=massive and sheet flows; LDT=lava-dyke transition; SDC=sheeted dyke complex; DGT=dyke-gabbro transition.

1993; Van Ark et al., 2007; Weekly et al., 2014) corresponds to a zone of multiple physical property changes within the extrusive-intrusive (lava-dyke) transition zone, at least at intermediate and faster spreading rates where the crust is formed without large-scale tectonic stretching and peridotite exhumation forming oceanic core complexes (Cann et al., 1997). These changes manifest as a seismic gradient >2 $s^{-1}$, a porosity decrease with a peak gradient of -0.1% $m^{-1}$ and a resistivity increase with a peak gradient of 1.5 x $10^{-2}$ Ω. It is suggested that the most likely single cause of a significant increase in seismic velocity is a reduction in porosity (Carlson, 2010), explained by the change from inherently more porous extrusive lavas to a much less porous or permeable sheeted dyke complex. Other factors, such as alteration (Carlson, 2011), fracturing fronts (Carlson, 2010) and changes in crack aspect ratio (Carlson, 2014), however, also influence the porosity and seismic velocity and are likely to occur at a similar depth to the lava-dyke transition zone, due to the inherent differences between these two lithological layers caused by their contrasting emplacement mechanisms. The abrupt change in mineralogy at 0.623 km bb in Hole 504B and 0.754 km bb in Hole 1256D, due to a higher temperature alteration regime, could reduce the porosity if this resulted in more mineral precipitation within pores than results from low temperature alteration (Anderson et al., 1982). Thus, it is likely that these other factors also contribute to the layer 2A/2B seismic signature.

Christeson et al. (2007) map the layer 2A/2B boundary at the exposed scarps of the Hess Deep and Blanco Transform Fault by stacking the layer 2A caustic event in MCS gathers to produce a seismic section. They argue that, as the layer 2A/2B boundary occurs at the top of the sheeted dyke section at the Hess Deep but mainly within the lava-dyke transition at the Blanco Transform Fault, the interface must be solely caused by an alteration front. The results from Holes 504B and 1256D suggest that this variation could equally be a function of the large difference in thickness of the lava-dyke transition zone between the Hess Deep (150 m) and Blanco Transform Fault (700 m), combined with the errors inherent in estimating the depth of the 2A/2B boundary using the 2A caustic event (since it is not a true reflection event) and the lateral heterogeneity between the seismic profiles and the mapped scarp faces.

Within both boreholes 504B and 1256D, the low temperature-to-greenschist facies alteration front occurs within the lava-dyke transition zone, despite differences in age and spreading rate. This suggests that the position of the alteration front is controlled by the inherent porosity change associated with the lithological transition zone; the onset of the predominance of sheeted dykes restricts significant circulation of cool seawater to within the more porous extrusive section and, thus, produces a boundary at the pressure-temperature conditions needed for greenschist facies alteration (>250°C). This conclusion is supported by hydrothermal flow simulations (Lowell et al., 2007), which model an increase in temperature, alongside precipitation differences, between the extrusives (modelled as a high permeability layer) and the dyke section (modelled as a low permeability layer). Further, well-preserved examples of hydrothermal alteration in the Troodos ophiolite exhibit sharp interfaces between low temperature alteration and higher temperature,

greenschist facies alteration at the boundary between pillow lavas and sheeted dykes (Gillis and Robinson, 1990; Cann and Gillis, 2004).

Carlson (2010) compares theoretical crack models with the sonic velocity logs at boreholes 504B and 1256D to suggest that changes in fracturing, unrelated to the lithology and alteration, could be solely responsible for the velocity variation with depth. At Hole 504B, a model consisting of a significant percentage of high aspect ratio (wide) cracks within the extrusive lavas and the uppermost part of the transition zone, with a downward change to a small percentage of low aspect ratio (narrow) cracks in the remaining transition zone and dykes, can explain the trends in porosity and velocity. Such a change to lower aspect ratio cracks should result in an increase in the Poisson's ratio (Collier and Singh, 1998), whereas there is little variation observed at this depth at borehole 504B, suggesting that changes in crack aspect ratio are not a dominant control on the seismic velocity here.

### 7.2.5 Summary

The SG seismic dataset presented in this study is the highest resolution and most densely sampled yet acquired at any deep crustal borehole. The results at borehole 504B from the WA modelling (Sections 3.2, 3.3.12 and 5.3.5) and MCS imaging (Section 6.3) approaches uniquely reveal the differences in outcome characteristics for the same crustal location, that is also directly borehole sampled for lithology and can provide absolute ground-truth via the full suites of geophysical downhole logs. The schematic diagram presented in Figure 7.5 summarises the results of each of the applied approaches and what they reveal about crustal structure and, consequently, how such models and images should be interpreted.

This study has shown that a positive change in vertical velocity gradient observed in smoothed and regularised inversion models relates to the top of a transition zone marked by the onset of intrusive sheet dykes, and the base of this zone is marked by a negative change in gradient that equates to the depth at which dykes predominate. The first-order discontinuity observed in discretised forward models, on the other hand, marks an alteration front relating to a rapid decrease in porosity. Neither the top or base of the transition zone, nor the location of the alteration front, results in an observable MCS reflection event.

On the basis of this new seismic interpretation, the gradient-depth method can be considered as a new proxy which, at borehole 504B, places the onset of the transition zone from layer 2A to layer 2B at 0.5 $\pm$0.1 km below the top basement, coincident with the top of a zone of significant decrease in in-situ measured porosity and containing the lithological lava-dyke transition zone and a change in alteration observed in core samples (Section 6.4). The 2A caustic (Section 6.3), commonly used to locate and determine the depth to the 2A/2B boundary, originates within this transition zone and its observation acts as a marker of thickness of this transition zone and its velocity gradient.

The use of absolute velocity, rather than velocity change, has historically resulted in the division of layer 2 into two sub-layers (2A and 2B) on-axis, and three sub-layers

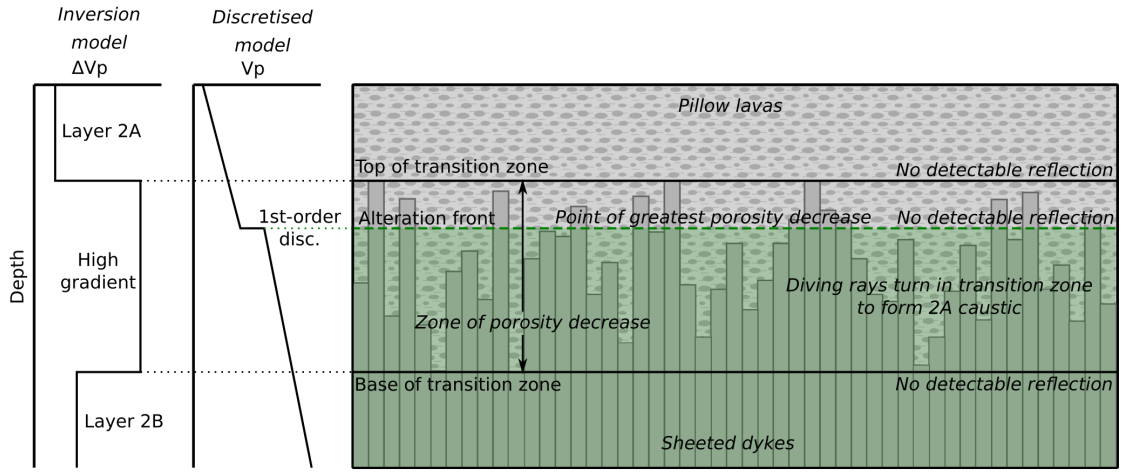


Figure 7.5: Generalised summary, based on the results at borehole 504B, of how particular seismic features correlate with changes in lithology and physical properties within the upper oceanic crust. The transition zone between extrusive lavas and sheeted dykes (and accompanying porosity decrease) is represented in smooth inversion models as a region of high velocity-depth gradient. The alteration front often occurring within this transition zone also represents a porosity front and is characterised in two-layer discretised models as a first-order discontinuity. The top and base of the transition zone, as well as the alteration front, do not produce reflections detectable at standard crustal imaging seismic wavelengths (or they are of low amplitude), and the 2A caustic observed on MCS gathers is controlled by the thickness and gradient of the transition zone.

(2A, 2B and 2C) off-axis, resulting in a mismatch between layer terminology and actual lithology. The results of this study suggest that the use of velocity change to define seismic layers maintains the on-axis definition of layer 2A and 2B as the oceanic crust ages off-axis. Consequently, the 2C term becomes superfluous since, using this approach, layer 2B on-axis is the equivalent lithology to that of layer 2B off-axis.

## 7.3 The layer 2/3 boundary

The interface between seismic layers 2 and 3, the layer 2/3 boundary, is a commonly observed boundary within seismic studies of oceanic crust which, similar to the layer 2A/2B boundary, has a debated origin (see Chapter 1). Layer 3 is defined by low velocity-depth gradients of $\sim$0.1 $s^{-1}$ (Carlson, 2001), and high seismic velocities of $\sim$6.6–7.6 km $s^{-1}$ (White et al., 1992). Although this study predominantly focussed on characterising the upper oceanic crust in the South Grid area, the 3D inversion models resolve crustal structure to $\sim$2 km depth, and the 2D forward models provides estimates of velocity to the base of the crust. Thus, it is possible to also estimate the position of the base of layer 2 from the SG results, and compare this to the lithology sampled in borehole 504B to better understand the nature of the layer 2/3 boundary.

### 7.3.1 Previous studies at borehole 504B

Based on various different geophysical observations, several different estimates have previously been made of the depth of the layer 2/3 boundary at borehole 504B. Swift et al. (1998b) interpreted a vertical seismic profile acquired in the borehole to place the layer 2/3 boundary at 0.875–0.925 km bb, at the top of the sheeted dyke complex. However, here, this is interpreted as the layer 2A/2B boundary. Detrick et al. (1994) approximated the velocity of layer 3 at borehole 504B to be 6.5 km $s^{-1}$ from a previous sonobuoy study of the area (Collins et al., 1989), and then extrapolated a velocity profile from an Oblique Seismic Experiment at the borehole (Little and Stephen, 1985), maintaining the same gradient, to place the layer 2/3 boundary at 1.2 ±0.2 km bb, where the velocity reaches 6.5 km $s^{-1}$. This depth is within the drilled sheeted dyke section, and close to an alteration front where amphibolite facies begin increasing in abundance. However, this method defines the top of layer 3 solely by velocity, as opposed to its characteristic low gradient, and does not take into account the differences in velocity derived from the different measuring approaches. Salisbury et al. (1996) also argued that the 2/3 boundary occurs within the sampled sheeted dyke section, regardless of whether it is defined using the method of Detrick et al. (1994), or where the velocity reaches the average layer 3 velocity of 6.7 km $s^{-1}$ defined by Raitt (1963) near the base of the borehole at ∼1.8 km bb. They argue that the latter position would suggest the boundary is primarily a metamorphic front within the sheeted dykes.

### 7.3.2 Results from this study

To address this debate using the new seismic velocity models derived during this study, the layer 2/3 boundary is determined at the position of borehole 504B in both the 2D forward models and Vp 3D inversion model, and compared to the lithological and alteration structure sampled within the borehole.

The average below-basement crustal structure at borehole 504B from the 2D forward models consists of three distinct layers. As described above, the upper two layers, identified as layers 2A and 2B, have velocity ranges of 4.5–5.5 km $s^{-1}$ and 5.7–6.7 km $s^{-1}$, and velocity-depth gradients of 1.7 $s^{-1}$ and 0.9 $s^{-1}$, respectively. The third layer, separated from the layer above by a change in gradient, has a narrow velocity range of 6.7–7.1 km $s^{-1}$ and a velocity-depth gradient of 0.1 $s^{-1}$ and, thus, is identified here as seismic layer 3. Therefore, the layer 2/3 boundary occurs at a depth of 1.7 ±0.2 km bb, and layer 3 is 3.3 ±0.3 km-thick. As the 3D inversion model is smooth and the layer 2/3 boundary is often defined using a distinct change in gradient, the boundary is less straightforward to locate via this approach. Given that the average P-wave velocity-gradient characteristic of layer 2 is ∼1 $s^{-1}$, and of layer 3 is ∼0.1 $s^{-1}$, the layer 2/3 boundary is arbitrarily defined in the inversion model as the depth at which the gradient falls below the mid-way point, ∼0.5 $s^{-1}$. This method aims to define layer 3 by its characteristic velocity-depth gradient, as opposed to its estimated absolute velocity range, and assumes that the inversion modelling has linearly smoothed

the same boundary represented by a discrete gradient change in the 2D forward model. Therefore, in the inversion model at borehole 504B, the layer 2/3 boundary occurs at 1.7 km bb, where the gradient reduces from 0.7 $s^{-1}$ to 0.4 $s^{-1}$. At this depth, Vp reaches 6.5 km $s^{-1}$ and Vs 3.6 km $s^{-1}$. This bottom layer 2B Vp velocity is consistent with a bottom 2B velocity of ∼6.6 km $s^{-1}$ observed in crust formed at the East Pacific Rise ranging in age from 0.5–8.3 Ma (Grevemeyer et al., 1998).

Across the 3D models, the average amplitude of velocity anomalies begins decreasing below 1.2 km bb, and is very low (>1.0 km $s^{-1}$ in Vp and >0.5 km $s^{-1}$ in Vs) below 1.7 km bb. Poisson's ratio also reaches a relatively constant value of ∼0.26 across the model space at ∼1.7 km bb. This consistency in seismic structure at this depth could also be indicative of reaching seismic layer 3, which is known to exhibit less variation in velocity and structure than layer 2.

At 1.7 km bb in borehole 504B, the core samples comprise massive, diabase dykes, which have experienced high temperature (>400°C) alteration. The Vp and Vs sonic logs exhibit relatively constant velocities of 6.65 km $s^{-1}$ and 3.49 km $s^{-1}$, respectively; porosity is consistently low (∼0.6%), core sample density consistent at ∼2.96 g $cm^{-3}$; and resistivity is relatively high at ∼2700 Ωm (deep laterolog), with a large difference between the shallow and deep measurements indicating massive structure with low permeability. Salisbury et al. (1996) investigate the relative abundance of alteration minerals down the borehole, and show that from ∼1.7 km to the base of the borehole, the percentage abundance of chlorite approaches zero, and the abundance of actinolite increases significantly, as actinolite and plagioclase replace clinopyroxene and chlorite, respectively. Since the porosity of the formation is close to 0%, the authors propose that velocity is primarily controlled by the petrology and temperature/confining pressure conditions, and that as $V_{cpx} > V_{act} \gg V_{plag} \gg V_{chl}$, the layer 2/3 boundary may represent a metamorphic front. However, Carlson and Miller (2004) argue that the decrease in high velocity clinopyroxene may compensate for the decrease in low velocity chlorite, and cancel out any total effect on the seismic structure.

Considering the 0.2 km sensitivity on the depth from the 2D forward model, the boundary could occur anywhere between 1.5 km bb and 1.9 km bb. At 1.5 km bb, within the diabase dykes section, there is no significant change in mineralogy, although there is a significant gradient decrease in both the sonic logs and the resistivity logs, potentially suggesting the reaching of a point of minimum, and then constant, porosity and permeability due to the confining pressure. The maximum depth suggested by the error bounds, 1.9 km bb, is 64 m below the depth of the current borehole, which is thought to be close to the dyke-gabbro transition due to increasing grain sizes in the diabase dykes, and a reduction of chilled margins indicating higher temperatures and slower cooling rates (Alt et al., 1993).

### 7.3.3 Summary

At borehole 504B, due to the uncertainty within the seismic velocity models, and the lack of ground-truth to 1.9 km bb, it is not possible to conclude what causes the layer 2/3 boundary at borehole 504B from the available information. It could represent the point at which open porosity and fractures are closed due to confining pressure, a metamorphic front from increasing mineral alteration with depth, or indeed another change, including the presence of a gabbroic sequence, as yet unsampled by drilling (Figure 7.6). At Hole

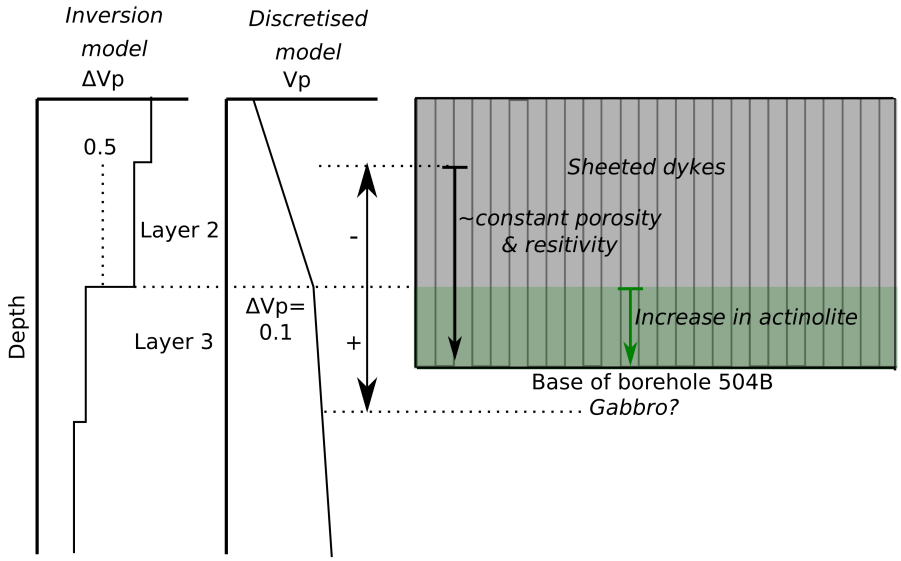


Figure 7.6: Summary diagram of the position of the layer 2/3 boundary at borehole 504B from the inversion model, where the gradient falls below 0.5 $s^{-1}$, and the discretised forward model, where there is a discrete change to a gradient of 0.1 $s^{-1}$, with the errors indicated by the vertical +/- arrow. This position lies within the sheeted dyke complex sampled at borehole 504B, where there is a downhole increase in actinolite, but the errors also encompass a change to relatively constant porosity and resistivity (upper bound), and unsampled rock below the base of the borehole (lower bound), which is hypothesised to be gabbroic (Alt et al., 1993).

1256D, the layer 2/3 boundary has been interpreted as a transition between 1.2–1.5 km bb, based on the 1D refraction profile (Wilson et al., 2006), where Vp increases from 6.4 km $s^{-1}$ to 6.6 km $s^{-1}$ and the velocity-depth gradient decreases from ~1.1 $s^{-1}$ above 1.2 km to 0.2 $s^{-1}$ below 1.5 km. Wilson et al. (2006) argue that, as 1.2 km bb occurs within the first unit of sampled gabbros and not above, that the layer 2/3 boundary does not represent the transition from sheeted dykes to intrusive gabbros. However, the gabbro lenses sampled within the borehole are highly altered and contain dyke clasts, thus may not be typical of the massive gabbros of the lower crust. Their thicknesses of 52 m and 24 m are also below the seismic resolution of a quarter wavelength, assuming a velocity of 6.5 km $s^{-1}$ and a dominant frequency of <30 Hz. These uncertainties, coupled with the inherent uncertainty associated with seismic models, suggests that at Hole 1256D, it is also not possible to confidently interpret the geological cause of the seismic layer 2/3 boundary. Another hundred metres of drilling and core analysis in Hole 504B, or indeed a few hundred

metres in Hole 1256D, especially if accompanied with a more extensive seismic survey, might have provided the evidence to conclude this debate.

## 7.4 Oceanic crustal structure at 7 Ma

The resulting 3D Vp model for the SG study area is smooth and homogeneous. Velocities increase from ∼4.2 km $s^{-1}$ at the top of layer 2A to ∼4.7 km $s^{-1}$ at the beginning of the high gradient zone, with a total 2A thickness of ∼0.8 km, and a bottom velocity where it meets 2B of ∼5.5 km $s^{-1}$. Layer 2B is ∼0.7–1.1 km-thick in the inversion model, increasing in velocity from 5.5 km $s^{-1}$ to ∼6.5 km $s^{-1}$. The 2D forward models also show little lateral variation, and exhibit a comparable average velocity structure, with a 0.6 km-thick layer 2A, with velocity increasing from 4.6 km $s^{-1}$ to 5.4 km $s^{-1}$, and a 1.3 km-thick layer 2B with velocity increasing from 5.7–6.8 km $s^{-1}$. The 2D models also constrain layer 3 thickness to be 3.2 km-thick, with velocity increasing gradually with depth from 6.8–7.0 km $s^{-1}$, giving a total crustal thickness of about 5.0 km.

Using the ground-truth at borehole 504B, this homogeneity suggests that the extrusive lava section, transition zone, and dyke section are of relatively consistent thicknesses throughout the study area. The decrease in the magnitude of velocity anomalies below ∼1.7 km bb, and high, invariant Poisson's ratio of ∼0.26, also suggest that the layer 2/3 boundary occurs at a similar depth across the study area.

### 7.4.1 Evolution of the oceanic crust

The layer 2A velocities defined using both 2D and 3D models in this study are significantly higher than those defined at newly-formed crust at ridge axes, including at other intermediate spreading ridges such as the Juan de Fuca Ridge. For example, Sohn et al. (2004) define the on-axis Vp structure at the East Pacific Rise at 9°50'N as consisting of a 100 m-thick upper layer 2A with a Vp of 2.2 km $s^{-1}$, above a 55 m-thick lower layer 2A where velocity rapidly increases. Layer 2B is at least 245 m-thick, and has an average velocity of 4.9 km $s^{-1}$ to where ray coverage diminishes at 400 m bb. Canales et al. (2005) discuss velocity models of the Cleft and Vance segments of the Juan de Fuca Ridge, which spread at a similar rate to the CRR with a full rate of 56 mm $yr^{-1}$, with average layer 2A velocity for both segments at 2.26 km $s^{-1}$ at the ridge axis. Upper layer 2B velocity is ∼5 km $s^{-1}$. However, this low layer 2A velocity increases with distance away from the axis, to 2.87 km $s^{-1}$ by 4.4 km off-axis (equivalent age of 0.16 Ma) and 3.18 km $s^{-1}$ by 9 km off-axis (equivalent age of 0.32 Ma). Layer 2B velocities don't show a consistent or substantial change.

Layer 2A velocity is commonly observed to increase as the crust ages (Section 1.1.3), with velocity approximately doubling within the first 10 Myr (Grevemeyer and Weigel, 1996). This has been attributed to the infilling of porosity, primarily small cracks and pores, with hydrothermal alteration products, which may occur more rapidly on ridge

flanks blanketed in a thick layer of sediment, compared with flanks with little sediment cover (Nedimović et al., 2008). Layer 2A velocity-age relationships proposed by Grevemeyer and Weigel (1996) and Nedimović et al. (2008) (for sedimented crust), and a hypothetical, average ridge axis 2A velocity of 2.3 km $s^{-1}$, give velocities of 4.7 and 4.0 km $s^{-1}$ at a crustal age of 6.9 Ma, respectively. These are similar to the observed upper layer 2 velocity of 4.2 km $s^{-1}$ at borehole 504B, and suggest that the process of mineral precipitation through hydrothermal circulation is occurring at similar rates at the CRR to that at other spreading ridges.

### 7.4.2 Crustal formation at the CRR

The thickness of the crust in the study area is shown to be 5.0 ± 0.2 km by the 2D forward models, consistent with a previous estimate (Collins et al., 1989). This is thinner than average oceanic crust, estimated to be 7.1 ± 0.8 km by White et al. (1992) and 6 ± 1 km by Grevemeyer et al. (2018b), although within the limits of expectation. The relative thinness of the crust could be interpret to indicate a lower melt supply with lower mantle temperatures (Klein and Langmuir, 1987; Su et al., 1994), however the relative smoothness of the seabed and top basement, along with the homogeneity of the seismic structure and inferred thickness of the extrusive layer, suggests a period of plentiful melt supply relative to spreading rate, allowing the crust to form without a great proportion of tectonic stretching through faulting. Studies of slower spreading ridges exhibit more lateral variability in upper crustal structure, thought to be caused by increased tectonic spreading (Hussenoeder et al., 2002), whereas the flanks of faster, magmatic spreading ridges exhibit more consistent structure (Toomey et al., 1990). Spreading rate estimates for the CRR suggest generally high spreading rates when the crust at boreole 504B was formed (Wilson and Hey, 1995; Wilson et al., 2018) compared to rates from 0–6 Ma. Geochemical studies of Hole 504B lavas reveal high Mg values, indicating short melt residence times in a steadily replenished magma chamber (Anderson et al., 1982), supporting this conclusion.

Although the Galapagos hotspot is currently >800 km from the CRR, hotspot movement and plate motion reconstructions suggest that in the past the CRR was significantly closer to the hotspot (Meschede and Barckhausen, 2000), suggesting a possible explanation for the increased spreading rate and melt supply ∼7 Ma. However, enriched geochemical signatures from the Galapagos hotspot seen in some EPR and GSC lavas (Geldmacher et al., 2013) have not been found in any chemical analysis of Hole 504B rocks (e.g. Alt et al., 1996), and Wilson and Hey (1995) suggest that hotspot-related asthenospheric material could not migrate along the Cocos-Nazca plate boundary beyond the ridge-offsetting >50 km-long transform faults, which would have prevented it from reaching the CRR according to their model of the ridge evolution. Thus the period of enhanced melt supply at ∼7 Ma was likely unrelated to the Galapagos hotspot, but possibly to a faster spreading rate.

### 7.4.3 Anisotropy in the upper oceanic crust

The results of azimuthal anisotropy analysis presented in Section 5.5.3 show significant anisotropy in both Vp and Vs with a fast direction of 097°, parallel to the strike of the abyssal hills (∼095°) and CRR (∼092°), in the upper 3.5 km of the igneous basement. Azimuthal anisotropy has been frequently observed in the oceanic crust, both at spreading ridges (Dunn and Toomey, 2001) and within older crust (Shearer and Orcutt, 1985), and is attributed to aligned faults and fractures formed close to the spreading centre as the crust is stretched, and subsides, as it moves off-axis. The Vp anisotropy patterns indicate a slight predominance of open, wider fractures, which suggests that not all open porosity has been sealed by 7 Ma. This conclusion is supported by the presumed presence of large volumes of voids and fractures at borehole 504B (Alt et al., 1993) ('presumed' as voids cannot be sampled). Anisotropy in the top 0.5 km of the crust, shown to correspond to seismic layer 2A and consist of extrusive lavas at borehole 504B, shows the weakest anisotropy signal, suggesting that the portion of the crust contains more randomly oriented void space. This is consistent with the more hummocky, random emplacement of pillow lava structures, which comprise the majority of the extrusive section at borehole 504B. Other common extrusive lithology types at the borehole, such as sheet flows and breccias, would not be expected to contribute to an azimuthal anisotropy signature.

From 0.5–1.5 km bb, however, the strength of anisotropy increases to significant levels within seismic layer 2B, corresponding to the sheeted dyke complex. This is unsurprising given that the dykes are thought to form ridge-parallel and so enhance anisotropic signals through ridge-parallel chilled margins and fractures between dykes. This pattern is supported by velocity models of layer 2 at the East Pacific Rise at 9°50'N (Sohn et al., 2004) which do not demonstrate azimuthal anisotropy within the extrusive layer, but do exhibit ∼4% anisotropy within the upper dykes, suggesting that fracture orientations are more random in the lavas.

## 7.5 Crustal variation around borehole 504B

The fast velocity within the upper crust at borehole 504B and across the 3D model is interpreted to indicate that the crust here has been mineralised and partially sealed by alteration products. This is supported by analysis of core samples from Hole 504B which exhibit extensive alteration. However, investigating any variations in velocity or Poisson's ratio across the model volume, as well as interpreting seismic anisotropy results, could elucidate fracturing patterns across the study area which control how and where fluids flow and, thus, where alteration may preferentially occur, or occur more intensely.

Notable anomalies in the Vp and Vs velocity models occur in the upper 1 km of the crust, comprising layer 2A and the top of layer 2B, with the greatest amplitudes in the top ∼0.5 km corresponding to the extrusive lava section. The largest positive anomalies in both Vp and Vs occur at Y=∼20 km and Y=∼32 km (Figures 3.21 and 5.10), extending

E–W across the model and from the top basement to ∼1 km in depth. The most significant negative anomaly occurs trending E–W across the model at Y=25 km, and is only evident in Vp (Figure 7.7). The general E–W trend of these anomalies suggests that they may be related to the basement ridges, troughs and faults which also strike E–W. The negative anomaly at Y=25 km occurs in a basement low with one large and two smaller basement faults running through it. The positive anomalies at Y=20 km and Y=32 km occur close to basement ridges, with the Y=20 km anomaly flanked by two large basement faults to the north and south, and the Y=32 km anomaly flanked by one large basement fault to the south, with another running through the anomaly. However, the amplitude of these anomalies is a maximum of 0.4 km $s^{-1}$ in Vp and 0.2 km $s^{-1}$ is Vs, with the majority of the anomaly at a lower amplitude of ∼0.2 km $s^{-1}$ in Vp and 0.1 km $s^{-1}$ in Vs. While these anomalies are mostly above the 5% of velocity, and 4 km-size shown to be resolvable by checkerboard testing, they are still relatively small perturbations. The Poisson's ratio model shows some slightly clearer patterns, with higher values extending E–W across the model at Y=20 and 32 km, and lows at Y=25 and 40 km. Thus generally, where Vp is high, Poisson's ratio is also high, and where Vp is low, Poisson's ratio is low. Comparing the structure at 0.7 km bb, (where the anomaly amplitude is highest) with the basement topography and faults (Figure 7.7), the areas of high Poisson's ratio ($\sigma \geq 0.24$) occur predominantly where the basement is slightly shallower or near ridges, and are mostly flanked by basement faults or both flanked and intersected. The areas of lower Poisson's ratio ($\sigma \sim 0.20$) occur predominantly in areas of deeper basement, are are mostly cross-cut by multiple faults. However, similarly to the Vp and Vs anomalies, the variation in Poisson's ratio from 0.20–0.24 is not particularly large.

To further investigate whether there may be a relationship between these anomalies, despite their small amplitude, and basement topography or faulting, a N–S cross-section was extracted from the models through the position of borehole 504B, converted to TWTT using the Vp velocities, and overlain onto the profile SG_I MCS image (Figure 7.8). In general the overlays demonstrate the smoothness and homogeneity of the Vp and Vs models, with velocity contours following the basement topography. The small, negative velocity anomalies in Vp at Y=25 km and Y=40 km are difficult to observe, although they do occur in a region of flat, relatively deep basement, and a low between two basement highs, respectively. The anomalies in the Poisson's ratio model are more prominent, with low values of 0.20 present at Y=25 km and Y=40 km. These Poisson's ratio anomalies are also shown in a depth cross section overlain with the interpreted basement faults, and in relation to the bathymetric map of the study area (Figure 7.9). The anomaly at Y=25 km is ∼6 km-wide at the top basement, and occurs in a region of flat, deep topography which is considerably faulted in the sediments and is cut by two major basement faults. The anomaly at Y=40 km is also ∼6 km wide at the top basement, and occurs mainly on the northern flank of a basement ridge at Y=41.5 km and into the intervening trough between this ridge, and an adjacent ridge at Y=36.5 km. This anomaly is intersected by cross-cutting north- and south-dipping major basement faults. Studying the cross-sections

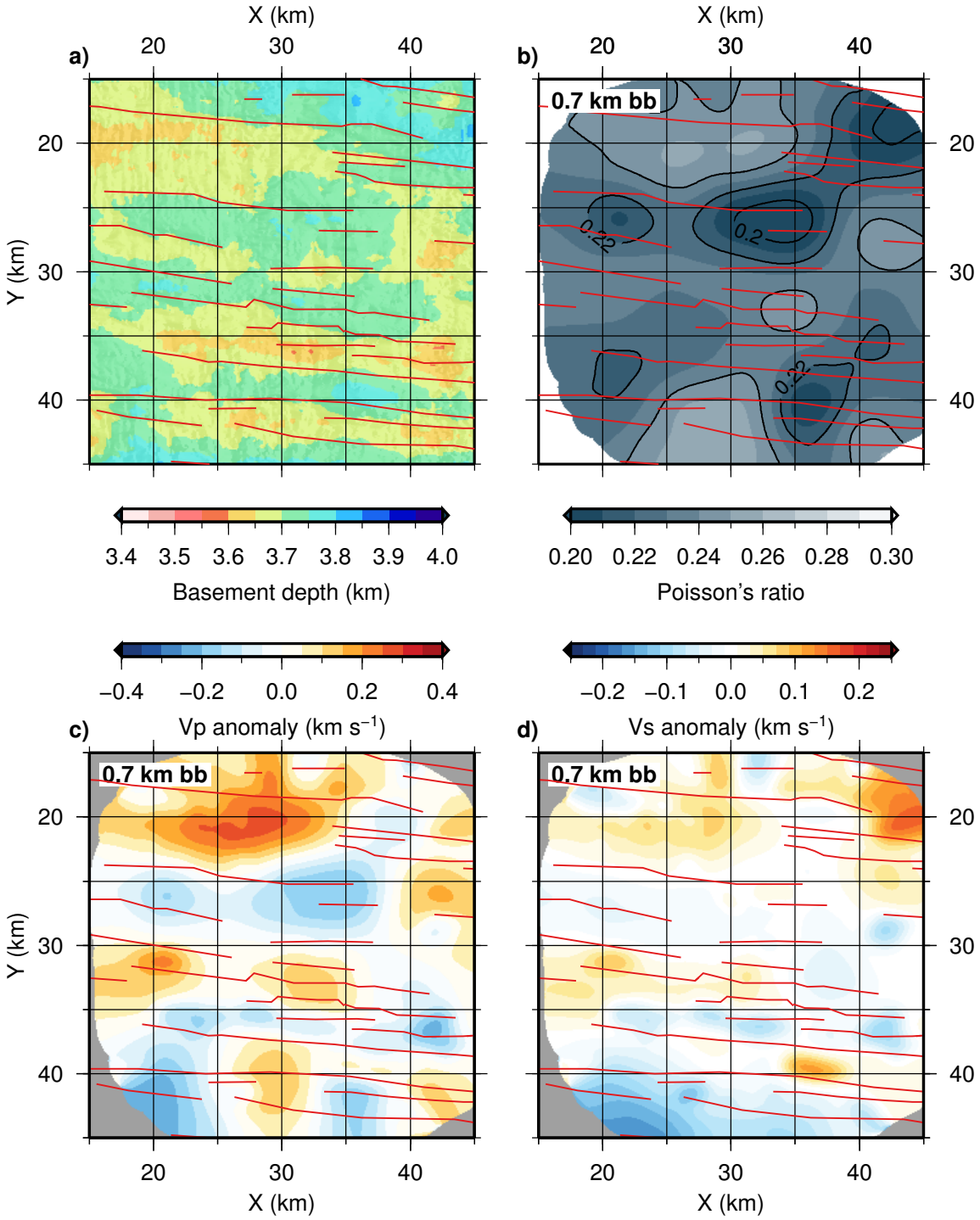


Figure 7.7: Basement topography (a) compared to the Poisson's ratio (b) and smoothed Vp (c) and Vs (d) anomaly models at 0.7 km bb. Red lines show basement faults interpreted from basement topography and slope (Section 2.2.2). The lowest values of Poisson's ratio (at Y=20 km and Y=40 km) occur in basement troughs.

through the model (Section 5.4) shows that these anomalies are predominantly confined to layer 2A, corresponding to the extrusive lavas and transition zone. These results could indicate that these areas of low Poisson's ratio are more fractured, containing more open

bulk porosity in the form of voids or wider, higher aspect ratio, more open fractures, and the area of higher Poisson's ratio in between them, including the crust sampled by borehole 504B, contains less open porosity and thinner, lower aspect ratio, more 'closed' fractures.

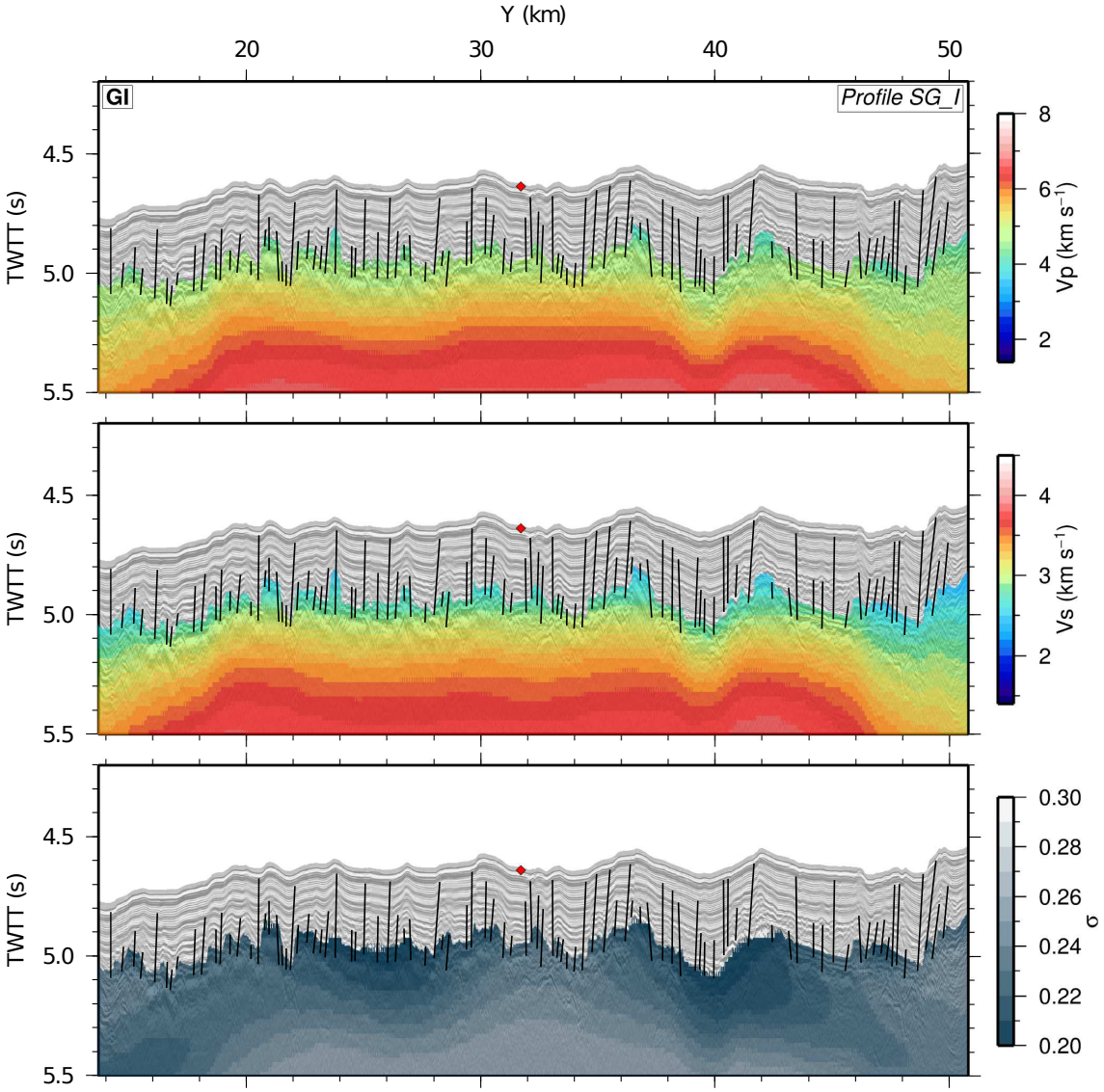


Figure 7.8: GI airgun array MCS image of profile SG_I, with interpreted faults (Section 2.4.4 - black lines) overlain with cross-sections from the Vp (top), Vs (middle) and Poisson's ratio (bottom) models, extracted through the location of borehole 504B (red diamond). Note that the vertical scale here is TWTT, which causes the sediment section to look disproportionately thick, and distorts depths in the igneous basement to look disproportionately thin or shallow.

### 7.5.1 Hydrothermal circulation patterns

The general homogeneity in the structure of the igneous basement in the study area suggests that the crust may have relatively constant lateral porosity and permeability. This could facilitate widespread and consistent fluid flow through the crust. However, even small basement faults and fractures, introducing heterogeneity into the permeability

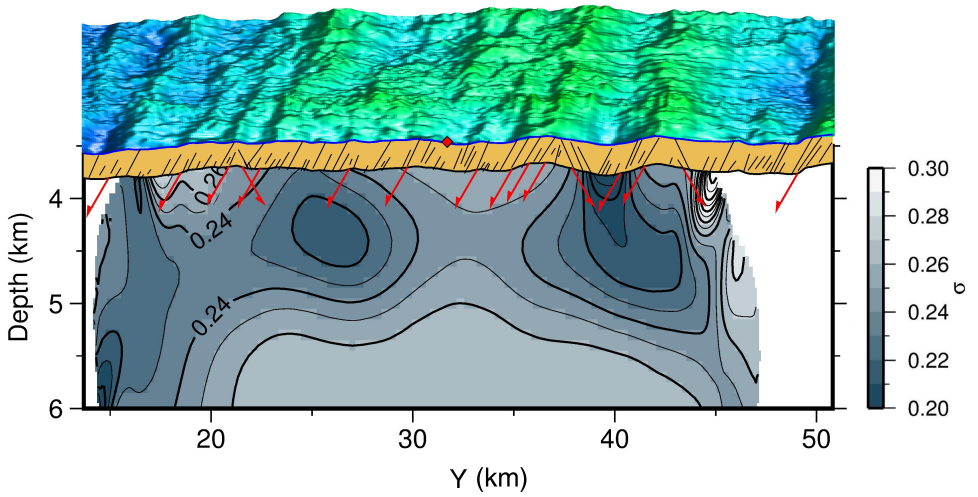


Figure 7.9: Poisson's ratio cross-section through borehole 504B (red diamond), showing the sediments (light brown), and overlying bathymetry (perspective map). Black lines show the interpreted faults through the sediment from the profile SG_I MCS section (Section 2.4.4), and red lines show the interpreted basement faults from the basement slope analysis (Section 2.2.2), which are plotted with a standard normal fault dip of 60°, and to arbitrarily penetrate ~400 m into the basement.

structure of the crust, may cause the focussing of fluid flow, especially when the crust was younger and some basement scarps remained unsedimented and open to the ocean. Focussing of fluids could then form areas of more intensely altered rock, with more pore space infilled with hydrothermal products.

The anomalies in Vp and Poisson's ratio could indicate such variations in the intensity of hydrothermal alteration. As a hypothesis, if it is assumed that the crust was initially regularly fractured everywhere, then the highs in Vp and Poisson's ratio (such as at Y=32 km and at borehole 504B) could represent areas which have experienced higher volumes of fluid flow which have resulted in greater 'sealing' of fractures and pore space. A possible explanation for why this area has experienced higher volumes of fluid flow and alteration is that it may form part of the hanging wall of the large north-dipping basement faults that form the north side of the basement ridge at Y=36 km. Models of fluid circulation within the oceanic crust suggest that ridge-parallel fractures can act as conduits for fluid flow (Haymon et al., 1991; Farahat et al., 2017) both at the ridge axis and on ridge flanks, and with ridge-parallel and ridge-perpendicular directions of fluid flow. If these faults acted as permeability pathways for fluids to enter or exit the crust, then fluids may have percolated upwards from the main fault, mineralising the overlying crust in the hanging wall of the fault. The regions of low Vp and Poisson's ratio anomalies, which tend to be more heavily cross-cut by faults as opposed to flanked by them (Figure 7.7), would then represent more fractured areas which contain more open porosity, and could currently be acting as fluid flow pathways through the crust laterally, or via high-permeability paths through the sediments introduced by the reactivation of basement faults (Swift et al., 1998a; Farahat et al., 2017).

## 7.6 Summary

In this chapter the results from this study have been interpreted and discussed. Firstly, the controlling factors on the seismic velocity of the oceanic crust were considered, to aid in the interpretation of the velocity structure at borehole 504B in terms of rock characteristics. It was shown that the gradient-depth profile approach used to characterise the upper crust at borehole 504B in Chapter 6 is applicable to another deep crustal borehole, 1256D, and that this method can help to locate the 2A/2B boundary, which predominantly represents the extrusive-intrusive transition. Further, this approach enables consistent terminology to be used for both on-axis and off-axis oceanic crust, negating the need to introduce a layer 2C.

Secondly, it was shown that at borehole 504B the seismic layer 2/3 boundary may occur within the sheeted dyke complex and be related to gradual downhole changes in porosity or alteration. However, uncertainty in the results means that this result is not conclusive, and the boundary could also represent a lithological change from dykes to gabbros below the base of the current borehole. Further studies are thus required to resolve what the layer 2/3 boundary represents.

Thirdly, the general seismic structure of the ∼7 Ma oceanic crust surrounding borehole 504B was considered in terms of the manner of its formation, and its evolution. This homogeneous and smooth section of crust is likely to have formed during a period of spreading with an enhanced melt supply, potentially caused by a spreading rate increase. The average velocity of the upper crust suggests that it has been mineralised by hydrothermal alteration processes at similar rates to the crust at other spreading ridges.

Finally, the observation of anomalies in the upper crust in the 3D velocity models results in a hypothesis that these may represent preferentially altered parts of the crust, potentially through the channelling of fluids along large basement faults leading to the mineralisation of the overlying hanging wall. Further studies are needed to test this hypothesis.

In the next, and final, chapter, the results and conclusions of this study will be summarised and suggestions for further work will be made.

# Chapter 8

# Conclusions and future work

## 8.1 Conclusions

The aims of this study were to characterise the seismic structure of the upper oceanic crust at borehole 504B and the surrounding area, in order to better understand the controls on the seismic velocity structure of the crust, what the seismic layers correspond to in the subsurface, and fracturing and alteration within aged crust on ridge flanks. The main conclusions are:

- the P-wave seismic structure of the upper crust at borehole 504B consists of a 0.8 km-thick layer 2A, with an average velocity within the top part of 4.5 km $s^{-1}$, and with a high gradient zone at its base, and a ∼0.9 km-thick layer 2B, with an average velocity of ∼6.0 km $s^{-1}$. These layers were defined using their velocity gradient as opposed to their absolute velocity, with a high gradient zone (>2.0 $s^{-1}$) at the base of layer 2A considered the defining characteristic of the layer 2A/2B boundary in inversion models, separating the lower-gradient (∼1 $s^{-1}$) upper part of layer 2A, and the moderate-gradient (<1.5 $s^{-1}$) layer 2B;

- the S-wave seismic structure at borehole 504B, previously undefined, follows a similar pattern to the P-wave structure. Layer 2A consists of a region of low Vs gradient (∼0.5 $s^{-1}$) with an average velocity of ∼2.6 km $s^{-1}$, followed by a high gradient region (>1.0 $s^{-1}$). Layer 2B has a decreasing gradient with depth, and an average velocity of ∼3.4 km $s^{-1}$. The similarity between the Vp and Vs profiles results in a relatively constant Poisson's ratio down the borehole, varying from 0.24 at the top, to 0.26 at the bottom;

- the use of velocity-depth gradient to define seismic layers, as opposed to absolute velocity, enables the comparison of velocity profiles produced via different approaches and at different scales. This method derives a simpler terminology for the structure of oceanic crust which is consistent for all ages. The boundary between layers 2A and 2B is represented in smoothed tomographic inversion models by a change in Vp gradient to >2 $s^{-1}$, representing a transition zone, while in forward ray-trace models

with discrete layers, a ∼2 km $s^{-1}$ first-order discontinuity occurs at the point of greatest change in physical properties. In addition, the 2A caustic arrival indicates the existence of a high gradient transition zone at the layer 2A/2B boundary;

- as observed at boreholes 504B and 1256D, the velocity change at the layer 2A/2B boundary, defined using the gradient-depth method, is caused by a reduction in porosity, primarily due to the change in lithology from extrusive lavas to the sheeted dyke complex, but a change to more intense, higher temperature alteration, which also occurs at this porosity front, is likely to also contribute to the seismic boundary. The gradient-depth method can be applied to seismic studies without a coincident borehole to help locate the extrusive-intrusive lithological transition, in magmatically-accreted crust formed in mid-ocean ridge settings. The use of this method to define the structure of the crust removes the need to introduce a 'layer 2C' to represent the intrusive dyke layer off-axis;

- the depth of the seismic layer 2/3 boundary at borehole 504B likely occurs within the sheeted dyke complex and is caused by gradual changes in porosity or alteration mineralogy although, due to uncertainties in depth determination, the boundary could occur below the base of the current drill hole. Thus, the true nature of the layer 2/3 boundary remains unknown;

- the crust surrounding borehole 504B exhibits a smooth and homogeneous velocity structure (both Vp and Vs), indicating little variation in its lithological and porosity structure laterally, either ridge-parallel or ridge-perpendicular. Total crustal thickness in the region is 5.0 ± 0.2 km, and it is interpreted to have most likely formed during a period of enhanced melt supply at the Costa Rica Rift, with little tectonic stretching. Mapping of the layer 2A caustic shows little variation in the depth of layer 2B in the igneous basement in a N–S direction crossing borehole 504B. The structure sampled in the borehole can thus be considered typical of the surrounding crust; and

- the oceanic crust in the study area has been mineralised via hydrothermal alteration to a similar extent to other ridge flanks, although anisotropy results indicate a significant amount of open fractures remain, particularly within the sheeted dyke section. Small velocity and Poisson's ratio anomalies suggest there could be zones of preferential alteration and fluid flow relating to faulting structures within the crust.

## 8.2 Future work

### 8.2.1 Seismic structure at borehole 504B

Although the SG dataset of this study is the most comprehensive yet to be acquired over borehole 504B and the surrounding region, alternative approaches to tomographic

inversion performed here have provided higher resolution velocity models of the upper crust (Christeson et al., 2012). Full-waveform inversion (FWI) techniques (e.g. Pratt et al., 1998) are capable of resolving velocity anomalies to scales of half the seismic wavelength (Virieux and Operto, 2009). The long-offset arrivals recorded on the SAP profiles are suitable for FWI, with Morgan (pers. comm) collaborating with the OSCAR project to produce FWI images. Initial analysis performed by Silverton et al. (pers. comm.), has produced detailed images of the sediment structure along profile SAP_B. The 3D velocity model produced in this study provides a well-constrained starting model to extend the FWI analysis into the upper oceanic crust. This should result in a velocity model with the highest resolution possible using the available data and the currently most advanced techniques. The FWI model should reveal small velocity anomalies in the upper crust at borehole 504B and along profile SAP_B (coincident with SG_I), which could indicate, in more detail, variations in the lithological structure of the crust, regions of more intense hydrothermal mineralisation, and likely pathways for fluid flow.

### 8.2.2 Testing the gradient-depth method

The gradient-depth method of characterising the seismic structure of the oceanic crust, and relating it to the intrusive/extensive transition, would benefit from further testing at other sites to determine its generic capability across all spreading rates and crustal formation styles. First and foremost, it would be beneficial to produce seismic velocity models of a more comparable nature at borehole 1256D to those presented for borehole 504B. This may be possible by re-processing the seismic site survey at site 1256D (Wilson et al., 2003), although may require the acquisition of a more comprehensive, 3D seismic dataset focussed explicitly on the borehole. Focussed analysis on the causes of seismic velocity change within the upper crust would also be beneficial in the interpretation of velocity models. Creating simple theoretical models, based on chosen rock characteristics such as porosity and lithology, and investigating the effect of changes the characteristics on the final velocity, and the nature of synthetic seismograms, could help derive basic relationships between these properties and the velocity-depth gradient, which could aid velocity model interpretation. An IODP expedition is planned to return to borehole 504B in 2020 to acquire downhole images using a Formation MicroScanner (FMS) tool. The detailed information acquired from these logs about downhole lithology and fracturing will help compensate for any inaccuracies in the mapped lithostratigraphy due to poor core recovery, and also aid in the understanding of the controls of rock characteristics on measured velocity.

As Holes 504B and 1256D are currently the only two boreholes to have drilled deep enough into the igneous oceanic crust, the testing of the gradient-depth method in other locations must await further drilling campaigns. An IODP Expedition to the southern Mid-Atlantic, scheduled for 2020-2021, aims to drill a series of boreholes through the sediment and top basement in a flow-line transect from the MAR to the South American

coastline. A 2D active seismic experiment was recently conducted along the same transect, and is currently being analysed by Christeson (pers. comm). Provided the boreholes penetrate deep enough into the upper crust, the comparison of the drilling results with seismic velocity models will be an effective test for the use of the gradient-depth method to locate the extrusive-intrusive transition.

### 8.2.3 Resolving the nature of the layer 2/3 boundary

The results from this study suggest that the seismic layer 2/3 boundary at borehole 504B likely occurs within the sheeted dyke complex, representing gradual downhole changes in porosity and mineralogy, as opposed to at the basalt-gabbro interface. However, uncertainties in the depth estimate mean that the boundary could occur below the bottom the current borehole, in unsampled crust. Further, at borehole 1256D, uncertainties in the depth estimate of the boundary from a 1D refraction profile (Shipboard Scientific Party, 2003b), along with the small thicknesses and highly deformed nature of the two gabbroic lenses sampled during drilling, suggest that the nature of the layer 2/3 boundary cannot be confidently interpreted there either. These conclusions support the need for further drilling in either, or both, of these deep boreholes. The maximum error bound on the layer 2/3 depth estimate lies just 64 m below the bottom of the current hole at borehole 504B, and the dyke-gabbro interface is hypothesised to also be close to the base of the hole (Alt et al., 1993). Just ∼100 m of further penetration is likely to enable a much clearer conclusion to be drawn from the available seismic data as to the causes of the layer 2/3 boundary. Likewise, at borehole 1256D, deepening the hole by just a few hundred metres to penetrate unequivocally into the plutonic complex could inform this debate, especially if accompanied by a more comprehensive seismic experiment than has currently been conducted at the site.

### 8.2.4 Alteration patterns and fluid flow pathways

Small velocity anomalies observed in the upper oceanic crust in this study led to the hypothesis that they may represent regions of more intense mineralisation, due to the focusing of fluid flow along large basement faults leading to increases in the deposition of hydrothermal products in the overlying hanging wall fault block. This hypothesis could be tested in a number of ways:

- the production of higher resolution seismic models using FWI (described above), would map these anomalies in more detail with respect to the basement topography;

- detailed interpretation of the GI airgun array seismic sections in the SG could provide a more comprehensive understanding of the history of faulting in the area, to compare to the velocity models alone;

- numerical simulations of hydrothermal circulation, using simplified permeability models based on the hypothesis, could indicate the likelihood of fluids flowing through the crust in this manner, and general estimates of the required permeabilities; and

- field studies of faults and alteration within ophiolites or comparable continental systems with hydrothermal circulation could provide evidence to support this hypothesis, or show that these systems are unlikely to form.

Results from this study also suggest that it is likely that the low-temperature to greenschist facies alteration front occurs at the same depth as the lava-dyke transition zone. Further testing of this hypothesis, which has further implications for understanding fluid flow and the temperature structure of oceanic crust, could be undertaken using more complete compilations of alteration regimes mapped within ophiolites, more detailed mapping of exposed tectonic escarpments such as at the Hess Deep and Blanco Transform Fault, and further numerical simulations of hydrothermal circulation cells.

### 8.2.5 3D variations in anisotropy

Seismic anisotropy was determined in the crust at borehole 504B, with the strongest signature in this study observed by comparing of travel time residuals with the azimuth of ray paths. Analysing anisotropy can indicate possible fluid pathways through the crust, as well as whether fractures have been sealed by hydrothermal alteration products or remain open. The method used in this study does not, however, allow for the detailed mapping of changes in anisotropy laterally, or with depth, as would be required to thoroughly investigate these processes. A technique to perform azimuth-dependent inversion to attempt to recover a 3D anisotropy model is described in Appendix E, however, this was not found to be successful for this study. Other authors, such as Weekly et al. (2014) and Dunn (2015), utilise sophisticated seismic inversion codes which also resolve for anisotropy, alongside velocity. These codes have enabled the mapping of changes in fracturing at the Juan de Fuca Ridge and Eastern Lau Spreading Centre, and acquiring similar models for the SG area would prove a valuable addition to the understanding of fracturing patterns within the crust, fluid flow pathways, and alteration patterns.

Another method used to determine anisotropy and fracturing within the crust is the analysis of the specific particle motion of crustal seismic arrivals using data recorded by three-component OBS geophone sensors (e.g. Shearer and Orcutt, 1985). Once oriented to their relative azimuth, this analysis can reveal S-wave splitting, the orientation of the fast and slow waves, and the time delay between their arrival, to give indications of fracture orientation and density. Initial analysis of S-wave arrival particle motion on the two horizontal geophones demonstrates that splitting likely occurs in this region (Figure 8.1), suggesting that this analysis could provide anisotropy estimates to complement the travel time residual results.

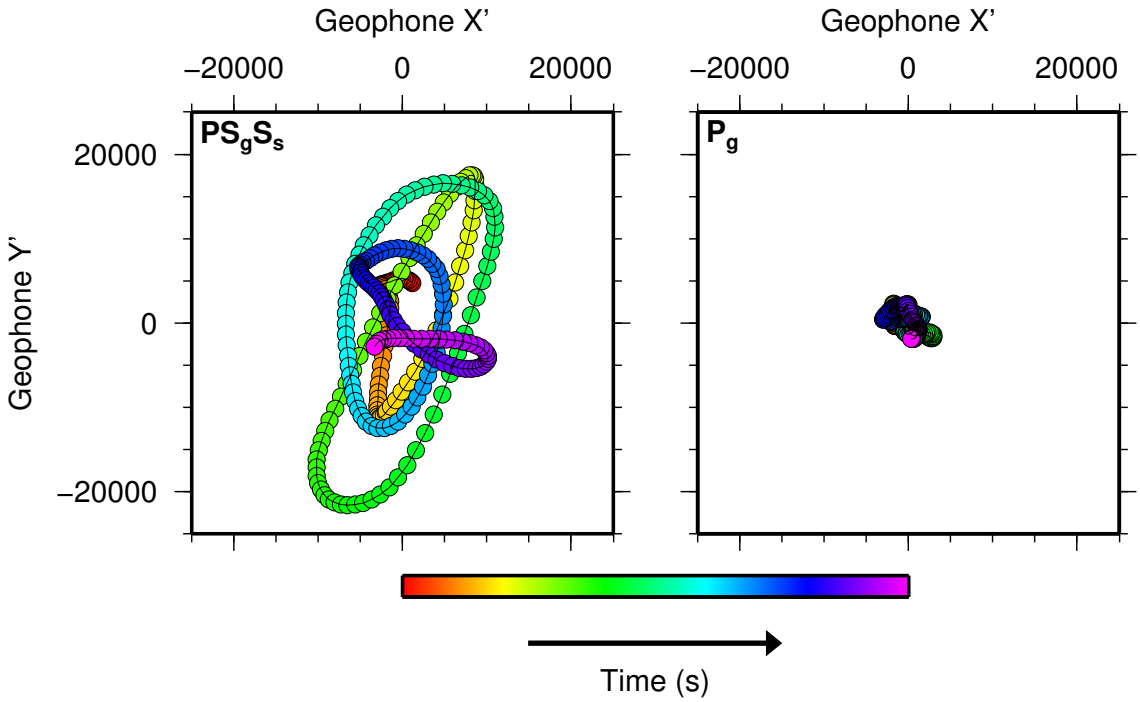


Figure 8.1: Amplitude of the S-wave crustal refraction, $PS_gS_s$ on the two horizontal geophones, compared with the P-wave crustal refraction, $P_g$. The amplitude is plotted for every sample (0.002 s increment) for the first 0.5 s of the arrival wavetrain, and is colour-coded by time. The S-wave arrival exhibits considerable directionality compared with the P-wave arrival, and also shows a 90° change in the dominant direction of motion towards the end of the sampled waveform.

### 8.2.6 Magmatic vs. tectonic crust

This study has focussed on understanding the velocity structure of magmatically-formed oceanic crust, and proposed methods of using velocity models to determine its lithological structure, which likely conforms to the traditional idea of the composition of oceanic crust of basaltic lavas, sheeted dykes and plutonic gabbros (Penrose Conference Participants, 1972). However, a significant proportion of all oceanic crust is dominantly created tectonically (Smith et al., 2008; Escartín et al., 2008), and exhibits huge variability in its mode of formation (e.g. Dick et al., 2003; Cannat et al., 2006), lithological composition (Tucholke and Lin, 1994; Canales et al., 2000), and seismic velocity structure (e.g. Muller et al., 1999). For example, at the ultra-slow spreading South West Indian Ridge, regions of the crust are thought to be composed predominantly of gabbro and exhumed, serpentinised peridotite, whereas proximal sections suggest a more magmatic origin (Muller et al., 2000). Therefore, a natural extension of this study would be to seek to better characterise the variability in the structure of oceanic crust through similar studies at a variety of settings, including mid-ocean ridges with rates from ultra-slow to super-fast, back-arc basin spreading centres, crust influenced by hotspot volcanism, and downgoing plates at subduction zones. The structure and composition of the oceanic crust has implications for the dynamics of subduction zone processes. For example, mineral composition influences slab dehydration (Schmidt and Poli, 1998; Zack et al., 2003; Rüpke et al., 2004) which

affects the nucleation of earthquakes (Kerrick and Connolly, 2001; Hacker et al., 2003) and the style of arc volcanism (Elliott et al., 1997; Kerrick and Connolly, 2001). Therefore, a better understanding of the structure of oceanic crust at formation, and how this evolves with age, would be significant for a wide variety of vital research questions.

## 8.3 Summary

The study has presented the most recent and comprehensive geophysical experiment yet conducted over borehole 504B, an often-used 'reference' point for the structure of oceanic crust. These new results, which suggest how the crust at borehole 504B may have been formed and altered as it aged, enhance our understanding of the seismic structure at the borehole and lead to a more consistent method to characterise and apply terminology to seismic velocity models. This clarification will aid the interpretation of velocity models at other locations in terms of lithological structure, alteration and fracturing within the crust, and result in a more consistent approach that, subsequently, enables their more reliable comparison to determine the diversity of crustal formation processes and how the crust they produce evolves over time. In turn, this will allow better understanding of subduction zone processes and, more importantly, what, and how, controls earthquake initiation, and styles of eruption at arc volcanoes.

# Bibliography

Adamson, A. C. (1985). Basement Lithostratigraphy, Deep Sea Drilling Project Hole 504B. In Anderson, R. N., Honnorez, J., and Becker, K., editors, *Initial Reports of the Deep Sea Drilling Project*, volume 83, chapter 3, pages 121–127. US Govt. Printing Office, Washington, DC. doi: 10.2973/dsdp.proc.83.103.1985.

Adcroft, A., Scott, J. R., and Marotzke, J. (2001). Impact of geothermal heating on the global ocean circulation. *Geophysical Research Letters*, 28(9):1735–1738. doi: 10.1029/2000GL012182.

Alt, J. C., Honnorez, J., Laverne, C., and Emmermann, R. (1986). Hydrothermal alteration of a 1 km section through the upper oceanic crust, Deep Sea Drilling Project Hole 504B: Mineralogy, chemistry and evolution of seawater-basalt interactions. *Journal of Geophysical Research*, 91(B10):10309–10335. doi: 10.1029/JB091iB10p10309.

Alt, J. C., Kinoshita, H., and Stokking, L. B. (1993). *Proceedings of the Ocean Drilling Program, Initial Reports*, volume 148. Ocean Drilling Program, College Station, Texas. doi: 10.2973/odp.proc.ir.148.1993.

Alt, J. C., Laverne, C., Coggon, R. M., Teagle, D. A. H., Banerjee, N. R., Morgan, S., Smith-Duque, C. E., Harris, M., and Galli, L. (2010). Subsurface structure of a submarine hydrothermal system in ocean crust formed at the East Pacific Rise, ODP/IODP Site 1256. *Geochemistry, Geophysics, Geosystems*, 11(10):1–28. doi: 10.1029/2010GC003144.

Alt, J. C., Laverne, C., Vanko, D. A., Tartarotti, P., Teagle, D. A. H., Bach, W., Zuleger, E., Ezringer, J., Honnorez, J., Pezard, P. A., Becker, K., Salisbury, M. H., and Wilkens, R. H. (1996). Hydrothermal alteration of a section of upper oceanic crust in the easter equatorial Pacific: A synthesis of results from Site 504 (DSDP Legs 69, 70, and 83, and ODP Legs 111, 137, 140, and 148). In Alt, J. C., Kinoshita, H., Stokking, L. B., and Michael, P. J., editors, *Proceedings of the Ocean Drilling Program, Scientific Results*, volume 148, chapter 34, pages 417–434. Ocean Drilling Program, College Station, Texas. doi: 10.2973/odp.proc.sr.148.159.1996.

Anderson, R. N., Honnorez, J., Becker, K., Adamson, A. C., Alt, J. C., Emmermann, R., Kempton, P. D., Kinoshita, H., Laverne, C., Mottl, M. J., and Newmark, R. L. (1982).

DSDP Hole 504B, the first reference section over 1 km through Layer 2 of the oceanic crust. *Nature*, 300(5893):589–594. doi: 10.1038/300589a0.

Archie, G. (1942). The Electrical Resistivity Log as an Aid in Determining Some Reservoir Characteristics. *Transactions of the AIME*, 146(01):54–62. doi: 10.2118/942054-G.

Barclay, A. H., Toomey, D. R., and Solomon, S. C. (1998). Seismic structure and crustal magmatism at the Mid-Atlantic Ridge, 35°N. *Journal of Geophysical Research: Solid Earth*, 103(B8):17827–17844. doi: 10.1029/98JB01275.

Barclay, A. H., Toomey, D. R., and Solomon, S. C. (2001). Microearthquake characteristics and crustal Vp/Vs structure at the Mid-Atlantic Ridge, 35°N. *Journal of Geophysical Research: Solid Earth*, 106(B2):2017–2034. doi: 10.1029/2000JB900371.

Barclay, A. H. and Wilcock, W. S. D. (2004). Upper crustal seismic velocity structure and microearthquake depths at the Endeavour Segment, Juan de Fuca Ridge. *Geochemistry, Geophysics, Geosystems*, 5(1):1–23. doi: 10.1029/2003GC000604.

Barnes, J. M., Morales Maqueda, M. A., Polton, J. A., and Megann, A. P. (2018). Idealised modelling of ocean circulation driven by conductive and hydrothermal fluxes at the seabed. *Ocean Modelling*, 122:26–35. doi: 10.1016/J.OCEMOD.2017.12.005.

Bascom, W. (1961). *A Hole in the Bottom of the Sea: The Story of the Mohole Project*. Doubleday, Garden City, NY.

Becker, K. and Sakai, H. (1988). *Proceedings of the Ocean Drilling Program, Initial Reports*, volume 111. Ocean Drilling Program, College Station, Texas. doi: 10.2973/odp.proc.ir.111.1988.

Becker, K., Sakai, H., Adamson, A. C., Alexandrovich, J., Alt, J. C., Anderson, R. N., Bideau, D., Gable, R., Herzig, P. M., Houghton, S., Ishizuka, H., Kawahata, H., Kinoshita, H., Langseth, M. G., Lovell, M. A., Malpas, J., Masuda, H., Merrill, R. B., Morin, R. H., Mottl, M. J., Pariso, J. E., Pezard, P., Phillips, J., Sparks, J., and Uhlig, S. (1989). Drilling deep into young oceanic crust, Hole 504B, Costa Rica Rift. *Reviews of Geophysics*, 27(1):79–102. doi: 10.1029/RG027i001p00079.

Becker, K., Von Herzen, R. P., Francis, T. J. G., Anderson, R. N., Honnorez, J., Adamson, A. C., Alt, J. C., Emmermann, R., Kempton, P. D., Kinoshita, H., Laverne, C., Mottl, M. J., and Newmark, R. L. (1982). In situ electrical resistivity and bulk porosity of the oceanic crust Costa Rica Rift. *Nature*, 300(5893):594–598. doi: 10.1038/300594a0.

Behn, M. D. and Ito, G. (2008). Magmatic and tectonic extension at mid-ocean ridges: 1. Controls on fault characteristics. *Geochemistry, Geophysics, Geosystems*, 9(8):1–22. doi: 10.1029/2008GC001965.

Beiersdorf, H. and Natland, J. H. (1983). Sedimentary and diagenetic processes in the central Panama Basin since the late Miocene: the lithology and composition of sediments from Deep Sea Drilling Project sites 504 and 505. In Cann, J. R., Langseth, M. G., Honnorez, J., Von Herzen, R. P., and White, S. M., editors, *Initial Reports of the Deep Sea Drilling Project*, volume 69, chapter 14, pages 343–383. US Govt. Printing Office, Washington, DC. doi: 10.2973/dsdp.proc.69.114.1983.

Berge, P. A., Fryer, G. J., and Wilkens, R. H. (1992). Velocity-porosity relationships in the upper oceanic crust: Theoretical considerations. *Journal of Geophysical Research*, 97(B11):15239–15254. doi: 10.1029/92JB01464.

Bird, P. (2003). An updated digital model of plate boundaries. *Geochemistry, Geophysics, Geosystems*, 4(3):1–52. doi: 10.1029/2001GC000252.

Bohlen, T., De Nil, D., Kohn, D., and Jetschny, S. (2016). SOFI2D: seismic modeling with finite differences 2D - elastic and viscoelastic version.

Boudier, F., Nicolas, A., and Ildefonse, B. (1996). Magma chambers in the Oman ophiolite: fed from the top and the bottom. *Earth and Planetary Science Letters*, 144(1-2):239–250. doi: 10.1016/0012-821X(96)00167-7.

Bratt, S. R. and Purdy, G. M. (1984). Structure and variability of oceanic crust on the flanks of the East Pacific Rise between 11° and 13°N. *Journal of Geophysical Research: Solid Earth*, 89(B7):6111–6125. doi: 10.1029/JB089iB07p06111.

Canales, J. P., Collins, J. A., Escartín, J., and Detrick, R. S. (2000). Seismic structure across the rift valley of the Mid-Atlantic Ridge at 23°20′ (MARK area): Implications for crustal accretion processes at slow spreading ridges. *Journal of Geophysical Research: Solid Earth*, 105(B12):28411–28425. doi: 10.1029/2000JB900301.

Canales, J. P., Detrick, R. S., Carbotte, S. M., Kent, G. M., Diebold, J. B., Harding, A., Babcock, J., Nedimović, M. R., and van Ark, E. (2005). Upper crustal structure and axial topography at intermediate spreading ridges: Seismic constraints from the southern Juan de Fuca Ridge. *Journal of Geophysical Research*, 110(B12104):1–27. doi: 10.1029/2005JB003630.

Canales, J. P., Dunn, R. A., Ito, G., Detrick, R. S., and Sallarès, V. (2014). Effect of Variations in Magma Supply on the Crustal Structure of Mid-Ocean Ridges. In Harpp, K. S., Mittelstaedt, E., D'Ozouville, N., and Graham, D. W., editors, *The Galápagos: A Natural Laboratory for the Earth Sciences*, chapter 17, pages 363–391. John Wiley & Sons, Inc. doi: 10.1002/9781118852538.ch17.

Cann, J. and Gillis, K. (2004). Hydrothermal insights from the Troodos ophiolite, Cyprus. In Davis, E. E. and Elderfield, H., editors, *Hydrogeology of the Oceanic Lithosphere*, chapter 9, pages 272–310. Cambridge University Press.

Cann, J. R. (1970). New Model for the Structure of the Ocean Crust. *Nature*, 226(5249):928–930. doi: 10.1038/226928a0.

Cann, J. R., Blackman, D. K., Smith, D. K., McAllister, E., Janssen, B., Mello, S., Avgerinos, E., Pascoe, A. R., and Escartin, J. (1997). Corrugated slip surfaces formed at ridge–transform intersections on the Mid-Atlantic Ridge. *Nature*, 385(6614):329–332. doi: 10.1038/385329a0.

Cann, J. R. and Von Herzen, R. P. (1983). Downhole logging at Deep Sea Drilling Project sites 501, 504, and 505, near the Costa Rica Rift. In Cann, J. R., Langseth, M. G., Honnorez, J., Von Herzen, R. P., and White, S. M., editors, *Initial Reports of the Deep Sea Drilling Project*, volume 69, chapter 10, pages 281–299. US Govt. Printing Office, Washington, DC. doi: 10.2973/dsdp.proc.69.110.1983.

Cannat, M., Sauter, D., Mendel, V., Ruellan, E., Okino, K., Escartin, J., Combier, V., and Baala, M. (2006). Modes of seafloor generation at a melt-poor ultraslow-spreading ridge. *Geology*, 34(7):605–608. doi: 10.1130/G22486.1.

Carlson, R. L. (1998). Seismic velocities in the uppermost oceanic crust: Age dependence and the fate of layer 2A. *Journal of Geophysical Research: Solid Earth*, 103(B4):7069–7077. doi: 10.1029/97JB03577.

Carlson, R. L. (2001). The effects of temperature, pressure, and alteration on seismic properties of diabase dike rocks from DSDP/ODP Hole 504B. *Geophysical Research Letters*, 28(20):3979–3982. doi: 10.1029/2001GL013426.

Carlson, R. L. (2010). How crack porosity and shape control seismic velocities in the upper oceanic crust: Modeling downhole logs from Holes 504B and 1256D. *Geochemistry, Geophysics, Geosystems*, 11(4):1–15. doi: 10.1029/2009GC002955.

Carlson, R. L. (2011). The effect of hydrothermal alteration on the seismic structure of the upper oceanic crust: Evidence from Holes 504B and 1256D. *Geochemistry, Geophysics, Geosystems*, 12(9):1–11. doi: 10.1029/2011GC003624.

Carlson, R. L. (2014). The influence of porosity and crack morphology on seismic velocity and permeability in the upper oceanic crust. *Geochemistry, Geophysics, Geosystems*, 15(1):10–27. doi: 10.1002/2013GC004965.

Carlson, R. L. and Herrick, C. N. (1990). Densities and porosities in the oceanic crust and their variations with depth and age. *Journal of Geophysical Research*, 95(B6):9153–9170. doi: 10.1029/JB095iB06p09153.

Carlson, R. L. and Miller, J. D. (2004). Influence of pressure and mineralogy on seismic velocities in oceanic gabbros: Implications for the composition and state of the lower oceanic crust. *Journal of Geophysical Research: Solid Earth*, 109(B9):1–17. doi: 10.1029/2003JB002699.

Christensen, N. I. (1970). Composition and evolution of the oceanic crust. *Marine Geology*, 8(2):139–154. doi: 10.1016/0025-3227(70)90002-2.

Christensen, N. I. (1996). Poisson's ratio and crustal seismology. *Journal of Geophysical Research: Solid Earth*, 101(B2):3139–3156. doi: 10.1029/95JB03446.

Christensen, N. I. and Salisbury, M. H. (1975). Structure and constitution of the lower oceanic crust. *Reviews of Geophysics*, 13(1):57–86. doi: 10.1029/RG013i001p00057.

Christensen, N. I. and Smewing, J. D. (1981). Geology and seismic structure of the northern section of the Oman ophiolite. *Journal of Geophysical Research: Solid Earth*, 86(B4):2545–2555. doi: 10.1029/JB086iB04p02545.

Christeson, G. L., Karson, J. A., and McIntosh, K. D. (2010). Mapping of seismic layer 2A/2B boundary above the sheeted dike unit at intermediate spreading crust exposed near the Blanco Transform. *Geochemistry, Geophysics, Geosystems*, 11(3):1–23. doi: 10.1029/2009GC002864.

Christeson, G. L., McIntosh, K. D., and Karson, J. A. (2007). Inconsistent correlation of seismic layer 2a and lava layer thickness in oceanic crust. *Nature*, 445(7126):418–421. doi: 10.1038/nature05517.

Christeson, G. L., Morgan, J. V., and Warner, M. R. (2012). Shallow oceanic crust: Full waveform tomographic images of the seismic layer 2A/2B boundary. *Journal of Geophysical Research: Solid Earth*, 117(B5):n/a–n/a. doi: 10.1029/2011JB008972.

Christeson, G. L., Morgan, S., Kodaira, S., Yamashita, M., Almeev, R. R., Michibayashi, K., Sakuyama, T., Ferré, E. C., and Kurz, W. (2016). Physical properties and seismic structure of Izu-Bonin-Mariana fore-arc crust: Results from IODP Expedition 352 and comparison with oceanic crust. *Geochemistry, Geophysics, Geosystems*, 17(12):4973–4991. doi: 10.1002/2016GC006638.

Christeson, G. L., Purdy, G. M., and Fryer, G. J. (1992). Structure of young upper crust at the East Pacific Rise near 9°30'N. *Geophysical Research Letters*, 19(10):1045–1048. doi: 10.1029/91GL00971.

Christeson, G. L., Purdy, G. M., and Fryer, G. J. (1994). Seismic constraints on shallow crustal emplacement processes at the fast spreading East Pacific Rise. *Journal of Geophysical Research: Solid Earth*, 99(B9):17957–17973. doi: 10.1029/94JB01252.

Christeson, G. L., Shaw, P. R., and Garmany, J. D. (1997). Shear and compressional wave structure of the East Pacific Rise, 9°-10°N. *Journal of Geophysical Research: Solid Earth*, 102(B4):7821–7835. doi: 10.1029/96JB03901.

Collier, J. S. and Singh, S. C. (1998). Poisson's ratio structure of young oceanic crust. *Journal of Geophysical Research: Solid Earth*, 103(B9):20981–20996. doi: 10.1029/98JB01980.

Collins, J. A., Purdy, M. G., and Brocher, T. M. (1989). Seismic velocity structure at Deep Sea Drilling Project site 504B, Panama Basin: Evidence for thin oceanic crust. *Journal of Geophysical Research*, 94(B7):9283–9302. doi: 10.1029/JB094iB07p09283.

Cooper, K. M., Goldstein, S. J., Sims, K. W., and Murrell, M. T. (2003). Uranium-series chronology of Gorda Ridge volcanism: new evidence from the 1996 eruption. *Earth and Planetary Science Letters*, 206(3-4):459–475. doi: 10.1016/S0012-821X(02)01083-X.

Crampin, S. (1984). Effective anisotropic elastic constants for wave propagation through cracked solids. *Geophysical Journal International*, 76(1):135–145. doi: 10.1111/j.1365-246X.1984.tb05029.x.

Crampin, S. (1993). A review of the effects of crack geometry on wave propagation through aligned cracks. *Canadian Journal of Exploration Geophysics*, 29:3–17.

CRRUST (1982). Geothermal regimes of the Costa Rica Rift, east Pacific, investigated by drilling, DSDP-IPOD Legs 68, 69, and 70. *Geological Society of America Bulletin*, 93(9):862–875. doi: 10.1130/0016-7606(1982)93<862:GROTCR>2.0.CO;2.

Cudrak, C. F. and Clowes, R. M. (1993). Crustal structure of Endeavour Ridge Segment, Juan de Fuca Ridge, from a detailed seismic refraction survey. *Journal of Geophysical Research*, 98(B4):6329–6349. doi: 10.1029/92JB02860.

Davis, E. E. (1982). Evidence for extensive basalt flows on the sea floor. *Geological Society of America Bulletin*, 93(10):1023–1029. doi: 10.1130/0016-7606(1982)93<1023:EFEBFO>2.0.CO;2.

Detrick, R., Collins, J., Stephen, R., and Swift, S. (1994). In situ evidence for the nature of the seismic layer 2/3 boundary in oceanic crust. *Nature*, 370(6487):288–290. doi: 10.1038/370288a0.

Detrick, R. S., Toomey, D. R., and Collins, J. A. (1998). Three-dimensional upper crustal heterogeneity and anisotropy around Hole 504B from seismic tomography. *Journal of Geophysical Research*, 103(B12):30485–30504. doi: 10.1029/98JB02409.

Dick, H. J. B., Lin, J., and Schouten, H. (2003). An ultraslow-spreading class of ocean ridge. *Nature*, 426(6965):405–412. doi: 10.1038/nature02128.

Dunn, R. A. (2015). Tracking stress and hydrothermal activity along the Eastern Lau Spreading Center using seismic anisotropy. *Earth and Planetary Science Letters*, 410:105–116. doi: 10.1016/j.epsl.2014.11.027.

Dunn, R. A., Lekić, V., Detrick, R. S., and Toomey, D. R. (2005). Three-dimensional seismic structure of the Mid-Atlantic Ridge (35°N): Evidence for focused melt supply and lower crustal dike injection. *Journal of Geophysical Research: Solid Earth*, 110(B09101):1–17. doi: 10.1029/2004JB003473.

Dunn, R. A. and Toomey, D. R. (2001). Crack-induced seismic anisotropy in the oceanic crust across the East Pacific Rise (9°30′N). *Earth and Planetary Science Letters*, 189(1-2):9–17. doi: 10.1016/S0012-821X(01)00353-3.

Elliott, T., Plank, T., Zindler, A., White, W., and Bourdon, B. (1997). Element transport from slab to volcanic front at the Mariana arc. *Journal of Geophysical Research: Solid Earth*, 102(B7):14991–15019. doi: 10.1029/97JB00788.

Emile-Geay, J. and Madec, G. (2008). Geothermal heating, diapycnal mixing and the abyssal circulation. *Ocean Science Discussions*, 5(3):281–325. doi: 10.5194/osd-5-281-2008.

Escartín, J., Cowie, P. A., Searle, R. C., Allerton, S., Mitchell, N. C., MacLeod, C. J., and Slootweg, A. P. (1999). Quantifying tectonic strain and magmatic accretion at a slow spreading ridge segment, Mid-Atlantic Ridge, 29°N. *Journal of Geophysical Research: Solid Earth*, 104(B5):10421–10437. doi: 10.1029/1998JB900097.

Escartín, J., Smith, D. K., Cann, J., Schouten, H., Langmuir, C. H., and Escrig, S. (2008). Central role of detachment faults in accretion of slow-spreading oceanic lithosphere. *Nature*, 455(7214):790–794. doi: 10.1038/nature07333.

Expedition 309 and 312 Scientists (2006). *Superfast spreading rate crust 3: a complete in situ section of upper oceanic crust formed at a superfast spreading rate*, volume 312. doi: 10.2204/iodp.pr.312.2006.

Farahat, N. X., Archer, D., and Abbot, D. S. (2017). Validation of the BASALT model for simulating off-axis hydrothermal circulation in oceanic crust. *Journal of Geophysical Research: Solid Earth*, 122(8):5871–5889. doi: 10.1002/2016JB013758.

Fisher, A. and Becker, K. (2000). Channelized fluid flow in oceanic crust reconciles heat-flow and permeability data. *Nature*, 403(6765):71–74. doi: 10.1038/47463.

Fisher, A. T. (1998). Permeability within basaltic oceanic crust. *Reviews of Geophysics*, 36(2):143–182. doi: 10.1029/97RG02916.

Francheteau, J., Armijo, R., Cheminee, J., Hekinian, R., Lonsdale, P., and Blum, N. (1992). Dyke complex of the East Pacific Rise exposed in the walls of Hess Deep and the structure of the upper oceanic crust. *Earth and Planetary Science Letters*, 111(1):109–121. doi: 10.1016/0012-821X(92)90173-S.

Fryer, G. J., Miller, D. J., and Berge, P. A. (1989). Seismic anisotropy and age-dependent structure of the upper oceanic crust. In Sinton, J. M., editor, *Evolution of Mid Ocean Ridges*, chapter 1, pages 1–8. American Geophysical Union, Washington, D.C. doi: 10.1029/GM057p0001.

Geldmacher, J., Hofig, T. W., Hauff, F., Hoernle, K., Garbe-Schonberg, D., and Wilson, D. S. (2013). Influence of the Galapagos hotspot on the East Pacific Rise during Miocene superfast spreading. *Geology*, 41(2):183–186. doi: 10.1130/G33533.1.

Gillis, K. M. and Robinson, P. T. (1990). Patterns and processes of alteration in the lavas and dykes of the Troodos Ophiolite, Cyprus. *Journal of Geophysical Research*, 95(B13):21523–21548. doi: 10.1029/JB095iB13p21523.

Goff, J. A. (1991). A global and regional stochastic analysis of near-ridge Abyssal Hill morphology. *Journal of Geophysical Research: Solid Earth*, 96(B13):21713–21737. doi: 10.1029/91JB02275.

Grevemeyer, I., Hayman, N. W., Peirce, C., Schwardt, M., Van Avendonk, H. J. A., Dannowski, A., and Papenberg, C. (2018a). Episodic magmatism and serpentinized mantle exhumation at an ultraslow-spreading centre. *Nature Geoscience*, 11(6):444–448. doi: 10.1038/s41561-018-0124-6.

Grevemeyer, I., Kaul, N., Villinger, H., and Weigel, W. (1999). Hydrothermal activity and the evolution of the seismic properties of upper oceanic crust. *Journal of Geophysical Research: Solid Earth*, 104(B3):5069–5079. doi: 10.1029/1998JB900096.

Grevemeyer, I., Ranero, C. R., and Ivandic, M. (2018b). Structure of oceanic crust and serpentinization at subduction trenches. *Geosphere*, 14(2):1–24. doi: 10.1130/GES01537.1.

Grevemeyer, I. and Weigel, W. (1996). Seismic velocities of the uppermost igneous crust versus age. *Geophysical Journal International*, 124(2):631–635. doi: 10.1111/j.1365-246X.1996.tb07041.x.

Grevemeyer, I., Weigel, W., and Jennrich, C. (1998). Structure and ageing of oceanic crust at 14°S on the East Pacific Rise. *Geophysical Journal International*, 135(2):573–584. doi: 10.1046/j.1365-246X.1998.00673.x.

Grindlay, N. R., Madsen, J. A., Rommevaux-Jestin, C., and Sclater, J. (1998). A different pattern of ridge segmentation and mantle Bouguer gravity anomalies along the ultraslow spreading Southwest Indian Ridge (15°30′E to 25°E). *Earth and Planetary Science Letters*, 161(1-4):243–253. doi: 10.1016/S0012-821X(98)00154-X.

Guerin, G., Goldberg, D. S., and Iturrino, G. J. (2008). Velocity and attenuation in young oceanic crust: New downhole log results from DSDP/ODP/IODP Holes 504B and 1256D. *Geochemistry, Geophysics, Geosystems*, 9(12):1–10. doi: 10.1029/2008GC002203.

Guerin, G. and Zakharova, N. (2011). IODP Expedition 335 Logging Summary. Technical report, Lamont Doherty Earth Observatory, Columbia University.

Hacker, B. R., Peacock, S. M., Abers, G. A., and Holloway, S. D. (2003). Subduction factory 2. Are intermediate-depth earthquakes in subducting slabs linked to metamorphic dehydration reactions? *Journal of Geophysical Research: Solid Earth*, 108(B1):1–16. doi: 10.1029/2001JB001129.

Harding, A. J., Kent, G. M., and Orcutt, J. A. (1993). A multichannel seismic investigation of upper crustal structure at 9°N on the East Pacific Rise: Implications for crustal accretion. *Journal of Geophysical Research: Solid Earth*, 98(B8):13925–13944. doi: 10.1029/93JB00886.

Harding, A. J., Orcutt, J. A., Kappus, M. E., Vera, E. E., Mutter, J. C., Buhl, P., Detrick, R. S., and Brocher, T. M. (1989). Structure of young oceanic crust at 13°N on the East Pacific Rise from expanding spread profiles. *Journal of Geophysical Research*, 94(B9):12163–12196. doi: 10.1029/JB094iB09p12163.

Harris, M., Coggon, R. M., Smith-Duque, C. E., Cooper, M. J., Milton, J. A., and Teagle, D. A. H. (2015). Channelling of hydrothermal fluids during the accretion and evolution of the upper oceanic crust: Sr isotope evidence from ODP Hole 1256D. *Earth and Planetary Science Letters*, 416:56–66. doi: 10.1016/j.epsl.2015.01.042.

Harris, M., Coggon, R. M., Wood, M., Smith-Duque, C. E., Henstock, T. J., and Teagle, D. A. (2017). Hydrothermal cooling of the ocean crust: Insights from ODP Hole 1256D. *Earth and Planetary Science Letters*, 462:110–121. doi: 10.1016/j.epsl.2017.01.010.

Hasterok, D. (2013). Global patterns and vigor of ventilated hydrothermal circulation through young seafloor. *Earth and Planetary Science Letters*, 380:12–20. doi: 10.1016/j.epsl.2013.08.016.

Haymon, R. M., Fornari, D. J., Edwards, M. H., Carbotte, S., Wright, D., and Macdonald, K. C. (1991). Hydrothermal vent distribution along the East Pacific Rise crest (9°09′–54′N) and its relationship to magmatic and tectonic processes on fast-spreading mid-ocean ridges. *Earth and Planetary Science Letters*, 104(2-4):513–534. doi: 10.1016/0012-821X(91)90226-8.

Henstock, T. J., Woods, A. W., and White, R. S. (1993). The accretion of oceanic crust by episodic sill intrusion. *Journal of Geophysical Research: Solid Earth*, 98(B3):4143–4161. doi: 10.1029/92JB02661.

Herron, T. J. (1982). Lava flow layer-East Pacific Rise. *Geophysical Research Letters*, 9(1):17–20. doi: 10.1029/GL009i001p00017.

Hey, R. (1977). Tectonic evolution of the Cocos-Nazca spreading center. *Geological Society of America Bulletin*, 88(10):1404–1420. doi: 10.1130/0016-7606(1977)88<i:TEOTCS>2.0.CO;2.

Hobart, M. A., Langseth, M. G., and Anderson, R. N. (1985). A geothermal and geophysical survey on the south flank of the Costa Rica Rift: Sites 504 and 505. In Anderson, R. N., Honnorez, J., and Becker, K., editors, *Initial Reports of the Deep Sea Drilling Project*, volume 83, chapter 22, pages 379–404. US Govt. Printing Office, Washington, DC. doi: 10.2973/dsdp.proc.83.122.1985.

Hobbs, R. W. and Peirce, C. (2015). RRS James Cook JC114 Cruise Report. Technical report.

Hofmann, M. and Morales Maqueda, M. A. (2009). Geothermal heat flux and its influence on the oceanic abyssal circulation and radiocarbon distribution. *Geophysical Research Letters*, 36(L03603):1–4. doi: 10.1029/2008GL036078.

Hooft, E. E. E., Detrick, R. S., Toomey, D. R., Collins, J. A., and Lin, J. (2000). Crustal thickness and structure along three contrasting spreading segments of the Mid-Atlantic Ridge, 33.5°-35°N. *Journal of Geophysical Research: Solid Earth*, 105(B4):8205–8226. doi: 10.1029/1999JB900442.

Hooft, E. E. E., Schouten, H., and Detrick, R. S. (1996). Constraining crustal emplacement processes from the variation in seismic layer 2A thickness at the East Pacific Rise. *Earth and Planetary Science Letters*, 142(3-4):289–309. doi: 10.1016/0012-821X(96)00101-X.

Houtz, R. and Ewing, J. (1976). Upper crustal structure as a function of plate age. *Journal of Geophysical Research*, 81(14):2490–2498. doi: 10.1029/JB081i014p02490.

Houtz, R. E. (1976). Seismic properties of layer 2A in the Pacific. *Journal of Geophysical Research*, 81(35):6321–6331. doi: 10.1029/JB081i035p06321.

Hudson, J. (1981). Wave speeds and attenuation of elastic waves in material containing cracks. *Geophysical Journal Royal Astronomical Society*, 64:133–150. doi: 10.1111/j.1365-246X.1981.tb02662.x.

Hussenoeder, S. A., Kent, G. M., and Detrick, R. S. (2002). Upper crustal seismic structure of the slow spreading Mid-Atlantic Ridge, 35°N: Constraints on volcanic emplacement processes. *Journal of Geophysical Research*, 107(B8):EPM 1–1–EPM 1–24. doi: 10.1029/2001JB001691.

IOC, IHO, and BODC (2003). Centernary Edition of the General Bathymetric Chart of the Oceans Digital Atlas.

IOC, SCOR, and IAPSO (2010). The international thermodynamic equation of seawater – 2010: Calculation and use of thermodynamic properties. *Intergovernmental Oceanographic Commission, Manuals and Guides*, 56:196.

Juteau, T., Bideau, D., Dauteuil, O., Manac'h, G., Naidoo, D. D., Nehlig, P., Ondreas, H., Tivey, M. A., Whipple, K. X., and Delaney, J. R. (1995). A submersible study in

the western Blanco fracture Zone, N.E. Pacific: Structure and evolution during the last 1.6 Ma. *Marine Geophysical Researches*, 17(5):399–430. doi: 10.1007/BF01371786.

Karson, J. A., Collins, J. A., and Casey, J. F. (1984). Geologic and seismic velocity structure of the crust/mantle transition in the Bay of Islands Ophiolite Complex. *Journal of Geophysical Research: Solid Earth*, 89(B7):6126–6138. doi: 10.1029/JB089iB07p06126.

Kelley, D. S., Karson, J. A., Blackman, D. K., Früh-Green, G. L., Butterfield, D. A., Lilley, M. D., Olson, E. J., Schrenk, M. O., Roe, K. K., Lebon, G. T., Rivizzigno, P., and The AT3-60 Shipboard Party (2001). An off-axis hydrothermal vent field near the Mid-Atlantic Ridge at 30° N. *Nature*, 412(6843):145–149. doi: 10.1038/35084000.

Kerrick, D. and Connolly, J. (2001). Metamorphic devolatilization of subducted oceanic metabasalts: implications for seismicity, arc magmatism and volatile recycling. *Earth and Planetary Science Letters*, 189(1-2):19–29. doi: 10.1016/S0012-821X(01)00347-8.

Klein, E. M. and Langmuir, C. H. (1987). Global correlations of ocean ridge basalt chemistry with axial depth and crustal thickness. *Journal of Geophysical Research*, 92(B8):8089–8115. doi: 10.1029/JB092iB08p08089.

Krijgsman, W., Hilgen, F. J., Raffi, I., Sierro, F. J., and Wilson, D. S. (1999). Chronology, causes and progression of the Messinian salinity crisis. *Nature*, 400(6745):652–655. doi: 10.1038/23231.

Langmuir, C. H., Klein, E. M., and Plank, T. (1992). Petrological Systematics of Mid-Ocean Ridge Basalts: Constraints on Melt Generation Beneath Ocean Ridges. In Phipps Morgan, J., Blackman, D. K., and Sinton, J. M., editors, *Mantle Flow and Melt Generation at Mid-Ocean Ridges*, volume 71, pages 183–280. American Geophysical Union (AGU). doi: 10.1029/GM071p0183.

Langseth, M. G. and Silver, E. A. (1996). The Nicoya Convergent Margin-A region of exceptionally low heat flow. *Geophysical Research Letters*, 23(8):891–894. doi: 10.1029/96GL00733.

Little, S. A. and Stephen, R. A. (1985). Costa Rica Rift borehole seismic experiment, Deep Sea Drilling Project hole 504B, leg 92. *Initial Reports of the Deep Sea Drilling Project*, 83. doi: 10.2973/dsdp.proc.83.129.1985.

Lowell, R. P., Gosnell, S., and Yang, Y. (2007). Numerical simulations of single-pass hydrothermal convection at mid-ocean ridges: Effects of the extrusive layer and temperature-dependent permeability. *Geochemistry, Geophysics, Geosystems*, 8(10):1–16. doi: 10.1029/2007GC001653.

Macdonald, K. C., Fox, P. J., Alexander, R. T., Pockalny, R., and Gente, P. (1996). Volcanic growth faults and the origin of Pacific abyssal hills. *Nature*, 380(6570):125–129. doi: 10.1038/380125a0.

MacLeod, C., Searle, R., Murton, B., Casey, J., Mallows, C., Unsworth, S., Achenbach, K., and Harris, M. (2009). Life cycle of oceanic core complexes. *Earth and Planetary Science Letters*, 287(3-4):333–344. doi: 10.1016/J.EPSL.2009.08.016.

Meschede, M. and Barckhausen, U. (2000). Plate Tectonic Evolution of the Cocos-Nazca Spreading Center. In Silver, E. A., Kimura, G., and Shipley, T. H., editors, *Proceedings of the Ocean Drilling Program, Scientific Results*, volume 170, chapter 7. Ocean Drilling Program, College Station, Texas. doi: 10.2973/odp.proc.sr.170.009.2000.

Metropolis, N., Rosenbluth, A. W., Rosenbluth, M. N., Teller, A. H., and Teller, E. (1953). Equation of State Calculations by Fast Computing Machines. *The Journal of Chemical Physics*, 21(6):1087–1092. doi: 10.1063/1.1699114.

Minshull, T. A., Sinha, M. C., and Peirce, C. (2005). Multi-disciplinary, sub-seabed 591 geophysical imaging. *Sea Technology*, 46:27–31.

Moscoso, E. and Grevemeyer, I. (2015). Bending-related faulting of the incoming oceanic plate and its effect on lithospheric hydration and seismicity: A passive and active seismological study offshore Maule, Chile. *Journal of Geodynamics*, 90:58–70. doi: 10.1016/j.jog.2015.06.007.

Mosegaard, K. and Tarantola, A. (1995). Monte Carlo sampling of solutions to inverse problems. *Journal of Geophysical Research: Solid Earth*, 100(B7):12431–12447. doi: 10.1029/94JB03097.

Muller, M. R., Minshull, T. A., and White, R. S. (1999). Segmentation and melt supply at the Southwest Indian Ridge. *Geology*, 27(10):867–870. doi: 10.1130/0091-7613(1999)027<0867:SAMSAT>2.3.CO;2.

Muller, M. R., Minshull, T. A., and White, R. S. (2000). Crustal structure of the Southwest Indian Ridge at the Atlantis II Fracture Zone. *Journal of Geophysical Research: Solid Earth*, 105(B11):25809–25828. doi: 10.1029/2000JB900262.

Müller, R. D., Sdrolias, M., Gaina, C., and Roest, W. R. (2008). Age, spreading rates, and spreading asymmetry of the world's ocean crust. *Geochemistry, Geophysics, Geosystems*, 9(4):1–19. doi: 10.1029/2007GC001743.

Nedimović, M. R., Carbotte, S. M., Diebold, J. B., Harding, A. J., Canales, J. P., and Kent, G. M. (2008). Upper crustal evolution across the Juan de Fuca ridge flanks. *Geochemistry, Geophysics, Geosystems*, 9(9):1–23. doi: 10.1029/2008GC002085.

Newmark, R. L., Anderson, R. N., Moos, D., and Zoback, M. D. (1985). Sonic and ultrasonic logging of Hole 504B and its implications for the structure, porosity, and stress regime of the upper 1 km of the oceanic crust. In Anderson, R. N., Honnorez, J., and Becker, K., editors, *Initial Reports of the Deep Sea Drilling Project*,

volume 83, chapter 27, pages 479–510. US Govt. Printing Office, Washington, DC. doi: 10.2973/dsdp.proc.83.127.1985.

Niu, Y. and O'Hara, M. J. (2008). Global Correlations of Ocean Ridge Basalt Chemistry with Axial Depth: a New Perspective. *Journal of Petrology*, 49(4):633–664. doi: 10.1093/petrology/egm051.

Ocean Drilling Program (2005). Archive of Core and Site/Hole Data and Photographs from the Ocean Drilling Program (ODP). doi: 10.7289/V5W37T8C.

Patten, C. G. C., Pitcairn, I. K., Teagle, D. A. H., and Harris, M. (2016). Sulphide mineral evolution and metal mobility during alteration of the oceanic crust: Insights from ODP Hole 1256D. *Geochimica et Cosmochimica Acta*, 193:132–159. doi: 10.1016/j.gca.2016.08.009.

Pearse, S. (2002). *Inversion and Modelling of Seismic Data to Assess the Evolution of the Rockall Trough*. PhD thesis, University of Cambridge.

Penrose Conference Participants (1972). GSA Penrose Field Conference on Ophiolites. *Geotimes*, 17:24–25.

Prada, M., Ranero, C., Sallarès, V., Zitellini, N., and Grevemeyer, I. (2016). Mantle exhumation and sequence of magmatic events in the Magnaghi–Vavilov Basin (Central Tyrrhenian, Italy): New constraints from geological and geophysical observations. *Tectonophysics*, 689:133–142. doi: 10.1016/j.tecto.2016.01.041.

Pratt, G., Shin, C., and Hicks, G. J. (1998). Gauss-Newton and full Newton methods in frequency-space seismic waveform inversion. *Geophysical Journal International*, 133(2):341–362. doi: 10.1046/j.1365-246X.1998.00498.x.

Purdy, G. M. and Detrick, R. S. (1986). Crustal structure of the Mid-Atlantic Ridge at 23°N from seismic refraction studies. *Journal of Geophysical Research: Solid Earth*, 91(B3):3739–3762. doi: 10.1029/JB091iB03p03739.

Purdy, G. M., Kong, L. S. L., Christeson, G. L., and Solomon, S. C. (1992). Relationship between spreading rate and the seismic structure of mid-ocean ridges. *Nature*, 355(6363):815–817. doi: 10.1038/355815a0.

Raitt, R. W. (1963). The Crustal Rocks. In Hill, M. N., editor, *The Sea*, chapter 6, pages 85–102. John Wiley & Sons, Inc, New York, volume 3 edition.

Ridley, W. (1994). Hydrothermal alteration in oceanic ridge volcanics: A detailed study at the Galapagos Fossil Hydrothermal field. *Geochimica et Cosmochimica Acta*, 59:2477–2494. doi: 10.1016/0016-7037(95)99269-M.

Rohr, K., Milkereit, B., and Yorath, C. J. (1988). Asymmetric deep crustal structure across the Juan de Fuca Ridge. *Geology*, 16(6):533–537. doi: 10.1130/0091-7613(1988)016<0533:ADCSAT>2.3.CO;2.

Rüpke, L. H., Morgan, J. P., Hort, M., and Connolly, J. A. (2004). Serpentine and the subduction zone water cycle. *Earth and Planetary Science Letters*, 223(1-2):17–34. doi: 10.1016/J.EPSL.2004.04.018.

Salisbury, M. H., Christensen, N. I., Becker, K., and Moos, D. (1985). The velocity structure of layer 2 at Deep Sea Drilling Project Site 504 from logging and laboratory experiments. In Anderson, R. N., Honnorez, J., and Becker, K., editors, *Initial Reports of the Deep Sea Drilling Project*, volume 83, chapter 30, pages 529–539. US Govt. Printing Office, Washington, DC. doi: 10.2973/dsdp.proc.83.130.1985.

Salisbury, M. H., Christensen, N. I., and Wilkens, R. H. (1996). Nature of the Layer 2/3 transition from a comparison of laboratory and logging velocities and petrology at the base of Hole 504B. In Alt, J. C., Kinoshita, H., Stokking, L. B., and Michael, P. J., editors, *Proceedings of the Ocean Drilling Program, Scientific Results*, volume 148, chapter 33, pages 409–414. Ocean Drilling Program, College Station, Texas. doi: 10.2973/odp.proc.sr.148.146.1996.

Schmidt, M. W. and Poli, S. (1998). Experimentally based water budgets for dehydrating slabs and consequences for arc magma generation. *Earth and Planetary Science Letters*, 163(1-4):361–379. doi: 10.1016/S0012-821X(98)00142-3.

Searle, R. (2013). *Mid-Ocean Ridges*. Cambridge University Press. doi: 10.1017/CBO9781139084260.

Shearer, P. and Orcutt, J. (1985). Anisotropy in the oceanic lithosphere – theory and observations from the Ngendei seismic refraction experiment in the southwest Pacific. *Geophysical Journal International*, 80(2):493–526. doi: 10.1111/j.1365-246X.1985.tb05105.x.

Shearer, P. M. (1988). Cracked media, Poisson's ratio and the structure of the upper oceanic crust. *Geophysical Journal International*, 92(2):357–362. doi: 10.1111/j.1365-246X.1988.tb01149.x.

Shearer, P. M. and Orcutt, J. a. (1986). Compressional and shear wave anisotropy in the oceanic lithosphere - the Ngendei seismic refraction experiment. *Geophysical Journal International*, 87(3):967–1003. doi: 10.1111/j.1365-246X.1986.tb01979.x.

Shillington, D. J., Bécel, A., Nedimović, M. R., Kuehn, H., Webb, S. C., Abers, G. A., Keranen, K. M., Li, J., Delescluse, M., and Mattei-Salicrup, G. A. (2015). Link between plate fabric, hydration and subduction zone seismicity in Alaska. *Nature Geoscience*, 8(12):961–964. doi: 10.1038/ngeo2586.

Shipboard Scientific Parties of Leg 68 (Site 501) Leg 69 and Leg 70 (1983). Sites 501 and 504: Sediments and Ocean Crust in an Area of High Heat Flow on the Southern Flank of the Costa Rica Rift. In Cann, J. R., Langseth, M. G., Honnorez, J., Von Herzen, R. P., and White, S. M., editors, *Initial Reports of the Deep Sea Drilling Project*, volume 69, chapter 2, pages 31–173. US Govt. Printing Office, Washington, DC. doi: 10.2973/dsdp.proc.69.102.1983.

Shipboard Scientific Party (1985). Hole 504B, Leg 83. In Anderson, R. N., Honnorez, J., and Becker, K., editors, *Initial Reports of the Deep Sea Drilling Project*, volume 83, chapter 2, pages 13–118. US Govt. Printing Office, Washington, DC. doi: 10.2973/dsdp.proc.83.102.1985.

Shipboard Scientific Party (1988). Site 504. In Becker, K. and Sakai, H., editors, *Proceedings of the Ocean Drilling Program, Initial Reports*, volume 111, chapter 3, pages 35–251. Ocean Drilling Program, College Station, Texas. doi: 10.2973/odp.proc.ir.111.103.1988.

Shipboard Scientific Party (1992). Site 504. In Dick, H. J. B., Erzinger, J., and Stokking, L. B., editors, *Proceedings of the Ocean Drilling Program, Initial Reports*, volume 140, chapter 2, pages 37–200. Ocean Drilling Program, College Station, Texas. doi: 10.2973/odp.proc.ir.140.102.1992.

Shipboard Scientific Party (1993). Site 504. In Alt, J. C., Kinoshita, H., and Stokking, L. B., editors, *Proceedings of the Ocean Drilling Program, Initial Reports*, volume 148, chapter 2, pages 27–121. Ocean Drilling Program, College Station, Texas. doi: 10.2973/odp.proc.ir.148.102.1993.

Shipboard Scientific Party (2003a). Leg 206 summary. In Wilson, D. S., Teagle, D. A. H., and Acton, G. D., editors, *Proceedings of the Ocean Drilling Program, Initial Reports*, volume 206, chapter 1. Ocean Drilling Program, College Station, Texas. doi: 10.2973/odp.proc.ir.206.101.2003.

Shipboard Scientific Party (2003b). Site 1256. In Wilson, D. S., Teagle, D. A. H., and Acton, G. D., editors, *Proceedings of the Ocean Drilling Program, Initial Reports*, volume 206, chapter 3. Ocean Drilling Program, College Station, Texas. doi: 10.2973/odp.proc.ir.206.103.2003.

Sinton, J. M., Smaglik, S. M., Mahoney, J. J., and Macdonald, K. C. (1991). Magmatic processes at superfast spreading mid-ocean ridges: Glass compositional variations along the East Pacific Rise 13°-23°S. *Journal of Geophysical Research: Solid Earth*, 96(B4):6133–6155. doi: 10.1029/90JB02454.

Smith, D. K., Escartín, J., Schouten, H., and Cann, J. R. (2008). Fault rotation and core complex formation: Significant processes in seafloor formation at slow-spreading mid-ocean ridges (Mid-Atlantic Ridge, 13°-15°N). *Geochemistry, Geophysics, Geosystems*, 9(3):1–23. doi: 10.1029/2007GC001699.

Sohn, R. A., Webb, S. C., and Hildebrand, J. A. (2004). Fine-scale seismic structure of the shallow volcanic crust on the East Pacific Rise at 9°50′N. *Journal of Geophysical Research*, 109(B12104):1–17. doi: 10.1029/2004JB003152.

Spence, G. D., Clowes, R. M., and Ellis, R. M. (1985). Seismic structure across the active subduction zone of western Canada. *Journal of Geophysical Research*, 90(B8):6754–6772. doi: 10.1029/JB090iB08p06754.

Spiess, F. N., Macdonald, K. C., Atwater, T., Ballard, R., Carranza, A., Cordoba, D., Cox, C., Garcia, V. M., Francheteau, J., Guerrero, J., Hawkins, J., Haymon, R., Hessler, R., Juteau, T., Kastner, M., Larson, R., Luyendyk, B., Macdougall, J. D., Miller, S., Normark, W., Orcutt, J., and Rangin, C. (1980). East Pacific Rise: hot springs and geophysical experiments. *Science*, 207(4438):1421–1433. doi: 10.1126/science.207.4438.1421.

Spudich, P. and Orcutt, J. (1980). A new look at the seismic velocity structure of the oceanic crust. *Reviews of Geophysics*, 18(3):627–645. doi: 10.1029/RG018i003p00627.

Stein, C. A. and Stein, S. (1992). A model for the global variation in oceanic depth and heat flow with lithospheric age. *Nature*, 356:133–135. doi: 10.1038/359123a0.

Stein, C. A. and Stein, S. (1994). Constraints on hydrothermal heat flux through the oceanic lithosphere from global heat flow. *Journal of Geophysical Research*, 99(B2):3081–3095. doi: 10.1029/93JB02222.

Stockwell, J. W. (1999). The CWP/SU: Seismic Unix package. *Computers & Geosciences*, 25(4):415–419. doi: 10.1016/S0098-3004(98)00145-9.

Su, W., Mutter, C. Z., Mutter, J. C., and Buck, W. R. (1994). Some theoretical predictions on the relationships among spreading rate, mantle temperature, and crustal thickness. *Journal of Geophysical Research: Solid Earth*, 99(B2):3215–3227. doi: 10.1029/93JB02965.

Swift, S. A., Kent, G. M., Detrick, R. S., Collins, J. A., and Stephen, R. A. (1998a). Oceanic basement structure, sediment thickness, and heat flow near Hole 504B. *Journal of Geophysical Research: Solid Earth*, 103(B7):15377–15391. doi: 10.1029/98JB00698.

Swift, S. A., Lizarralde, D., Stephen, R. A., and Hoskins, H. (1998b). Velocity structure in upper ocean crust at Hole 504B from vertical seismic profiles. *Journal of Geophysical Research: Solid Earth*, 103(B7):15361–15376. doi: 10.1029/98JB00766.

Talley, L. D. (2007). *Hydrographic Atlas of the World Ocean Circulation Experiment (WOCE). Volume 2: Pacific Ocean.* International WOCE Project Office, Southampton, UK.

Tartarotti, P., Fontana, E., and Crispini, L. (2009). Deformation pattern in a massive ponded lava flow at ODP-IODP Site 1256: A core and log approach. *Geochemistry, Geophysics, Geosystems*, 10(5):1–26. doi: 10.1029/2008GC002346.

Teagle, D. A. H., Alt, J. C., Umino, S., Miyashita, S., Banerjee, N. R., Wilson, D. S., and the Expedition 309/312 Scientists (2006). *Proceedings of the Integrated Ocean Drilling Program*, volume 309/312. Integrated Ocean Drilling Program Management International, Inc., Washington, DC. doi: 10.2204/iodp.proc.309312.2006.

Tominaga, M., Teagle, D. A. H., Alt, J. C., and Umino, S. (2009). Determination of the volcanostratigraphy of oceanic crust formed at superfast spreading ridge: Electrofacies analyses of ODP/IODP Hole 1256D. *Geochemistry, Geophysics, Geosystems*, 10(1):1–31. doi: 10.1029/2008GC002143.

Tong, C., White, R., and Warner, M. (2004). Effects of tectonism and magmatism on crack structure in oceanic crust: A seismic anisotropy study. *Geology*, 32(1):25–28. doi: 10.1130/G19962.1.

Toomey, D. R., Purdy, G. M., Solomon, S. C., and Wilcock, W. S. D. (1990). The three-dimensional seismic velocity structure of the East Pacific Rise near latitude 9° 30′ N. *Nature*, 347(6294):639–645. doi: 10.1038/347639a0.

Tucholke, B. E. and Lin, J. (1994). A geological model for the structure of ridge segments in slow spreading ocean crust. *Journal of Geophysical Research: Solid Earth*, 99(B6):11937–11958. doi: 10.1029/94JB00338.

Van Ark, E. M., Detrick, R. S., Canales, J. P., Carbotte, S. M., Harding, a. J., Kent, G. M., Nedimovic, M. R., Wilcock, W. S. D., Diebold, J. B., and Babcock, J. M. (2007). Seismic structure of the Endeavour Segment, Juan de Fuca Ridge: Correlations with seismicity and hydrothermal activity. *Journal of Geophysical Research*, 112(B02401):1–22. doi: 10.1029/2005JB004210.

Van Avendonk, H. J. A., Hayman, N. W., Harding, J. L., Grevemeyer, I., Peirce, C., and Dannowski, A. (2017). Seismic structure and segmentation of the axial valley of the Mid-Cayman Spreading Center. *Geochemistry, Geophysics, Geosystems*, 18(6):2149–2161. doi: 10.1002/2017GC006873.

Vanko, D. A. (1988). Temperature, pressure, and composition of hydrothermal fluids, with their bearing on the magnitude of tectonic uplift at mid-ocean ridges, inferred from fluid inclusions in oceanic layer 3 rocks. *Journal of Geophysical Research: Solid Earth*, 93(B5):4595–4611. doi: 10.1029/JB093iB05p04595.

Vera, E. E. and Diebold, J. B. (1994). Seismic imaging of oceanic layer 2A between 9°30′N and 10°N on the East Pacific Rise from two-ship wide-aperture profiles. *Journal of Geophysical Research: Solid Earth*, 99(B2):3031–3041. doi: 10.1029/93JB02107.

Vera, E. E., Mutter, J. C., Buhl, P., Orcutt, J. A., Harding, A. J., Kappus, M. E., Detrick, R. S., and Brocher, T. M. (1990). The structure of 0- to 0.2-m.y.-old oceanic crust at 9°N on the East Pacific Rise from expanded spread profiles. *Journal of Geophysical Research*, 95(B10):15529–15556. doi: 10.1029/JB095iB10p15529.

Vidale, J. E. (1990). Finite-difference calculation of traveltimes in three dimensions. *Geophysics*, 55(5):521–526. doi: 10.1190/1.1442863.

Virieux, J. and Operto, S. (2009). An overview of full-waveform inversion in exploration geophysics. *GEOPHYSICS*, 74(6):WCC1–WCC26. doi: 10.1190/1.3238367.

Von Damm, K. L. (1990). Seafloor Hydrothermal Activity: Black Smoker Chemistry and Chimneys. *Annual Review of Earth and Planetary Sciences*, 18(1):173–204. doi: 10.1146/annurev.ea.18.050190.001133.

Weekly, R. T., Wilcock, W. S. D., Toomey, D. R., Hooft, E. E. E., and Kim, E. (2014). Upper crustal seismic structure of the Endeavour segment, Juan de Fuca Ridge from traveltime tomography: Implications for oceanic crustal accretion. *Geochemistry, Geophysics, Geosystems*, 15(4):1296–1315. doi: 10.1002/2013GC005159.

Wessel, P. and Smith, W. (1998). New, improved version of Generic Mapping Tools released. *Eos*, 79(47):579. doi: 10.1029/98EO00426.

White, R. S., McKenzie, D., and O'Nions, R. K. (1992). Oceanic crustal thickness from seismic measurements and rare earth element inversions. *Journal of Geophysical Research*, 97(B13):19683–19715. doi: 10.1029/92JB01749.

White, R. S. and Whitmarsh, R. B. (1984). An investigation of seismic anisotropy due to cracks in the upper oceanic crust at 45 N, Mid-Atlantic Ridge. *Geophysical Journal International*, 79(2):439–467. doi: 10.1111/j.1365-246X.1984.tb02234.x.

Wilkens, R. H., Fryer, G. J., and Karsten, J. (1991). Evolution of porosity and seismic structure of upper oceanic crust: Importance of aspect ratios. *Journal of Geophysical Research*, 96(B11):17981–17995. doi: 10.1029/91JB01454.

Wilkens, R. H. and Langseth, M. G. (1983). Physical properties of sediments of the Costa Rica Rift, Deep Sea Drilling Project sites 504 and 505. In Cann, J. R., Langseth, M. G., Honnorez, J., Von Herzen, R. P., and White, S. M., editors, *Initial Reports of the Deep Sea Drilling Project*, volume 69, chapter 40, pages 659–673. US Govt. Printing Office, Washington, DC. doi: 10.2973/dsdp.proc.69.140.1983.

Wilson, D. J., Hobbs, R. W., Gregory, E. P. M., and Peirce, C. (2018). Intermediate spreading-rate oceanic crust is created by alternating periods of magma-rich and magma-poor spreading. *Geophysical Journal International*.

Wilson, D. S., Hallenborg, E., Harding, A. J., and Kent, G. M. (2003). Data report: Site survery results from cruise EW9903. In Wilson, D. S., Teagle, D. A. H., and Acton, G. D., editors, *Proceedings of the Ocean Drilling Program, Initial Reports*, volume 206, chapter 4. Ocean Drilling Program, College Station, Texas. doi: 10.2973/odp.proc.ir.206.104.2003.

Wilson, D. S. and Hey, R. N. (1995). History of rift propagation and magnetization intensity for the Cocos-Nazca spreading Center. *Journal of Geophysical Research: Solid Earth*, 100(B6):10041–10056. doi: 10.1029/95JB00762.

Wilson, D. S., Teagle, D. A. H., Alt, J. C., Banerjee, N. R., Umino, S., Miyashita, S., Acton, G. D., Anma, R., Barr, S. R., Belghoul, A., Carlut, J., Christie, D. M., Coggon, R. M., Cooper, K. M., Cordier, C., Crispini, L., Durand, S. R., Einaudi, F., Galli, L., Gao, Y., Geldmacher, J., Gilbert, L. A., Hayman, N. W., Herrero-Bervera, E., Hirano, N., Holter, S., Ingle, S., Jiang, S., Kalberkamp, U., Kerneklian, M., Koepke, J., Laverne, C., Vasquez, H. L. L., Maclennan, J., Morgan, S., Neo, N., Nichols, H. J., Park, S.-H., Reichow, M. K., Sakuyama, T., Sano, T., Sandwell, R., Scheibner, B., Smith-Duque, C. E., Swift, S. A., Tartarotti, P., Tikku, A. A., Tominaga, M., Veloso, E. A., Yamasaki, T., Yamazaki, S., and Ziegler, C. (2006). Drilling to Gabbro in Intact Ocean Crust. *Science*, 312(5776):1016–1020. doi: 10.1126/science.1126090.

Zack, T., Tomascak, P. B., Rudnick, R. L., Dalpé, C., and McDonough, W. F. (2003). Extremely light Li in orogenic eclogites: The role of isotope fractionation during dehydration in subducted oceanic crust. *Earth and Planetary Science Letters*, 208(3-4):279–290. doi: 10.1016/S0012-821X(03)00035-9.

Zelt, C. A. (1998). Lateral velocity resolution from three-dimensional seismic refraction data. *Geophysical Journal International*, 135(3):1101–1112. doi: 10.1046/j.1365-246X.1998.00695.x.

Zelt, C. A. and Barton, P. J. (1998). Three-dimensional seismic refraction tomography: A comparison of two methods applied to data from the Faeroe Basin. *Journal of Geophysical Research*, 103(B4):7187–7210. doi: 10.1029/97JB03536.

Zelt, C. A. and Forsyth, D. A. (1994). Modeling wide-angle seismic data for crustal structure: Southeastern Grenville Province. *Journal of Geophysical Research: Solid Earth*, 99(B6):11687–11704. doi: 10.1029/93JB02764.

Zelt, C. A. and Smith, R. B. (1992). Seismic traveltime inversion for 2-D crustal velocity structure. *Geophysical Journal International*, 108(1):16–34. doi: 10.1111/j.1365-246X.1992.tb00836.x.

# Appendices

## Appendix A

Bolt MCS stacks for the 12 shot profiles in the South Grid, processed using the sequence described in Section 2.4.3.

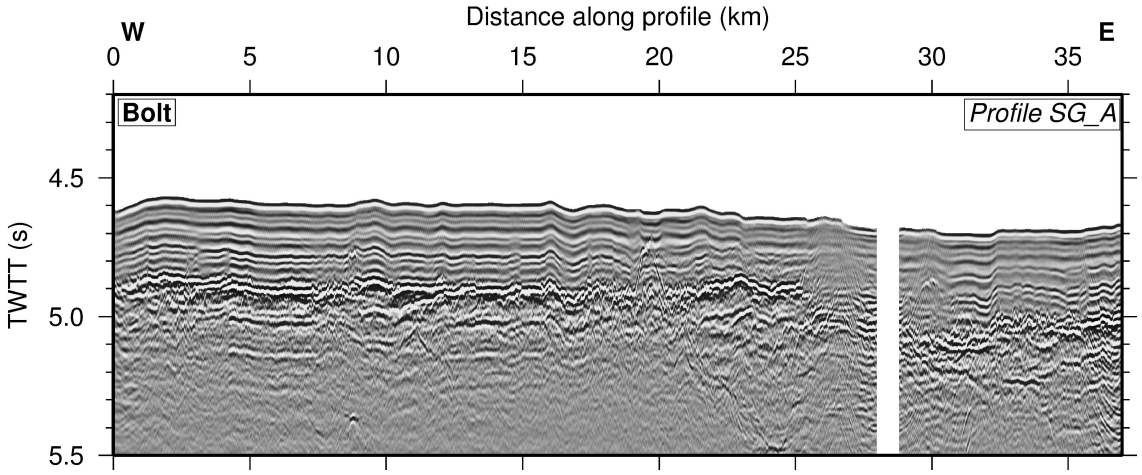


Figure A.1: Final MCS stack of the Bolt data for profile SG_A. The absence of data at ∼28 km along profile was caused by a system failure.

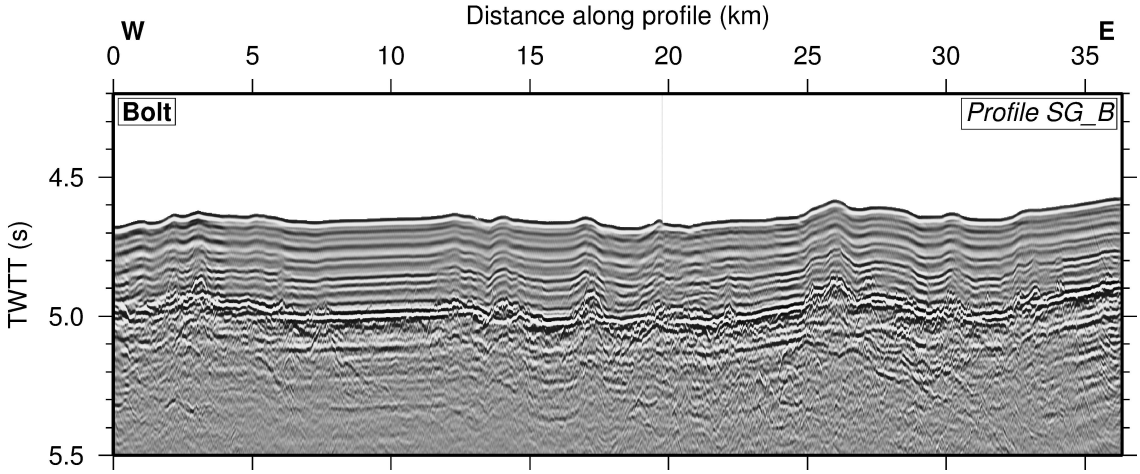


Figure A.2: Final MCS stack of the Bolt data for profile SG_B.

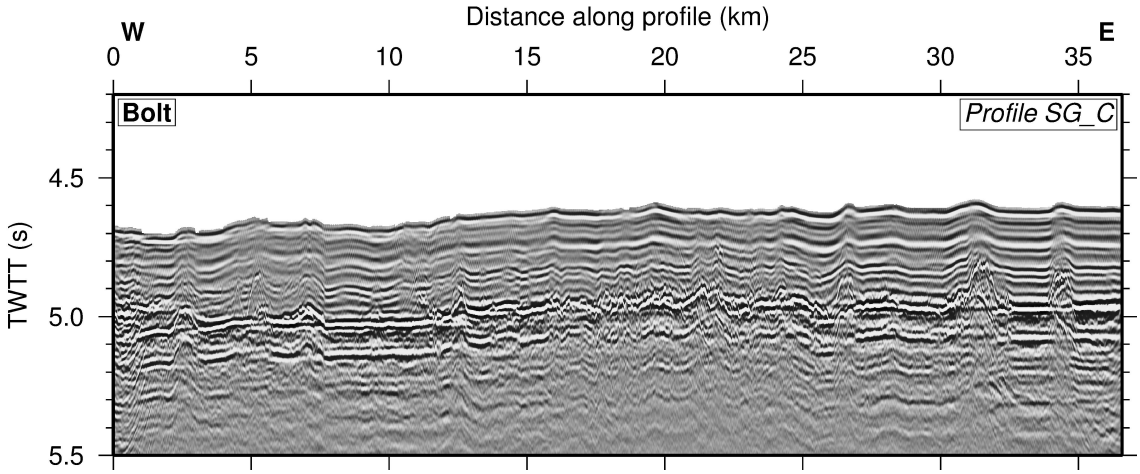


Figure A.3: Final MCS stack of the Bolt data for profile SG_C.

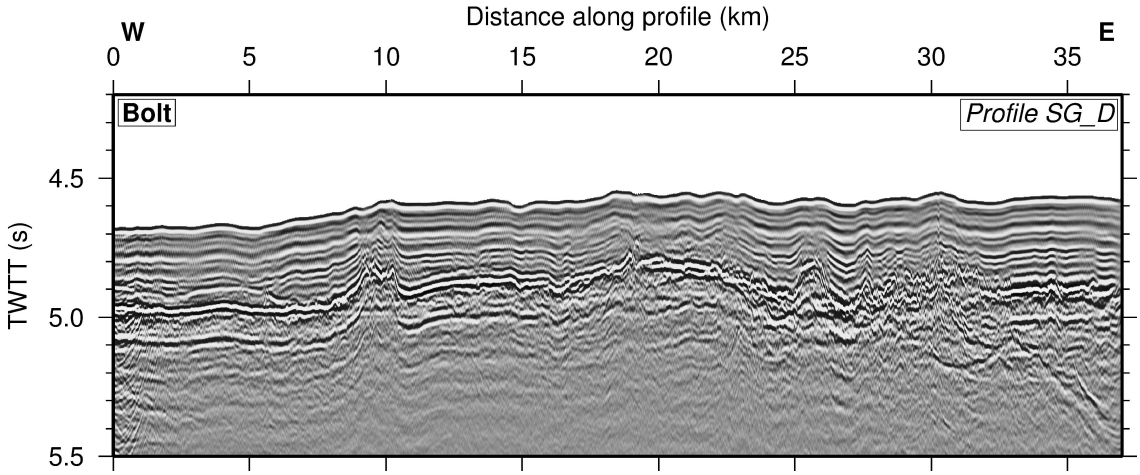


Figure A.4: Final MCS stack of the Bolt data for profile SG_D.

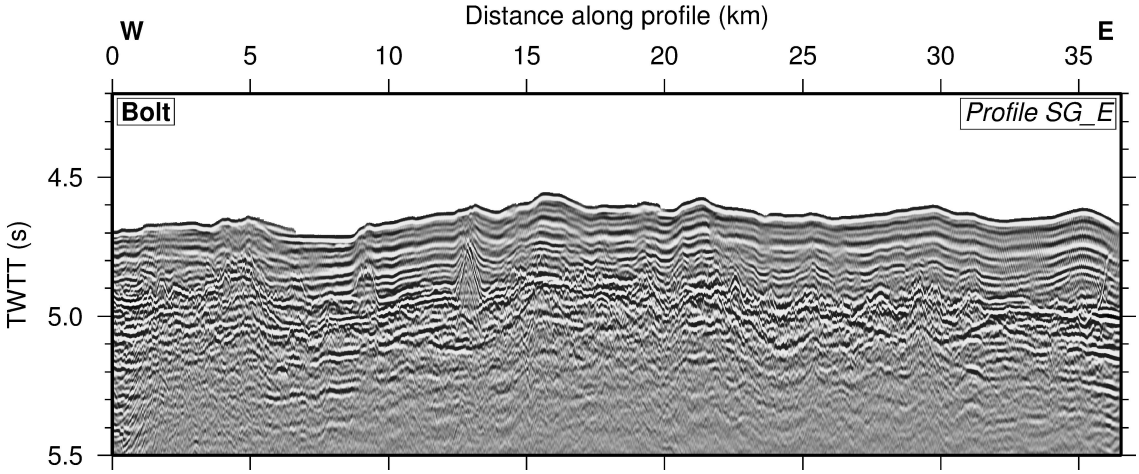


Figure A.5: Final MCS stack of the Bolt data for profile SG_E.

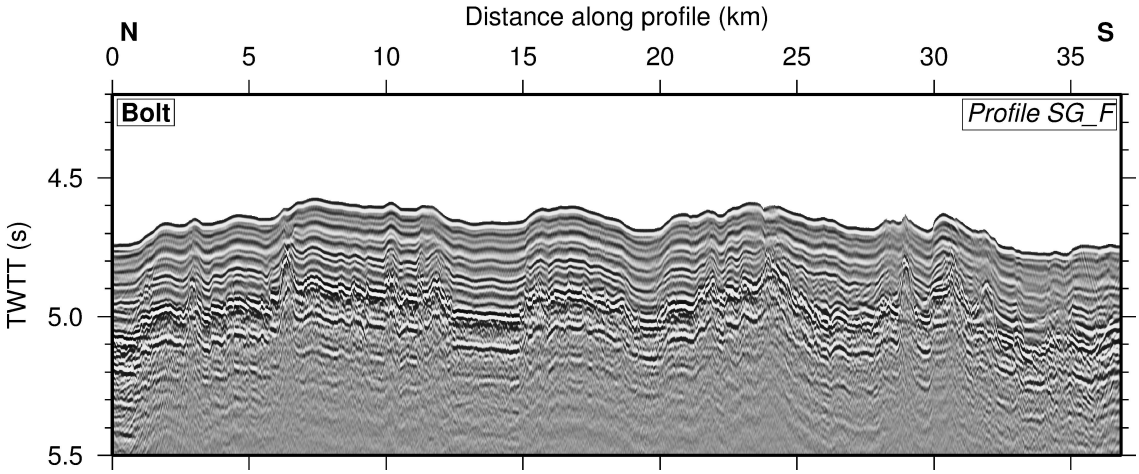


Figure A.6: Final MCS stack of the Bolt data for profile SG_F.

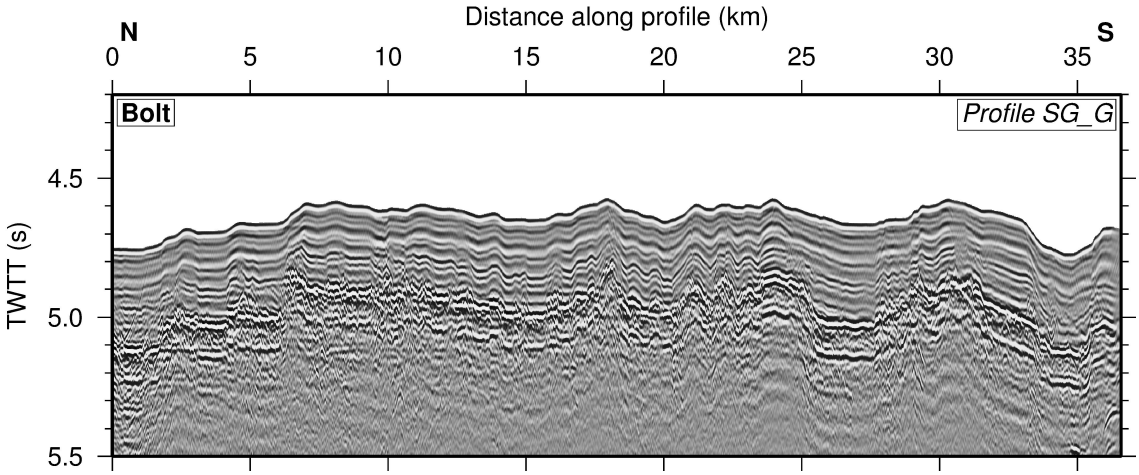


Figure A.7: Final MCS stack of the Bolt data for profile SG_G.

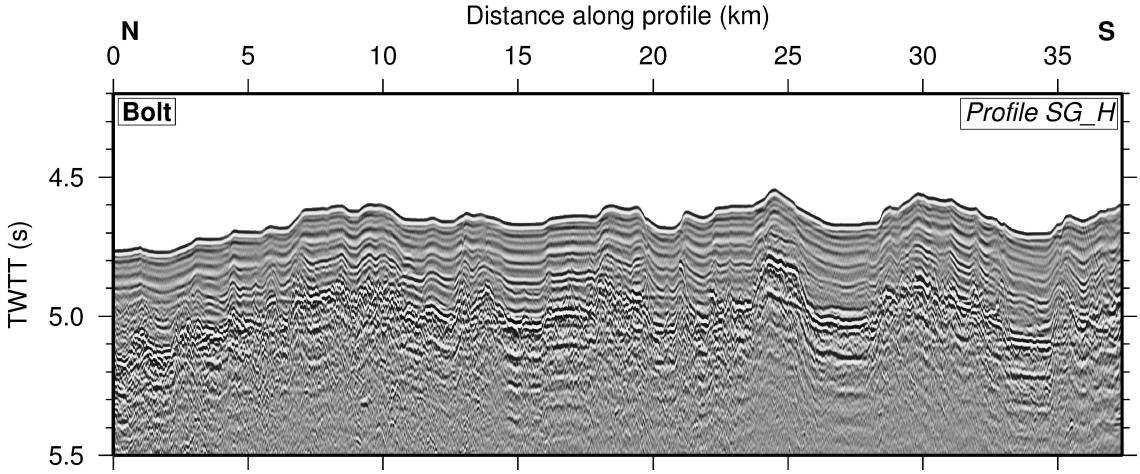


Figure A.8: Final MCS stack of the Bolt data for profile SG_H.

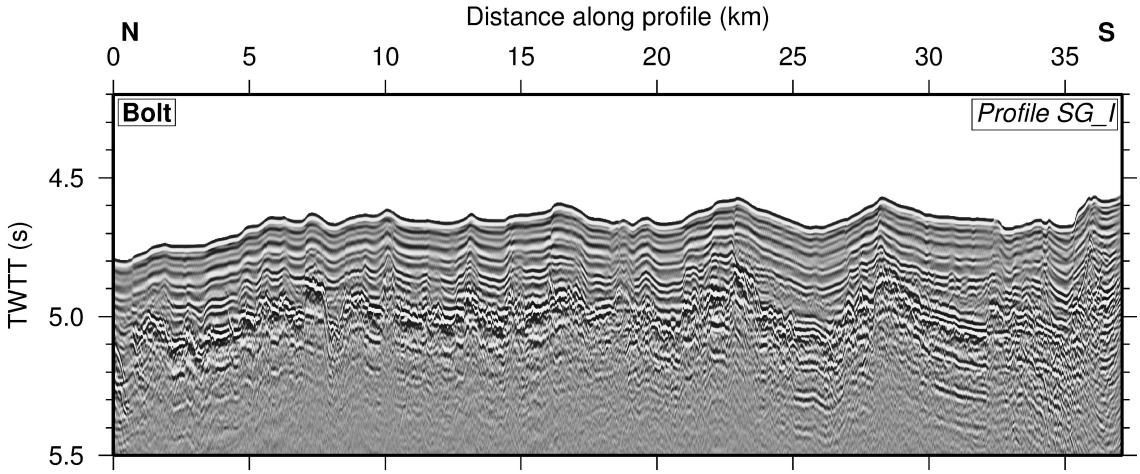


Figure A.9: Final MCS stack of the Bolt data for profile SG_I.

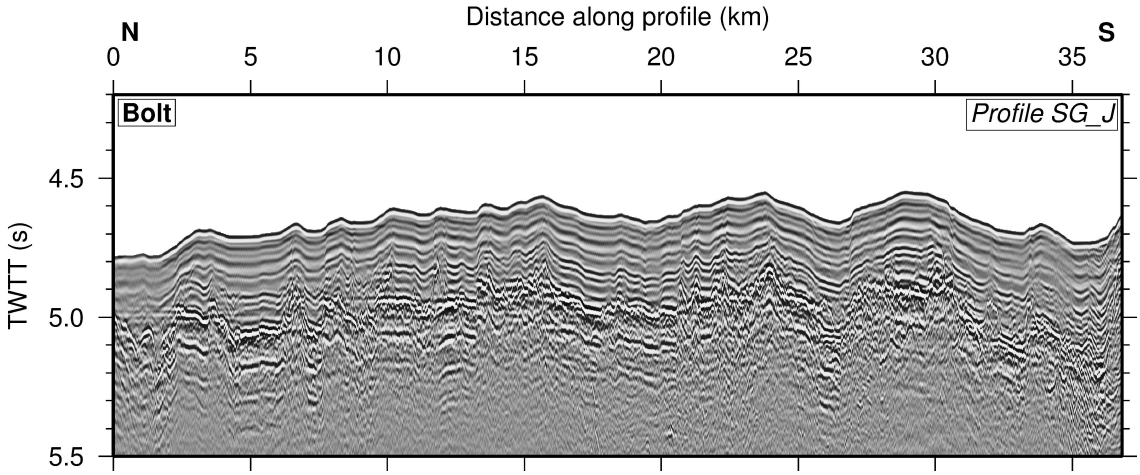


Figure A.10: Final MCS stack of the Bolt data for profile SG_J.

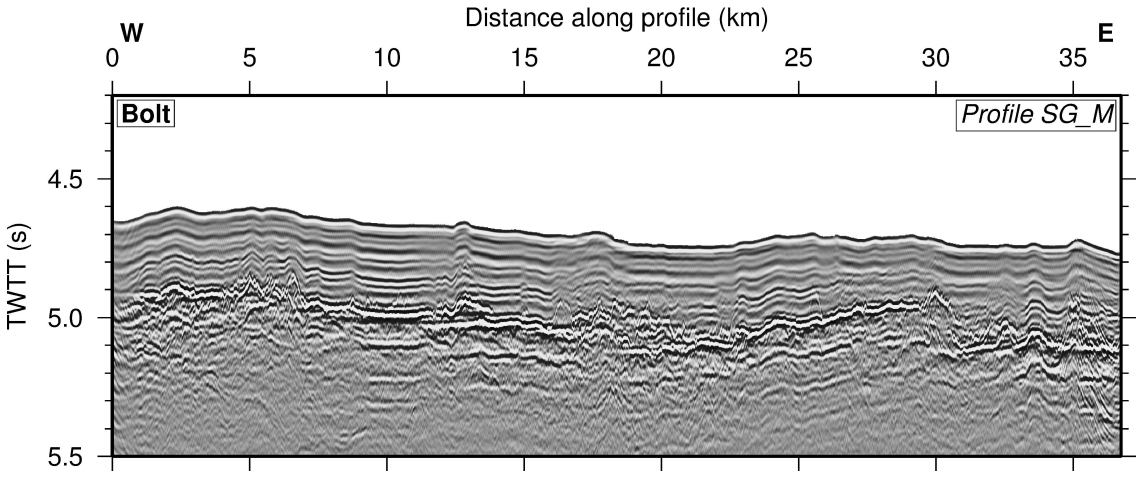


Figure A.11: Final MCS stack of the Bolt data for profile SG_M.

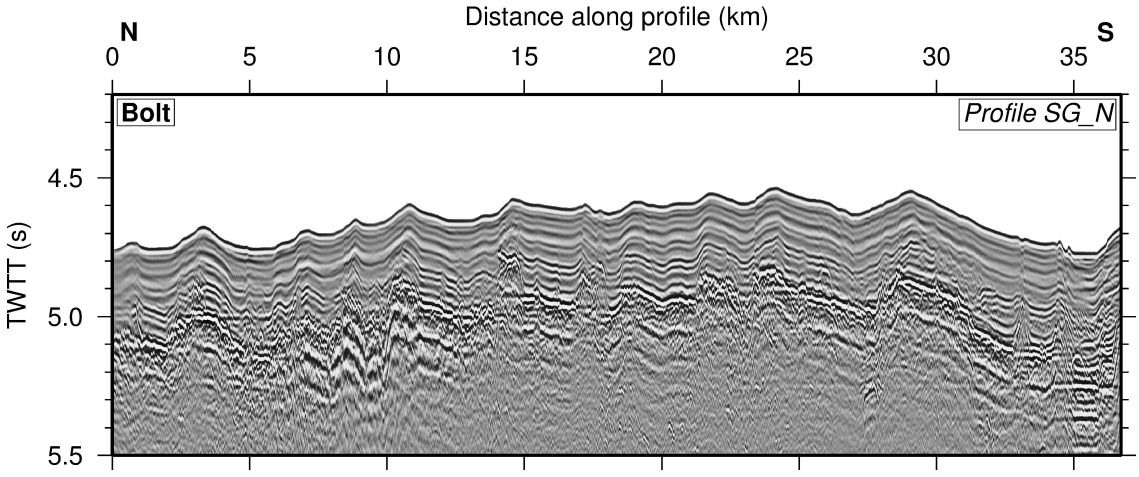


Figure A.12: Final MCS stack of the Bolt data for profile SG_N.

# Appendix B

Specifications of the OBSs used in this study, provided by the Ocean Bottom Instrumentation Facility, Durham, UK, including the hydrophone characteristics (Table B.1), the geophone response curve (Figure B.1), and the instrument filter response to a square wave (Figure B.2).

| Hydrophone characteristics | |
|---|---|
| Pre-Amplifier | Yes |
| Pre-Amplifier type | Current Mode c/w 402 Ohm termination |
| Sensitivity | -185dB re: 1V/uPa |
| Frequency response | 0.05 Hz to 7500 Hz |
| Operating Voltage | 12-30 Vdc at 2.8 mA |
| Gain | 13 dB |

Table B.1: Characteristics of the hydrophone sensors used in the South Grid OBSs.

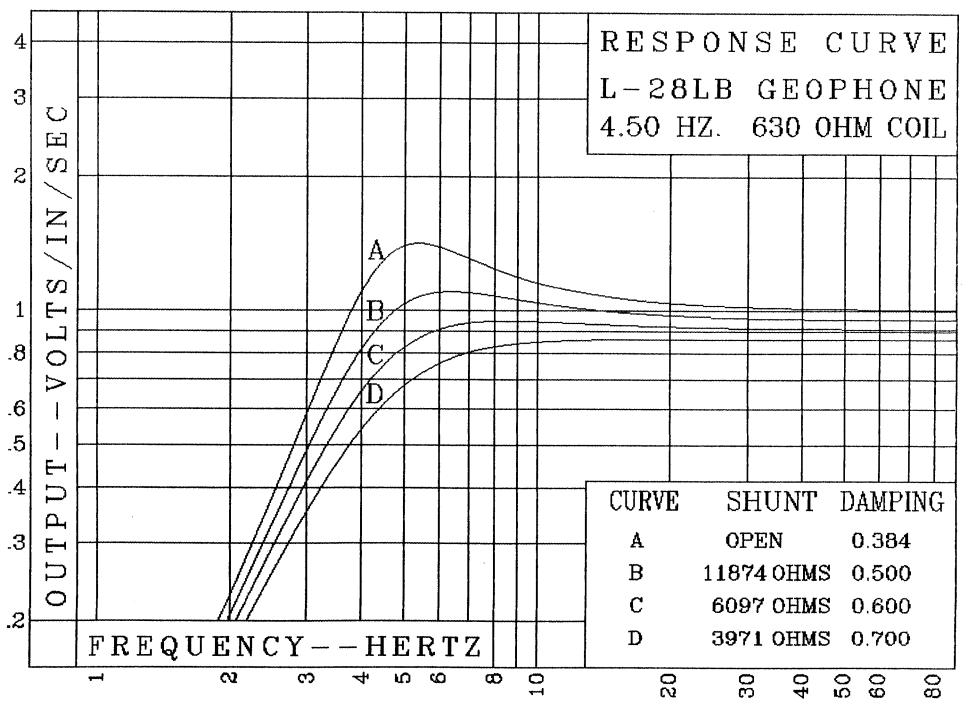


Figure B.1: Response curves for geophone sensors - curve D represents the geophones used in the South Grid OBSs.

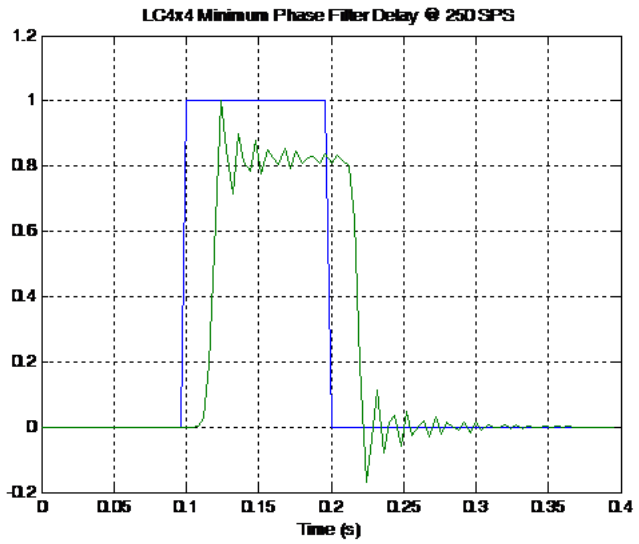


Figure B.2: OBS filter response to a square wave input at 250 Hz.

# Appendix C

Deployment positions and relocated positions of the South Grid OBSs (Table C.1). OBS SG_02 has no relocated position as it did not record any data.

| OBS | Deployment | | | Relocated | | |
|---|---|---|---|---|---|---|
| | Lon | Lat | Depth (km) | Lon | Lat | Depth (km) |
| SG_01 | -83.689 | 1.324 | 3.498 | -83.690 | 1.323 | 3.487 |
| SG_02 | -83.733 | 1.324 | 3.452 | - | - | - |
| SG_03 | -83.777 | 1.324 | 3.430 | -83.778 | 1.325 | 3.425 |
| SG_04 | -83.823 | 1.324 | 3.419 | -83.824 | 1.325 | 3.422 |
| SG_05 | -83.867 | 1.324 | 3.437 | -83.868 | 1.324 | 3.421 |
| SG_06 | -83.868 | 1.279 | 3.477 | -83.867 | 1.278 | 3.469 |
| SG_07 | -83.823 | 1.279 | 3.302 | -83.825 | 1.281 | 3.452 |
| SG_08 | -83.779 | 1.279 | 3.472 | -83.779 | 1.280 | 3.463 |
| SG_09 | -83.733 | 1.279 | 3.472 | -83.732 | 1.279 | 3.470 |
| SG_10 | -83.689 | 1.279 | 3.446 | -83.688 | 1.282 | 3.430 |
| SG_11 | -83.688 | 1.234 | 3.452 | -83.688 | 1.235 | 3.445 |
| SG_12 | -83.733 | 1.234 | 3.452 | -83.733 | 1.234 | 3.444 |
| SG_13 | -83.778 | 1.234 | 3.443 | -83.777 | 1.234 | 3.426 |
| SG_14 | -83.821 | 1.233 | 3.462 | -83.822 | 1.234 | 3.449 |
| SG_15 | -83.868 | 1.233 | 3.495 | -83.868 | 1.233 | 3.491 |
| SG_16 | -83.868 | 1.189 | 3.437 | -83.868 | 1.188 | 3.426 |
| SG_17 | -83.823 | 1.188 | 3.431 | -83.824 | 1.187 | 3.426 |
| SG_18 | -83.779 | 1.188 | 3.354 | -83.780 | 1.187 | 3.385 |
| SG_19 | -83.733 | 1.189 | 3.385 | -83.733 | 1.189 | 3.419 |
| SG_20 | -83.689 | 1.189 | 3.419 | -83.690 | 1.188 | 3.405 |
| SG_21 | -83.688 | 1.143 | 3.440 | -83.689 | 1.142 | 3.429 |
| SG_22 | -83.733 | 1.143 | 3.465 | -83.733 | 1.143 | 3.452 |
| SG_23 | -83.778 | 1.143 | 3.425 | -83.780 | 1.142 | 3.407 |
| SG_24 | -83.823 | 1.143 | 3.428 | -83.825 | 1.142 | 3.417 |
| SG_25 | -83.868 | 1.143 | 3.484 | -83.869 | 1.142 | 3.490 |

Table C.1: Summary of the deployment and relocated positions of the OBSs in the South Grid. Relocated positions were determined as described in Section 2.5.2.

# Appendix D

Final 2D forward models with fit tables for shot profiles SG_A (Figure D.1, Table D.1), SG_E (Figure D.2, Table D.2), SG_F (Figure D.3, Table D.3) and SG_J (Figure D.4, Table D.4).

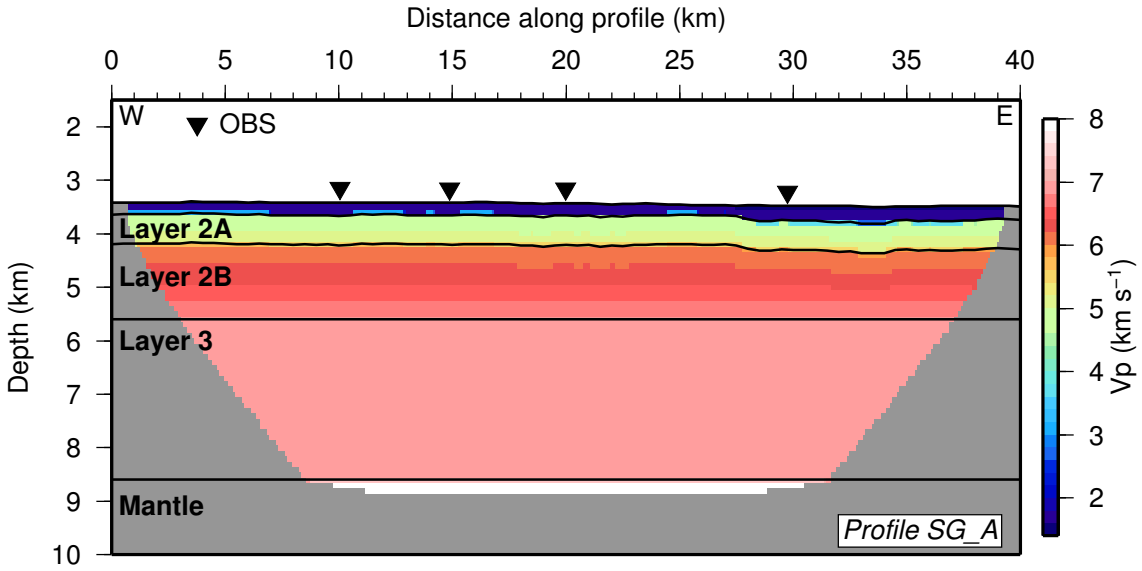


Figure D.1: Final 2D forward model for profile SG_A, masked by ray coverage.

| Phase | Uncertainty (ms) | Number of picks | RMS misfit (ms) | $\chi^2$ |
|---|---|---|---|---|
| $P_{g1}$ | 15 | 85 | 11 | 0.508 |
| $P_{g2}$ | 23 | 610 | 14 | 0.338 |
| $P_{g3}$ | 32 | 554 | 16 | 0.246 |
| $P_n$ | 32 | 374 | 27 | 0.735 |
| Total | - | 1623 | 18 | 0.425 |

Table D.1: Final forward model fit for profile SG_A.

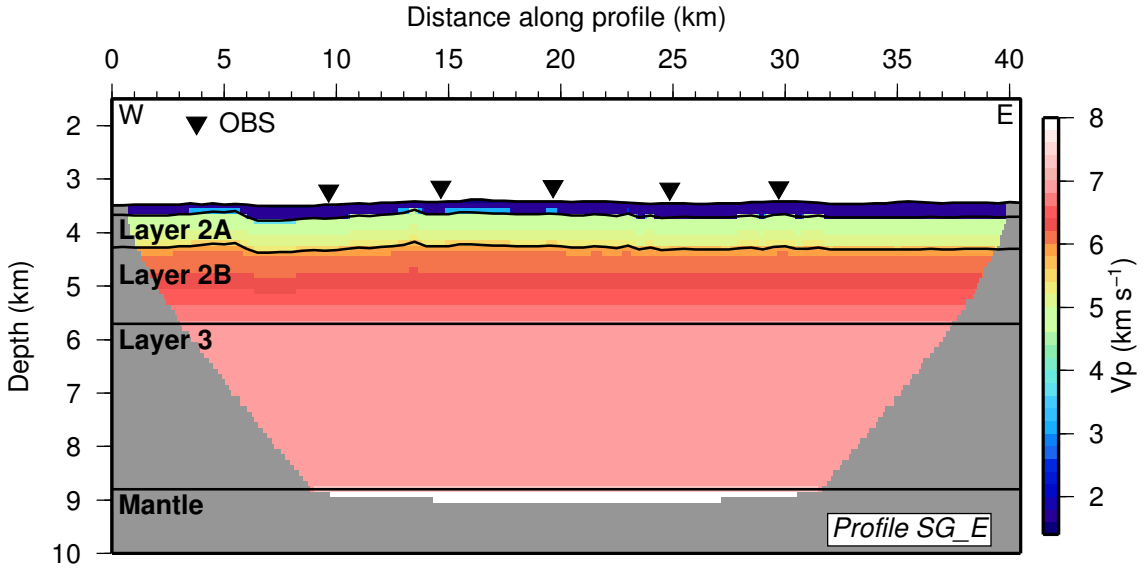


Figure D.2: Final 2D forward model for profile SG_E, masked by ray coverage.

| Phase | Uncertainty (ms) | Number of picks | RMS misfit (ms) | $\chi^2$ |
|---|---|---|---|---|
| $P_{g1}$ | 15 | 134 | 22 | 2.257 |
| $P_{g2}$ | 23 | 670 | 25 | 1.166 |
| $P_{g3}$ | 32 | 532 | 29 | 0.834 |
| $P_n$ | 32 | 389 | 45 | 2.018 |
| Total | - | 1725 | 32 | 1.338 |

Table D.2: Final forward model fit for profile SG_E.

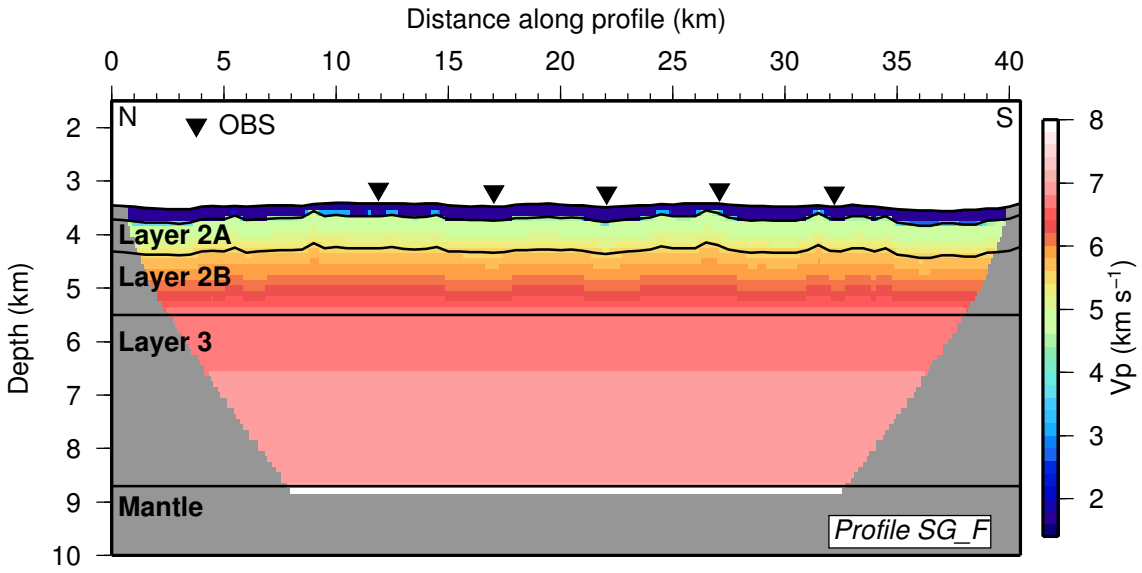


Figure D.3: Final 2D forward model for profile SG_F, masked by ray coverage.

| Phase | Uncertainty (ms) | Number of picks | RMS misfit (ms) | $\chi^2$ |
|---|---|---|---|---|
| $P_{g1}$ | 15 | 102 | 16 | 1.220 |
| $P_{g2}$ | 23 | 517 | 27 | 1.341 |
| $P_{g3}$ | 32 | 488 | 20 | 0.378 |
| $P_n$ | 32 | 367 | 82 | 6.653 |
| Total | - | 1474 | 46 | 2.332 |

Table D.3: Final forward model fit for profile SG_F.

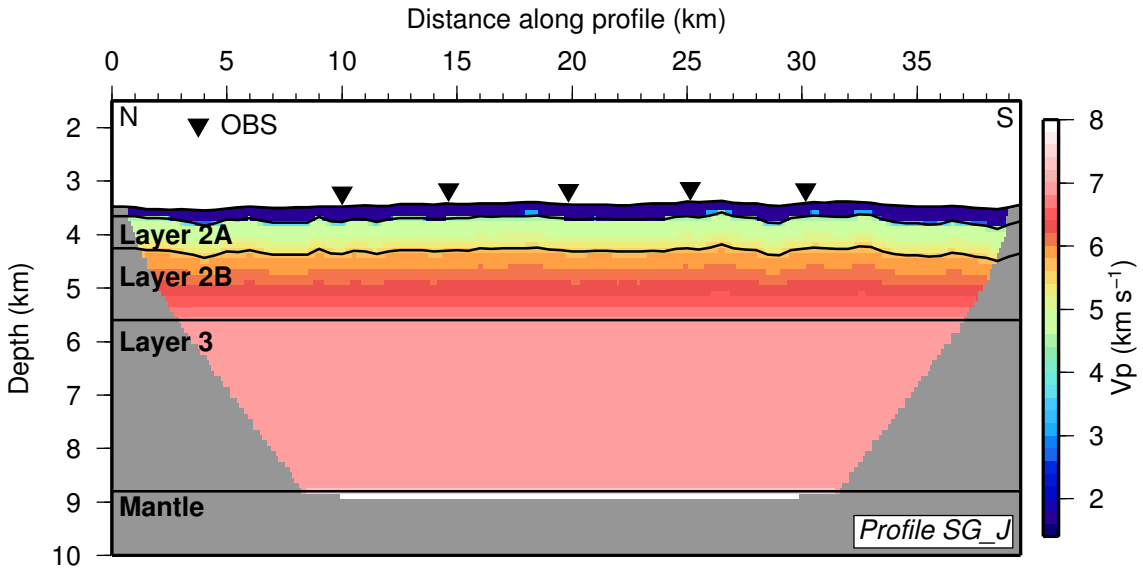


Figure D.4: Final 2D forward model for profile SG_J, masked by ray coverage.

| Phase | Uncertainty (ms) | Number of picks | RMS misfit (ms) | $\chi^2$ |
|---|---|---|---|---|
| $P_{g1}$ | 15 | 133 | 24 | 2.649 |
| $P_{g2}$ | 23 | 826 | 24 | 1.100 |
| $P_{g3}$ | 32 | 718 | 21 | 0.430 |
| $P_n$ | 32 | 156 | 36 | 0.488 |
| Total | - | 1833 | 24 | 0.896 |

Table D.4: Final forward model fit for profile SG_J.

# Appendix E

A description of the rationale, methods and results of the azimuth-dependent inversion technique.

## Azimuth-dependent inversion

Variations in anisotropy spatially across the study area were analysed using the travel time residual method (Section 5.5) in order to investigate changes in fracturing. This approach, however, does not enable the investigation of lateral changes in anisotropy, aside from on the order of half the size of the model space. To investigate smaller-scale variations in fracturing within the study area a technique was developed to perform azimuth-dependent 3D inversions. This involved pre-selecting the travel time picks to be used in inversion based on their shot-receiver azimuth, enabling inversions using solely the observed data whose ray paths travel that direction. The inversion could be run using a range of different azimuthal selections, and the resulting models compared to investigate whether picks from different azimuths produce different velocity models, indicating azimuthal anisotropy.

### Method and inversion parameters

Initially, to test the technique, the Vp pick dataset was split by shot-receiver azimuth into two different groups, with the intention to subsequently test an array of different azimuth combinations. These initial two groups were a N–S trending dataset, containing travel time picks with azimuths from 315°–045° and 135°–225°, and an E–W trending dataset, with azimuths from 045°–135° and 225°–315°. These datasets had a total of 57,049 and 63,742 picks, respectively. Inversions were then run separately for each dataset, following the same procedure as that for the 3D Vp preferred inversion (Section 3.3.12): using the same starting model, seabed and basement interfaces, and inversion parameters where possible. Due to the significantly reduced numbers of picks (compared to 120,263 of the full dataset), however, the two-stage inversion technique used for the Vp and Vs models was not appropriate for use here. Reducing the cell size to as small as 1 km laterally resulted in unstable inversions and artefacts in the final result, due to the poorer ray coverage from the diminished datasets. Thus the azimuthal inversions were only run for the first stage (I) of the established inversion procedure, using the larger cell size of 2 km x 0.3 km. To allow the inversion process to still reach a good fit to the data ($\chi^2$ <10) the freedom parameter $\lambda$ was adjusted from 500 to 200.

To compare the final velocity models (here referred to as the NS and EW models) from the two azimuthal (NS and EW) inversions, the 3D NS model was subtracted from the 3D EW model, to create a 3D difference model.

**Results**

The NS and EW inversions reached $\chi^2$ fits of 3.1 and 3.6, respectively, within five iterations. Both inversions produced smooth, relatively homogeneous velocity models (Figure E.1), with large edge effects from the poorly-sampled, slower, edges of the models. The general lack of detail, greater edge-effects, and larger $\chi^2$ values when compared to the full dataset Vp model ($\chi^2$=1.1) are most likely due to inverting solely with a larger cell size of 2 km x 0.3 km, and the reduced ray coverage from the smaller datasets.

The 3D difference model does not show significant velocity variation between the NS and EW models on average, with a general positive anomaly (indicated a higher velocity in the EW model) across the whole 3D model of only 0.05 km $s^{-1}$. A larger amplitude positive anomaly of up to 0.2 km $s^{-1}$ is visible in the N–S cross-section extending down from the basement at Y=$\sim$35 km and Y=$\sim$42 km beneath two basement ridges. However, even this anomaly represents a small difference in velocity, which may be characteristic of the relatively low amplitude of anisotropy present in the study area, or an indication that this method cannot resolve changes in velocity with azimuth. The relatively poor fit of these final models ($\chi^2$>3, when compared to the close fit of the full inversion model of $\chi^2$=1.1 may explain the absence of a stronger anisotropic signature. The lack of ray coverage of the azimuthal inversion models could also make these small differences more difficult to resolve.

The lateral resolution of these models was investigated using checkerboard testing, following the methods described in Section 4.2. The results show that the smallest standard checkerboard size which can be well-resolved (semblance value $\geq$0.7) in any part of the azimuthal models is 6 x 6 km, and which can be well-resolved throughout the entire central areas is 10 x 10 km. To define the well-resolved areas of the difference model, the semblance values for the NS and EW models were combined, with well-resolved areas required to have semblance values of $\geq$0.7 in both the input models. This significantly reduces the size of the model space able to be interpreted, and does not allow the confident interpretation of small-scale velocity differences, as was the purpose of this technique.

Therefore, due to the poor fit and lateral resolution, and tendency for these inversions to become unstable at smaller cell sizes, this technique was not successful at investigating anisotropy changes spatially across the 3D models in this study. It may be more appropriate, for this type of study, to instead examine anisotropy variations using inversion codes and methods which are capable of resolving anisotropy alongside velocity, such as utilised in Dunn (2015). However, the method presented here could be effective at investigating anisotropy when applied to smaller study areas with dense data coverage.

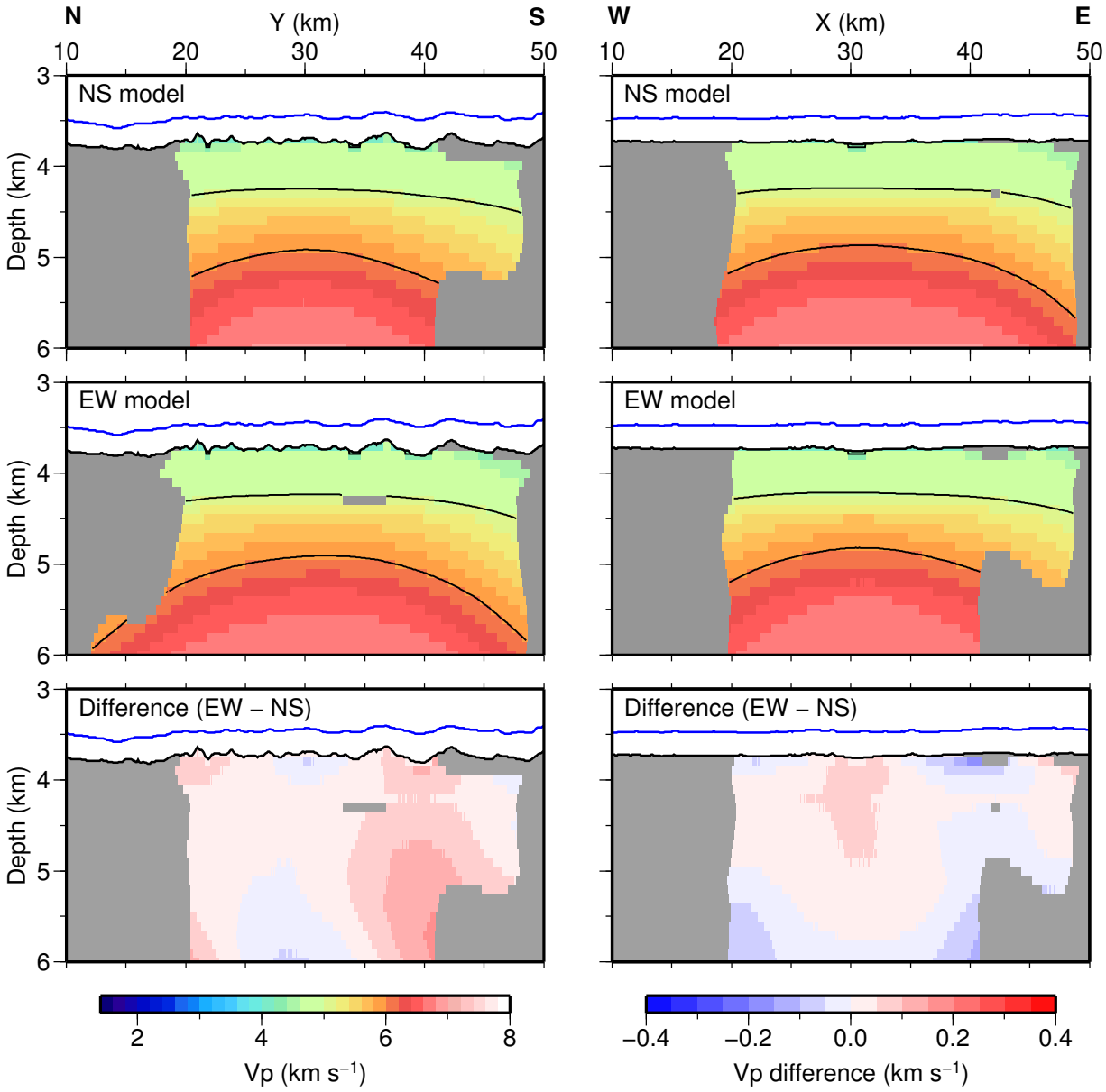


Figure E.1: Cross-sections along the locations of shot profiles SG_I and SG_C through the final models of the NS inversion (top), and EW inversion (middle), masked by the 0.7 semblance contour from a 10 x 10 km-sized checkerboard test. The difference model (bottom) shows red colours when the EW model has a faster velocity, and blue when slower, and is masked by the limits of the 0.7 semblance contour from both input models. Seabed=blue line; basement=black line; contours plotted every 1 km $s^{-1}$ starting at 4 km $s^{-1}$.